DETECTORS FOR THE COSMOLOGY LARGE ANGULAR SCALE SURVEYOR (CLASS)

by

Sumit Dahal

A dissertation submitted to Johns Hopkins University
in conformity with the requirements for the degree of
Doctor of Philosophy

Baltimore, Maryland
June 2020

© 2020 Sumit Dahal
All rights reserved

Abstract

The Cosmology Large Angular Scale Surveyor (CLASS) observes the cosmic microwave background (CMB) polarization over large angular scales with the aim of detecting and characterizing the inflationary gravitational waves and measuring the optical depth to reionization. CLASS is a ground-based, multi-frequency microwave polarimeter that surveys 70% of the microwave sky every day from the Atacama Desert. CLASS consists of four telescopes: a 40 GHz receiver probing the polarized synchrotron emission, a 150/220 GHz dichroic receiver mapping the polarized dust, and two 90 GHz receivers optimized for CMB observation near the minimum of polarized Galactic emission. The high sensitivity CMB polarization measurement for CLASS is made possible by its background-limited detector arrays. The detector arrays for all CLASS telescopes contain smooth-walled feedhorns that couple to transition-edge sensor (TES) bolometers through symmetric planar orthomode transducers (OMTs). This thesis begins by introducing the inflationary paradigm and its observational signature in the CMB polarization. In the second chapter, I describe the CLASS science goals, and discuss the instrument design and survey strategy implemented to achieve these goals. The third chapter introduces the CLASS detectors optimized for high sensitivity and control over systematics required for precise measurement of the CMB polarization over large angular scales. The fourth and fifth chapters focus on the design, assembly, and in-lab characterization of the 90 and the 150/220 GHz detector arrays, respectively. Finally, I present the on-sky performance of the CLASS detectors in the sixth chapter.

Advisor: Prof. Charles L. Bennett
Co-Advisor: Prof. Tobias A. Marriage

Acknowledgments

This work would not have been possible without the unwavering support from many amazing individuals throughout the past five years. First and foremost, I would like to thank my advisor, Professor Charles Bennett. His insightful guidance, dedication to the well being of his students, and enthusiasm towards science never cease to amaze and inspire me. I have also been fortunate to have Professor Tobias Marriage as my co-advisor. He has always been available (even past midnight sometimes) to help me; whether it's on Slack or inside the lab closing a cryostat for the 100th time. From hiking a canyon in Colorado to walking in a desert in Abu Dhabi, he has been an ideal mentor and friend to me.

Working with the CLASS collaboration has truly been an exciting experience. While I am thankful to the entire collaboration for making CLASS such a fun project to work for, I would like to give a shout-out to those who have gone above and beyond to help me since my first day in CLASS. I would probably not have enjoyed working with the detectors as much without the constant help and support from John Appel. John, thank you for teaching me the intricacies of the detectors and readout, and bearing with me as I constantly bombarded you with questions (although I must have paid this off

with the two intramural soccer trophies). I am also thankful to John Karakla who never hesitated to pause his own work to help me in the lab. At the JHU lab, I am also immensely grateful for the help regarding detector assembly and testing from Aamir Ali, Carolina Nunez, and Rahul Datta. My work has also heavily benefited from the constant guidance and feedback from our collaborators at NASA Goddard, especially from Thomas Essinger-Hileman, Karwan Rostem, and Kevin Denis. It has also been my privilege to have Duncan Watts as a collaborator and friend – the only person who could help me understand a science problem while spotting my bench press.

Finally, special thanks to my friends and family whose behind-the-scenes support and encouragement made this possible. To my family, thank you for believing in me; I am forever indebted to the sacrifices you have made to make my dream a reality. To Bastian, Deniz, Erini, Kirsten, Manwei, Rachael, and Raymond, thank you for making the past five years fun and adventurous. To Meredith, thank you for keeping me sane and making me look forward to something everyday.

Preface

This dissertation is based on my graduate work conducted during the past five years at the Johns Hopkins University as a part of the CLASS collaboration. In August 2015, when I joined the collaboration, the CLASS site was being constructed. A mere four years later, CLASS had all its four frequencies on the sky. This incredible feat could not have been possible without the dedicated team effort from all the collaborators across various institutions. Below, I summarize my contributions to CLASS.

- **Site work:** During the past five years, I spent a total of 143 days (spread across six different trips) at the CLASS site. At the site, I led the installation of the 90 GHz and the dichroic 150/220 GHz detector arrays in two different CLASS receivers. In addition, I worked on assembling the cryogenic receivers for those detector arrays and contributed to various aspects of the site operation during my time at the site.
- **Cryogenic Lenses and Filters:** I made all four cryogenic lenses for the two CLASS 90 GHz receivers. These lenses were made from high density polyethylene using a CNC mill. To optimize their in-band transmission, I also anti-reflection (AR) coated them with simulated dielectrics based on a square array of holes about a fifth of a wavelength in diameter, cut

into their surfaces. Chapter 2 describes the lens making and AR coating processes in further detail. Using the same methods, I also made the Nylon and the Teflon filters, described in Chapter 2, that suppress the out-of-band power inside the 90 GHz cryostat receivers.

- **Detector Work:** My major contribution to CLASS comes from my detector-related work for the 90 GHz and the dichroic 150/220 GHz detector arrays. Most of this work has been presented at conferences and published in conference proceedings and peer-reviewed journals. Chapters 4 and 5 are primarily based on the contents from my first author publications but have been modified and/or expanded for this dissertation. While CLASS detectors are fabricated by our collaborators at NASA Goddard, I led the detector testing efforts and assembly for the two detector arrays described in detail in Chapters 4 and 5.
- **Data Analysis:** In Chapter 6, I show the on-sky performance results for all the four CLASS frequency bands. I describe the telescope optical efficiency estimates that utilized dedicated planet observations, the passband measurements using Fourier transform spectrometers, and the sensitivity measurements based on CMB observations. While I am leading this ongoing data analysis effort, it includes contributions from other CLASS collaborators.

Table of Contents

Abstract ii

Acknowledgments iv

Preface vi

Table of Contents viii

List of Acronyms xii

List of Tables xiv

List of Figures xv

1 Introduction 1

1.1 Evolution of the Universe 2

1.2 The Cosmic Microwave Background 6

1.2.1 Temperature Anisotropy 7

1.2.2 Polarization Anisotropy 13

1.3 Inflation 19

2 **CLASS Overview** 36

2.1 Science Goals . . . 37

2.1.1 Inflation . . . 37

2.1.2 Reionization . . . 39

2.1.3 Neutrino Mass . . . 40

2.1.4 Other Science . . . 42

2.2 Galactic Foregrounds . . . 43

2.2.1 Synchrotron . . . 45

2.2.2 Thermal Dust . . . 45

2.3 CLASS Strategy . . . 46

2.4 Instrument Design . . . 49

2.4.1 Telescope Mount . . . 50

2.4.2 Polarization Modulator . . . 51

2.4.3 Cryogenic Receiver . . . 56

2.4.3.1 Filters . . . 59

2.4.3.2 Lenses . . . 61

3 **CLASS Detectors** 74

3.1 Optical Coupling . . . 75

3.1.1 Smooth-walled Feedhorns . . . 76

3.1.2 Planar Ortho-mode Transducers . . . 78

3.1.3 Photonic Chokes and Quarter-Wave Backshorts . . . 79

3.2 CMB Detectors . . . 81

3.3 Transition-Edge Sensors . . . 86

3.3.1 Responsivity . . . 90

3.3.2 Stability . . . 95

3.3.3 Sensitivity . . . 97

3.4 Detector Readout . . . 104

3.4.1 Superconducting Quantum Interference Devices . . . 104

3.4.2 Time-Division Multiplexing . . . 107

3.4.3 Multi-channel Electronics . . . 113

3.4.4 SQUID Tuning . . . 115

4 90 GHz Detector Array 130

4.1 Focal Plane Design and Assembly . . . 131

4.2 Detector Design . . . 137

4.3 Detector Characterization . . . 138

4.3.1 Dark Properties . . . 138

4.3.2 Optical Passband . . . 144

4.3.3 Noise Performance . . . 146

4.3.4 Sensitivity Projections . . . 148

5 Dichroic 150/220 GHz Detector Array 155

5.1 Detector Design . . . 156

5.2 Module Design and Assembly . . . 158

5.3 Detector Characterization 162
5.3.1 Electrothermal Parameters 162
5.3.2 Optical Passband 164
5.3.3 Noise and Sensitivity 166

6 On-sky Performance of CLASS Detectors 172

6.1 Focal Plane Arrays 173
6.1.1 Q-band 173
6.1.2 W-band 175
6.1.3 G-band 177
6.2 Optical Loading 178
6.2.1 Frequency Bands 178
6.2.2 Optical Power 183
6.3 Noise Performance 183
6.4 Planet Observations 187
6.4.1 Calibration to Antenna Temperature 190

A 150/220 GHz Detector Array Assembly Procedure 198

B Venus Observations 205

B.1 Observations and Results 206
B.1.1 Brightness Temperature 207
B.1.2 Phase 211
B.2 Discussion 211

List of Acronyms

AR	Anti-reflection
CE7	Controlled-Expansion 7 (SiAl alloy)
CLASS	Cosmology Large Angular Scale Surveyor
CMB	Cosmic Microwave Background
DR	Dilution Refrigerator
FAS	Flux-activated Switch
FLL	Flux-Locked Loop
FTS	Fourier Transform Spectrometer
HDPE	High-Density Polyethylene
HF	High-Frequency
Λ**CDM**	Lambda Cold Dark Matter
MCE	Multi-channel Electronics
MUX	Multiplexer

NEP	Noise-equivalent Power
NEQ	Noise-equivalent (Stokes) Q
NET	Noise-equivalent Temperature
OMT	Ortho-mode Transducer
PCB	Printed Circuit Board
PSD	Power Spectral Density
PTFE	Polytetrafluoroethylene
PWV	Precipitable water vapor
RS	Row Select
SQUID	Superconducting QUantum Interference Device
SSA	SQUID Series Array
TDM	Time-Division Multiplexing
TES	Transition-Edge Sensor
TOD	Time-ordered Data
VPM	Variable-delay Polarization Modulator

List of Tables

1.1 Best-fit ΛCDM parameters for a spatially-flat Universe from the full *Planck* mission TT, TE, EE+lowE+lensing data 12

3.1 Multiplexing and readout parameters for CLASS detectors . . 114

4.1 First W-band detector array average measured and target parameters 142

5.1 Mean and standard deviation of detector parameters, NEP_G (estimated from T_c and κ using Equation 3.18), and yield for the three CLASS HF modules 164

6.1 Summary of Median TES Bolometer Parameters 174

6.2 Measured (and Simulated) Bandwidths $\Delta\nu$ and Effective Center Frequencies ν_e for Diffuse Sources (in GHz) 181

6.3 On-sky Optical Performance Summary of CLASS telescopes . 193

List of Figures

1.1 The CMB spectrum as measured by the *COBE* FIRAS instrument (Fixsen et al., 1996). The data remarkably fits a blackbody spectrum at 2.725 K. 7

1.2 (Top) The *Planck* 2018 all-sky map of CMB temperature anisotropy. (Bottom) The corresponding *Planck* 2018 CMB temperature power spectrum. The light blue curve shows the base-ΛCDM theoretical spectrum best fit to the *Planck* TT, TE, EE+lowE+lensing likelihoods. These best fit parameters are summarized in Table 1.1. The lower panel shows the residuals from the model fit along with 1σ error bars including the cosmic variance. Figure credit: ESA and Planck Collaboration (2018) 10

1.3 Depiction of net linear polarization created after Thomson scattering of unpolarized incident radiation with quadrupole anisotropy. The blue oscillations represent the hot, while the orange oscillations represent the cold radiation. Figure credit: CAPMAP at the University of Chicago and M. Petroff 13

1.4 The polarization on the sky can be decomposed into curl-free E-mode and divergence-free B-mode patterns as shown here. E-modes have radial pattern around the cold spots (blue) and tangential pattern around hot spots (red). However, B-modes have characteristic swirling patterns around the cold and hot spots with different orientations as shown here. Analogous to the electric and magnetic fields, E-modes have even parity, while B-modes have odd parity. E-modes can be converted to B-modes and vice-versa by rotating each polarization vector by 45°. Figure from Krauss, Dodelson, and Meyer (2010) 16

1.5 Summary of the CMB angular power spectra measurements made till 2017. The CMB temperature anisotropy (TT) has been measured to near the cosmic variance limit. The E-mode polarization anisotropy (EE) and the TE cross-correlation have been well measured at angular scales $\lesssim 5^\circ$, but their uncertainty at large angular scales is much higher. While the lensing B-modes (BB) have been detected at small angular scales, the B-modes from primordial graviational waves which peak at large angular scales have not been detected yet. Figure credit: D. Watts 18

1.6 A toy model illustration of a single-field slow-roll inflaton potential. At early times, inflation occurs as the potential $V(\phi)$ dominates the energy density of the universe such that $V(\phi) \gg \frac{1}{2}\dot{\phi}^2$. As the field slowly rolls from this "false vacuum" state towards the "true vacuum" state ($V = 0$), inflation ends at ϕ_{end} when $\frac{1}{2}\dot{\phi}^2 \approx V(\phi)$. Finally, during reheating, the inflaton potential is converted to photons and the standard big-bang universe begins. The CMB fluctuations we observe today are created as inflation expands the quantum fluctuations $\delta\phi$ to cosmological scales. Figure from Baumann (2009) 26

2.1 (Left) B-mode power spectra for $r = 0.1, 0.01$, and 0.001 showing the recombination peak at $\ell \sim 100$ and the reionization peak at $\ell \lesssim 10$. At small angular scales, B-modes are dominated by gravitational lensing of E-modes. The red band shows the projected CLASS sensitivity to measure B-modes at $r \sim 0.01$ level independent of the lensing foreground. Figure credit: D. Watts. (Right) Thanks to experiments with increasing CMB polarization sensitivity, the upper limits on r have been decreasing over the past two decades. As the upper limits on r continue to improve, lensing will become an increasingly important error term for experiments observing at small angular scales ($\ell \gtrsim 100$). The red point highlights the improvement in the measurement of r with the projected CLASS B-mode sensitivity at large angular scales. Figure prepared by author for thesis. 38

2.2 (Left) The best fit models for *WMAP* 9-year ($\tau = 0.083$) and *Planck* "pre 2016" data ($\tau = 0.055$) along with measurements from BICEP2/Keck and SPTpol experiments. The red band shows the CLASS sensitivity (assuming *WMAP* 9-year value for τ) that can distinguish between the two best fit models. (Right) Constraints in A_s and τ from *WMAP* 9-year and *Planck* 2015 temperature and polarization data that highlights the degeneracy between the two quantities. CLASS can improve the uncertainty in τ to near the cosmic variance limit by breaking this degeneracy through the E-mode polarization measurement at large angular scales. Figure credit: D. Watts 39

2.3 (Left) *WMAP* and *Planck* measurements of the present density fluctuations parameterized through σ_8 is limited by the degeneracy between A_s and τ (Figure 2.2). Through low-ℓ E-mode measurement, CLASS can break this degeneracy to improve the constrains on σ_8. (Right) The improvement in the *Planck* 2015 and BAO constraints on the sum of neutrino masses Σm_ν with the addition of nearly cosmic variance limited measurement of τ by CLASS. Figure from Harrington et al. (2016) 41

2.4 Summary of brightness temperature rms as a function of frequency and foreground sources for temperature (top) and polarization (bottom). For the temperature plot, the lower and upper edges of each line represent 81% and 93% sky fraction, respectively. The temperature and polarization plots were obtained from Planck Collaboration et al. (2016) and Planck Collaboration et al. (2018), respectively. 44

2.5 Summary of multipole vs frequency coverage for current ground-based and balloon-borne CMB polarization experiments. CLASS is uniquely designed to measure both the reionization and recombination peaks of the primordial B-mode signal (top panel) at large angular scales while straddling the foreground minimum (right panel). Figure from Watts et al. (2015) 47

2.6 Sky coverage and atmospheric loading are the two important factors in deciding CLASS's location at 5200 m altitude in the Atacama Desert of Chile. (Left) This location, near the equator at $\approx -23^\circ$ latitude, allows CLASS to survey 70% of the sky at 45° elevation. (Right) Estimate of brightness temperature vs frequency for different PWV levels. While the high and dry CLASS site conditions reduce the noise from atmospheric loading, the CLASS frequency bands (blue) were chosen to avoid the prominent atmospheric oxygen and water emission lines. Figure from Essinger-Hileman et al. (2014). 48

2.7 (Left) Photograph of one of the two identical telescope configurations. Each configuration has a mount that houses two receivers inside a metal structure that acts as a comoving ground shield. (Right) Diagram of the 40 GHz telescope showing light rays from the sky converging onto the focal plane. All four CLASS telescopes have similar design including the baffle, VPM (section 2.4.2), two mirrors, and the cryogenic receiver (section 2.4.3) shown here. 51

2.8 (Left) Schematic of the CLASS VPM with a stationary wire grid placed in front of a movable mirror. While the incoming light polarized parallel to the wires reflects off the grid, the orthogonal polarization passes through the grid and reflects off the mirror. The relative phase delay between the two polarization states is proportional to the grid-mirror distance. (Right) The assembled CLASS 90 GHz VPM showing the copper-plated tungsten wire grid placed in front of a 60 cm diameter flat aluminum mirror. Figure from Harrington et al. (2018). 52

2.9 (Top-Left) Illustration of polarization modulation. If the modulation is fast compared to the drift time-scale, the polarized signal can be recovered with high fidelity. (Top-Right) VPM modulation transfer functions for incident U and V polarizations. The dashed vertical lines indicate the throw for the CLASS 40 GHz VPM. As the grid-mirror distance varies, the incoming polarization gets modulated between U and V. Figure from Padilla et al. (2020) (Bottom) Simulations illustrating the effectiveness of VPM in recovering polarization at large angular scales in the presence of polarized $1/f$ noise. The leftmost map shows the input Q map showing features at large angular scales, which are recovered by a VPM that modulates the sky signal before the addition of the polarized $1/f$ noise. Without a VPM, the reconstructed map is contaminated by the $1/f$ noise. Figure from Miller et al. (2016). 55

2.10 CLASS 90 GHz cryogenic receiver design highlighting some key components inside the receiver. All four CLASS telescopes share a similar receiver design that is optimized to provide a cold and stable operating environment for the detectors in order to achieve low-noise and high-sensitivity sky observations. Figure from Iuliano et al. (2018) 57

2.11 Manufacturing and measuring the CLASS 90 GHz 1 K lens (Top-left) An HDPE block being machined on a Tormach CNC mill at the Johns Hopkins University (Top-center) A completed 1 K lens for the 90 GHz receiver (Top-right) A comparison of the simulated dielectrics AR coating for 90 GHz (above) and 40 GHz (below) lenses. As the AR parameters scale with the wavelength, the drilled holes in the 90 GHz coating are small (depth and pitch are both $\sim$ 0.6 mm) compared to 40 GHz (depth: 1.4 mm, pitch: 1.8 mm). So the 90 GHz coating is only visible here through the difference in texture between the lens surface and the flange. (Bottom) The measurement of the lens surface using a Faro arm show that the surface errors due to machining are within $\pm$ 0.003 inch on both sides. The colored grid is an interpolation between the measured data points (black dots). To prevent damage to the AR-coated surface, the lens measurement is done before the holes are drilled onto the surface. 62

3.1 Illustration of the optical coupling for CLASS detectors. (Left) Light from the telescope optics is incident on an array of smooth-walled feedhorns with planar OMTs at their base. A metalized enclosure forms a quarter-wave backshort termination for the OMTs and suppresses the coupling of stray light to the microwave circuit. (Right) Schematic of the CLASS detector chip showing the components of the microwave circuit used to couple the two linear orthogonal polarization modes of the incoming radiation to the TES bolometers. Figure credit: D. Chuss. . 76

3.2 Schematic of the cross-section of the CLASS detector chip showing the TES and the OMT antenna regions. The photonic choke wafer, the detector wafer, and the backshort assembly are bonded together using the indium bumps to form the CLASS detector chip. The photonic choke with array of square silicon pillars coated with aluminum acts as an interface between the feedhorns and the detector wafer. The detector wafer is patterned out of a 100 mm silicon-on-insulator wafer with the 5 μm float zone single-crystal silicon device layer, the Benzocyclobutene (BCB) polymer bonding layer, and the niobium ground plane. The backshort assembly consists of a spacer wafer that sets the quarter-wave distance and a cap wafer that provides the reflective surface for OMT termination and forms the metalized enclosure for stray light control. Figure from Rostem et al. (2016). 80

3.3 Illustration of the electrothermal circuit of a TES bolometer. (Left) The thermal circuit of a TES can be modeled as a bolometer with heat capacity C, temperature T, and resistance R that is connected to a thermal bath at temperature T_{bath} through a weak thermal link. The thermal conductance G of this link determines the power P_{bath} that flows from the bolometer to the bath. The TES is heated by the power from the absorbed radiation P_γ and the Joule power $P_J = V^2/R$, where V is the voltage bias across the TES. (Right) The electrical circuit of a TES can be modeled as a variable resistor R that is voltage biased by applying a DC current bias I_{b} to the circuit. The TES is connected in series with an input inductor L_{in} and in parallel with a shunt resistor $R_{\text{sh}} \ll R$ so that P_{J} decreases as R rises. A change in P_γ is transduced into a changing current I through the TES and the inductor, which changes the magnetic flux through the nearby DC SQUID S1 (described in Section 3.4.1). The feedback inductor L_{fb} cancels the changes in flux in S1 and thus maintains the SQUID in its linear regime. This flux feedback response is also our measured signal. Each color in the electrical model represents a different microfabricated chip in the CLASS detector assembly: the TES (green) is on the detector chip, while the shunt resistor (blue) and the SQUID (pink) are on separate chips thermally connected to the bath (see Figure 3.6). Figure from Niemack (2008). 88

3.4 Different detector noise components of a CLASS Q-band TES bolometer. The measured $\mathrm{NEP}_{\mathrm{det}}$ of 11 $\mathrm{aW}\sqrt{\mathrm{s}}$ at the 10 Hz CLASS signal band (set by the VPM modulation frequency) is dominated by the expected phonon noise (or G noise) of 8.5 $\mathrm{aW}\sqrt{\mathrm{s}}$. The difference can be accounted for by a combination of Johnson noise, SQUID noise, and $1/f$ noise. For comparison, the average photon noise for the CLASS Q-band detectors in the field is $\sim$ 16 $\mathrm{aW}\sqrt{\mathrm{s}}$. As NEPs are added in quadrature, $\mathrm{NEP}_{\mathrm{det}}$ makes a sub-dominant contribution to the total NEP, making CLASS detectors background-limited. Figure from Appel et al. (2014). 98

3.5 (Top) Schematic representation of a DC SQUID consisting of two Josephson junctions (blue) connected in parallel in a superconducting loop. The SQUID acts as a flux-to-voltage transducer that can be used to make sensitive measurements of changes in the TES bolometer current. Figure from O'Sullivan and Murphy (2012). (Bottom-Left) As described by equation 3.24, a change in the magnetic flux inside the SQUID loop results in periodic oscillations of the measured voltage within the two limits (solid lines) as shown by the dotted and dashed lines for different bias currents: I_c, $2I_c$, $3I_c$, and $4I_c$. (Bottom-Right) The SQUID voltage to applied flux (V–ϕ) curves corresponding to the different bias currents. The voltage oscillations are maximum when the bias current $I = 2I_c$. For $I > 2I_c$, the V–ϕ curves are more sinusoidal but have smaller peak-to-peak amplitudes. These plots were obtained for Josephson junctions with $R = 1\ \Omega$ and $I_c = 100\ \mu\text{A}$ from Battistelli et al. (2008a). . 106

3.6 Schematic showing the readout for a single CLASS bolometer with zoomed-in images of the components at each stages. At 100 mK stage, the detector pixel is connected to the MUX chip through the Al flex circuit and the interface chip. The MUX chip contains the first-stage SQUID (SQ1) and the flux-activated switch (FAS). Refer to Figure 3.7 for the detailed circuit diagram of the MUX chip. The interface chip houses the Nyquist inductor and the shunt resistor. The MUX and interface chips are glued onto a printed circuit board (PCB) that connects the detector bias (DB), SQ1 bias (SQ1B), SQ1 feedback (SQ1FB), and row select (RS) lines to the twisted pairs of NbTi Tekdata cables (shown as straight red lines). The curved red lines are the Al wire-bonds used to electrically connect the components on the 100 mK stage. The connection between the MUX, interface, and detector is designed to be fully superconducting to avoid stray resistance affecting the bias loop circuit of the TES. The SQ1 signal is amplified by the SQUID series array (SSA) module within a magnetic shielding box mounted on the 4 K stage of the receiver. Finally, the 4 K PCB with the SSA modules is connected to the room temperature multichannel electronics (MCE) that handles the data acquisition and the biasing of the TES and the cold readout components. While the images shown here are for the CLASS G-band detectors, the overall schematics are same for all CLASS frequency bands. 109

3.7 Schematic of a single column for the MUX11d system used to read out the CLASS detectors. Each TES is inductively coupled to a distinctive SQ1 via the input coil. The summed signal from the SQ1s in a column is then amplified by the SSA before transmitting it to the warm electronics (the MCE). The MCE (illustrated in Figure 3.8) sequentially addresses each row by driving its FAS normal. At any given time, all but one row of SQ1s are bypassed through the switches. The SQUIDs operate in a flux-locked loop in order to linearize the readout through the SQ1 feedback. The red lines are the same Al wirebonds shown in Figure 3.6 that electrically connect the MUX chip to other 100 mK components. Figure from Henderson et al. (2016). 111

3.8 Extension of the schematic in Figure 3.7 illustrating the two-dimensional TDM architecture and showing the interaction of different MCE components with the cold readout. The blue outlines show the MUX chips, the green box highlights the SSA module, and the red outlines show the MCE-sourced signals. Except the row-select lines used to address different rows, the MCE signal lines run along each column and therefore must be shared with every detector in that column. The fast-switching lines (the red stars) can assign individual values to different rows within the column to fine-tune the SQUID biasing parameters. Figure from Grayson (2016). 112

3.9 A Bode plot showing the magnitude (gain) and phase of the frequency response for the CLASS MCE Butterworth filter applied to the data timestream before downsampling the data. The gain and the phase are defined with respect to a 4-pole filter transfer function (equation 3.26). While the frequency response at the 10 Hz CLASS signal band is flat, the response at high frequencies is significantly reduced to prevent high-frequency noise aliasing. Although the MCE filter parameters for all the CLASS MCEs are the same, the f_{cutoff} for the G-band filter ($\sim$ 30 Hz) is half compared to the Q- and W-band filters as f_{cutoff} scales with f_{MUX} shown in Table 3.1. 116

3.10 The SQUID tuning and screening procedure for a typical CLASS G-band readout channel. (Top-Left) The SQUID SA V–ϕ curves help select the SA bias that maximizes the peak-to-peak voltage response and the lock-point to linearize the SA (the dashed cross-hair) for further tuning steps. (Top-Right) The RS flux required to drive the FAS normal while keeping the SA locked is identified. (Middle-Left) The SQ1 feedback is ramped up, and the SA feedback required to keep the SA locked is measured for different SQ1 biases in order to optimize the SQ1 bias and the SA feedback for the FLL operation. (Middle-Right) Before initializing the FLL, these SQ1 V–ϕ curves are used to further optimize the SQUID parameters identified above, measure the gain of the entire SQUID chain, and identify the problematic SQUID channels. (Bottom) The diagnostic TES V–ϕ curves are used to screen the problematic detectors that are either broken or stay normal with very long V–ϕ period (visible here through the slopy V–ϕ response with reduced period for illustration). . 118

4.1 Fully assembled first CLASS W-band focal plane mounted in the cryostat. The focal plane consists of seven individual detector modules mounted on a Au-plated copper web interface, which is then mounted onto the mixing chamber plate of a pulse-tube cooled dilution refrigerator. Each module contains 37 smooth-walled copper feedhorns that guide light to the dual-polarization-sensitive detectors on the focal plane. 131

4.2 (Top) 3D model showing cut sections of the W-band focal plane. Starting from CE7 baseplate and moving counter-clockwise, we show the detector wafer and readout circuit stack. First, the hybridized detector wafer is mounted on a Au-plated CE7 baseplate using three BeCu tripod spring clips and a side spring (not shown). The readout circuit with MUX and shunt chips on a PCB is then stacked on top of the detector wafer. The entire readout circuit assembly is sandwiched between two niobium sheets for magnetic shielding. (Bottom) Cross-section view (not to scale) of the detector chip and readout circuit stack. The sketch highlights how the base of a feedhorn mates with a cylindrical extrusion on the CE7 baseplate. The photonic-choke (orange), the detector wafer (pink), and the backshort assembly (yellow) are all hybridized during fabrication and mounted onto the baseplate as a single assembly. The top of the backshort assembly and the heat-sink pads on the detector wafer are gold bonded to the baseplate for heat sinking. The sketch also shows sets of aluminum bonds used to connect the detector bond pads to the readout circuit. Two copper sheets in the readout stack are connected to the backplate of each module for heat sinking. 132

4.3 (Top) 20-point approximation of the W-band smooth-wall feedhorn profile. The inset shows a single feedhorn machined from oxygen-free high-conductivity copper. (Bottom) W-band feedhorn co-polar E-plane and H-plane, and cross-polar beam measurements averaged across the 77–108 GHz frequency band, along with their models. The measurements were done in the Goddard Electromagnetic Anechoic Chamber and show excellent agreement (within 2%) with the models. The cross polarization across the passband is less than -30 dB, and the beam has a FWHM of 18.7°. The two vertical lines at ±16° show where the beams truncate on the receiver cold stop. The edge taper at 16° is ≈ -9 dB. 134

4.4 (Left) CLASS W-band detector wafer showing the 37 dual-polarization-sensitive detectors. All the detectors are connected to the bond pads on the lower edge of the wafer. (Right) Zoomed-in images of the detector circuit (top) and the TES island (bottom). For a detailed description about the W-band detector architecture refer to Rostem et al. (2016). 137

4.5 The main plot shows the P_{sat} values obtained for one of the W-band detectors at multiple bath temperatures. The orange line shows the model in Equation 4.1 fit to the data. The fit for this particular detector gives T_{c} and κ values of 161 mK and 22.4 nW/K^4, respectively. The inset shows the I-V curves used to calculate the P_{sat} values. The curves from red to blue correspond to bath temperatures from 70 mK to 165 mK with steps of 5 mK. Each curve terminates at the point where the TES becomes superconducting. 139

4.6 The distribution of T_{c} (top) and P_{sat} at $T_{\mathrm{bath}} = 50$ mK (bottom) values for all the optically-sensitive detectors in the first W-band focal plane. The X and Y axes represent the focal plane position compared to the detector at the center. The left and right sides of each circle show the H and V detectors respectively which are sensitive to separate orthogonal linear polarizations. The black spots show the detectors that did not yield expected I-V response for analysis. These plots show the status of the first W-band detector array before deployment. The modular design of the focal plane makes it is possible to improve the TES uniformity across the focal plane by swapping modules to choose the best module combination possible among the assembled modules before deployment. 141

4.7 Histograms of ΔT_c, $\Delta\kappa$, and ΔP_sat for 426 optically-sensitive detectors on the first W-band focal plane. These values were calculated by taking the difference of the individual detector parameter values with the average within their modules. Since each module has a separate detector bias line and all the detectors within a module share the same bias line, uniformity across the Δ values reflects the optimal detector biasing condition. P_sat values were calculated at T_bath = 50 mK. The σ values on the upper left corner inside each box are the standard deviations for each distribution. 143

4.8 The main plot shows the simulated and the measured passbands of the W-band detectors measured using a Fourier Transform Spectrometer. The half-power points on the two band edges for this measurement are at 78 and 108 GHz, and the out-of-band response is less than -30 dB. This measured passband is in good agreement with the simulation, and we see no evidence of optical power coupled at higher frequencies. The inset shows the apodized interferogram used to obtain the passband through a fast Fourier transform. The interferogram is a result of co-adding noise-weighted FTS signals from 21 detectors in one of the modules in the focal plane. The x-axis of the interferogram represents the position (centered at the white-light point) of the FTS movable mirror on a linear stage. The y-axes for both plots have been normalized to arbitrary units (a.u.). 145

4.9 Noise spectra of 48 science-grade detectors in one of the modules in the W-band focal plane. The CLASS signal band is shown by the vertical yellow patch centered at the VPM modulation frequency of 10 Hz. The horizontal orange line indicates an estimated photon NEP in the field of 32 $\mathrm{aW}\sqrt{\mathrm{s}}$. The total NEP for CLASS detectors is dominated by photon noise. . . . 147

5.1 The HF detector array at the CLASS telescope site in Chile during the receiver assembly. The array consists of three identical hexagonal modules mounted onto the mixing chamber plate of a pulse-tube cooled dilution refrigerator using a Au-coated copper web interface seen here. There are 1020 polarization-sensitive TES bolometers on the focal plane split equally between 150 and 220 GHz frequency bands. The focal plane assembly procedure is described in detail in Appendix A. 156

5.2 (Left) CLASS HF detector wafer with 85 dichroic dual-polarization pixels fabricated on a monocrystalline silicon layer. Detector readout signals are routed to the bond pads located near four edges of the wafer. (Right) Zoomed-in image of a single detector pixel (top) and a TES island (bottom). The optical signal on the microstrip transmission lines coming from the OMTs is separated into two bands by a diplexer plus on-chip filters and terminated on the TES bolometers. For a single frequency band, the detector architecture is similar to the CLASS 90 GHz design presented in Chapter 4. 157

5.3 (Top) The front and back images of one of the HF feedhorn arrays made of Au-plated CE7. (Bottom-Left) The HF feedhorn profile that has approximately 15 mm length, 1.5 mm input waveguide diameter, and 6.5 mm horn diameter. The feedhorn has an input waveguide cutoff of 2.59 mm, i.e., 115.67 GHz. (Bottom-Right) The co-polar E-plane, H-plane, and cross-polar feedhorn response models. The responses shown for the 150 and the 220 GHz frequencies have been averaged across 132–162 GHz and 202–238 GHz passbands, respectively. The cross polarization response across both bands is less than -20 dB. The two vertical lines at ±19.5° show where the beams truncate at the receiver cold stop. The edge illumination at 19.5° is $\approx$ -11 dB for the 150 GHz frequency band and $\approx$ -12 dB for the 220 GHz band. 159

5.4 (Left) Model of unfolded HF module during assembly. The detector wafer (black) is mounted on top of Au-plated CE7 feedhorn array using two BeCu tripod clips. Four layers of Al flex circuits with decreasing circumradius (starting from bottom: coral, brown, light blue, and pink) are stacked on top of the wafer and connected to separate readout packages. These packages contain MUX and interface chips (blue) mounted onto a PCB (green) sandwiched between two Nb sheets (not shown). The inset shows intricate layers of Al bonds from the wafer to different flex circuit layers (the topmost layer is not visible here). Au bonds heat sink the detector wafer to the feedhorn array. (Right) An assembled HF module. After assembly, all four readout packages are folded up and bolted to the CE7. Support structures are bolted to the bottom through a backplate. Refer to Appendix A for a detailed discussion on the assembly procedure. 160

5.5 T_{c}, κ, and P_{sat} (at $T_{\mathrm{bath}} = 50$ mK) distributions for the 408 (292) working 150 (220) GHz TES bolometers in the CLASS HF detector array. The mean and standard deviation of these parameters for individual HF modules are shown in Table 5.1. 163

5.6 Measured passbands (filled) of CLASS detector arrays compared to simulation (dashed) and atmospheric transmission model (dash-dot) at the CLASS site with PWV of 1 mm. The atmospheric model is based on Pardo, Cernicharo, and Serabyn (2001). The passbands were measured in lab with a polarizing FTS and have been corrected for the feedhorn's frequency-dependent gain and the transmission through cryostat filters. 165

5.7 Noise spectra of CLASS HF detectors operated in the dark. The horizontal lines show the $\mathrm{NEP}_{\mathrm{dark}}$ components and estimated photon noise. The vertical yellow patch shows the CLASS audio signal band centered at the VPM modulation frequency of 10 Hz. The measured average NEP of 22 $\mathrm{aW}\sqrt{\mathrm{s}}$ for 150 GHz and 25 $\mathrm{aW}\sqrt{\mathrm{s}}$ for 220 GHz match well with the expected G noise values (from Table 5.1) as the SQUID noise and the Johnson noise are negligible when added in quadrature. Given the noise spectra and estimated photon noise, all the working HF detectors are photon-noise limited. 167

6.1 Model of the compact (355 × 260 × 64 mm) FTS used to measure the passbands of the CLASS 150 and 220 GHz detectors. (Refer to Wei 2012 for details on the FTS used for the passband measurements of the 40 and 90 GHz detectors.) The four polarizers in the FTS are labeled A through D. The black lines trace one of the two paths of the central ray through the FTS for one polarization, whereas the red lines show the other path between the two beam splitters labelled B and C for the same polarization. The optical delay between the two paths created by the moving mirror results in an interference pattern at the output, which is used to measure the passband of the detector placed in front of the output. Figure from Pan et al. (2019). . . 179

6.2 Average measured (dotted-black) and simulated (solid-blue) spectral response for different CLASS frequency bands overplotted with the atmospheric transmission model at the CLASS site with PWV = 1 mm (red dash-dot). The atmospheric transmission model was obtained from the ALMA atmospheric transmission calculator based on the ATM code described in Pardo, Cernicharo, and Serabyn (2001). The bandwidths and center frequencies for these passbands for different diffuse sources are shown in Table 6.2. (Refer to the text for the comparison of this plot to the one presented in Chapter 5.) 180

6.3 Array-averaged NEP vs P_γ for different CLASS frequency bands. The blue data points were acquired with the VPM ON, characterized by the presence of the VPM synchronous signal (VSS), whereas the red data points were acquired either with the VPM OFF or with the cryostat window covered. The orange curves are the fits for Equation 6.3 with $\mathrm{NEP_d}$ and $\Delta\nu$ as free parameters, and the shaded regions are the 1σ uncertainties. The best-fit values are shown for each frequency band. While the Q-band NEP model was fitted to the blue points, the fit for the three higher frequencies were obtained from the red points (see text for details). The green points are the lab-measured $\mathrm{NEP_d}$ values. The histograms show the spread of P_γ during the observing campaign. 184

6.4 The distribution of total optical efficiency for CLASS detectors. The efficiency numbers for the 40, the 90, and the 150 and 220 GHz detectors were obtained from the dedicated Moon, Venus, and Jupiter observations, respectively. The dashed lines represent the respective array median values shown in Equation 6.11. The 40 GHz efficiency values shown here were obtained after the April 2018 upgrade and without the TG filter installed; the TG filter lowers the array median shown here by $\sim 19\%$ to 0.43. 192

A.1 **Test Setup:** Before the detector wafers are assembled in a final module configuration, we assemble and test them in a simpler test setup shown here. The setup is designed for a quick turnaround to verify that the detectors in a particular wafer are optically sensitive and the TES parameters are close to target. Assembling this setup takes a few days as compared to a few weeks for the final module assembly. The feedback from this detector testing helps improve the fabrication of the subsequent batch of wafers, if necessary. In this test setup, we mount the detector wafer on a Au-plated copper baseplate with cylindrical waveguide holes (left). For the ease of testing, we wirebond only quarter of the total number of detectors with bond pads located on one of the sides of the hexagon. In the image shown (right), we have bonded this particular wafer to the Al flex circuit, the shunt and MUX chips, and the PCB designed for the CLASS 90 GHz readout (see Chapter 4). After an initial testing, we replaced one of the shunt chips with an interface chip containing both the shunt resistor and a Nyquist inductor to analyze the readout noise and detector stability. The data from this test setup helped us choose a 310 nH Nyquist inductor for the final module assembly to keep the high-frequency detector noise aliasing below 1% of the noise level in the TES audio bandwidth. 199

A.2 **Feedhorn and Detector Wafer Assembly:** The CLASS HF module assembly begins by assembling the Au-plated CE7 feedhorn array and the hybridized detector wafer assembly. (Left) First, we mount the feedhorn array on a 3D-printed jig that mechanically supports the feedhorn array and can be mounted on a wirebonder. (Right) The wafer assembly is then mounted on the feedhorn array using three BeCu tripod clips. Each clip is deflected by ~ 0.5 mm using a custom-made screw, which puts sufficient force on the wafer to keep it stationary and ensures proper operation of the photonic choke-joints. Since the screws have #1-64 threads, a one and a quarter turn of the screw head after it comes in contact with the tripod clip provides the desired 0.5 mm deflection. The two alignment pins and a BeCu side spring maintain proper alignment of the feedhorn waveguides to the OMTs on the detector wafer. The two square alignment holes on the wafer assembly are designed such that the alignment is achieved when one of the pins is pushed against a corner of the square (locking the wafer from sliding across that point) and the other pin is pushed against a side of the square (locking the wafer from rotating about that point). This entire assembly is then mounted on a wirebonder. Next, a series of Au wirebonds are put down to thermally connect the heat-sink pads on the detector wafer and the top of the backshort to the CE7. 200

A.3 **Readout Circuit Assembly:** While the feedhorn and detector wafer are being assembled as shown in Figure A.2, the readout circuits can be assembled simultaenously in a separate setup. As shown in the image on the left, first, a Au-plated copper structure that supports the readout package in the HF module is mounted on a 3D-printed jig. A PCB with twisted pairs of NbTi signal cables soldered onto it is bolted to the copper support. A Nb sheet (not shown here) is sandwiched between the PCB and the copper support for magnetic shielding. Then, the MUX and the interface (containing shunt resistors and Nyquist inductors) chips are glued onto the PCB with rubber cement. One end of the Al flex circuit is also bolted to the copper package as shown here. The jig is then moved to the wirebonder. A set of Al wirebonds are put down to electrically connect the Al traces to the signal cables through the interface and the MUX chips, and the vias on the PCB. The four MUX chips on each side of the readout package are also strung together through Al wirebonds to form a multiplexing column with 44 channels each. For a schematic of the wirebonds used to connect the different readout components, refer to Figure 3.6. The above readout package assembly is repeated for three more circuits as shown in the image on the right. While the Al flex circuit for the four readout packages are different, the assembly procedure is the same. 201

A.4 **Stacking the Readout Circuits:** The detector-feedhorn assembly (Figure A.2) and the four readout circuits (Figure A.3) are carefully moved to a new jig to form a single assembly shown here. The readout circuits (RCs) labelled RC 9, RC 10, RC 11, and RC 12 here are stacked on top of the detector wafer in that particular order so that the top layers do not cover the exposed Al traces of the bottom layers. This ensures that we can wirebond from the detector bond pads to all the four layers of the flex circuits. A stiff copper structure is mounted on the top to keep the flex circuits stationary while wirebonding. Notice that the third tripod clip is removed during this process, which could be re-introduced after the flex circuits are folded up. However, since this third clip is not entirely necessary to keep the detector wafer stationary, we instead tighten the remaining two screws to achieve a 0.75 mm deflection on each (as compared to 0.5 mm for three screws shown in Figure A.2). 202

A.5 **Final Wirebonding:** Next, we move the jig in Figure A.4 to a wirebonder to put down the final set of Al wirebonds from the detector bond pads to the Al traces on four sides of the wafer as shown here. While the bottom two flex circuit layers (RCs 9 and 10) are bonded to the detector bond pads located on the right half of the wafer, the top two layers (RCs 11 and 12) are bonded to the left half of the wafer. The RCs are designed such that the 150 and the 220 GHz detectors are mapped separately to two RCs per frequency band. Finally, a Cu spring is connected across the two tripod clip screws to prevent the screw from turning during cryogenic cycling. 202

A.6 **Magnetic Shielding:** A Nb sheet is placed on top of each PCB using four Cu spacers (not shown). The spacers thermally connect the Nb to the module and keep the sheets safely above the Al wirebonds. The inner side of these sheets facing the wirebonds are also lined with polyimide Kapton insulation. Together with the Nb underneath the PCBs, these sheets form a magnetic insulation for the MUX chips. 203

A.7 **Folding:** This is the final step of the module assembly where we remove the 3D-printed jig and fold up the Al flex circuits. The left and the right images show the side view (near the feedhorn array) and the back view of the folded module, respectively. On the feedhorn side, three Au-plated copper supports (only two of them are visible here) are used to mechanically support the feedhorn array to the rest of the module. (In the final module configuration, as shown in Figure A.9, the screws and the alignment pins on the feedhorn array supports are replaced so that their heads are flush with the support's surface.) A hexagonal backplate is used on the opposite side to support the readout packages and the flex circuits. Finally, three I-shaped supports are bolted to the backplate, which will be used to mount the module to the cryostat. 203

A.8 **Assembled Modules:** (Left) A fully assembled HF module. The module contains 340 polarization-sensitive bolometers split equally between the 150 GHz and the 220 GHz frequency bands. (Right) The entire assembly procedure described from Figure A.1 to Figure A.7 is repeated two more times to assemble a total of three modules for the CLASS HF detector array. The wider NbTi cables seen here with the 100-pin connectors carry the row select (RS) lines, while the smaller cables with the 15-pin connectors carry the SQUID feedback (FB) and the SQUID and TES bias lines. 204

A.9 **CLASS HF Focal Plane:** A Au-plated copper web interface is used to mount the three CLASS HF modules to the cryostat. While the feedback and bias lines seen in Figure A.8 are directly connected to the 4K SQUID Series Array board (not shown), the RS lines are daisy-chained together (one of the chain links is visible here with a Connector-9). The end of this chain (shown here with Connector-12) is shorted using a custom-made connector to complete the electrical circuit. Refer to Section 3.4 for further details on the CLASS detector readout. The reflective surface visible behind the modules is the backplate of a magnetic shielding can. 204

B.1 (Left) The Venus to Moon (top) and Venus to Jupiter (bottom) brightness temperature ratios as compared to the Venus peak amplitude measured by the CLASS 40 and 90 GHz detectors, respectively. Each data point corresponds to the result obtained from the stacked maps for a particular detector. For a given detector, the brightness temperature ratio was calculated by scaling the measured peak amplitudes to a fiducial reference solid angle $\Omega_{\text{ref}} = 5.5 \times 10^{-8}$ sr . The inverse-variance weighted mean ratios (dashed-line) for the 40 and 90 GHz detectors are 2.23 ± 0.01 and 2.11 ± 0.01, respectively. (Right) Histograms of the brightness temperature ratios. Multiplying the CLASS-measured ratios with the known brightness temperatures of the Moon and Jupiter gives the final Venus brightness temperatures at 40 and 90 GHz, respectively. 208

B.2 Fractional solar illumination of Venus vs measured brightness temperature during the Venus observing campaign. Each data point corresponds to an array-averaged brightness temperature value obtained from that particular date. While the fractional illumination decreases from 44% to 8% during these observations, we do not observe any statistically significant phase-dependence of the measured temperatures. The best fit lines (red) correspond to a gradient of -0.03 ± 0.11 and 0.06 ± 0.09 for the 40 and the 90 GHz observations, respectively. The shaded regions show the 1σ uncertainties for the fits. 210

B.3 Microwave spectrum of Venus. We compare the CLASS measurements with previous measurements from Millimeter Wave Observatory (MWO; Ulich et al. 1980), Very Large Array (VLA; Butler et al. 2001), and Very Small Array (VSA; Hafez et al. 2008). The solid blue line is an atmospheric model with no SO_2 and H_2SO_4 from Butler et al. (2001). The blue dashed line is a linear extrapolation (in log space) of the model towards shorter wavelengths. The green dashed line is the expected temperature from the best-fit spectral index at 33 GHz from Hafez et al. (2008). 213

Chapter 1

Introduction

"How did it all begin?" This question has vexed humanity for thousands of years. For instance, based on their limited observations, ancient Egyptians built a mythical model of the universe where the sun god *Ra* travelled across the star-covered body of the sky goddess *Nut* to be swallowed and reborn daily (Allen, 2015). This was an eternal and self-creating universe. As observations became more sophisticated, astronomers and philosophers created models of the universe based on empirical evidence and reason. Throughout human history, our understanding of the universe has gone through several paradigm shifts. It was not until the last few decades, thanks to advancements in astronomical observations, that cosmologists were able to put together a standard model of cosmology that remarkably explains the content and evolution of the universe.

1.1 Evolution of the Universe

In the current standard model of cosmology, the universe started from an extremely hot and dense state about 13.8 billion years ago and has been expanding and cooling ever since. To better understand this evolution of the universe, let us start with Einstein's field equations that relate the geometry of the universe to its matter-energy content:

$$G_{\mu\nu} = 8\pi G T_{\mu\nu}, \tag{1.1}$$

where $G_{\mu\nu}$ is the Einstein tensor that describes space-time geometry, $T_{\mu\nu}$ is the stress-energy tensor that describes the matter-energy content, and G is the Newton's constant of gravitation. The Einstein tensor $G_{\mu\nu} = R_{\mu\nu} - \frac{1}{2} g_{\mu\nu} g^{\alpha\beta} R_{\alpha\beta}$, where the Ricci tensor $R_{\mu\nu} = \partial_\alpha \Gamma^\alpha_{\mu\nu} - \partial_\nu \Gamma^\alpha_{\mu\alpha} - \Gamma^\alpha_{\beta\alpha}\Gamma^\beta_{\mu\nu} - \Gamma^\alpha_{\beta\nu}\Gamma^\beta_{\mu\alpha}$, and the Christoffel symbols $\Gamma^\mu_{\alpha\beta} = \frac{1}{2} g^{\mu\nu}(\partial_\beta g_{\alpha\nu} + \partial_\alpha g_{\beta\nu} - \partial_\nu g_{\alpha\beta})$[1]. The $g_{\mu\nu}$ is the metric to be solved for, which is analogous to solving for the gravitational potential in Newtonian gravitation.

For spaces with maximally symmetric subspaces, the exact solution to Einstein's field equations is uniquely given by the Friedmann-Lemaître-Robertson-Walker (FLRW) metric (Friedman, 1922). The space being maximally symmetric in cosmological scales ($\gtrsim$ 150 Mpc) can be understood as a combination of homogeneity and isotropy, which is also known as the cosmological principle. Homogeneity refers to the property of having no preferential location, i.e., it looks the same no matter where you are in the universe (translational invariance). Isotropy refers to the property of having no preferential direction, i.e., it looks the same no matter which direction you look at (rotational invariance). The FLRW metric can be written in spherical coordinates as:

---

[1] Throughout this chapter, I use natural units where $c = \hbar = 1$ and follow the Einstein notation that implies summation over the repeated indices.

$$ds^2 = g_{\mu\nu}dx^\mu dx^\nu = -dt^2 + a^2(t)\left[\frac{dr^2}{1-\kappa r^2} + r^2 d\Omega^2\right], \tag{1.2}$$

where ds^2 is the relativistic invariant interval, $a(t)$ is a scale factor, κ is a constant that represents the curvature of the space, and $d\Omega^2 = d\theta^2 + \sin^2\theta d\phi^2$ is the regular 2-sphere metric. The constant κ can be -1, 0, or 1, corresponding to hyperbolic, flat/Euclidean, and spherical spaces, respectively. So far cosmological observations are consistent with a flat universe, so we can set $\kappa = 0$ (Planck Collaboration, 2018).

All the time-evolution information of the expanding universe is contained in the scale factor $a(t)$. Therefore, the "proper distance" (d), as measured at a given time by a physical yardstick, between two galaxies can be written as $d = a(t)r$, where r is a "comoving distance" that factors out the expansion of space. So the relative velocity between the two galaxies at a given time (t) is:

$$v(t) \equiv \dot{d}(t) = \frac{\dot{a}(t)}{a(t)}d. \tag{1.3}$$

Defining the Hubble parameter $H(t) \equiv \dot{a}(t)/a(t)$ and its current value as the Hubble constant $H_0 \equiv H(t_0)$, we get $v_0 = H_0 d$. This is the famous relation that Edwin Hubble first showed in 1929. He found that other galaxies in our local neighbourhood were moving further away from us with a velocity roughly proportional to their distance from us (Hubble, 1929). The current best constraints of H_0 are 74.03 ± 1.42 km s^{-1} Mpc^{-1} from cosmic distance ladder measurements (Riess et al., 2019) and 67.4 ± 0.5 km s^{-1} Mpc^{-1} from cosmic microwave background (CMB) measurements (Planck Collaboration, 2018). This discrepancy in H_0 value obtained from local vs early universe measurements is an area of active research (Freedman et al., 2019; Addison et al., 2018; Bonvin et al., 2017).

We now revisit Einstein's equations (Equation 1.1). For the FLRW metric, one can compute the Christoffel symbols and Ricci tensors to calculate the left-hand side of the equation. For the right-hand side, if we assume that the universe is described by a perfect fluid, the stress-energy tensor can be written as $T_{\mu\nu} = (p+\rho)u_\mu u_\nu + pg_{\mu\nu}$, where ρ is the proper density, p is the proper pressure, and u_μ is the four-velocity of the fluid. With some algebra, Equation 1.1 reduces to the following two independent equations:

$$\left(\frac{\dot{a}}{a}\right)^2 = \frac{8\pi G}{3}\rho, \tag{1.4}$$

$$\frac{\ddot{a}}{a} = -\frac{4\pi G}{3}(\rho + 3p). \tag{1.5}$$

Equation 1.4 is called the Friedmann equation, which shows how the expansion of the universe is related to its energy density. Equation 1.5, known as the acceleration equation, tells us that the expansion accelerates if $\rho + 3p < 0$.

We can also combine Equation 1.4 and 1.5 to obtain:

$$\dot{\rho} + 3\frac{\dot{a}}{a}(\rho + p) = 0, \tag{1.6}$$

which is the fluid equation that tells us how the energy density changes with time. Note that we can also derive Equation 1.6 from the first law of thermodynamics as the homogeneous and isotropic expansion of the universe is an adiabatic process (see Chap. 4, Ryden 2003). Out of Equations 1.4, 1.5, and 1.6, only two of them are independent, but we have three unknowns: a, ρ, and p. So we use an equation of state, $p = w\rho$, where w is a dimensionless number that parameterizes the components of the universe. Assuming a single-component universe with a single equation of state, Equation 1.6 now has the solution $\rho \propto a^{-3(1+w)}$. Using this solution in Equation 1.5, we find the acceleration criterion for the universe: $\ddot{a} > 0 \Rightarrow w < -1/3$.

In concordance Lambda-Cold Dark Matter (ΛCDM) cosmology (which is the most commonly used and currently accepted cosmological model), the universe has three main components: matter, radiation, and dark energy. Matter consists of essentially collisionless non-relativistic particles which exert no pressure, hence $w = 0$ and $\rho \propto a^{-3}$. For radiation, $\rho \propto a^{-4}$ and $w = 1/3$ because its energy density is reduced both from the dilution of photon density and redshift of photon wavelength as the Universe expands. If matter and radiation were the only components, the universe would be decelerating (as $w > -1/3$) due to their attractive gravitational force. However, we have strong lines of observational evidence suggesting that the expansion of the universe is accelerating (Riess et al., 1998; Perlmutter et al., 1999). Therefore the third component, dark energy, must have $w < -1/3$. As such, it drives the accelerated expansion of space. Our current best constraint on the equation of state for dark energy is $w = -1.03 \pm 0.03$ (Planck Collaboration, 2018). This is consistent with the dark energy being a cosmological constant (Λ)

with no time evolution, which can be related to the intrinsic vacuum energy density. The dark energy is currently the dominant component in the universe as summarized in Table 1.1.

1.2 The Cosmic Microwave Background

One of the strongest pieces of evidence favoring a hot "big-bang" model of the universe came from the discovery of the CMB by Penzias and Wilson (1965). Using a 20-foot horn-reflector antenna, they discovered an excess noise of 3.5 ± 1.0 K at 4080 MHz coming from the sky in all directions. Later, this excess radiation was confirmed to have a blackbody spectrum, as shown in Figure 1.1, with a temperature of 2.725 ± 0.002 K by the *COBE* FIRAS instrument (Mather et al., 1999). No known terrestrial source could explain this blackbody radiation observed in all directions. The most natural astronomical source was the relic radiation from a hot and dense early universe.

At the beginning of the universe, due to rapid Thomson scattering between the photons and electrons, and Coulomb interactions between the electrons and baryons, the universe existed as a single tightly coupled photon-baryon fluid. Around 380,000 years later, as the universe expanded and cooled below ~ 3000 K, photons decoupled from matter allowing free electrons to combine with protons. Hence, this period is known as the epoch of recombination. Today, we observe the relic photons that free streamed throughout the universe from the surface of last scattering as nearly isotropic thermal radiation with a temperature of 2.725 K.

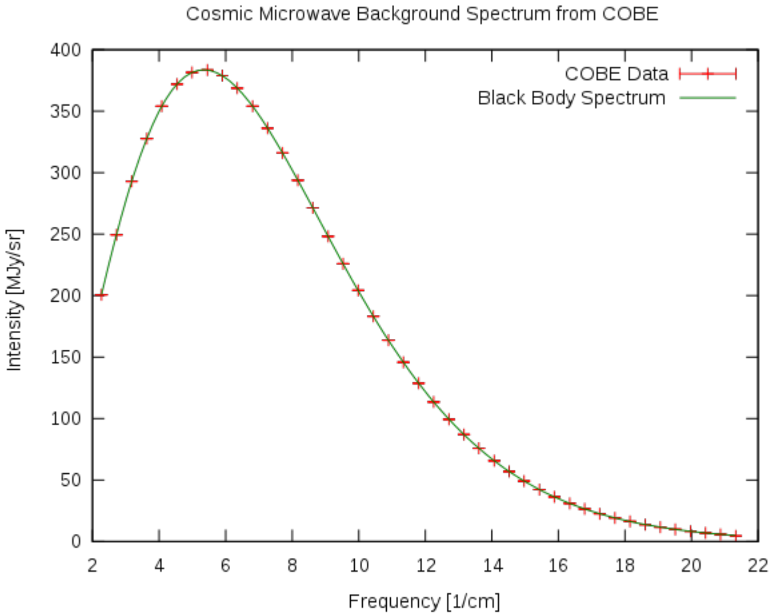

Figure 1.1: The CMB spectrum as measured by the *COBE* FIRAS instrument (Fixsen et al., 1996). The data remarkably fits a blackbody spectrum at 2.725 K.

1.2.1 Temperature Anisotropy

While the *COBE* FIRAS instrument established the CMB to have a blackbody spectrum, the *COBE* DMR instrument discovered CMB temperature variations at the level of 30 μK, i.e., roughly 1 part in 100,000 (Smoot et al., 1992). Since the CMB was last scattered during "decoupling" and has streamed to us nearly unchanged, the CMB anisotropy reveals rich information about the early universe. The largest anisotropy is a dipolar pattern in the CMB with amplitude $\sim$ 3.4 mK (Fixsen et al., 1996), which is primarily due to the Earth's motion with respect to the rest frame of the CMB such that the CMB photons appear redshifted or blueshifted depending on the observation direction relative to our motion. Once we remove this local Doppler effect, we see the 10^{-5} level anisotropy as shown in Figure 1.2. Individual hot and cold spots in the CMB do not reveal any useful cosmological information; rather it is the statistics of the anisotropy that is predicted by the model. The CMB temperature anisotropy in the direction $\hat{\mathbf{n}} \equiv (\theta, \phi)$ on the celestial sphere can be expanded using spherical harmonics $Y_{\ell m}(\hat{\mathbf{n}})$ as:

$$\Theta(\hat{\mathbf{n}}) \equiv \frac{\Delta T(\hat{\mathbf{n}})}{T_{\mathrm{CMB}}} = \sum_{\ell=1}^{\infty} \sum_{m=-\ell}^{m=\ell} a_{\ell m} Y_{\ell m}(\hat{\mathbf{n}}), \tag{1.7}$$

where $\Delta T(\hat{\mathbf{n}}) = T(\hat{\mathbf{n}}) - T_{\mathrm{CMB}}$ and the $a_{\ell m}$ coefficients can be calculated as:

$$a_{\ell m} = \int Y^*_{\ell m}(\hat{\mathbf{n}}) \Theta(\hat{\mathbf{n}}) d\Omega. \tag{1.8}$$

The index ℓ, called the multipole moment, can be related to a corresponding angular scale on the sky α, where $\alpha \approx 180^\circ/\ell$. Current cosmological data show that the CMB temperature fluctuations $\Theta(\hat{\mathbf{n}})$ are Gaussian distributed. This means that the expansion coefficients $a_{\ell m}$ are also drawn from a Gaussian distribution with the expectation value $\langle a_{\ell m} \rangle = 0$ and variance:

$$\langle a_{\ell m} a^*_{\ell' m'} \rangle = \delta_{\ell \ell'} \delta_{m m'} C_\ell \, , \tag{1.9}$$

where C_ℓ is the underlying angular power spectrum. The above average is taken over many ensembles, and the variance is independent of m due to the isotropy of the universe. The power spectrum obtained from our observations $\Theta(\hat{\mathbf{n}})$ is just one realization from an ensemble of C_ℓ distribution. For a given multipole, we have 2ℓ+1 independent m-modes, so we can write the observed spectrum ($\hat{C}_\ell$) and ensemble averaged power spectrum (C_ℓ) as:

$$\hat{C}_\ell = \frac{1}{2\ell + 1} \sum_{m=-\ell}^{\ell} |a_{\ell m}|^2, \quad C_\ell = \frac{1}{2\ell + 1} \sum_{m=-\ell}^{\ell} \langle |a_{\ell m}|^2 \rangle. \tag{1.10}$$

C_ℓ describes the physics of the Universe, whereas we observe $\hat{C}_\ell$. We only have one Universe to observe, and hence only one realization of a given model. Therefore, our estimation of any given C_ℓ has an unavoidable uncertainty called the cosmic variance (ΔC_ℓ). From Equation 1.10, we can see that $\hat{C}_\ell / C_\ell$ has a χ^2 distribution with $2\ell + 1$ degrees of freedom; therefore, $\Delta C_\ell = \sqrt{\frac{2}{2\ell+1}} C_\ell$. It is important to note that if CMB temperature fluctuations are Gaussian, the power spectrum is all we need to parameterize the statistics of the temperature anisotropy. All higher order correlations are zero and provide no extra information. Figure 1.2 shows the CMB temperature anisotropy and its corresponding power spectra as measured by the *Planck* mission. The effect of cosmic variance is prominent in the low-ℓ region of the power spectra. As shown in Figure 1.2, it is customary to scale the CMB power spectra as $D_\ell = \ell(\ell+1)/2\pi \ C_\ell$ as it gives a flat plateau at large angular scales and brings out the peak structures at smaller scales.

The CMB power spectrum provides a wealth of cosmological information. At large angular scales ($\ell \lesssim 90$), the gravitational redshift of photons climbing out of primordial density fluctuations, known as the Sachs-Wolfe effect[2] (Sachs and Wolfe, 1967), dominates the power spectrum. Since these large angular scales are so far apart that they have not had time to interact, this nearly scale invariant spectrum reveals information about the initial conditions of the universe. The spectral tilt parameter (n_s) in Table 1.1 obtained from the fit to the power spectrum characterizes the overall tilt of the CMB spectrum (with

---

[2] To be more precise, this is called a Non-Integrated Sachs-Wolfe effect which occurs at the surface of last scattering. In contrast, the Integrated Sachs-Wolfe effect is produced between the last scattering surface and today as the CMB photons pass through different gravitational potential wells.

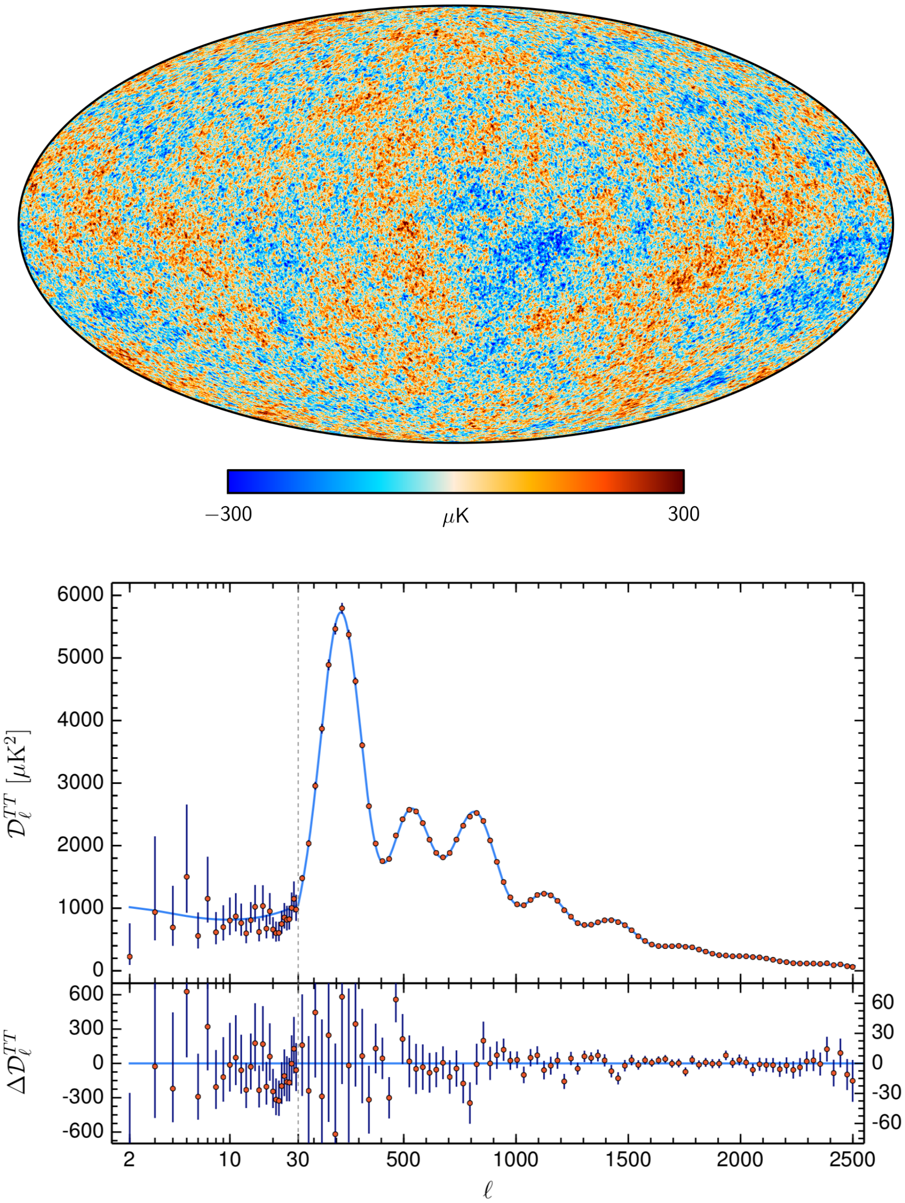

Figure 1.2: (Top) The *Planck* 2018 all-sky map of CMB temperature anisotropy. (Bottom) The corresponding *Planck* 2018 CMB temperature power spectrum. The light blue curve shows the base-ΛCDM theoretical spectrum best fit to the *Planck* TT, TE, EE+lowE+lensing likelihoods. These best fit parameters are summarized in Table 1.1. The lower panel shows the residuals from the model fit along with 1σ error bars including the cosmic variance. Figure credit: ESA and Planck Collaboration (2018)

$n_s = 1$ being a scale-invariant flat spectrum), and is one of the six parameters that describes the ΛCDM model.

At angular scales $\lesssim 1.5^\circ$ corresponding to $\ell \gtrsim 100$, we see a series of peaks and troughs produced by the so-called acoustic oscillations. These oscillations occur as the photon-baryon fluid is alternately compressed by gravity and rarefied by radiation pressure. The series of peaks correspond to various modes with increasing number of oscillations completed before recombination. For instance, the first peak corresponds to an oscillation mode that just had enough time to compress once before photon-baryon decoupling, the second peak fully compressed and rarefied in the same timescale and so on. Therefore, these peaks are the harmonics of the fundamental scale corresponding to the distance sound waves could have traveled before recombination, known as the sound horizon. The angular size of the sound horizon is parameterized by the θ_{MC} parameter in Table 1.1.

As seen in Figure 1.2, the oscillations at higher multipoles (smaller angular scales) are damped. This happens due to diffusion damping, also known as Silk damping (Silk, 1968), and the finite duration of recombination, i.e., recombination and last scattering takes place at a slightly different epoch. Before recombination, as photons random walk (diffuse) within their mean free path through the baryons, hot and cold regions are mixed, thus, destroying small scale perturbations. As recombination proceeds, the ionization fraction decreases and the mean free path of the photons increases. This leads to an increase in the diffusion length of the photons, which we observe as the damping of the acoustic peaks at higher multipoles.

Table 1.1: Best-fit ΛCDM parameters for a spatially-flat Universe from the full *Planck* mission TT, TE, EE+lowE+lensing data

Parameter	Description	Value
Fit Parameters		
$\Omega_b h^2$	Physical baryon density	0.02233 ± 0.00015
$\Omega_c h^2$	Physical cold dark matter density	0.1198 ± 0.0012
$100\theta_{MC}$	Acoustic scale parameter	1.04089 ± 0.00031
$\ln(10^{10} A_s)$	Curvature fluctuations, $k = 0.05$ Mpc^{-1}	3.043 ± 0.014
n_s	Spectral tilt	0.9652 ± 0.0042
τ	Optical depth to reionization	0.0540 ± 0.0074
Derived Parameters		
$\Omega_m h^2$	Physical matter density	0.1428 ± 0.0011
$\Omega_\Lambda h^2$	Physical dark energy density	0.3107 ± 0.0082
H_0 [kms^{-1}Mpc^{-1}]	Current Hubble constant	67.37 ± 0.54
t_0 [Gyr]	Age of the Universe	13.801 ± 0.024
σ_8	Density fluctuations, 8 h^{-1} Mpc scale	0.8101 ± 0.0061
z_{re}	Redshift of reionization	7.64 ± 0.74
r_{drag} [Mpc]	Comoving sound horizon	147.18 ± 0.29

The relative amplitudes of the acoustic peaks and their exact location in the spectrum provide valuable cosmological information. For instance, the location of the first peak strongly depends on the curvature/flatness of the universe, while the relative amplitudes of the even and odd numbered peaks depend on the density of baryons and dark matter in the universe. For further details about the cosmological implications of the CMB power spectra, refer to Hu and Dodelson (2002). The observed CMB power spectrum provides strong constraints on the six parameters that fully describe the ΛCDM model of the Universe as shown in Table 1.1. These values are obtained from the best fit to the *Planck* temperature and polarization (described in Section 1.2.2) spectra from the full *Planck* mission data (Planck Collaboration, 2018).

1.2.2 Polarization Anisotropy

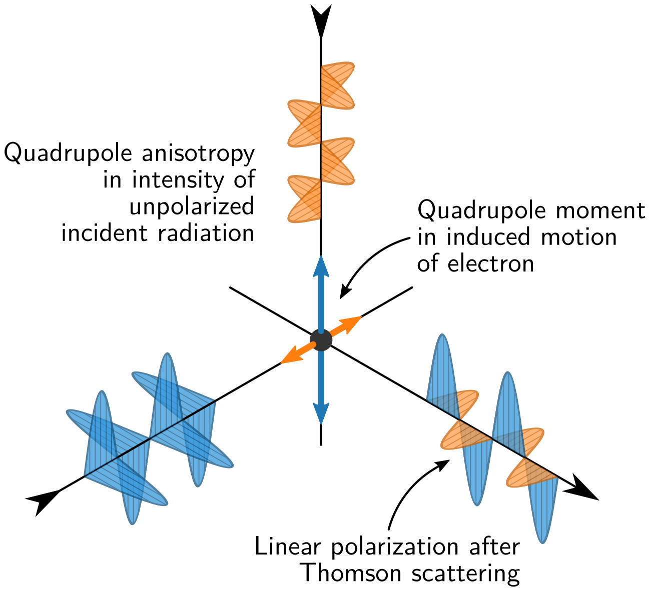
Quadrupole anisotropy
in intensity of
unpolarized
incident radiation
Quadrupole moment
in induced motion
of electron
Linear polarization after
Thomson scattering

Figure 1.3: Depiction of net linear polarization created after Thomson scattering of unpolarized incident radiation with quadrupole anisotropy. The blue oscillations represent the hot, while the orange oscillations represent the cold radiation. Figure credit: CAPMAP at the University of Chicago and M. Petroff

Thomson scattering of the CMB radiation by free electrons can result in polarization of the CMB photons. The scattering of an isotropic radiation produces no net polarization because the orthogonal polarization states from incident directions separated by 90° balance each other (Hu and White, 1997). However, if a local quadrupole moment exists in the incoming radiation field as seen by an electron (for example: cold spots above and below the electron, and hot spots to the left and right), then the outgoing radiation after scattering will have a net linear polarization as shown in Figure 1.3. In the primordial plasma where photons are tightly coupled to the charged electrons, rapid

Thomson scattering randomizes photons' directions with no possibility of quadrupole anisotropy and polarization. As recombination proceeds, the increased mean free path of the photons allows the photons to probe spatial variations and enables any existing quadrupole anisotropy to polarize the CMB photons. However, by the time of last scattering, most of the electrons have recombined into neutral hydrogen. Therefore, with reduced number of scatterers available to produce polarization, the CMB polarization fluctuations are at one part in 10^6 level, i.e., an order of magnitude below the temperature anisotropy (Kamionkowski, Kosowsky, and Stebbins, 1997).

Similar to the temperature anisotropy discussed in Section 1.2.1, we now discuss the mathematical formalism to study the polarization anisotropy. Monochromatic electromagnetic radiation with angular frequency ω propagating in the $\hat{z}$ direction can be represented by two electric field vectors:

$$E_x = a_x(t)\cos[\omega t - \theta_x(t)], \;\; E_y = a_y(t)\cos[\omega t - \theta_y(t)], \tag{1.11}$$

where $a_{x,y}$ and $\theta_{x,y}$ are the amplitudes and phase differences, respectively, which vary on timescales much longer than $2\pi/\omega$. We can then define the Stokes parameters as:

$$\begin{aligned} I &\equiv \langle a_x^2 \rangle + \langle a_y^2 \rangle, \\ Q &\equiv \langle a_x^2 \rangle - \langle a_y^2 \rangle, \\ U &\equiv \langle 2a_x a_y \cos(\theta_x - \theta_y) \rangle, \\ V &\equiv \langle 2a_x a_y \sin(\theta_x - \theta_y) \rangle, \end{aligned} \tag{1.12}$$

where $\langle ... \rangle$ represent time averages. The Stokes parameters I and V measure the total intensity and circular polarization, respectively, and are coordinate-independent. On the other hand, the Stokes Q and U measure the two orthogonal states of the linear polarization and are coordinate-dependent. For instance, if we rotate the $x-y$ coordinates by an angle α to $x'-y'$, I and V remain unchanged but Q and U transform as:

$$\begin{aligned} Q' &= Q\cos 2\alpha + U\sin 2\alpha \\ U' &= U\cos 2\alpha - Q\sin 2\alpha. \end{aligned} \tag{1.13}$$

Therefore, we can construct two combinations from Q and U that transform as spin-2 quantities:

$$(Q \pm iU)' = e^{\mp 2i\alpha}(Q \pm iU). \tag{1.14}$$

Similar to Equation 1.7 for temperature anisotropy, we can expand $(Q \pm iU)$ into spin-2 weighted spherical harmonics ${}_{\pm 2}Y_{lm}$ (Goldberg et al., 1967):

$$(Q \pm iU)(\hat{\mathbf{n}}) = \sum_{\ell=1}^{\infty} \sum_{m=-\ell}^{m=\ell} a_{\pm 2,\ell m}\ {}_{\pm 2}Y_{\ell m}(\hat{\mathbf{n}}), \tag{1.15}$$

where expansion coefficients $a_{\pm 2,\ell m}$ are:

$$a_{\pm 2,\ell m} = \left[\frac{(l-2)!}{(l+2)!}\right]^{1/2} \int Y^*_{\ell m}(\hat{\mathbf{n}})\eth^2(Q \pm iU)(\hat{\mathbf{n}})d\Omega, \tag{1.16}$$

where $\eth$ is spin raising operator for $a_{-2,\ell m}$ and lowering operator for $a_{2,\ell m}$, and Y_{lm} is the usual spherical harmonics function. Refer to Zaldarriaga and Seljak (1997) for detailed derivation of these quantities.

Since Stokes V is not generated by Thomson scattering, the full-sky CMB

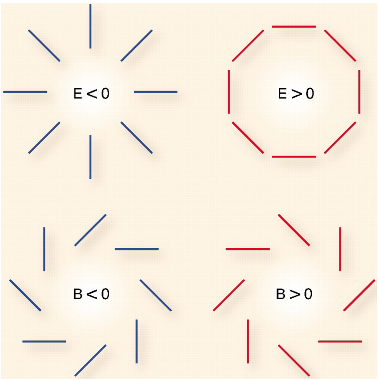

Figure 1.4: The polarization on the sky can be decomposed into curl-free E-mode and divergence-free B-mode patterns as shown here. E-modes have radial pattern around the cold spots (blue) and tangential pattern around hot spots (red). However, B-modes have characteristic swirling patterns around the cold and hot spots with different orientations as shown here. Analogous to the electric and magnetic fields, E-modes have even parity, while B-modes have odd parity. E-modes can be converted to B-modes and vice-versa by rotating each polarization vector by 45°. Figure from Krauss, Dodelson, and Meyer (2010)

polarization anisotropy can be characterized using equation 1.15. However, if we want to make statements about physics that are not dependent on the coordinate system we choose, we need some coordinate-independent representation of these spin-2 quantities. The $a_{\pm 2,\ell m}$ can be linearly combined into spin-0 modes known as "E-modes" and "B-modes" (Kamionkowski, Kosowsky, and Stebbins, 1997; Zaldarriaga and Seljak, 1997) as follows:

$$a_{E,\ell m} \equiv -(a_{2,\ell m} + a_{-2,\ell m})/2, \;\; a_{B,\ell m} \equiv i(a_{2,\ell m} - a_{-2,\ell m})/2. \tag{1.17}$$

The corresponding rotationally invariant expansions are:

$$\begin{aligned} E(\hat{\mathbf{n}}) &= \sum_{\ell=1}^{\infty} \sum_{m=-\ell}^{m=\ell} a_{E,\ell m} Y_{\ell m}(\hat{\mathbf{n}}) \\ B(\hat{\mathbf{n}}) &= \sum_{\ell=1}^{\infty} \sum_{m=-\ell}^{m=\ell} a_{B,\ell m} Y_{\ell m}(\hat{\mathbf{n}}). \end{aligned} \tag{1.18}$$

Figure 1.4 shows the polarization patterns associated with E- and B-modes. In analogy with electric and magnetic fields, the curl-free polarization components are called E-modes, while the divergence-free components are called B-modes.

Since polarization fluctuations are also Gaussian distributed, we can generalize the ensemble averaged power spectrum from equation 1.10 as:

$$C_\ell^{XY} = \frac{1}{2\ell+1} \sum_{m=-\ell}^{\ell} \langle a^*_{X,\ell m} a_{Y,\ell m} \rangle, \qquad X, Y \in \{T, E, B\}. \tag{1.19}$$

While T, E, and B are all rotationally invariant, under parity inversion (for example: reflection about the x-axis), T and E remain unchanged but B changes sign. In other words, T and E have $(-1)^\ell$ parity and B has $(-1)^{\ell+1}$ parity. Therefore, although equation 1.19 has six different power spectra, $C_\ell^{TB} = C_\ell^{EB} = 0$. So, the statistics of the CMB temperature and polarization maps are determined entirely by the remaining four power spectra C_ℓ^{TT}, C_ℓ^{TE}, C_ℓ^{EE}, and C_ℓ^{BB} (Kamionkowski and Kovetz, 2016). Figure 1.5 shows the summary of the measurements of these four CMB power spectra by various space and ground-based experiments.

To understand the features in the E and B power spectra, we need to look into the physics that produces these polarization modes. Density and temperature fluctuations are scalar quantities; therefore, they must be curl-free. On the other hand, tensor perturbations like inflationary gravitational waves (described in Section 1.3) can produce both gradient and curl components. Since B-modes can only be produced by tensor perturbations, detection of primordial B-modes in the CMB is considered a "smoking gun" evidence

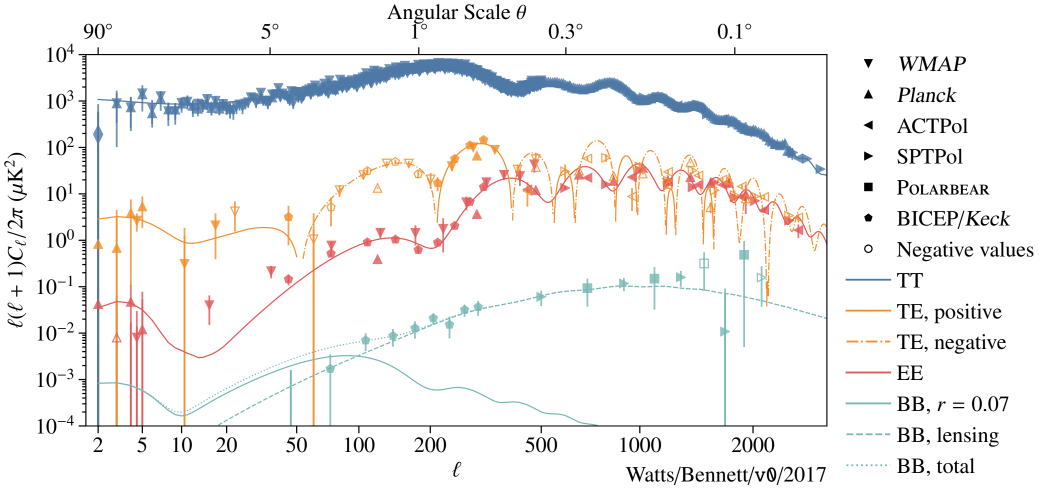

Figure 1.5: Summary of the CMB angular power spectra measurements made till 2017. The CMB temperature anisotropy (TT) has been measured to near the cosmic variance limit. The E-mode polarization anisotropy (EE) and the TE cross-correlation have been well measured at angular scales $\lesssim 5°$, but their uncertainty at large angular scales is much higher. While the lensing B-modes (BB) have been detected at small angular scales, the B-modes from primordial graviational waves which peak at large angular scales have not been detected yet. Figure credit: D. Watts

for inflation (described in Section 1.3). As the primordial B-modes have not been detected yet, there are no data points for C_ℓ^{BB} in Figure 1.5 at large angular scales. However, at smaller angular scales, B-modes can be produced through rotation of E-modes (refer to Figure 1.4) by weak gravitational lensing by matter distribution along the line of sight. These lensing B-modes have already been detected by various experiments (BICEP2 Collaboration et al., 2016; Sherwin et al., 2017; POLARBEAR Collaboration et al., 2017; Sayre et al., 2019).

While the overall amplitude of C_ℓ^{BB} scales as the tensor-to-scalar ratio (r), the spectrum has a characteristic shape with two peaks at large angular scales as shown in Figure 1.5. The peak at $\ell \sim 100$, known as the "recombination peak", comes from gravitational waves entering the horizon around the time of decoupling. At $\ell \lesssim 10$, re-scattering of the CMB photons by free electrons that were ionized by ultraviolet radiation from the first stars create a "reionization bump". So, in addition to r, the amplitude of this bump depends on the optical depth to reionization (τ)[3], which is currently the least constrained ΛCDM parameter (Table 1.1). For E-modes, at $\ell \gtrsim 200$, the polarization power is sourced primarily by density fluctuations at the surface of last scattering. However, at large angular scales ($2 \leqslant \ell \leqslant 20$), E-modes roughly scale as $C^{EE}_{2\leqslant\ell\leqslant 20} \propto \tau^2$ due to rescattering after reionization (Page et al., 2007). Therefore, we can better constraint τ, and hence understand the star formation history of the universe better, by measuring E-modes at large angular scales. This is one of the major goals of the Cosmology Large Angular Scale Surveyor (CLASS), described in the subsequent chapters of this thesis.

1.3 Inflation

In our discussion so far, we have mentioned how the six-parameter ΛCDM model successfully describes the evolution of the Universe with its predictions matching our observations. However, a few facts we glossed over in Section 1.1 include the flatness, homogeneity, and isotropy of the universe; these features can be problematic without extensions to the current standard model. Why is the Universe flat within a fraction of a percent today? Why is the CMB homogeneous and isotropic to within a part in 10^5? Our standard model would tell us that the Universe would have been even flatter and more homogeneous in the past. These problems can be solved with a postulated period of exponential expansion ($a \propto e^{Ht}$) in the early universe called inflation (Guth, 1981). It is worth discussing how inflation solves these (and a few other) problems in the standard cosmological model.

---

[3] $\tau \equiv \int_{t_{\rm lss}}^{t_0} n_{\rm e}(t)\sigma_T dt$, where $n_{\rm e}(t)$ is the average free electron number density from the time of last scattering ($t_{\rm lss}$) till today (t_0), and σ_T is the Thomson scattering cross-section.

1. **Flatness Problem:** Recall that we set $\kappa = 0$ in the FLRW metric (equation 1.2) to obtain the Friedmann equation (equation 1.4). We can generalize equation 1.4 by including an equivalent curvature density term as follows:
$$H^2 = \left(\frac{\dot{a}}{a}\right)^2 = \frac{8\pi G}{3}\rho - \frac{\kappa}{a^2} \ . \tag{1.20}$$
We can notice that there is a critical density $\rho_c = 3H^2/8\pi G$ where the universe is flat (κ = 0). If $\rho > \rho_c$, we get a closed universe ($\kappa > 0$), and if $\rho < \rho_c$, we get an open universe ($\kappa < 0$). By defining a density parameter $\Omega \equiv \rho/\rho_c$, we can simplify equation 1.20 as:
$$1 - \Omega = -\frac{\kappa}{(aH)^2} = -\frac{\kappa}{\dot{a}^2} \ . \tag{1.21}$$
Our observations suggest that our current Universe is spatially flat to an accuracy of 0.2% i.e. $|1 - \Omega_0| \leq 0.002$ (Planck Collaboration, 2018). From Section 1.1, we know that $\rho_r \propto a^{-4}$ and $\rho_m \propto a^{-3}$ for radiation and matter, respectively. So, Equation 1.21 tells us that $|1 - \Omega_r| \propto a^2 \propto t$ during the radiation-dominated era and $|1 - \Omega_m| \propto a \propto t^{2/3}$ during the matter-dominated era. This means that throughout most of the cosmic history, Ω has been increasingly deviating from 1. So, if we were to extrapolate the measured constraints on Ω_0 backward in time towards

the early universe, we would get an incredibly small deviation of Ω from 1. For instance, at $t \sim 1$ s, $|1-\Omega| \lesssim 10^{-16}$ and at $t \sim 10^{-43}$ s (Planck time), $|1-\Omega| \lesssim 10^{-62}$ (see Chap. 11, Ryden 2003).

Rather than dismissing what appears to be an extremely "fine-tuned" flatness of the Universe as a coincidence, inflation provides a possible solution. During inflation, equation 1.21 tells us that $|1-\Omega| \propto e^{-2Ht}$ as $a \propto e^{Ht}$. This means that as inflation proceeds, it drives the Universe towards flatness. For instance, lets take an inflation model where a increases by a factor of e^N during inflation (referred to as N "e-foldings") with $N = 100$. In this model, even if the Universe was strongly curved before inflation i.e. $|1-\Omega| \sim 1$, after 100 e-foldings, $|1-\Omega| \sim e^{200} \sim 10^{-87}$. Although there are limited observational constraints on what N could be, $N \approx 60$ could be enough to explain our current observations (Liddle and Leach, 2003).

2. **Horizon Problem:** The near isotropy and homogeneity of the CMB to within a part in 10^5, even over the regions of the sky that were never in causal contact, presents a significant challenge for standard cosmology. For the FLRW metric, the particle horizon distance (maximum distance a light ray can travel between initial time $t = 0$ and final time t) can be written as:

$$d_{\text{horizon}}(t) = \int_0^t \frac{dt'}{a(t')} = \int_0^{a(t)} \frac{da}{Ha^2} \ , \tag{1.22}$$

where a change of variable was used in the last equation to perform the integral over a. For the surface of last scattering with redshift $z \sim 1100$, we integrate from 0 to $a = 1/(1+z) \approx 0.001$ to get $d_{\text{horizon}}(t_{\text{ls}}) = 0.34$ Mpc.

The corresponding angular size on the sky is:

$$\theta_{\text{horizon}} = \frac{d_{\text{horizon}}(t_{\text{ls}})}{d_A} = \frac{0.34\ \text{Mpc}}{12.6\ \text{Mpc}} \approx 1.5^\circ, \tag{1.23}$$

where d_A is the angular-diamater distance to the surface of last scattering. Therefore, regions separated by $\theta \gtrsim 1.5^\circ$ were never in causal contact. Yet, we see that the CMB is isotropic to within a part in 10^5 on scales larger than 1.5° (Figure 1.5). During inflation, however, Equation 1.22 shows that the size of the horizon shrinks as $1/a$. So, for 60 e-folding inflation, the size of the horizon at the end is a factor of e^{-60} smaller compared to the size prior to inflation. So, scales that enter our horizon now could have been in causal contact before or during inflation leading to the observed CMB homogeneity and isotropy.

3. **Monopole Problem:** One of the inevitable predictions of the Grand Unified Theory (GUT) models that unite the electroweak and the strong forces is the existence of magnetic monopoles (Preskill, 1979). As the temperature of the Universe dropped below the GUT temperatures ($\sim 10^{28}$ K), the Universe would have gone through a symmetry-breaking phase transition creating abundant point-like topological defects i.e. magnetic monopoles (See Chap. 11, Ryden 2003). However, we have not detected any magnetic monopoles yet, despite numerous attempts from astrophysical observations, cosmic-ray experiments, and particle colliders (Turner, Parker, and Bogdan, 1982; MACRO Collaboration, 2002; Detrixhe et al., 2011; Adrián-Martínez et al., 2012; MoEDAL Collaboration et al., 2016). Inflation explains this lack of magnetic monopoles as it

exponentially dilutes the monopole abundance to an undetectable level. So, if the GUT phase transition happens prior to inflation, the number density of monopoles would be reduced by a factor of e^{-3N} by the end of inflation, making the probability of detection today astronomically small.

4. **Origin of Large Scale Structure:** In addition to solving the above three problems, inflation also explains the origin of large scale structure. Inflation expands the quantum fluctuations in matter density prior to inflation to cosmological scales, explaining the anisotropy observed in the CMB (Figure 1.2). These gravitational fluctuations provide the seed for formation of structures like stars, galaxies, and clusters of galaxies.

With these motivations behind an inflationary epoch in the early universe, we now discuss the physics behind such an inflationary period. Although the exact mechanism that drives inflation is still uncertain, we can look at a general model that is consistent with our current observations. In Section 1.1, we discussed how a cosmological constant with no time evolution drives the current acceleration of the universe. At early times, however, we need a dynamic field as the accelerated expansion must end after a period of time. The simplest model involves a single scalar field $\phi(t)$ called the "inflaton" that is homogeneous (no position-dependence) and minimally coupled to gravity. We can write the Lagrangian density ($\mathcal{L}$) and the action (S_ϕ) of this scalar field as:

$$\mathcal{L} = \frac{1}{2} g^{\mu\nu} \partial_\mu \phi \partial_\nu \phi - V(\phi), \quad S_\phi = \int d^4x \sqrt{-g} \mathcal{L}, \tag{1.24}$$

where g is the determinant of the metric $g_{\mu\nu}$ and $V(\phi)$ is the potential of the inflaton field. Now we can calculate the stress-energy tensor for the scalar field as follows:

$$T_{\mu\nu} \equiv -\frac{2}{\sqrt{-g}}\frac{\delta S_\phi}{\delta g^{\mu\nu}} = \partial_\mu\phi\partial_\nu\phi - g_{\mu\nu}\left(\frac{1}{2}\partial_\alpha\phi\partial^\alpha\phi + V(\phi)\right). \tag{1.25}$$

We can calculate $T_{\mu\nu}$ for the FLRW metric and get the energy-density and pressure of the field through $T_{00} = \rho$ and $T_{ij} = pg_{ij}$, which results in:

$$\begin{aligned} \rho &= \frac{1}{2}\dot{\phi} + V(\phi) \\ p &= \frac{1}{2}\dot{\phi} - V(\phi). \end{aligned} \tag{1.26}$$

We notice that $T_{\mu\nu}$ for the scalar field takes the form of a perfect fluid equation (see section 1.1) with the equation of state parameter:

$$w = \frac{\frac{1}{2}\dot{\phi} - V(\phi)}{\frac{1}{2}\dot{\phi} + V(\phi)} \approx -1 \text{ if } V \gg \dot{\phi}^2. \tag{1.27}$$

So, in the limit that the potential energy dominates over the kinetic energy, we recover a cosmological constant and satisfy the acceleration condition ($w < -1/3$). We also do not want the potential to decay too quickly, otherwise it will not flatten the universe sufficiently. We need to sustain an accelerated expansion for a sufficiently long period of time. To get this condition, we look at the equation of motion for the field by substituting ρ and p from equation 1.26 into equation 1.6:

$$\ddot{\phi} + 3H\dot{\phi} + \frac{\partial V}{\partial \phi} = 0. \tag{1.28}$$

Equation 1.28 is the same as the equation of motion for a particle rolling down a potential while being impeded by a frictional force. In this case, the expansion of the universe acts as a friction term, known as the Hubble friction. If $H\dot{\phi} \gg \ddot{\phi}$, we get the slow-roll approximation for inflation. These conditions are usually summarized with the two slow-roll parameters as follows:

$$\begin{aligned} \epsilon &\equiv -\frac{\dot{H}}{H^2} \sim \frac{\dot{\phi}^2}{V} \ll 1 \\ \eta &\equiv -\frac{\ddot{\phi}}{H\dot{\phi}} \ll 1. \end{aligned} \tag{1.29}$$

Now, by definition, inflation ends when $\epsilon \sim \eta \sim 1$. Figure 1.6 illustrates a toy model for a slow-roll inflaton potential. The field starts at a metastable so-called false vacuum state, and continues to roll down towards the true vacuum state with $V = 0$. Accelerated expansion occurs as long as $V(\phi) \gg \frac{1}{2}\dot{\phi}^2$ and ends at ϕ_{end} when $\frac{1}{2}\dot{\phi}^2 \approx V(\phi)$. The potential energy lost by the inflaton field from its transition from the false to the true vacuum is carried away by photons that reheat the universe. This can be viewed as the beginning of the standard big-bang universe. The standard big-bang model does not describe an event or beginning of the universe, but rather is a model of the evolution of the universe after inflation. However, many authors refer to the big bang as an event such as the start of inflation.

Since inflation explains primordial perturbations through quantum fluctuations in the spacetime metric, any valid model must be consistent with our current observations. Single-field slow-roll inflation makes a number of such predictions about the primordial perturbations that are consistent with all current cosmological data: (1) the perturbations are adiabatic; (2) their spectrum should be nearly but not precisely scale invariant; (3) their distribution should be very nearly Gaussian; and (4) there should be super-horizon perturbations

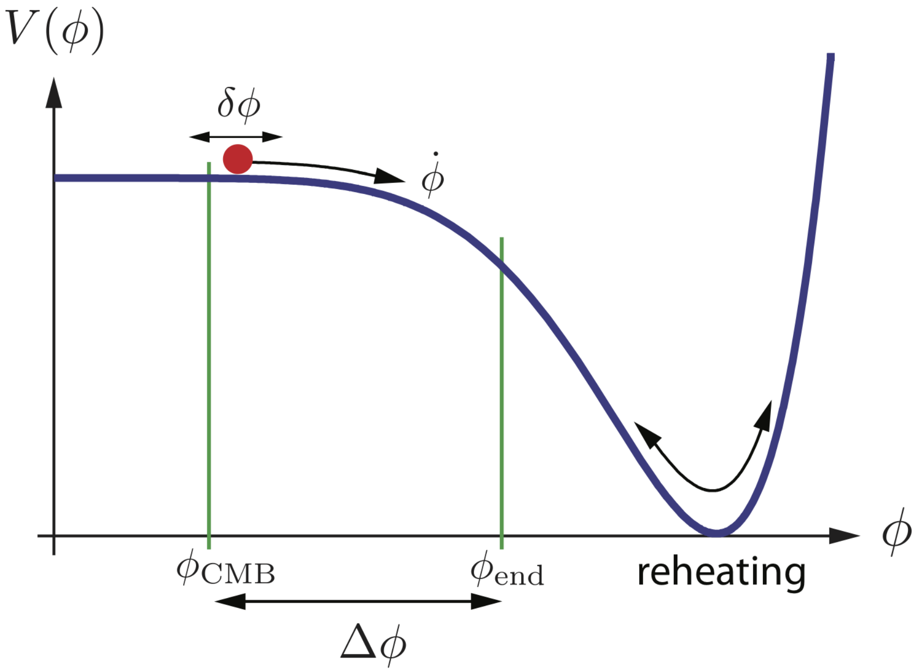

Figure 1.6: A toy model illustration of a single-field slow-roll inflaton potential. At early times, inflation occurs as the potential $V(\phi)$ dominates the energy density of the universe such that $V(\phi) \gg \frac{1}{2}\dot{\phi}^2$. As the field slowly rolls from this "false vacuum" state towards the "true vacuum" state ($V = 0$), inflation ends at $\phi_{\rm end}$ when $\frac{1}{2}\dot{\phi}^2 \approx V(\phi)$. Finally, during reheating, the inflaton potential is converted to photons and the standard big-bang universe begins. The CMB fluctuations we observe today are created as inflation expands the quantum fluctuations $\delta\phi$ to cosmological scales. Figure from Baumann (2009)

at the time of CMB decoupling (Kamionkowski and Kovetz, 2016). Since the precise mathematical treatment of these cosmological perturbations is outside the scope of this work, we just discuss the relevant details here, primarily based on Baumann (2009). The first-order perturbations can be decomposed into independent scalar, vector, and tensor modes. However, since the vector modes decay rapidly during expansion and are not created by inflation, we do not consider them further.

We can compute the scalar power spectrum $P_{\mathcal{R}}(k)$ for a comoving curvature perturbation $\mathcal{R}(\mathbf{x}, t)$ as:

$$\langle \mathcal{R}_{\mathbf{k}} \mathcal{R}_{\mathbf{k'}} \rangle = (2\pi)^3 \delta(\mathbf{k} + \mathbf{k'}) P_{\mathcal{R}}(k). \tag{1.30}$$

The scalar power spectrum is often defined as a dimensionless quantity $\Delta^2_{\mathcal{R}}$:

$$\Delta^2_{\mathcal{R}} \equiv \frac{k^3}{2\pi^2} P_{\mathcal{R}}(k) = A_s(k_*) \left(\frac{k}{k_*} \right)^{n_s(k_*)-1}, \tag{1.31}$$

where the second equation shows a power law approximation of the power spectrum at a pivot scale k_* and with a spectral index $n_s - 1 \equiv \frac{d \ln \Delta^2_{\mathcal{R}}}{d \ln k}$. For slow-roll inflation $n_s - 1 = 2\eta - 6\epsilon$ (Kamionkowski and Kovetz, 2016), where η and ϵ are the slow-roll parameters from equation 1.29. Therefore, a small deviation from scale invariance ($n_s = 1$) supports inflation. As shown in Table 1.1, recent *Planck* data indicates $n_s = 0.965 \pm 0.004$ (Planck Collaboration, 2018).

Similar to the scalar power spectrum, we can compute the power spectrum for tensor metric perturbations. These tensor perturbations are the primordial gravitational waves produced during inflation and have two polarization modes: h^+ and $h^\times$. By defining the tensor power spectrum as the sum of the power spectra of the two polarizations, we can calculate the quantities analogous to equations 1.30 and 1.31 as follows:

$$\begin{gathered} \langle h_{\mathbf{k}} h_{\mathbf{k'}} \rangle = (2\pi)^3 \delta(\mathbf{k} + \mathbf{k'}) P_h(k) \\ \Delta^2_h \equiv 2\, \frac{k^3}{2\pi^2} P_h(k) = A_t(k_*) \left(\frac{k}{k_*} \right)^{n_t(k_*)} . \end{gathered} \tag{1.32}$$

For a slow-roll inflation, the tensor spectral index $n_t = -2\epsilon$ (Kamionkowski and Kovetz, 2016). We can notice that n_t is always negative because the energy density keeps decreasing with time in slow-roll inflation.

In the slow-roll approximation, $\Delta^2_{\mathcal{R}}$ and Δ^2_h can also be calculated explicitly (see Baumann 2009) in terms of H and ϵ as follows:

$$\Delta^2_{\mathcal{R}} = \frac{1}{8\pi^2}\frac{H^2}{M^2_{\mathrm{Pl}}\epsilon}, \qquad \Delta^2_h = \frac{2}{\pi^2}\frac{H^2}{M^2_{\mathrm{Pl}}}, \tag{1.33}$$

where $M_{Pl} = (8\pi G)^{-1/2}$ is the reduced Planck mass. The primordial gravitational wave amplitude is often normalized to the scalar fluctuations amplitude as a tensor-to-scalar ratio:

$$r \equiv \frac{\Delta^2_h}{\Delta^2_{\mathcal{R}}} = 16\epsilon = -8n_t. \tag{1.34}$$

The current best constraint on the tensor-to-scalar ratio is $r < 0.07$ (95% CL) at $\mathrm{k}_* = 0.05\ \mathrm{Mpc}^{-1}$ (BICEP2 Collaboration et al., 2016). The value of r is a direct measure of the energy scale of inflation. Using the measured value of $\Delta^2_{\mathcal{R}} \sim 10^{-9}$ (Table 1.1) and $\Delta^2_h \propto H^2 \approx V$, we get:

$$V^{1/4} \sim \left(\frac{r}{0.01}\right)^{1/4} 10^{16}\ \mathrm{GeV}. \tag{1.35}$$

So, $r \sim 0.01 \Rightarrow V^{1/4} \sim 10^{16}$ GeV, corresponding to the GUT energy scale. Inflation, therefore, provides a means of testing physics at energy scales $\sim 10^{12}$ times higher than those accessible to terrestrial particle accelerators today. At these GUT energy scales, inflation provides insights into the quantum nature of gravity, as gravitational wave production during inflation is purely a quantum process (Krauss and Wilczek, 2014). Thus, in addition to solving the shortcomings in the standard big-bang cosmology, inflation provides evidence for interesting new physics inaccessible through other means. Therefore finding direct evidence of inflation is one of the highest priority scientific goals for modern cosmology as reflected in the Decadal Survey of Astronomy and Astrophysics (National Research Council, 2010).

As discussed in section 1.2.2, the detection of primordial B-modes in the CMB would be compelling evidence for inflation. With the advancements in detector technology and the prospects of higher sensitivity CMB telescopes, $r \gtrsim 10^{-3}$ could be experimentally accessible within the next decade. There is a global effort to detect primordial B-modes from ground-based and balloon-borne CMB telescopes as well as with a space mission in the near future. In this thesis, I focus on the CLASS telescope array that aims to detect and characterize the primordial B-mode signal at the $r = 0.01$ level. In the next chapter, I discuss the challenges associated with detecting the B-mode signal and how CLASS is designed to address those challenges.

References

Addison, G. E., D. J. Watts, C. L. Bennett, M. Halpern, G. Hinshaw, and J. L. Weiland (2018). “Elucidating ΛCDM: Impact of Baryon Acoustic Oscillation Measurements on the Hubble Constant Discrepancy”. In: *The Astrophysical Journal* 853.2, 119, p. 119. DOI: `10.3847/1538-4357/aaa1ed`. arXiv: `1707.06547 [astro-ph.CO]`.

Adrián-Martínez, S. et al. (2012). “Search for relativistic magnetic monopoles with the ANTARES neutrino telescope”. In: *Astroparticle Physics* 35.10, pp. 634–640. DOI: `10.1016/j.astropartphys.2012.02.007`. arXiv: `1110.2656 [astro-ph.HE]`.

Allen, James P. (2015). “Egyptian Cosmology and Cosmogony”. In: *Handbook of Archaeoastronomy and Ethnoastronomy*. Ed. by Clive L.N. Ruggles. New York, NY: Springer New York, pp. 1471–1475. DOI: `10.1007/978-1-4614-6141-8_147`.

Baumann, Daniel (2009). “TASI Lectures on Inflation”. In: *arXiv e-prints*, arXiv:0907.5424, arXiv:0907.5424. arXiv: `0907.5424 [hep-th]`.

BICEP2 Collaboration, Keck Array Collaboration, P. A. R. Ade, Z. Ahmed, R. W. Aikin, K. D. Alexand er, D. Barkats, S. J. Benton, C. A. Bischoff, J. J. Bock, R. Bowens-Rubin, J. A. Brevik, I. Buder, E. Bullock, V. Buza, J. Connors, B. P. Crill, L. Duband, C. Dvorkin, J. P. Filippini, S. Fliescher, J. Grayson, M. Halpern, S. Harrison, S. R. Hildebrandt, G. C. Hilton, H. Hui, K. D. Irwin, J. Kang, K. S. Karkare, E. Karpel, J. P. Kaufman, B. G. Keating, S. Kefeli, S. A. Kernasovskiy, J. M. Kovac, C. L. Kuo, E. M. Leitch, M. Lueker, K. G. Megerian, T. Namikawa, C. B. Netterfield, H. T. Nguyen, R. O’Brient, IV Ogburn R. W., A. Orland o, C. Pryke, S. Richter, R. Schwarz, C. D. Sheehy, Z. K. Staniszewski, B. Steinbach, R. V. Sudiwala, G. P. Teply, K. L. Thompson, J. E. Tolan, C. Tucker, A. D. Turner, A. G. Vieregg, A. C. Weber, D. V. Wiebe, J. Willmert, C. L. Wong, W. L. K. Wu, and K. W. Yoon (2016). “BICEP2/Keck Array VIII: Measurement of Gravitational Lensing from Large-scale B-mode Polarization". In: ApJ 833.2, 228, p. 228. DOI: 10.3847/1538-4357/833/2/228. arXiv: 1606.01968 [astro-ph.CO].

Bonvin, V., F. Courbin, S. H. Suyu, P. J. Marshall, C. E. Rusu, D. Sluse, M. Tewes, K. C. Wong, T. Collett, C. D. Fassnacht, T. Treu, M. W. Auger, S. Hilbert, L. V. E. Koopmans, G. Meylan, N. Rumbaugh, A. Sonnenfeld, and C. Spiniello (2017). "H0LiCOW - V. New COSMOGRAIL time delays of HE 0435-1223: H_0 to 3.8 per cent precision from strong lensing in a flat ΛCDM model". In: *Monthly Notices of the Royal Astronomical Society* 465.4, pp. 4914–4930. DOI: 10.1093/mnras/stw3006. arXiv: 1607.01790 [astro-ph.CO].

Detrixhe, M., D. Besson, P. W. Gorham, P. Allison, B. Baughmann, J. J. Beatty, K. Belov, S. Bevan, W. R. Binns, C. Chen, P. Chen, J. M. Clem, A. Connolly, D. De Marco, P. F. Dowkontt, M. A. DuVernois, C. Frankenfeld, E. W. Grashorn, D. P. Hogan, N. Griffith, B. Hill, S. Hoover, M. H. Israel, A. Javaid, K. M. Liewer, S. Matsuno, B. C. Mercurio, C. Miki, M. Mottram, J. Nam, R. J. Nichol, K. Palladino, A. Romero-Wolf, L. Ruckman, D. Saltzberg, D. Seckel, G. S. Varner, A. G. Vieregg, and Y. Wang (2011). "Ultrarelativistic magnetic monopole search with the ANITA-II balloon-borne radio interferometer". In: *Phys. Rev. D* 83 (2), p. 023513. DOI: 10.1103/PhysRevD.83.023513.

Fixsen, D. J., E. S. Cheng, J. M. Gales, J. C. Mather, R. A. Shafer, and E. L. Wright (1996). "The Cosmic Microwave Background Spectrum from the Full COBE FIRAS Data Set". In: ApJ 473, p. 576. DOI: 10.1086/178173. arXiv: astro-ph/9605054 [astro-ph].

Freedman, Wendy L., Barry F. Madore, Dylan Hatt, Taylor J. Hoyt, In Sung Jang, Rachael L. Beaton, Christopher R. Burns, Myung Gyoon Lee, Andrew J. Monson, Jillian R. Neeley, M. M. Phillips, Jeffrey A. Rich, and Mark Seibert (2019). "The Carnegie-Chicago Hubble Program. VIII. An Independent Determination of the Hubble Constant Based on the Tip of the Red Giant Branch". In: *The Astrophysical Journal* 882.1, p. 34. DOI: 10.3847/1538-4357/ab2f73.

Friedman, A. (1922). "Über die Krümmung des Raumes". In: *Zeitschrift für Physik* 10.1, pp. 377–386. DOI: 10.1007/BF01332580.

Goldberg, J. N., A. J. Macfarlane, E. T. Newman, F. Rohrlich, and E. C. G. Sudarshan (1967). "Spin-s Spherical Harmonics and $\eth$". In: *Journal of Mathematical Physics* 8.11, pp. 2155–2161. DOI: 10.1063/1.1705135.

Guth, Alan H. (1981). "The Inflationary Universe: A Possible Solution to the Horizon and Flatness Problems". In: *Phys. Rev.* D23, pp. 347–356. DOI: 10.1103/PhysRevD.23.347.

Hu, Wayne and Scott Dodelson (2002). “Cosmic Microwave Background Anisotropies”. In: ARA&A 40, pp. 171–216. DOI: `10.1146/annurev.astro.40.060401.093926`. arXiv: `astro-ph/0110414 [astro-ph]`.

Hu, Wayne and Martin White (1997). “A CMB polarization primer”. In: *New Astronomy* 2.4, pp. 323 –344. DOI: `https://doi.org/10.1016/S1384-1076(97)00022-5`.

Hubble, Edwin (1929). “A relation between distance and radial velocity among extra-galactic nebulae”. In: *Proceedings of the National Academy of Sciences* 15.3, pp. 168–173. DOI: `10.1073/pnas.15.3.168`.

Kamionkowski, Marc, Arthur Kosowsky, and Albert Stebbins (1997). “Statistics of cosmic microwave background polarization”. In: Phys. Rev. D 55.12, pp. 7368–7388. DOI: `10.1103/PhysRevD.55.7368`. arXiv: `astro-ph/9611125 [astro-ph]`.

Kamionkowski, Marc and Ely D. Kovetz (2016). “The Quest for B Modes from Inflationary Gravitational Waves”. In: ARA&A 54, pp. 227–269. DOI: `10.1146/annurev-astro-081915-023433`. arXiv: `1510.06042 [astro-ph.CO]`.

Krauss, Lawrence M., Scott Dodelson, and Stephan Meyer (2010). “Primordial Gravitational Waves and Cosmology”. In: *Science* 328.5981, p. 989. DOI: `10.1126/science.1179541`. arXiv: `1004.2504 [astro-ph.CO]`.

Krauss, Lawrence M. and Frank Wilczek (2014). “Using cosmology to establish the quantization of gravity”. In: Phys. Rev. D 89.4, 047501, p. 047501. DOI: `10.1103/PhysRevD.89.047501`. arXiv: `1309.5343 [hep-th]`.

Liddle, Andrew R. and Samuel M. Leach (2003). “How long before the end of inflation were observable perturbations produced?” In: Phys. Rev. D 68.10, 103503, p. 103503. DOI: `10.1103/PhysRevD.68.103503`. arXiv: `astro-ph/0305263 [astro-ph]`.

MACRO Collaboration (2002). “Final results of magnetic monopole searches with the MACRO experiment”. In: *European Physical Journal C* 25.4, pp. 511–522. arXiv: `hep-ex/0207020 [hep-ex]`.

Mather, J. C., D. J. Fixsen, R. A. Shafer, C. Mosier, and D. T. Wilkinson (1999). “Calibrator Design for the COBE Far-Infrared Absolute Spectrophotometer (FIRAS)”. In: ApJ 512.2, pp. 511–520. DOI: `10.1086/306805`. arXiv: `astro-ph/9810373 [astro-ph]`.

MoEDAL Collaboration, B. Acharya, J. Alexandre, K. Bendtz, P. Benes, J. Bernabéu, M. Campbell, S. Cecchini, J. Chwastowski, A. Chatterjee, M. de Montigny, D. Derendarz, A. De Roeck, J. R. Ellis, M. Fairbairn, D. Felea, M. Frank, D. Frekers, C. Garcia, G. Giacomelli, D. Hașegan, M. Kalliokoski, A. Katre, D. W. Kim, M. G. L. King, K. Kinoshita, D. H. Lacarrère, S. C.

Lee, C. Leroy, A. Lionti, A. Margiotta, N. Mauri, N. E. Mavromatos, P. Mermod, D. Milstead, V. A. Mitsou, R. Orava, B. Parker, L. Pasqualini, L. Patrizii, G. E. Păvălaș, J. L. Pinfold, M. Platkevič, V. Popa, M. Pozzato, S. Pospisil, A. Rajantie, Z. Sahnoun, M. Sakellariadou, S. Sarkar, G. Semenoff, G. Sirri, K. Sliwa, R. Soluk, M. Spurio, Y. N. Srivastava, R. Staszewski, M. Suk, J. Swain, M. Tenti, V. Togo, M. Trzebinski, J. A. Tuszyński, V. Vento, O. Vives, Z. Vykydal, T. Whyntie, A. Widom, and J. H. Yoon (2016). "Search for magnetic monopoles with the MoEDAL prototype trapping detector in 8 TeV proton-proton collisions at the LHC". In: *arXiv e-prints*, arXiv:1604.06645, arXiv:1604.06645. arXiv: `1604.06645 [hep-ex]`.

National Research Council (2010). *New Worlds, New Horizons in Astronomy and Astrophysics*. Washington, DC: The National Academies Press. ISBN: 978-0-309-15799-5. DOI: `10.17226/12951`.

Page, L., G. Hinshaw, E. Komatsu, M. R. Nolta, D. N. Spergel, C. L. Bennett, C. Barnes, R. Bean, O. Doré, J. Dunkley, M. Halpern, R. S. Hill, N. Jarosik, A. Kogut, M. Limon, S. S. Meyer, N. Odegard, H. V. Peiris, G. S. Tucker, L. Verde, J. L. Weiland, E. Wollack, and E. L. Wright (2007). "Three-Year Wilkinson Microwave Anisotropy Probe (WMAP) Observations: Polarization Analysis". In: ApJS 170.2, pp. 335–376. DOI: `10.1086/513699`. arXiv: `astro-ph/0603450 [astro-ph]`.

Penzias, A. A. and R. W. Wilson (1965). "A Measurement of Excess Antenna Temperature at 4080 Mc/s." In: ApJ 142, pp. 419–421. DOI: `10.1086/148307`.

Perlmutter, S., G. Aldering, G. Goldhaber, R. A. Knop, P. Nugent, P. G. Castro, S. Deustua, S. Fabbro, A. Goobar, D. E. Groom, I. M. Hook, A. G. Kim, M. Y. Kim, J. C. Lee, N. J. Nunes, R. Pain, C. R. Pennypacker, R. Quimby, C. Lidman, R. S. Ellis, M. Irwin, R. G. McMahon, P. Ruiz-Lapuente, N. Walton, B. Schaefer, B. J. Boyle, A. V. Filippenko, T. Matheson, A. S. Fruchter, N. Panagia, H. J. M. Newberg, W. J. Couch, and The Supernova Cosmology Project (1999). "Measurements of Ω and Λ from 42 High-Redshift Supernovae". In: ApJ 517.2, pp. 565–586. DOI: `10.1086/307221`. arXiv: `astro-ph/9812133 [astro-ph]`.

Planck Collaboration (2018). "Planck 2018 results. VI. Cosmological parameters". In: *arXiv e-prints*, arXiv:1807.06209. arXiv: `1807.06209`.

POLARBEAR Collaboration, P. A. R. Ade, M. Aguilar, Y. Akiba, K. Arnold, C. Baccigalupi, D. Barron, D. Beck, F. Bianchini, D. Boettger, J. Borrill, S. Chapman, Y. Chinone, K. Crowley, A. Cukierman, R. Dünner, M. Dobbs, A. Ducout, T. Elleflot, J. Errard, G. Fabbian, S. M. Feeney, C. Feng, T. Fujino, N. Galitzki, A. Gilbert, N. Goeckner-Wald, J. C. Groh, G. Hall, N. Halverson,

T. Hamada, M. Hasegawa, M. Hazumi, C. A. Hill, L. Howe, Y. Inoue, G. Jaehnig, A. H. Jaffe, O. Jeong, D. Kaneko, N. Katayama, B. Keating, R. Keskitalo, T. Kisner, N. Krachmalnicoff, A. Kusaka, M. Le Jeune, A. T. Lee, E. M. Leitch, D. Leon, E. Linder, L. Lowry, F. Matsuda, T. Matsumura, Y. Minami, J. Montgomery, M. Navaroli, H. Nishino, H. Paar, J. Peloton, A. T. P. Pham, D. Poletti, G. Puglisi, C. L. Reichardt, P. L. Richards, C. Ross, Y. Segawa, B. D. Sherwin, M. Silva-Feaver, P. Siritanasak, N. Stebor, R. Stompor, A. Suzuki, O. Tajima, S. Takakura, S. Takatori, D. Tanabe, G. P. Teply, T. Tomaru, C. Tucker, N. Whitehorn, and A. Zahn (2017). "A Measurement of the Cosmic Microwave Background B-mode Polarization Power Spectrum at Subdegree Scales from Two Years of polarbear Data". In: ApJ 848.2, 121, p. 121. DOI: `10.3847/1538-4357/aa8e9f`. arXiv: `1705.02907 [astro-ph.CO]`.

Preskill, John P. (1979). "Cosmological Production of Superheavy Magnetic Monopoles". In: *Phys. Rev. Lett.* 43 (19), pp. 1365–1368. DOI: `10.1103/PhysRevLett.43.1365`.

Riess, Adam G., Alexei V. Filippenko, Peter Challis, Alejandro Clocchiatti, Alan Diercks, Peter M. Garnavich, Ron L. Gilliland, Craig J. Hogan, Saurabh Jha, Robert P. Kirshner, B. Leibundgut, M. M. Phillips, David Reiss, Brian P. Schmidt, Robert A. Schommer, R. Chris Smith, J. Spyromilio, Christopher Stubbs, Nicholas B. Suntzeff, and John Tonry (1998). "Observational Evidence from Supernovae for an Accelerating Universe and a Cosmological Constant". In: AJ 116.3, pp. 1009–1038. DOI: `10.1086/300499`. arXiv: `astro-ph/9805201 [astro-ph]`.

Riess, Adam G., Stefano Casertano, Wenlong Yuan, Lucas M. Macri, and Dan Scolnic (2019). In: *The Astrophysical Journal* 876.1, p. 85. DOI: `10.3847/1538-4357/ab1422`.

Ryden, Barbara (2003). *Introduction to Cosmology*. San Francisco, USA: Addison-Wesley, p. 244.

Sachs, R. K. and A. M. Wolfe (1967). "Perturbations of a Cosmological Model and Angular Variations of the Microwave Background". In: ApJ 147, p. 73. DOI: `10.1086/148982`.

Sayre, J. T., C. L. Reichardt, J. W. Henning, P. A. R. Ade, A. J. Anderson, J. E. Austermann, J. S. Avva, J. A. Beall, A. N. Bender, B. A. Benson, F. Bianchini, L. E. Bleem, J. E. Carlstrom, C. L. Chang, H. C. Chiang, R. Citron, C. Corbett Moran, T. M. Crawford, A. T. Crites, T. de Haan, M. A. Dobbs, W. Everett, J. Gallicchio, E. M. George, A. Gilbert, N. Gupta, N. W. Halverson, N. Harrington, G. C. Hilton, G. P. Holder, W. L. Holzapfel, J. D. Hrubes, N. Huang,

J. Hubmayr, K. D. Irwin, L. Knox, A. T. Lee, D. Li, A. Lowitz, J. J. McMahon, S. S. Meyer, L. M. Mocanu, J. Montgomery, A. Nadolski, T. Natoli, J. P. Nibarger, G. Noble, V. Novosad, S. Padin, S. Patil, C. Pryke, J. E. Ruhl, B. R. Saliwanchik, K. K. Schaffer, C. Sievers, G. Smecher, A. A. Stark, C. Tucker, K. Vanderlinde, T. Veach, J. D. Vieira, G. Wang, N. Whitehorn, W. L. K. Wu, and V. Yefremenko (2019). "Measurements of B-mode Polarization of the Cosmic Microwave Background from 500 Square Degrees of SPTpol Data". In: *arXiv e-prints*, arXiv:1910.05748, arXiv:1910.05748. arXiv: `1910.05748 [astro-ph.CO]`.

Sherwin, Blake D., Alexander van Engelen, Neelima Sehgal, Mathew Madhavacheril, Graeme E. Addison, Simone Aiola, Rupert Allison, Nicholas Battaglia, Daniel T. Becker, James A. Beall, J. Richard Bond, Erminia Calabrese, Rahul Datta, Mark J. Devlin, Rolando Dünner, Joanna Dunkley, Anna E. Fox, Patricio Gallardo, Mark Halpern, Matthew Hasselfield, Shawn Henderson, J. Colin Hill, Gene C. Hilton, Johannes Hubmayr, John P. Hughes, Adam D. Hincks, Renée Hlozek, Kevin M. Huffenberger, Brian Koopman, Arthur Kosowsky, Thibaut Louis, Loïc Maurin, Jeff McMahon, Kavilan Moodley, Sigurd Naess, Federico Nati, Laura Newburgh, Michael D. Niemack, Lyman A. Page, Jonathan Sievers, David N. Spergel, Suzanne T. Staggs, Robert J. Thornton, Jeff Van Lanen, Eve Vavagiakis, and Edward J. Wollack (2017). "Two-season Atacama Cosmology Telescope polarimeter lensing power spectrum". In: *Phys. Rev. D* 95 (12), p. 123529. DOI: `10.1103/PhysRevD.95.123529`.

Silk, Joseph (1968). "Cosmic Black-Body Radiation and Galaxy Formation". In: ApJ 151, p. 459. DOI: `10.1086/149449`.

Smoot, G. F., C. L. Bennett, A. Kogut, E. L. Wright, J. Aymon, N. W. Boggess, E. S. Cheng, G. de Amici, S. Gulkis, M. G. Hauser, G. Hinshaw, P. D. Jackson, M. Janssen, E. Kaita, T. Kelsall, P. Keegstra, C. Lineweaver, K. Loewenstein, P. Lubin, J. Mather, S. S. Meyer, S. H. Moseley, T. Murdock, L. Rokke, R. F. Silverberg, L. Tenorio, R. Weiss, and D. T. Wilkinson (1992). "Structure in the COBE Differential Microwave Radiometer First-Year Maps". In: ApJ 396, p. L1. DOI: `10.1086/186504`.

Turner, Michael S., E. N. Parker, and T. J. Bogdan (1982). "Magnetic monopoles and the survival of galactic magnetic fields". In: *Phys. Rev. D* 26 (6), pp. 1296–1305. DOI: `10.1103/PhysRevD.26.1296`.

Zaldarriaga, Matias and Uroš Seljak (1997). "All-sky analysis of polarization in the microwave background". In: Phys. Rev. D 55.4, pp. 1830–1840. DOI: `10.1103/PhysRevD.55.1830`. arXiv: `astro-ph/9609170 [astro-ph]`.

Chapter 2

CLASS Overview

CLASS observes the CMB polarization over large angular scales ($\theta \gtrsim 1^\circ$) with the aim of characterizing the primordial gravitational waves and measuring the optical depth due to reionization. CLASS is located at an altitude of 5200 m in the Atacama Desert of Chile, which allows the observation of 70% of the microwave sky every day while minimizing the noise from atmospheric loading. CLASS consists of four telescopes: two 90 GHz telescopes optimized for CMB observation near the minimum of polarized Galactic emission, a 40 GHz telescope probing the polarized synchrotron emission, and a 150/220 GHz dichroic receiver mapping the polarized dust. To achieve the high sensitivity and stability required to map the CMB polarization over large angular scales, CLASS employs a unique combination of large sky coverage, broad frequency range, rapid front-end polarization modulation, and background-limited detectors. In this chapter, I describe CLASS's science goals, challenges associated with making a large angular scale CMB polarization measurement, and the observation strategy and experimental design employed by CLASS to address those challenges.

2.1 Science Goals

Precise measurement of the CMB polarization at large angular scales enables us to test and characterize the inflationary paradigm, pinpoint the epoch of reionization, constrain the mass of neutrinos, and probe new physics beyond the standard model. CLASS is optimized to measure both the recombination and reionization peaks in the CMB polarization spectra in order to achieve these goals. In particular, measurement of the B-mode spectrum will provide constraints on the primordial gravitational waves and hence provide evidence for (or against) inflation, whereas measurement of the E-mode spectrum will constrain the epoch of reionization and the sum of neutrino masses.

2.1.1 Inflation

As discussed in section 1.2.2, detecting the B-mode polarization pattern in the CMB induced by primordial gravitational waves would be compelling evidence for inflation. CLASS is designed to detect and characterize the primordial gravitational waves at the level of $r = 0.01$. Figure 2.1 shows the projected CLASS sensitivity along with different theoretical B-mode spectra that scale with the value of r at large angular scales. CLASS probes B-modes at these low multipoles ($\ell \lesssim 150$) as the power in the primordial signal is boosted by recombination and reionization (see section 1.2.2). At higher multipoles, however, gravitational lensing of much brighter E-modes into B-modes dominates the spectrum. This lensing signal has already been measured by multiple experiments (Sayre et al., 2019; POLARBEAR Collaboration et al., 2017; Louis et al., 2017; BICEP2 Collaboration et al., 2016).

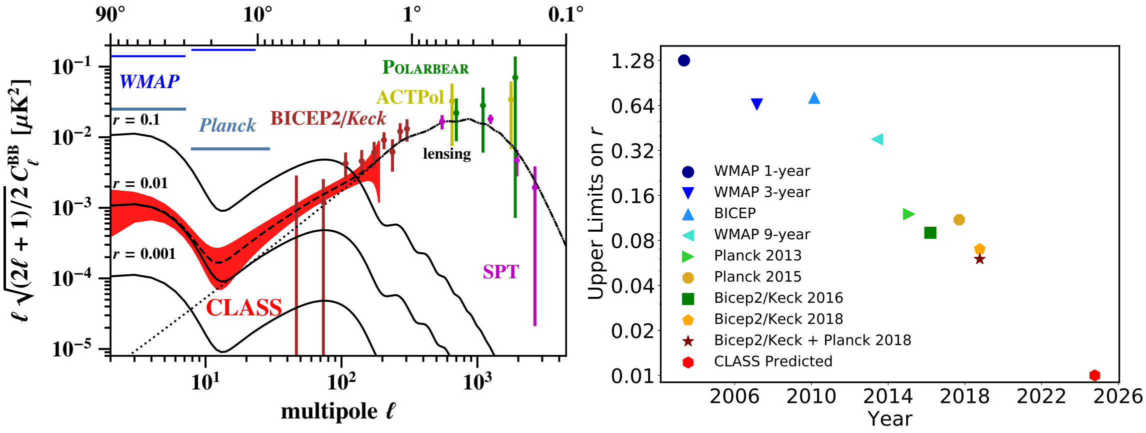

Figure 2.1: (Left) B-mode power spectra for $r = 0.1$, 0.01, and 0.001 showing the recombination peak at $\ell \sim 100$ and the reionization peak at $\ell \lesssim 10$. At small angular scales, B-modes are dominated by gravitational lensing of E-modes. The red band shows the projected CLASS sensitivity to measure B-modes at $r \sim 0.01$ level independent of the lensing foreground. Figure credit: D. Watts. (Right) Thanks to experiments with increasing CMB polarization sensitivity, the upper limits on r have been decreasing over the past two decades. As the upper limits on r continue to improve, lensing will become an increasingly important error term for experiments observing at small angular scales ($\ell \gtrsim 100$). The red point highlights the improvement in the measurement of r with the projected CLASS B-mode sensitivity at large angular scales. Figure prepared by author for thesis.

Over the past two decades, with better understanding of Galactic foregrounds (described in section 2.2) and experiments with increasing CMB polarization sensitivity, the upper limits on r have been decreasing as shown in Figure 2.1. As the upper limits on r continue to improve, lensing will become an increasingly important error term. Any tentative detection from ground-based experiments at small angular scales ($\ell \gtrsim 100$) at the $r \sim 0.01$ level will necessarily include a large correction for the lensing foreground. On the other hand, at large angular scales, B-modes at the $r \sim 0.01$ level can be measured independent of the lensing foreground. Therefore, CLASS is designed to make CMB polarization measurements at large angular scales.

2.1.2 Reionization

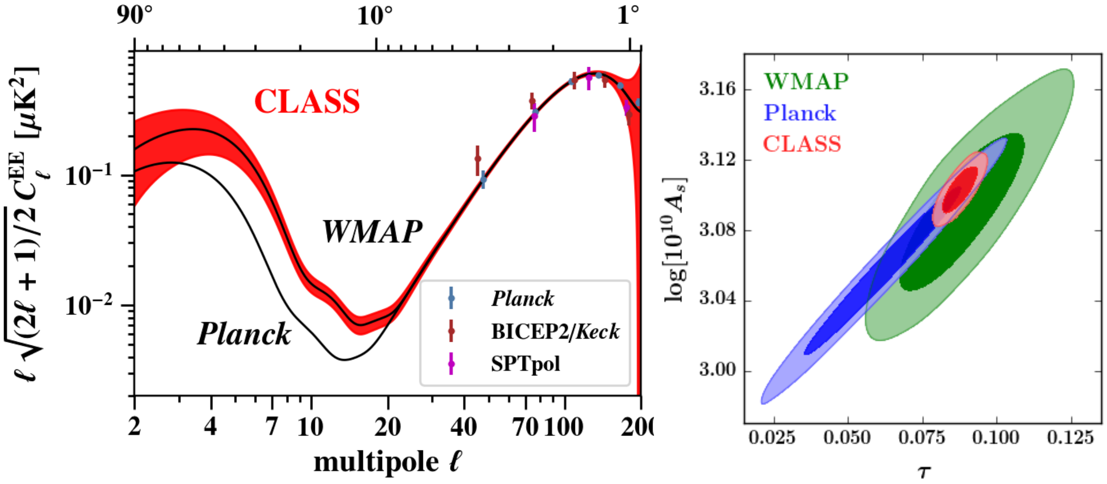

Figure 2.2: (Left) The best fit models for *WMAP* 9-year ($\tau = 0.083$) and *Planck* "pre 2016" data ($\tau = 0.055$) along with measurements from BICEP2/Keck and SPTpol experiments. The red band shows the CLASS sensitivity (assuming *WMAP* 9-year value for τ) that can distinguish between the two best fit models. (Right) Constraints in A_s and τ from *WMAP* 9-year and *Planck* 2015 temperature and polarization data that highlights the degeneracy between the two quantities. CLASS can improve the uncertainty in τ to near the cosmic variance limit by breaking this degeneracy through the E-mode polarization measurement at large angular scales. Figure credit: D. Watts

Cosmic reionization from the formation of the first stars and galaxies in the Universe is a critical but poorly-understood phase in the standard cosmological picture. As shown in Table 1.1, the optical depth due to reionization τ is the least constrained standard ΛCDM parameter. This is primarily because reionization suppresses the temperature anisotropy except at the lowest multipoles (Zaldarriaga and Seljak, 1997); therefore, τ is almost degenerate with the amplitude as $C_\ell^{TT} \propto A_s e^{-2\tau}$ for $\ell \gtrsim 20$. This anisotropy suppression happens since the CMB photons are rescattered by free electrons during reionization, erasing fluctuations below the horizon scale at last scattering. We can break this degeneracy by measuring the polarization spectra at large angular scales where the spectrum roughly scales as $C^{EE}_{2\leqslant\ell\leqslant20} \propto \tau^2$ (Page et al., 2007). Figure 2.2 shows the CLASS sensitivity to measure the E-mode polarization at large angular scales. Through this measurement, CLASS can break the $A_s e^{-2\tau}$ degeneracy in temperature anisotropy measurements and constrain τ to nearly cosmic variance limit with $\sigma_\tau \sim 0.003$ (Watts et al., 2018). So, even future experiments cannot meaningfully improve on this τ measurement with data from the CMB alone. In addition, beyond measuring τ, CLASS's low-ℓ polarization measurement can provide constraints on different reionization scenarios from instantaneous to extended redshift models (Watts et al., 2020).

2.1.3 Neutrino Mass

From neutrino oscillation experiments, we have strong evidence that neutrinos have non-zero masses (Fukuda et al., 1998; Ahmad et al., 2001). However, their absolute mass scale and hierarchy are not well known. While the oscillation experiments are useful for studying the mixing and the differences in the masses of the different types of neutrinos, their constraints on the total neutrino mass (Σm_ν) is limited: $\Sigma m_\nu > 60$ meV for a “normal hierarchy” with two lighter and one heavier neutrino, and $\Sigma m_\nu > 100$ meV for an “inverted hierarchy” with two massive neutrinos (Allison et al., 2015). While it is possible to measure absolute neutrino masses through lab experiments using the kinematic effect of a non-zero neutrino mass in ordinary beta decay or through neutrino-less double beta decay (if neutrinos are Majorana particles), these measurements are extremely challenging (Hannestad, 2010). One viable

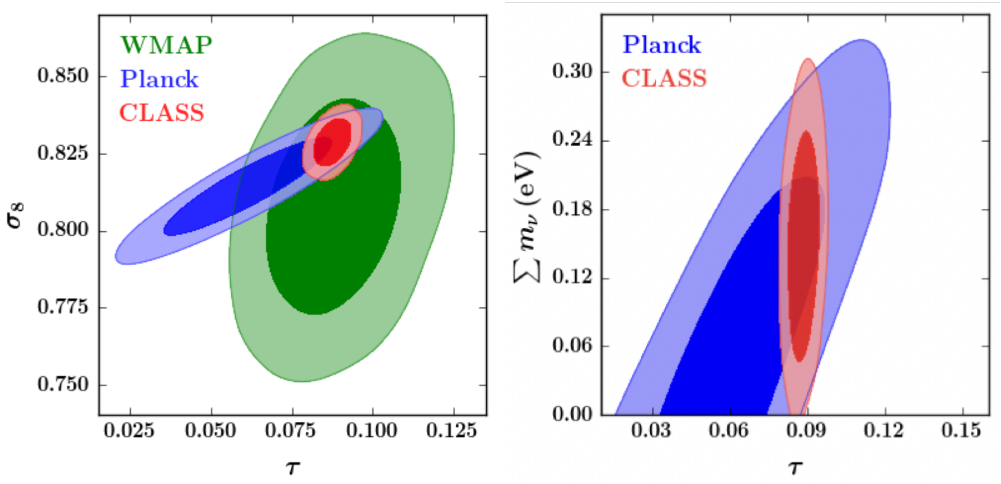

Figure 2.3: (Left) *WMAP* and *Planck* measurements of the present density fluctuations parameterized through σ_8 is limited by the degeneracy between A_s and τ (Figure 2.2). Through low-ℓ E-mode measurement, CLASS can break this degeneracy to improve the constrains on σ_8. (Right) The improvement in the *Planck* 2015 and BAO constraints on the sum of neutrino masses Σm_ν with the addition of nearly cosmic variance limited measurement of τ by CLASS. Figure from Harrington et al. (2016)

alternative is to look for the effect of neutrino masses in cosmological structure formation.

In the standard model, massive neutrinos were relativistic in the early universe, even when the CMB decoupled. Due to their weak interactions, they free-streamed out of over-dense regions suppressing the growth of matter perturbations inside the horizon (Allison et al., 2015). The suppression of the matter power spectrum observed today is proportional to Σm_ν (Hu, Eisenstein, and Tegmark, 1998). The estimate of matter fluctuations today, usually parameterized by the amplitude of dark matter density fluctuations at $8\,h^{-1}$ Mpc scale, σ_8, is based on the amplitude of primordial scalar fluctuations A_s. Therefore, due to the $A_s e^{-2\tau}$ degeneracy discussed in section 2.1.2, the uncertainty in σ_8 is driven by the uncertainty in τ (or A_s) as shown in Figure 2.3.

With CLASS's ability to break the $A_s - \tau$ degeneracy, the constraints on σ_8 and Σm_ν can be significantly improved. Allison et al. (2015) have shown that with a CLASS-like low-ℓ measurement combined with future CMB lensing and Baryonic Acoustic Oscillation (BAO) measurements, the error in Σm_ν can be reduced down to $\sigma(\Sigma m_\nu) \approx 15$ meV, providing a 4σ detection even in the minimum-allowed $\Sigma m_\nu = 60$ meV case.

2.1.4 Other Science

In addition to the three major science goals discussed above, CLASS is well suited to probe new physics and cosmic anomalies beyond the standard model with its high-sensitivity large-scale CMB polarization measurement of over 70% of the sky. For instance, although the standard ΛCDM model does not predict any significant primordial circular polarization (section 1.2.2), CLASS can probe other theoretical models that contain circularly polarized emission mechanisms (De and Tashiro, 2015; Giovannini, 2009; Carroll, Field, and Jackiw, 1990). With the first two years of 40 GHz observations, CLASS has already put upper limits on the circular polarization from 0.4 to 13.5 μK^2 in the $1 \leq \ell \leq 120$ range, a two orders-of-magnitude improvement over previous limits (Padilla et al., 2020). This measurement will further improve after inclusion of more data from all four CLASS telescopes. CLASS has also reported the first detection of atmospheric circular polarization at 40 GHz due to the Zeeman splitting of the dipole transitions of atmospheric molecular oxygen induced by the Earth's magnetic field (Petroff et al., 2020).

With high sensitivity polarization maps over 70% of the sky, CLASS can also test large-scale cosmic anomalies. Although the possible anomalies in *WMAP* and *Planck* data are not statistically significant (Bennett et al., 2011; Schwarz et al., 2016), CLASS can provide the most stringent test to date for these anomalies through its large-scale polarization data. Finally, CLASS will characterize the polarized Galactic foregrounds (discussed in section 2.2) over 70% of the sky at multiple frequencies. This information will not only provide legacy data for future CMB experiments but also improve our understanding of the Milky Way and the nearby Magellanic clouds.

2.2 Galactic Foregrounds

In Section 2.1, we discussed how the precise measurement of CMB polarization at large angular scales has profound implications across multiple disciplines including cosmology, astrophysics, and particle physics. However, the measurement is challenging as the faint CMB signal is buried among much brighter Galactic foregrounds (and potential systematic effects). As shown in Figure 2.4, the contribution from Galactic foregrounds is at a minimum around $70 - 100$ GHz (depending on sky location) for both intensity and polarization. This frequency range is therefore a primary consideration while designing CMB experiments. Ground-based experiments like CLASS have an additional constraint due to atmospheric absorption at microwave frequencies, which we discuss in detail in section 2.4. Here we focus on foreground sources of microwave emission that are Galactic in origin. While free-free emission from electron-ion collision and electric dipole radiation from spinning dust grains produce microwave radiation (Figure 2.4, top panel), their contribution to

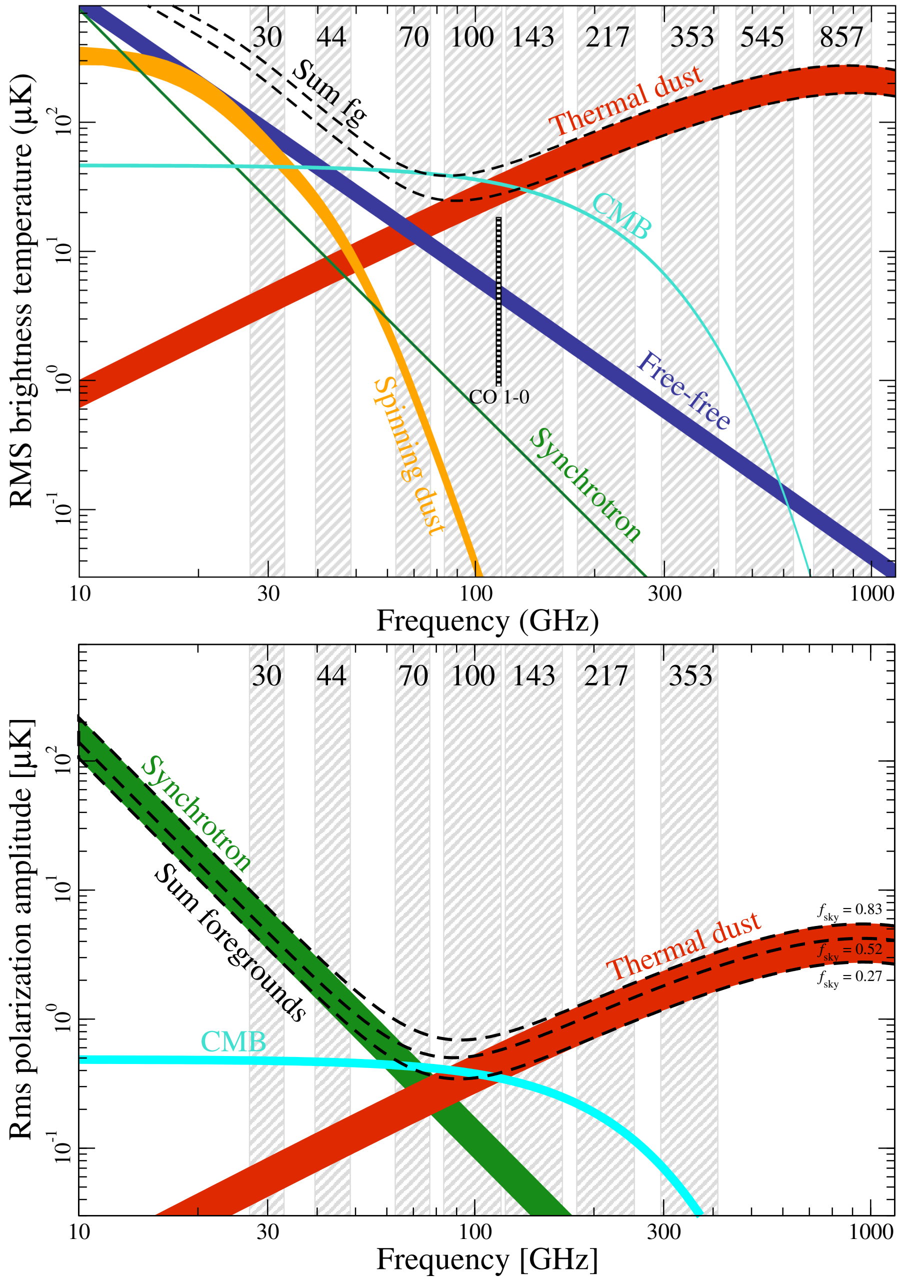

Figure 2.4: Summary of brightness temperature rms as a function of frequency and foreground sources for temperature (top) and polarization (bottom). For the temperature plot, the lower and upper edges of each line represent 81% and 93% sky fraction, respectively. The temperature and polarization plots were obtained from Planck Collaboration et al. (2016) and Planck Collaboration et al. (2018), respectively.

polarization is small enough that it has yet to be detected. Therefore, these two foreground sources are not considered further (Figure 2.4, bottom panel). The two dominant polarized Galactic foregrounds for CMB observations are synchrotron and thermal dust emission.

2.2.1 Synchrotron

Relativistic cosmic-ray electrons accelerating in the Galactic magnetic field produce diffuse synchrotron emission, which is the dominant polarized foreground component at frequencies $\lesssim 70$ GHz (Figure 2.4, bottom panel). Above 20 GHz, its brightness temperature spectrum can be approximated by a power law $T(\nu) \propto \nu^{\beta_s}$ with $\beta_s \approx -3$, but with significant flattening at lower frequencies (Planck Collaboration et al., 2016). There is also a considerable spatial variation in the power law index across the sky with $-3.1 < \beta_s < -2.5$ (Fuskeland et al., 2014). The synchrotron radiation is instrinsically strongly polarized in the direction perpendicular to the Galactic magnetic field. Although for a perfectly regular magnetic field, the synchrotron polarization fraction may exceed 70% (Pacholczyk, 1970), *WMAP* observations indicate that the polarization fraction is about 3% in the Galactic plane and about 20% at high Galactic latitudes (Page et al., 2007).

2.2.2 Thermal Dust

As shown in Figure 2.4, at frequencies $\gtrsim$ 100 GHz, thermal dust emission is the dominant polarized foreground component. *Planck* observations have found this emission to be consistent with a modified blackbody (often referred to as a grey-body) with intensity $I_\nu \propto B_\nu(T_\mathrm{d})\nu^{\beta_\mathrm{d}}$, where $B_\nu(T_\mathrm{d})$ is the Planck blackbody intensity at temperature $T_\mathrm{d} \sim 20$ K and spectral index $\beta_\mathrm{d} \sim 1.5$ (Planck Collaboration et al., 2016). As the Galactic magnetic fields tend to align the major axis of asymmetric dust grains perpendicular to the direction of the magnetic field, polarization is induced perpendicular to the field. While the polarization fraction varies considerably across the sky (reaching up to $\sim 20\%$), there is no region in the sky clean enough to enable primordial B-mode detection without foreground subtraction (Planck Collaboration et al., 2016).

The polarized amplitude for the CMB shown in Figure 2.4 is dominated by the E-mode component. So the foreground emission on large angular scales is brighter than the B-mode signal at all frequencies. Relying on the fact that the thermal dust and the synchrotron emissions both have different frequency dependence than the CMB, it is possible to separate the CMB signal from the foreground components. However, this requires high-sensitivity multi-frequency observations aimed at characterizing the foregrounds as well as measuring the CMB near the foreground minimum (Watts et al., 2015).

2.3 CLASS Strategy

To recover the CMB polarization at large angular scales in the presence of polarized Galactic foregrounds, CLASS maps 70% of the microwave sky at four frequency bands between 40 and 220 GHz. As upper limits on r decrease, primordial B-modes will dominate over lensing B-modes at increasingly large scales. Therefore, as shown in Figure 2.5, CLASS is designed to measure

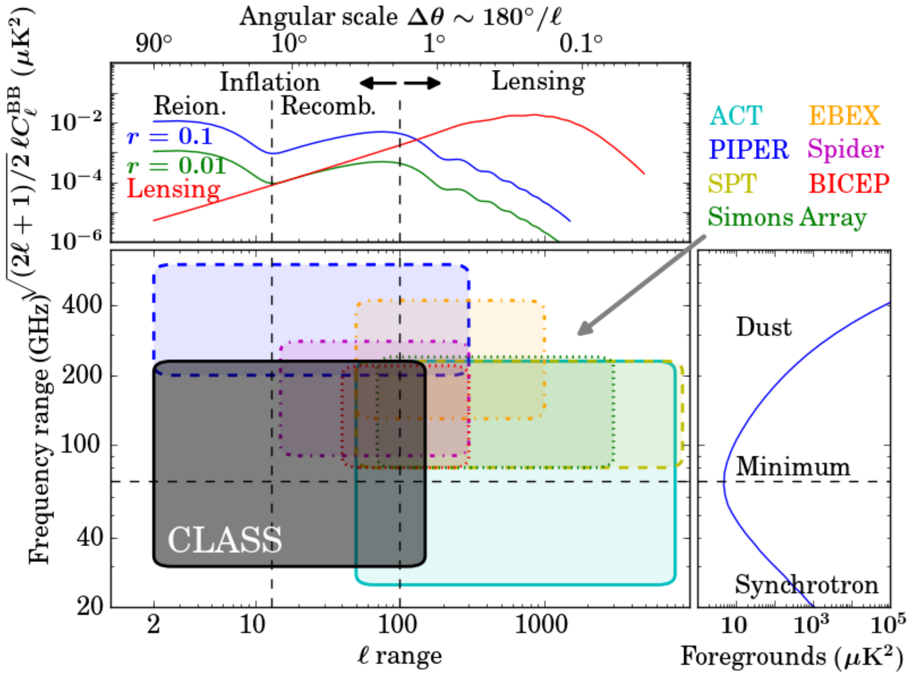

Figure 2.5: Summary of multipole vs frequency coverage for current ground-based and balloon-borne CMB polarization experiments. CLASS is uniquely designed to measure both the reionization and recombination peaks of the primordial B-mode signal (top panel) at large angular scales while straddling the foreground minimum (right panel). Figure from Watts et al. (2015)

the reionization and recombination peaks at large angular scales to detect and characterize the primordial gravitational waves at the $r \sim 0.01$ level independent of the lensing foreground. CLASS's ability to constrain τ also comes from measuring the E-modes at these large angular scales (Section 2.1.2). In addition, CLASS's frequency coverage is optimized to measure the CMB polarization while straddling the foreground minimum. Among the four CLASS telescopes, the two 90 GHz receivers are optimized to achieve high CMB polarization sensitivity near the foreground minimum, while the 40 GHz and the dichroic 150/220 GHz receivers are designed to probe the polarized synchrotron and thermal dust emissions, respectively. As shown in Figure 2.5,

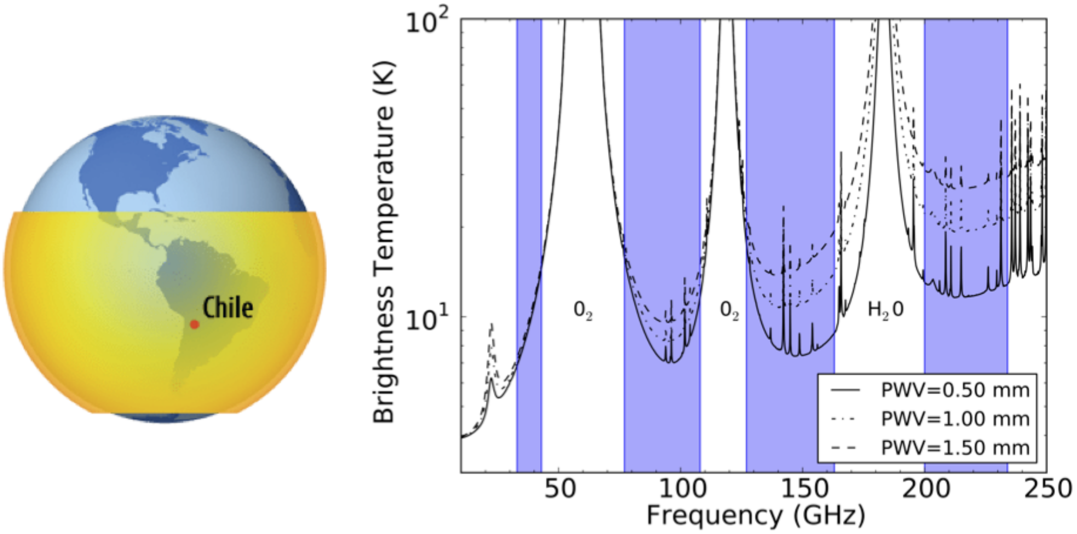

Figure 2.6: Sky coverage and atmospheric loading are the two important factors in deciding CLASS's location at 5200 m altitude in the Atacama Desert of Chile. (Left) This location, near the equator at $\approx -23°$ latitude, allows CLASS to survey 70% of the sky at 45° elevation. (Right) Estimate of brightness temperature vs frequency for different PWV levels. While the high and dry CLASS site conditions reduce the noise from atmospheric loading, the CLASS frequency bands (blue) were chosen to avoid the prominent atmospheric oxygen and water emission lines. Figure from Essinger-Hileman et al. (2014).

CLASS aims to measure both the recombination and reionization peaks in the CMB polarization spectra through a unique combination of frequency and sky coverage.

CLASS's large sky coverage is made possible by its instrument design (described in Section 2.4) and its location in the Atacama Desert of Chile. For observations at 45° elevation, the CLASS site at $\approx -23°$ latitude enables 70% sky coverage as shown in Figure 2.6. For comparison, observations at the same elevation from the South Pole (where other CMB polarization experiments like BICEP and SPT are located) can only cover about 25% of the sky (Essinger-Hileman et al., 2014), which makes measurement of the reionization bump at $\ell \lesssim 10$ impossible. An additional reason for the selection of the CLASS site located at 5200 m altitude in the Atacama Desert is the reduction in noise due to low and stable atmospheric loading conditions. On one hand, the high altitude reduces the baseline loading due to less atmospheric oxygen. On the other hand, the precipitable water vapor (PWV) that measures the variable portion of the atmospheric emission is low with a median of ~ 1.3 mm[1] at the CLASS location. Therefore, the high and dry CLASS site has the advantage of having low and stable atmospheric loading, while allowing a large sky coverage. The frequency bands for CLASS telescopes were also optimized to maximize the CMB sensitivity while avoiding the prominent atmospheric oxygen and water emission lines as shown in Figure 2.6.

2.4 Instrument Design

While the location of CLASS allows access to the CMB polarization on the largest angular scales under low atmospheric loading conditions, making the measurement itself is challenging. In addition to possible contamination from polarized foregrounds, the CMB polarization has extremely low signal-to-noise ratio. Therefore, first of all, detecting primordial B-modes at the $r = 0.01$ level requires high sensitivity to measure nK-scale fluctuations of the 2.73 K uniform background. Secondly, the intensity signal from the atmosphere and the CMB are both orders of magnitude higher than the polarization signal of interest (see Figure 2.4 and 2.6). So, systematic errors like instrumental polarization (where the instrument undesirably converts unpolarized intensity to a polarized signal) need to be carefully mitigated in the instrument design. In this section, we discuss the CLASS instrument design that is optimized to make high sensitivity CMB polarization measurements while controlling systematic errors.

---

[1] APEX weather monitor, www.apex-telescope.org/weather/

2.4.1 Telescope Mount

The four CLASS telescopes share two identical mounts, shown in Figure 2.7, that can rotate in three axes: azimuth (-200° to $+560^\circ$), elevation (20° to 90°), and boresight (-45° to $+45^\circ$). The CLASS observation strategy is to scan azimuthally across 720° at $\sim 1^\circ\,\mathrm{s}^{-1}$ keeping a constant elevation of 45°. This scan strategy covers the entire CLASS survey area ($\sim 70\%$ of the sky) every day, except for an avoidance region of 20° around the Sun. The telescope boresight angle is changed every day by 15°, nominally covering seven boresight angles from -45° to $+45^\circ$ each week. As the boresight rotation changes the polarization direction of the detectors on the sky relative to the horizon, it helps to break degeneracies when solving for the polarization maps from the raw detector timestreams. In addition, it provides an important systematics check to separate polarized ground pickup from celestial polarization. To mitigate the ground pickup, the receivers are housed inside a comoving ground shield and a forebaffle as shown in Figure 2.7.

All CLASS telescopes share a similar optical design (Figure 2.7, right panel). The incoming light through the forebaffle encounters the polarization modulator (described in section 2.4.2) first, before being reflected into the cryogenic receiver (described in section 2.4.3) by the primary and secondary mirrors.

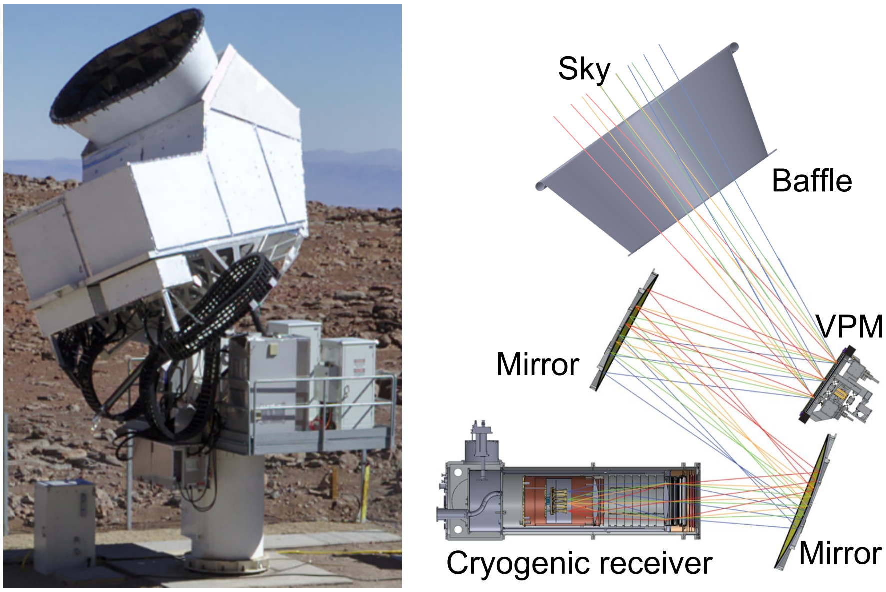

Figure 2.7: (Left) Photograph of one of the two identical telescope configurations. Each configuration has a mount that houses two receivers inside a metal structure that acts as a comoving ground shield. (Right) Diagram of the 40 GHz telescope showing light rays from the sky converging onto the focal plane. All four CLASS telescopes have similar design including the baffle, VPM (section 2.4.2), two mirrors, and the cryogenic receiver (section 2.4.3) shown here.

Both the primary and secondary mirrors are 1.5-meter off-axis ellipsoids made from aluminum and operate at ambient temperature. The mirrors are oversized to limit warm beam spill over the edges, reducing excess loading on the detectors and sources of instrumental polarization from uncontrolled surfaces. The CLASS optical design is described in detail in Eimer et al. (2012).

2.4.2 Polarization Modulator

CLASS uses a variable-delay polarization modulator (VPM) as the first optical element in the telescope as shown in Figure 2.7. By rapidly modulating the incoming polarization, the VPM allows a “lock-in” style polarization

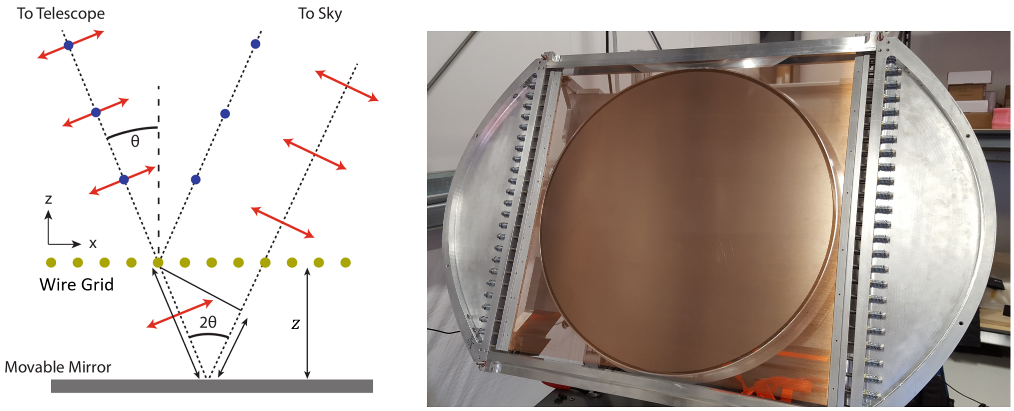

Figure 2.8: (Left) Schematic of the CLASS VPM with a stationary wire grid placed in front of a movable mirror. While the incoming light polarized parallel to the wires reflects off the grid, the orthogonal polarization passes through the grid and reflects off the mirror. The relative phase delay between the two polarization states is proportional to the grid-mirror distance. (Right) The assembled CLASS 90 GHz VPM showing the copper-plated tungsten wire grid placed in front of a 60 cm diameter flat aluminum mirror. Figure from Harrington et al. (2018).

measurement while separating instrumental from celestial polarization as the first element in the optical chain. The VPM consists of a linearly polarizing wire grid placed in front of and parallel to a movable flat mirror as shown in Figure 2.8. While the incoming light polarized parallel to the grid wires reflects off the polarizer, the light polarized perpendicular to the wires passes through the grid and reflects off the mirror. Therefore, varying the distance between the wire grid and the mirror introduces a phase shift between the two polarization states. The details of the CLASS VPMs are presented in Chuss et al. (2012), Miller et al. (2016), and Harrington et al. (2018). Here we briefly discuss the characteristics of an ideal (lossless with perfect polarization isolation) VPM.

In the limit where the light wavelength (λ) is much larger than the diameter of the metal wires in the grid, the phase delay (ϕ) is proportional to the grid-mirror distance (z) as:

$$\phi(z) = \frac{4\pi}{\lambda} z \cos\theta, \tag{2.1}$$

where θ is the incident angle as shown in Figure 2.8 (Chuss et al., 2012). In general, polarization transformations of the Stokes parameters through an optical element are facilitated using Mueller matrices as: $\boldsymbol{S}' = \mathbf{M}\boldsymbol{S}$, where $\mathbf{M}$ is a 4×4 Mueller matrix associated with the optical element, and $\boldsymbol{S}$ and $\boldsymbol{S}'$ are the vectors of Stokes parameters before and after the transformation, respectively. For a linearly polarized detector aligned at 45° with respect to the wire grid, we choose a coordinate system where positive Stokes Q is defined along the wires of the VPM grid. The polarization transformation by the VPM can then be written as:

$$\begin{pmatrix} I' \\ Q' \\ U' \\ V' \end{pmatrix} = \begin{pmatrix} 1 & 0 & 0 & 0 \\ 0 & 1 & 0 & 0 \\ 0 & 0 & \cos\phi & \sin\phi \\ 0 & 0 & -\sin\phi & \cos\phi \end{pmatrix} \begin{pmatrix} I \\ Q \\ U \\ V \end{pmatrix}, \tag{2.2}$$

where $\phi = \phi(z)$ is the phase delay from Equation 2.1 (Harrington et al., 2018). Now, from Equations 2.2 and 2.1, we notice that as z varies, the VPM modulates the incoming signal between Stokes U and Stokes V (see Figure 2.9, top-right panel). If we rotate the coordinate system by 45° with respect to the grid wires, the VPM would produce $Q \leftrightarrow V$ modulation instead. Therefore, through boresight rotation, we can measure both Stokes Q and U on the sky with a single linearly polarized detector (not simultaneously). Furthermore, as the modulation happens between one of the linear polarizations (Q or U) and circular polarization (V), a VPM is inherently sensitive to V. Since the CMB is not expected to be circularly polarized (section 1.2.2), the CLASS V maps can be used as null maps to put powerful constraints on systematic uncertainties.

Figure 2.9 (top-right panel) shows how the VPM switches the Stokes U for the incoming light into Stokes V and then into Stokes $-U$ during one operation cycle (Padilla et al., 2020). If this modulation happens faster than the drifts due to atmospheric loading, then the polarized signal can be recovered with high fidelity as illustrated in Figure 2.9 (top-left panel), as the atmosphere is effectively unpolarized. CLASS modulates the VPM at 10 Hz, moving the signal band above most of the low-frequency, so-called $1/f$, noise originating from instrumental and atmospheric drifts. This is crucial for CLASS to recover the CMB polarization at large angular scales. Figure 2.9 (bottom panel) shows a simulation from Miller et al. (2016) that illustrates the effectiveness of the VPM in recovering polarization at large angular scales in the presence of atmospheric variability.

The end-to-end simulation in Figure 2.9 demonstrates that fast polarization modulation is not only effective but also necessary to recover CMB polarization at large angular scales. A number of CMB polarization experiments have demonstrated polarization modulation with ambient-temperature or cryogenic half-wave plates (HWPs) that modulate between the two linear polarization states as the light passes through the rotating HWP (Bryan et al., 2010; Kusaka et al., 2014; Takakura et al., 2017). However, the use of the VPM instead of other modulation technologies like HWPs has various advantages:

1. Temperature-to-polarization leakage caused by instrumental polarization of initially unpolarized signal is an important systematic effect

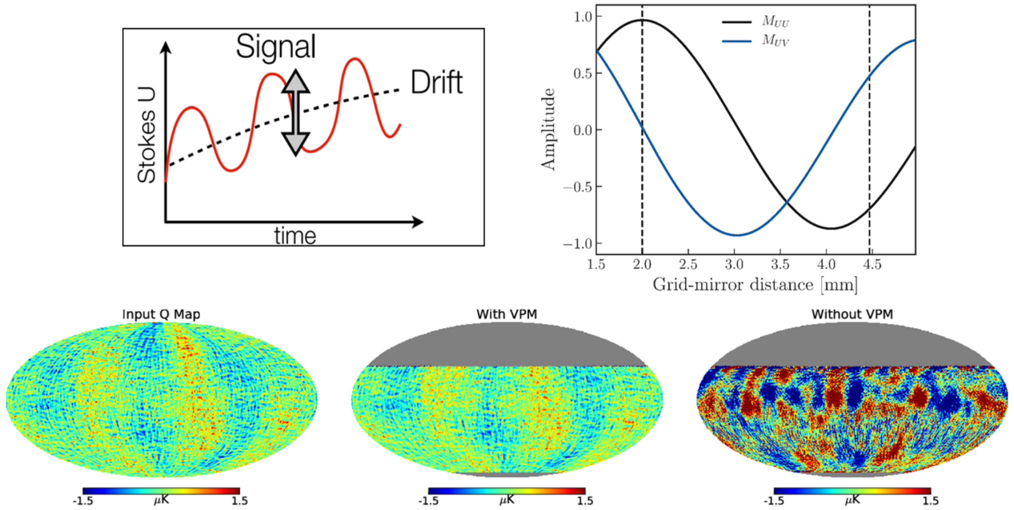

Figure 2.9: (Top-Left) Illustration of polarization modulation. If the modulation is fast compared to the drift time-scale, the polarized signal can be recovered with high fidelity. (Top-Right) VPM modulation transfer functions for incident U and V polarizations. The dashed vertical lines indicate the throw for the CLASS 40 GHz VPM. As the grid-mirror distance varies, the incoming polarization gets modulated between U and V. Figure from Padilla et al. (2020) (Bottom) Simulations illustrating the effectiveness of VPM in recovering polarization at large angular scales in the presence of polarized $1/f$ noise. The leftmost map shows the input Q map showing features at large angular scales, which are recovered by a VPM that modulates the sky signal before the addition of the polarized $1/f$ noise. Without a VPM, the reconstructed map is contaminated by the $1/f$ noise. Figure from Miller et al. (2016).

that can leak the much larger unpolarized sky signal into the detected polarized signal. Therefore, it is advantageous to have a polarization modulator as the first element of the telescope to modulate celestial polarization but not instrumental polarization. The VPM design with only reflective optical elements is straightforward to scale to large aperture sizes desirable for the first optical element. The size of the HWPs is usually limited by the size of available dielectric substrates like sapphire.

2. The reflective elements of the VPM also allow its use at ambient temperature without the sensitivity hit associated with a warm HWP or

other dielectric element. However, it is worth noting that the microwave emissivity of the VPM wire grid scales with the temperature; therefore, a VPM operated in a cryogenic environment would provide even better sensitivity (Lazear et al., 2014; Chuss et al., 2014).

3. Unlike HWPs, VPMs are inherently sensitive to Stokes V, allowing its use as a null channel to provide powerful constraints on systematic uncertainties.

2.4.3 Cryogenic Receiver

So far, we have discussed some key features of the CLASS instrument design including the use of a VPM and the boresight rotation that provide CLASS with the control of systematic errors necessary to recover the CMB polarization at large angular scales. The detection of this faint signal is made possible by high-sensitivity detectors that operate below 100 mK. While the rest of the chapters in this work are dedicated towards discussing the design and performance of CLASS detectors, here we focus on the CLASS cryogenic receiver system that keeps the detectors at their operating temperature. The CLASS receivers also keep the re-imaging optics at cryogenic temperatures to minimize the emission from the dielectric materials, and host an array of filters that suppress the infrared power reaching the detectors.

All four CLASS telescopes share a similar design shown in Figure 2.10. The details are presented in Iuliano et al. (2018), and we discuss some key features here. The CLASS receivers are built on custom-made Bluefors[2] cryostats that

---

[2] BlueFors Cryogenics, www.bluefors.com

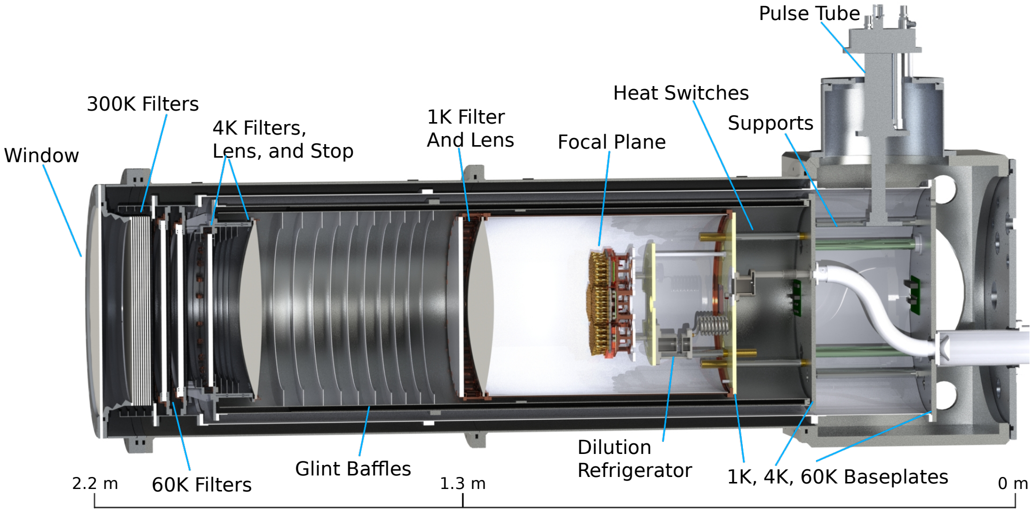
Pulse Tube
Heat Switches
Supports
300K Filters
4K Filters, Lens, and Stop
1K Filter And Lens
Focal Plane
Window
Dilution Refrigerator
1K, 4K, 60K Baseplates
Glint Baffles
60K Filters
2.2 m
1.3 m
0 m

Figure 2.10: CLASS 90 GHz cryogenic receiver design highlighting some key components inside the receiver. All four CLASS telescopes share a similar receiver design that is optimized to provide a cold and stable operating environment for the detectors in order to achieve low-noise and high-sensitivity sky observations. Figure from Iuliano et al. (2018)

use a combination of Pulse Tube (PT) and Dilution Refrigerator (DR) to cool down the system. The PT uses pulses of high-pressure helium to transport the heat out of the cryostat, while the DR exploits a phase transition in a mixture of ^{3}He and ^{4}He isotopes in order to provide continuous cooling. The base temperature for detector operation is achieved through different physical temperature stages where the inner stages are successively isolated from the outer stages with cylindrical radiation shields as shown in Figure 2.10. The CLASS cryostat has five temperature stages: 300 K, 60 K, 4 K, 1 K, and 100 mK[3]. The PT provides a cooling power of 40 W at the 60 K stage (when the stage is at 45 K) and 1.5 W at the 4 K stage (Iuliano et al., 2018). During the cool down process, the 4 K, 1 K and 100 mK stages are thermally linked through gas-gap heat switches shown in Figure 2.10. As these stages reach $\lesssim$ 4 K, the thermal link is decoupled and the DR is turned on, allowing the 1 K and 100 mK stages to further cool down to their base temperatures. The DR provides 100 mW and 300 μW of cooling power at the 1 K and 100 mK stages, respectively. An advantage of DR over other technologies like adsorption refrigerators and adiabatic demagnetization refrigerators (ADRs) is that the DR can continuously maintain a base temperature below 100 mK with its comparatively larger cooling power without the need for cryogenic cycling.

---

[3] These stage names are just a rough representation of the temperature gradient inside the cryostat, the actual operating temperature of these stages depend on the loading on the respective stages and are usually lower than these values (Iuliano et al., 2018).

The outermost 300 K stage, which is exposed to ambient temperature, maintains vacuum inside the cryostat. The 300 K stage has a 46 cm diameter window made of 0.125 inch thick ultra-high molecular weight polyethylene (UHMWPE) that can hold vacuum and is transmissive in the microwave. The window is anti-reflection (AR) coated on both sides with a layer of porous polytetrafluoroethylene (PTFE) whose thickness is optimized for maximum in-band transmission depending on the frequency band of the detectors. About 70 W of optical power enters through this window; however, the coldest stage has a cooling power of 300 μW. Therefore, as shown in Figure 2.10, a series of filters are used in each stage of the cryostat to reduce the power reaching the 100 mK stage by more than a factor of 10^5 while ensuring maximum in-band transmission. The 4 K and 1 K stages also have one cryogenic lens each that re-image the incoming light onto the focal plane at the 100 mK stage.

2.4.3.1 Filters

CLASS uses a combination of absorptive, reflective, and scattering filters inside the receiver cryostat to suppress the out-of-band power transmitted through the window and reduce the optical loading on the detectors. While the exact filtering scheme (thickness, quantity, AR coating, etc) is optimized separately for different receivers based on the frequency band of the detectors being used (refer to Iuliano et al. 2018 for details), we briefly discuss the different types of filters used:

1. **Foam:** A stack of extruded polystyrene (XPS) foam filters is used near the window to block infrared power while passing in-band microwave radiation. The stack forms a radio-transparent multi-layer insulation (RT-MLI) which reduces the thermal loading by a factor roughly proportional to $1/(N+1)$ for a stack with N layers (Choi et al., 2013). For CLASS receivers, $N \sim 10$ with each sheet about 0.1 inch thick. As compared to other filters, the foam filters are relatively easy to make and do not require AR coating.

2. **Metal Mesh:** The 60 K and 4K stages of the 40 GHz and 90 GHz CLASS receivers use metal-mesh filters to reflect the infrared power. These filters contain a square grid pattern of aluminum on a mylar or polypropylene film. The spacing of the aluminum grid pattern is tuned to optimize the frequency cutoff for these low-pass filters. At low frequencies, the square elements of the capacitive grid are too small (compared to the wavelength) to efficiently couple to the incoming radiation, ensuring

that the metal-mesh is highly transmissive at millimeter wavelengths. However, as the wavelength approaches the size of the grid element, the transmission falls steeply and nearly all incoming infrared radiation is reflected (see Essinger-Hileman et al. 2014 for details).

3. **PTFE:** The 60 K and 4 K filter assemblies shown in Figure 2.10 consist of metal-mesh and PTFE filters to improve the filtering of infrared radiation. PTFE absorbs strongly at frequencies $\gtrsim 1$ THz, and the absorbed power is conducted along the cryostat walls to the respective PT stages. The PTFE filters are 0.5 inch thick and AR coated using a simulated-dielectric technique (described in section 2.4.3.2) to optimize their in-band transmission.

4. **Nylon:** As PTFE does not efficiently absorb below 1 THz, a final nylon filter is added at the 1 K stage to provide thermal filtering below 1 THz for the 40 and 90 GHz receivers. Since nylon's cutoff frequency is closer to CLASS frequency bands, it also prevents higher frequency leakage onto the detectors. However, the closer cutoff also leads to higher in-band absorption. Therefore, the filter thickness and simulated dielectrics AR-coating parameters were optimized and tested through lab measurements to minimize the in-band loss (Iuliano et al., 2018).

5. **Low-pass Edge Filter:** For the high frequency 150/220 GHz instrument, the higher in-band absorption of nylon becomes prohibitive. Therefore, instead of nylon, we use a custom-made low-pass edge filter with sharp frequency cutoff made by stacking several metal mesh filters (Ade et al., 2006).

2.4.3.2 Lenses

As shown in Figure 2.10, in addition to the optical filters, the cryogenic receiver has several other key optical components: blackened glint baffling structures to control stray light, a 4 K cold aperture stop to minimize the warm spill, and two cryogenic lenses to re-image the incoming light onto the focal plane. Following the optical path in Figure 2.7, we notice that the primary and secondary mirrors re-image the VPM onto the 4 K cold aperture stop inside the receiver. The cold stop is designed to allow for controlled illumination on the VPM (in the time-reversed sense), and reduce the loading on the detectors from warm beam spill. The incoming light passing through the cold stop is nearly a spherical wave; therefore, the two lenses at 4 K and 1 K are used to re-image these nearly-spherical waves onto a flat focal plane (Eimer et al., 2012).

For the 40 GHz and the 90 GHz receivers, the lenses are made of high-density polyethylene (HDPE). At these frequencies, HDPE has a number of advantages over other dielectrics: it has low millimeter-wave loss and higher index of refraction ($n = 1.53$ at room temperature) than other similar-loss dielectrics, is easily machined, and can be readily AR coated. At 150/220 GHz, the loss through the thick HDPE becomes prohibitive and the dual layer AR coating to accommodate both 150 and 220 GHz frequency bands becomes challenging. Therefore, silicon lenses with AR layers cut into them with a dicing saw are used for the high frequency receiver (Datta et al., 2013).

The HDPE lenses for the 40 and 90 GHz receivers are machined using a

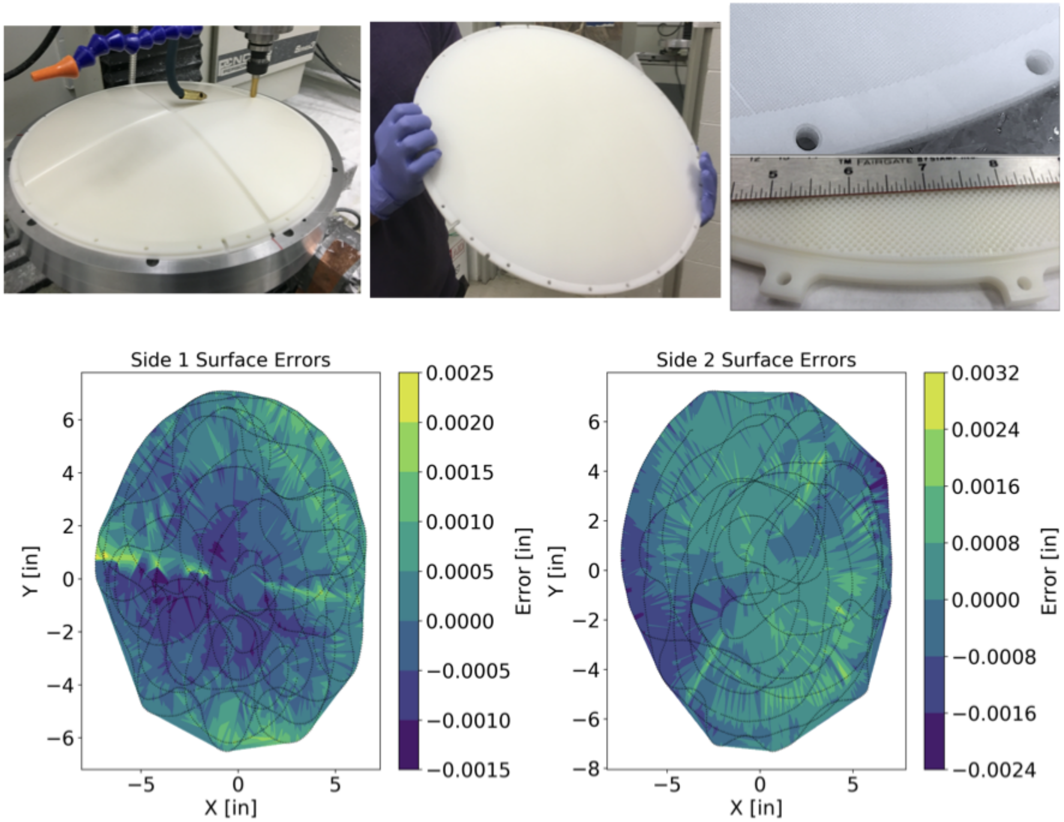

Figure 2.11: Manufacturing and measuring the CLASS 90 GHz 1 K lens (Top-left) An HDPE block being machined on a Tormach CNC mill at the Johns Hopkins University (Top-center) A completed 1 K lens for the 90 GHz receiver (Top-right) A comparison of the simulated dielectrics AR coating for 90 GHz (above) and 40 GHz (below) lenses. As the AR parameters scale with the wavelength, the drilled holes in the 90 GHz coating are small (depth and pitch are both $\sim$ 0.6 mm) compared to 40 GHz (depth: 1.4 mm, pitch: 1.8 mm). So the 90 GHz coating is only visible here through the difference in texture between the lens surface and the flange. (Bottom) The measurement of the lens surface using a Faro arm show that the surface errors due to machining are within ± 0.003 inch on both sides. The colored grid is an interpolation between the measured data points (black dots). To prevent damage to the AR-coated surface, the lens measurement is done before the holes are drilled onto the surface.

Tormach[4] CNC mill at the Johns Hopkins University. Figure 2.11 shows the final surface on a 90 GHz 1 K lens being machined. Before this step, the HDPE was first annealed to relieve internal stresses that could deform the lens, then rough-cut, and annealed for a second time with an aluminum jig holding the rough-cut surfaces in place. The annealing step for HDPE is performed by raising its temperature to 120 °C (just below its melting point of ~ 130 °C) over the course of 4 hours, leaving the temperature there for 48 hours, and then cooling back down to room temperature over the next 48 hours. After the final surfaces are cut, both sides of the lens surfaces are measured using a Faro arm[5]. Figure 2.11 shows that the surface errors due to machining are within ± 0.03 inch for the 90 GHz 1 K lens, which is within the required tolerance for the 90 GHz optical design.

After the lens surfaces are measured and are shown to be within the required design tolerances, we use a simulated dielectrics technique to AR coat the lenses in order to reduce the loss due to reflections. In this technique, subwavelength features are cut into the optical surface to create a layer of lower mean density, reducing the effective index of refraction of the AR coated surface layer. Compared to heat pressing materials of lower density on the optical surface, the simulated dielectrics have a couple advantages: there is no risk of delamination or separation during cryogenic cycling, and the AR parameters can be significantly fine-tuned to better match the optical material. The CLASS HDPE lenses are AR coated by machining an array of cylindrical holes into the lens surface in a square grid as shown in Figure 2.11.

---

[4] www.tormach.com

[5] www.faro.com/products/3d-manufacturing/faroarm

The effective dielectric layer has an index of refraction $n \sim 1.25$ and is $\lambda/4n$ thick, where λ is the free-space wavelength. The exact diameter, depth, and spacing of the holes for the AR layers are optimized through electromagnetic simulations using HFSS[6] and are verified through lab measurements (Iuliano et al., 2018). The details of the HFSS simulations are presented in Harrington (2018). For instance, the 90 GHz lenses have an AR layer with 0.602 mm depth and 0.638 mm grid spacing optimized for a 0.533 mm diameter drill bit. The PTFE and nylon filters (section 2.4.3.1) are also AR-coated in a similar way.

Throughout this chapter, we have discussed the CLASS instrument design and observation strategy that makes the recovery of the CMB polarization at large angular scales possible. The unique combination of large sky coverage, broad frequency range, and rapid front-end polarization modulation provides CLASS with the high stability and control over systematic errors necessary to characterize both the reionization and recombination peaks of the CMB polarization spectra. The missing ingredient in the discussion so far is the background-limited CLASS detector that makes the high-sensitivity CMB polarization detection possible. The rest of the chapters in this thesis are dedicated to describe the design, assembly, characterization, and on-sky performance of the CLASS detectors.

---

[6] www.ansys.com/Products/Electronics/ANSYS-HFSS

References

Ade, Peter A. R., Giampaolo Pisano, Carole Tucker, and Samuel Weaver (2006). “A review of metal mesh filters”. In: Proc. SPIE. Vol. 6275. Society of Photo-Optical Instrumentation Engineers (SPIE) Conference Series, 62750U. DOI: 10.1117/12.673162.

Ahmad, Q. R. et al. (2001). “Measurement of the Rate of $\nu_e + \mathrm{d} \rightarrow \mathrm{p} + \mathrm{p} + \mathrm{e}^-$ Interactions Produced by ^{8}B Solar Neutrinos at the Sudbury Neutrino Observatory”. In: Phys. Rev. Lett. 87.7, 071301, p. 071301. DOI: 10.1103/PhysRevLett.87.071301. arXiv: nucl-ex/0106015 [nucl-ex].

Allison, R., P. Caucal, E. Calabrese, J. Dunkley, and T. Louis (2015). “Towards a cosmological neutrino mass detection”. In: Phys. Rev. D 92.12, 123535, p. 123535. DOI: 10.1103/PhysRevD.92.123535. arXiv: 1509.07471 [astro-ph.CO].

Bennett, C. L., R. S. Hill, G. Hinshaw, D. Larson, K. M. Smith, J. Dunkley, B. Gold, M. Halpern, N. Jarosik, A. Kogut, E. Komatsu, M. Limon, S. S. Meyer, M. R. Nolta, N. Odegard, L. Page, D. N. Spergel, G. S. Tucker, J. L. Weiland, E. Wollack, and E. L. Wright (2011). “Seven-year Wilkinson Microwave Anisotropy Probe (WMAP) Observations: Are There Cosmic Microwave Background Anomalies?” In: ApJS 192.2, 17, p. 17. DOI: 10.1088/0067-0049/192/2/17. arXiv: 1001.4758 [astro-ph.CO].

BICEP2 Collaboration, Keck Array Collaboration, P. A. R. Ade, Z. Ahmed, R. W. Aikin, K. D. Alexand er, D. Barkats, S. J. Benton, C. A. Bischoff, J. J. Bock, R. Bowens-Rubin, J. A. Brevik, I. Buder, E. Bullock, V. Buza, J. Connors, B. P. Crill, L. Duband, C. Dvorkin, J. P. Filippini, S. Fliescher, J. Grayson, M. Halpern, S. Harrison, S. R. Hildebrandt, G. C. Hilton, H. Hui, K. D. Irwin, J. Kang, K. S. Karkare, E. Karpel, J. P. Kaufman, B. G. Keating, S. Kefeli, S. A. Kernasovskiy, J. M. Kovac, C. L. Kuo, E. M. Leitch, M. Lueker, K. G. Megerian, T. Namikawa, C. B. Netterfield, H. T. Nguyen, R. O’Brient, IV Ogburn R. W., A. Orland o, C. Pryke, S. Richter, R. Schwarz, C. D. Sheehy, Z. K. Staniszewski, B. Steinbach, R. V. Sudiwala, G. P. Teply,

K. L. Thompson, J. E. Tolan, C. Tucker, A. D. Turner, A. G. Vieregg, A. C. Weber, D. V. Wiebe, J. Willmert, C. L. Wong, W. L. K. Wu, and K. W. Yoon (2016). "BICEP2/Keck Array VIII: Measurement of Gravitational Lensing from Large-scale B-mode Polarization". In: ApJ 833.2, 228, p. 228. DOI: 10.3847/1538-4357/833/2/228. arXiv: 1606.01968 [astro-ph.CO].

Bryan, Sean A., Peter A. R. Ade, Mandana Amiri, Steve Benton, Richard Bihary, James J. Bock, J. Richard Bond, Joseph A. Bonetti, H. Cynthia Chiang, Carlo R. Contaldi, Brendan P. Crill, Daniel O'Dea, Olivier Dore, Marzieh Farhang, Jeffrey P. Filippini, Laura Fissel, Natalie Gandilo, Sunil Golwala, Jon E. Gudmundsson, Matthew Hasselfield, Mark Halpern, Kyle R. Helson, Gene Hilton, Warren Holmes, Viktor V. Hristov, Kent D. Irwin, William C. Jones, Chao Lin Kuo, Carrie J. MacTavish, Peter Mason, Tracy Morford, Thomas E. Montroy, C. Barth Netterfield, Alexandra S. Rahlin, Carl D. Reintsema, Daniel Riley, John E. Ruhl, Marcus C. Runyan, Matthew A. Schenker, Jamil Shariff, Juan Diego Soler, Amy Transrud, Rebecca Tucker, Carole Tucker, and Anthony Turner (2010). "Modeling and characterization of the SPIDER half-wave plate". In: Proc. SPIE. Vol. 7741. Society of Photo-Optical Instrumentation Engineers (SPIE) Conference Series, 77412B. DOI: 10.1117/12.857837.

Carroll, Sean M., George B. Field, and Roman Jackiw (1990). "Limits on a Lorentz- and parity-violating modification of electrodynamics". In: *Phys. Rev. D* 41 (4), pp. 1231–1240. DOI: 10.1103/PhysRevD.41.1231.

Choi, J., H. Ishitsuka, S. Mima, S. Oguri, K. Takahashi, and O. Tajima (2013). "Radio-transparent multi-layer insulation for radiowave receivers". In: *Review of Scientific Instruments* 84.11, 114502-114502-6, pp. 114502–114502–6. DOI: 10.1063/1.4827081. arXiv: 1306.5040 [astro-ph.IM].

Chuss, D. T., J. R. Eimer, D. J. Fixsen, J. Hinderks, A. J. Kogut, J. Lazear, P. Mirel, E. Switzer, G. M. Voellmer, and E. J. Wollack (2014). "Variable-delay polarization modulators for cryogenic millimeter-wave applications". In: *Review of Scientific Instruments* 85.6, 064501, p. 064501. DOI: 10.1063/1.4879499. arXiv: 1403.1652 [astro-ph.IM].

Chuss, David T., Edward J. Wollack, Ross Henry, Howard Hui, Aaron J. Juarez, Megan Krejny, S. Harvey Moseley, and Giles Novak (2012). "Properties of a variable-delay polarization modulator". In: Appl. Opt. 51.2, p. 197. DOI: 10.1364/AO.51.000197. arXiv: 1106.5984 [astro-ph.IM].

Datta, R., C. D. Munson, M. D. Niemack, J. J. McMahon, J. Britton, E. J. Wollack, J. Beall, M. J. Devlin, J. Fowler, P. Gallardo, J. Hubmayr, K. Irwin, L. Newburgh, J. P. Nibarger, L. Page, M. A. Quijada, B. L. Schmitt,

S. T. Staggs, R. Thornton, and L. Zhang (2013). “Large-aperture wide-bandwidth antireflection-coated silicon lenses for millimeter wavelengths”. In: Appl. Opt. 52.36, p. 8747. DOI: 10.1364/AO.52.008747. arXiv: 1307.4715 [astro-ph.IM].

De, Soma and Hiroyuki Tashiro (2015). “Circular polarization of the CMB: A probe of the first stars”. In: *Phys. Rev. D* 92 (12), p. 123506. DOI: 10.1103/PhysRevD.92.123506.

Eimer, Joseph R., Charles L. Bennett, David T. Chuss, Tobias Marriage, Edward J. Wollack, and Lingzhen Zeng (2012). “The cosmology large angular scale surveyor (CLASS): 40 GHz optical design”. In: Proc. SPIE. Vol. 8452. Society of Photo-Optical Instrumentation Engineers (SPIE) Conference Series, p. 845220. DOI: 10.1117/12.925464.

Essinger-Hileman, Thomas, Aamir Ali, Mandana Amiri, John W. Appel, Derek Araujo, Charles L. Bennett, Fletcher Boone, Manwei Chan, Hsiao-Mei Cho, David T. Chuss, Felipe Colazo, Erik Crowe, Kevin Denis, Rolando Dünner, Joseph Eimer, Dominik Gothe, Mark Halpern, Kathleen Harrington, Gene C. Hilton, Gary F. Hinshaw, Caroline Huang, Kent Irwin, Glenn Jones, John Karakla, Alan J. Kogut, David Larson, Michele Limon, Lindsay Lowry, Tobias Marriage, Nicholas Mehrle, Amber D. Miller, Nathan Miller, Samuel H. Moseley, Giles Novak, Carl Reintsema, Karwan Rostem, Thomas Stevenson, Deborah Towner, Kongpop U-Yen, Emily Wagner, Duncan Watts, Edward J. Wollack, Zhilei Xu, and Lingzhen Zeng (2014). “CLASS: the cosmology large angular scale surveyor”. In: Proc. SPIE. Vol. 9153. Society of Photo-Optical Instrumentation Engineers (SPIE) Conference Series, p. 91531I. DOI: 10.1117/12.2056701.

Fukuda, Y. et al. (1998). “Evidence for Oscillation of Atmospheric Neutrinos”. In: Phys. Rev. Lett. 81.8, pp. 1562–1567. DOI: 10.1103/PhysRevLett.81.1562. arXiv: hep-ex/9807003 [hep-ex].

Fuskeland, U., I. K. Wehus, H. K. Eriksen, and S. K. Næss (2014). “Spatial Variations in the Spectral Index of Polarized Synchrotron Emission in the 9 yr WMAP Sky Maps”. In: ApJ 790.2, 104, p. 104. DOI: 10.1088/0004-637X/790/2/104. arXiv: 1404.5323 [astro-ph.CO].

Giovannini, Massimo (2009). “V-mode polarization of the cosmic microwave background”. In: Phys. Rev. D 80.12, 123013, p. 123013. DOI: 10.1103/PhysRevD.80.123013. arXiv: 0909.3629 [astro-ph.CO].

Hannestad, Steen (2010). “Neutrino physics from precision cosmology”. In: *Progress in Particle and Nuclear Physics* 65.2, pp. 185–208. DOI: 10.1016/j.ppnp.2010.07.001. arXiv: 1007.0658 [hep-ph].

Harrington, Kathleen (2018). “Variable-delay Polarization Modulators for the CLASS Telescopes”. PhD dissertation. The Johns Hopkins University.

Harrington, Kathleen, Tobias Marriage, Aamir Ali, John W. Appel, Charles L. Bennett, Fletcher Boone, Michael Brewer, Manwei Chan, David T. Chuss, Felipe Colazo, Sumit Dahal, Kevin Denis, Rolando Dünner, Joseph Eimer, Thomas Essinger-Hileman, Pedro Fluxa, Mark Halpern, Gene Hilton, Gary F. Hinshaw, Johannes Hubmayr, Jeffrey Iuliano, John Karakla, Jeff McMahon, Nathan T. Miller, Samuel H. Moseley, Gonzalo Palma, Lucas Parker, Matthew Petroff, Bastián. Pradenas, Karwan Rostem, Marco Sagliocca, Deniz Valle, Duncan Watts, Edward Wollack, Zhilei Xu, and Lingzhen Zeng (2016). “The Cosmology Large Angular Scale Surveyor”. In: Proc. SPIE. Vol. 9914. Society of Photo-Optical Instrumentation Engineers (SPIE) Conference Series, 99141K. DOI: `10.1117/12.2233125`.

Harrington, Kathleen, Joseph Eimer, David T. Chuss, Matthew Petroff, Joseph Cleary, Martin DeGeorge, Theodore W. Grunberg, Aamir Ali, John W. Appel, Charles L. Bennett, Michael Brewer, Ricardo Bustos, Manwei Chan, Jullianna Couto, Sumit Dahal, Kevin Denis, Rolando Dünner, Thomas Essinger-Hileman, Pedro Fluxa, Mark Halpern, Gene Hilton, Gary F. Hinshaw, Johannes Hubmayr, Jeffrey Iuliano, John Karakla, Tobias Marriage, Jeffrey McMahon, Nathan J. Miller, Carolina Nuñez, Ivan L. Padilla, Gonzalo Palma, Lucas Parker, Bastian Pradenas Marquez, Rodrigo Reeves, Carl Reintsema, Karwan Rostem, Deniz Augusto Nunes Valle, Trevor Van Engelhoven, Bingjie Wang, Qinan Wang, Duncan Watts, Janet Weiland, Edward Wollack, Zhilei Xu, Ziang Yan, and Lingzhen Zeng (2018). “Variable-delay polarization modulators for the CLASS telescopes”. In: Proc. SPIE. Vol. 10708. Society of Photo-Optical Instrumentation Engineers (SPIE) Conference Series, p. 107082M. DOI: `10.1117/12.2313614`. arXiv: `1807.03807 [astro-ph.IM]`.

Hu, Wayne, Daniel J. Eisenstein, and Max Tegmark (1998). “Weighing Neutrinos with Galaxy Surveys”. In: Phys. Rev. Lett. 80.24, pp. 5255–5258. DOI: `10.1103/PhysRevLett.80.5255`. arXiv: `astro-ph/9712057 [astro-ph]`.

Iuliano, Jeffrey, Joseph Eimer, Lucas Parker, Gary Rhoades, Aamir Ali, John W. Appel, Charles Bennett, Michael Brewer, Ricardo Bustos, David Chuss, Joseph Cleary, Jullianna Couto, Sumit Dahal, Kevin Denis, Rolando Dünner, Thomas Essinger-Hileman, Pedro Fluxa, Mark Halpern, Kathleen Harrington, Kyle Helson, Gene Hilton, Gary Hinshaw, Johannes Hubmayr, John Karakla, Tobias Marriage, Nathan Miller, Jeffrey John McMahon, Carolina Nuñez, Ivan Padilla, Gonzalo Palma, Matthew Petroff, Bastian

Pradenas Márquez, Rodrigo Reeves, Carl Reintsema, Karwan Rostem, Deniz Augusto Nunes Valle, Trevor Van Engelhoven, Bingjie Wang, Qinan Wang, Duncan Watts, Janet Weiland, Edward J. Wollack, Zhilei Xu, Ziang Yan, and Lingzhen Zeng (2018). "The Cosmology Large Angular Scale Surveyor receiver design". In: Proc. SPIE. Vol. 10708. Society of Photo-Optical Instrumentation Engineers (SPIE) Conference Series, p. 1070828. DOI: `10.1117/12.2312954`. arXiv: `1807.04167 [astro-ph.IM]`.

Kusaka, A., T. Essinger-Hileman, J. W. Appel, P. Gallardo, K. D. Irwin, N. Jarosik, M. R. Nolta, L. A. Page, L. P. Parker, S. Raghunathan, and et al. (2014). "Modulation of cosmic microwave background polarization with a warm rapidly rotating half-wave plate on the Atacama B-Mode Search instrument". In: *Review of Scientific Instruments* 85.2, p. 024501. DOI: `10.1063/1.4862058`.

Lazear, Justin, Peter A. R. Ade, Dominic Benford, Charles L. Bennett, David T. Chuss, Jessie L. Dotson, Joseph R. Eimer, Dale J. Fixsen, Mark Halpern, Gene Hilton, James Hinderks, Gary F. Hinshaw, Kent Irwin, Christine Jhabvala, Bradley Johnson, Alan Kogut, Luke Lowe, Jeff J. McMahon, Timothy M. Miller, Paul Mirel, S. Harvey Moseley, Samelys Rodriguez, Elmer Sharp, Johannes G. Staguhn, Eric R. Switzer, Carole E. Tucker, Amy Weston, and Edward J. Wollack (2014). "The Primordial Inflation Polarization Explorer (PIPER)". In: Proc. SPIE. Vol. 9153. Society of Photo-Optical Instrumentation Engineers (SPIE) Conference Series, p. 91531L. DOI: `10.1117/12.2056806`.

Louis, Thibaut, Emily Grace, Matthew Hasselfield, Marius Lungu, Loïc Maurin, Graeme E. Addison, Peter A. R. Ade, Simone Aiola, Rupert Allison, Mandana Amiri, Elio Angile, Nicholas Battaglia, James A. Beall, Francesco de Bernardis, J. Richard Bond, Joe Britton, Erminia Calabrese, Hsiao-mei Cho, Steve K. Choi, Kevin Coughlin, Devin Crichton, Kevin Crowley, Rahul Datta, Mark J. Devlin, Simon R. Dicker, Joanna Dunkley, Rolando Dünner, Simone Ferraro, Anna E. Fox, Patricio Gallardo, Megan Gralla, Mark Halpern, Shawn Henderson, J. Colin Hill, Gene C. Hilton, Matt Hilton, Adam D. Hincks, Renée Hlozek, S. P. Patty Ho, Zhiqi Huang, Johannes Hubmayr, Kevin M. Huffenberger, John P. Hughes, Leopoldo Infante, Kent Irwin, Simon Muya Kasanda, Jeff Klein, Brian Koopman, Arthur Kosowsky, Dale Li, Mathew Madhavacheril, Tobias A. Marriage, Jeff McMahon, Felipe Menanteau, Kavilan Moodley, Charles Munson, Sigurd Naess, Federico Nati, Laura Newburgh, John Nibarger, Michael D. Niemack, Michael R. Nolta, Carolina Nuñez, Lyman A. Page, Christine Pappas, Bruce Partridge, Felipe Rojas, Emmanuel Schaan, Benjamin L. Schmitt, Neelima Sehgal, Blake D. Sherwin, Jon Sievers, Sara Simon, David N. Spergel, Suzanne T. Staggs, Eric R. Switzer, Robert Thornton, Hy Trac, Jesse Treu, Carole Tucker, Alexander Van Engelen, Jonathan T. Ward, and Edward J. Wollack (2017). "The Atacama Cosmology Telescope: two-season ACTPol spectra and parameters". In: J. Cosmology Astropart. Phys. 2017.6, 031, p. 031. DOI: `10.1088/1475-7516/2017/06/031`. arXiv: `1610.02360 [astro-ph.CO]`.

Miller, N. J., D. T. Chuss, T. A. Marriage, E. J. Wollack, J. W. Appel, C. L. Bennett, J. Eimer, T. Essinger-Hileman, D. J. Fixsen, K. Harrington, S. H. Moseley, K. Rostem, E. R. Switzer, and D. J. Watts (2016). "Recovery of Large Angular Scale CMB Polarization for Instruments Employing Variable-delay Polarization Modulators". In: ApJ 818.2, 151, p. 151. DOI: `10.3847/0004-637X/818/2/151`. arXiv: `1509.04628 [astro-ph.IM]`.

Pacholczyk, A. G. (1970). *Radio astrophysics. Non-thermal processes in galactic and extragalactic sources.*

Padilla, Ivan L., Joseph R. Eimer, Yunyang Li, Graeme E. Addison, Aamir Ali, John W. Appel, Charles L. Bennett, Ricardo Bustos, Michael K. Brewer, Manwei Chan, David T. Chuss, Joseph Cleary, Jullianna Couto, Sumit Dahal, Kevin Denis, Rolando Dünner, Thomas Essinger-Hileman, Pedro Fluxá, Dominik Gothe, Saianeesh K. Haridas, Kathleen Harrington, Jeffrey Iuliano, John Karakla, Tobias A. Marriage, Nathan J. Miller, Carolina Núñez, Lucas Parker, Matthew A. Petroff, Rodrigo Reeves, Karwan Rostem, Robert W. Stevens, Deniz Augusto Nunes Valle, Duncan J. Watts, Janet L. Weiland, Edward J. Wollack, and Zhilei Xu (2020). "Two-year Cosmology Large Angular Scale Surveyor (CLASS) Observations: A Measurement of Circular Polarization at 40 GHz". In: ApJ 889.2, 105, p. 105. DOI: `10.3847/1538-4357/ab61f8`. arXiv: `1911.00391 [astro-ph.CO]`.

Page, L., G. Hinshaw, E. Komatsu, M. R. Nolta, D. N. Spergel, C. L. Bennett, C. Barnes, R. Bean, O. Doré, J. Dunkley, M. Halpern, R. S. Hill, N. Jarosik, A. Kogut, M. Limon, S. S. Meyer, N. Odegard, H. V. Peiris, G. S. Tucker, L. Verde, J. L. Weiland, E. Wollack, and E. L. Wright (2007). "Three-Year Wilkinson Microwave Anisotropy Probe (WMAP) Observations: Polarization Analysis". In: ApJS 170.2, pp. 335–376. DOI: `10.1086/513699`. arXiv: `astro-ph/0603450 [astro-ph]`.

Petroff, Matthew A., Joseph R. Eimer, Kathleen Harrington, Aamir Ali, John W. Appel, Charles L. Bennett, Michael K. Brewer, Ricardo Bustos, Manwei Chan, David T. Chuss, Joseph Cleary, Jullianna Denes Couto, Sumit

Dahal, Rolando Dünner, Thomas Essinger-Hileman, Pedro Fluxá Rojas, Dominik Gothe, Jeffrey Iuliano, Tobias A. Marriage, Nathan J. Miller, Carolina Núñez, Ivan L. Padilla, Lucas Parker, Rodrigo Reeves, Karwan Rostem, Deniz Augusto Nunes Valle, Duncan J. Watts, Janet L. Weiland, Edward J. Wollack, and Zhilei Xu (2020). "Two-year Cosmology Large Angular Scale Surveyor (CLASS) Observations: A First Detection of Atmospheric Circular Polarization at Q band". In: ApJ 889.2, 120, p. 120. DOI: `10.3847/1538-4357/ab64e2`. arXiv: `1911.01016 [astro-ph.IM]`.

Planck Collaboration et al. (2016). "Planck 2015 results. X. Diffuse component separation: Foreground maps". In: A&A 594, A10, A10. DOI: `10.1051/0004-6361/201525967`. arXiv: `1502.01588 [astro-ph.CO]`.

Planck Collaboration et al. (2018). "Planck 2018 results. IV. Diffuse component separation". In: *arXiv e-prints*, arXiv:1807.06208, arXiv:1807.06208. arXiv: `1807.06208 [astro-ph.CO]`.

POLARBEAR Collaboration, P. A. R. Ade, M. Aguilar, Y. Akiba, K. Arnold, C. Baccigalupi, D. Barron, D. Beck, F. Bianchini, D. Boettger, J. Borrill, S. Chapman, Y. Chinone, K. Crowley, A. Cukierman, R. Dünner, M. Dobbs, A. Ducout, T. Elleflot, J. Errard, G. Fabbian, S. M. Feeney, C. Feng, T. Fujino, N. Galitzki, A. Gilbert, N. Goeckner-Wald, J. C. Groh, G. Hall, N. Halverson, T. Hamada, M. Hasegawa, M. Hazumi, C. A. Hill, L. Howe, Y. Inoue, G. Jaehnig, A. H. Jaffe, O. Jeong, D. Kaneko, N. Katayama, B. Keating, R. Keskitalo, T. Kisner, N. Krachmalnicoff, A. Kusaka, M. Le Jeune, A. T. Lee, E. M. Leitch, D. Leon, E. Linder, L. Lowry, F. Matsuda, T. Matsumura, Y. Minami, J. Montgomery, M. Navaroli, H. Nishino, H. Paar, J. Peloton, A. T. P. Pham, D. Poletti, G. Puglisi, C. L. Reichardt, P. L. Richards, C. Ross, Y. Segawa, B. D. Sherwin, M. Silva-Feaver, P. Siritanasak, N. Stebor, R. Stompor, A. Suzuki, O. Tajima, S. Takakura, S. Takatori, D. Tanabe, G. P. Teply, T. Tomaru, C. Tucker, N. Whitehorn, and A. Zahn (2017). "A Measurement of the Cosmic Microwave Background B-mode Polarization Power Spectrum at Subdegree Scales from Two Years of polarbear Data". In: ApJ 848.2, 121, p. 121. DOI: `10.3847/1538-4357/aa8e9f`. arXiv: `1705.02907 [astro-ph.CO]`.

Sayre, J. T., C. L. Reichardt, J. W. Henning, P. A. R. Ade, A. J. Anderson, J. E. Austermann, J. S. Avva, J. A. Beall, A. N. Bender, B. A. Benson, F. Bianchini, L. E. Bleem, J. E. Carlstrom, C. L. Chang, H. C. Chiang, R. Citron, C. Corbett Moran, T. M. Crawford, A. T. Crites, T. de Haan, M. A. Dobbs, W. Everett, J. Gallicchio, E. M. George, A. Gilbert, N. Gupta, N. W. Halverson, N. Harrington, G. C. Hilton, G. P. Holder, W. L. Holzapfel, J. D. Hrubes, N. Huang,

J. Hubmayr, K. D. Irwin, L. Knox, A. T. Lee, D. Li, A. Lowitz, J. J. McMahon, S. S. Meyer, L. M. Mocanu, J. Montgomery, A. Nadolski, T. Natoli, J. P. Nibarger, G. Noble, V. Novosad, S. Padin, S. Patil, C. Pryke, J. E. Ruhl, B. R. Saliwanchik, K. K. Schaffer, C. Sievers, G. Smecher, A. A. Stark, C. Tucker, K. Vanderlinde, T. Veach, J. D. Vieira, G. Wang, N. Whitehorn, W. L. K. Wu, and V. Yefremenko (2019). "Measurements of B-mode Polarization of the Cosmic Microwave Background from 500 Square Degrees of SPTpol Data". In: *arXiv e-prints*, arXiv:1910.05748, arXiv:1910.05748. arXiv: `1910.05748 [astro-ph.CO]`.

Schwarz, Dominik J., Craig J. Copi, Dragan Huterer, and Glenn D. Starkman (2016). "CMB anomalies after Planck". In: *Classical and Quantum Gravity* 33.18, 184001, p. 184001. DOI: `10.1088/0264-9381/33/18/184001`. arXiv: `1510.07929 [astro-ph.CO]`.

Takakura, Satoru, Mario Aguilar, Yoshiki Akiba, Kam Arnold, Carlo Baccigalupi, Darcy Barron, Shawn Beckman, David Boettger, Julian Borrill, Scott Chapman, Yuji Chinone, Ari Cukierman, Anne Ducout, Tucker Elleflot, Josquin Errard, Giulio Fabbian, Takuro Fujino, Nicholas Galitzki, Neil Goeckner-Wald, Nils W. Halverson, Masaya Hasegawa, Kaori Hattori, Masashi Hazumi, Charles Hill, Logan Howe, Yuki Inoue, Andrew H. Jaffe, Oliver Jeong, Daisuke Kaneko, Nobuhiko Katayama, Brian Keating, Reijo Keskitalo, Theodore Kisner, Nicoletta Krachmalnicoff, Akito Kusaka, Adrian T. Lee, David Leon, Lindsay Lowry, Frederick Matsuda, Tomotake Matsumura, Martin Navaroli, Haruki Nishino, Hans Paar, Julien Peloton, Davide Poletti, Giuseppe Puglisi, Christian L. Reichardt, Colin Ross, Praween Siritanasak, Aritoki Suzuki, Osamu Tajima, Sayuri Takatori, and Grant Teply (2017). "Performance of a continuously rotating half-wave plate on the POLARBEAR telescope". In: J. Cosmology Astropart. Phys. 2017.5, 008, p. 008. DOI: `10.1088/1475-7516/2017/05/008`. arXiv: `1702.07111 [astro-ph.IM]`.

Watts, D. J., G. E. Addison, C. L. Bennett, and J. L. Weiland (2020). "Beyond Optical Depth: Future Determination of Ionization History from the Cosmic Microwave Background". In: ApJ 889.2, 130, p. 130. DOI: `10.3847/1538-4357/ab5fd5`. arXiv: `1910.00590 [astro-ph.CO]`.

Watts, Duncan J., David Larson, Tobias A. Marriage, Maximilian H. Abitbol, John W. Appel, Charles L. Bennett, David T. Chuss, Joseph R. Eimer, Thomas Essinger-Hileman, Nathan J. Miller, Karwan Rostem, and Edward J. Wollack (2015). "Measuring the Largest Angular Scale CMB B-mode Polarization with Galactic Foregrounds on a Cut Sky". In: ApJ 814.2, 103, p. 103. DOI: 10.1088/0004-637X/814/2/103. arXiv: 1508.00017 [astro-ph.CO].

Watts, Duncan J., Bingjie Wang, Aamir Ali, John W. Appel, Charles L. Bennett, David T. Chuss, Sumit Dahal, Joseph R. Eimer, Thomas Essinger-Hileman, Kathleen Harrington, Gary Hinshaw, Jeffrey Iuliano, Tobias A. Marriage, Nathan J. Miller, Ivan L. Padilla, Lucas Parker, Matthew Petroff, Karwan Rostem, Edward J. Wollack, and Zhilei Xu (2018). "A Projected Estimate of the Reionization Optical Depth Using the CLASS Experiment's Sample Variance Limited E-mode Measurement". In: ApJ 863.2, 121, p. 121. DOI: 10.3847/1538-4357/aad283. arXiv: 1801.01481 [astro-ph.CO].

Zaldarriaga, Matias and Uroš Seljak (1997). "All-sky analysis of polarization in the microwave background". In: Phys. Rev. D 55.4, pp. 1830–1840. DOI: 10.1103/PhysRevD.55.1830. arXiv: astro-ph/9609170 [astro-ph].

Chapter 3

CLASS Detectors

To measure the nK-scale CMB polarization fluctuations, CLASS requires high-sensitivity polarimeters that mitigate sources of systematic errors like cross-polarization, beam asymmetries, and out-of-band leakage. To meet these requirements, all four CLASS receivers use feedhorn-coupled transition-edge sensor (TES) bolometers. A TES[1] is a thermal sensor that measures the deposited power through the strongly temperature-dependent resistance of a superconducting film that is biased on its superconducting transition. CLASS uses arrays of TES bolometers whose per-detector measurement sensitivity is only limited by the inherent fluctuations of the incoming radiation, hence they are called background-limited detectors. In this chapter, I describe how the incoming radiation is coupled to the detectors, and motivate the use of TES bolometers by comparing them to other CMB detector technologies. Then, I give a brief overview of the CLASS TES and its readout, which provide the required sensitivity and stability to measure the CMB polarization.

---

[1] The TES was invented in 1938 by Johns Hopkins University Chemistry Professor, Donald Hatch Andrews. He published the idea in 1938 and demonstrated it in 1942 by measuring the change in resistance of a tantalum wire in its superconducting transition, caused by an incoming infrared signal (Andrews et al., 1942).

3.1 Optical Coupling

In Chapter 2, we discussed the optical design of the CLASS telescope with the VPM as the first optical element followed by two ambient-temperature mirrors and cryogenic lenses that focus the incoming radiation onto the focal plane. Now, we discuss the optical components on the focal plane that couple light from the receiver optics to the TES bolometers. Since the optical coupling influences the polarization properties, angular response, bandwidth, and efficiency of the detectors, it plays a crucial role in determining the telescope sensitivity and controlling systematic errors. Various optical coupling schemes including phased-array antennas (Kuo et al., 2008), feedhorn-coupled orthomode tranducer (OMT) probes (McMahon et al., 2009), and lenslet-coupled sinuous antennas (O'Brient et al., 2008) have been used to measure the CMB polarization. While I refer the readers to Abitbol et al. (2017) for a summary on the pros and cons of these different approaches, I focus on the feedhorn-coupled OMT probes used for CLASS detectors in this thesis.

All CLASS focal planes have a similar design as illustrated in Figure 3.1. The light from the telescope is incident on an array of feedhorns that coherently funnel the incoming radiation to the symmetric planar OMTs at their bases. The OMT probe antennas couple the two linear orthogonal polarizations into separate pairs of microstrip transmission lines. Then, a "magic-tee" is used to difference the signal from opposite antennas, and on-chip filters are used to define the precise passband. Finally, the microwave signal is terminated onto the TES. We now briefly discuss these major optical coupling components that are present in all four CLASS detector arrays.

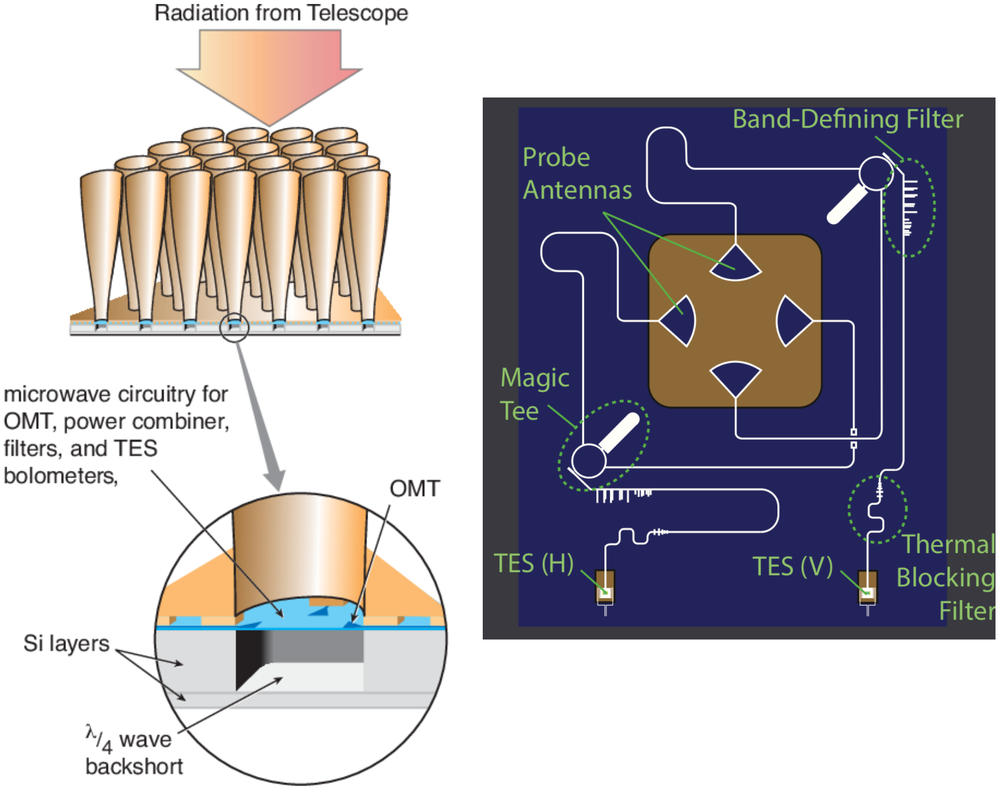
Radiation from Telescope
microwave circuitry for OMT, power combiner, filters, and TES bolometers,
OMT
Si layers
$^{\lambda}/_{4}$ wave backshort
Band-Defining Filter
Probe Antennas
Magic Tee
TES (H)
TES (V)
Thermal Blocking Filter

Figure 3.1: Illustration of the optical coupling for CLASS detectors. (Left) Light from the telescope optics is incident on an array of smooth-walled feedhorns with planar OMTs at their base. A metalized enclosure forms a quarter-wave backshort termination for the OMTs and suppresses the coupling of stray light to the microwave circuit. (Right) Schematic of the CLASS detector chip showing the components of the microwave circuit used to couple the two linear orthogonal polarization modes of the incoming radiation to the TES bolometers. Figure credit: D. Chuss.

3.1.1 Smooth-walled Feedhorns

At radio and microwave frequencies, corrugated feedhorns have been widely used as they offer excellent beam symmetry, main beam efficiency, and cross-polar response over wide bandwidths (Zeng et al., 2010). In addition, the feedhorns provide a sharp low-frequency cutoff to reject out-of-band coupling and do not require anti-reflection coatings needed for other coupling schemes like lenslet arrays and phased-array antennas. However, the corrugated features inside the horn are difficult to machine; therefore the corrugated feedhorn's improved optical performance comes at the expense of higher manufacturing cost. Over the last decade, the corrugated feedhorns used by several CMB polarization experiments have been manufactured through stacking of silicon platelets machined using photolithography and deep reactive ion etching (Britton et al., 2010; Nibarger et al., 2012). This manufacturing process is both costly and time-consuming.

CLASS uses a novel monotonically-profiled, smooth-walled feedhorn that has comparable performance to the corrugated profile. The smooth-walled feed was developed and patented by CLASS scientists at Johns Hopkins University and the NASA Goddard Space Flight Center. The CLASS Q-band feedhorn design was demonstrated to have a 30% fractional bandwidth (30 – 45 GHz) over which the cross-polarization response is better than -30 dB and the power reflection is below -28 dB (Zeng et al., 2010; Zeng, 2012). The feedhorns for other CLASS frequency bands also have similar performance (see Chapters 4 and 5). The monotonic feedhorn profile makes the feedhorn manufacturing comparatively easier and cheaper to scale for large-format detector arrays required to achieve higher instrument sensitivity. The smooth-walled feedhorns for the CLASS Q- and W-band detector arrays are directly machined from copper. For the G-band detectors, which have smaller pixel sizes, the feedhorn arrays are made from a silicon-aluminum alloy as it provides a better coefficient of thermal expansion (CTE) match with the silicon wafer (Ali et al., 2018). The feedhorn profiles, beams, and assembly with the detector wafers for the W-band and the G-band focal planes are described in detail in Chapters 4 and 5, respectively.

3.1.2 Planar Ortho-mode Transducers

As shown in Figure 3.1, at the base of each feedhorn, there is a symmetric planar OMT that couples the incoming radiation onto microstrip transmission lines. The OMT microwave circuitry is fabricated out of superconducting niobium on a monocrystalline silicon layer. The monocrystalline silicon was chosen for several reasons: (1) it has low dielectric loss, resulting in high optical efficiency, (2) the electrical permittivity of the dielectric is highly uniform, reducing the variability of electrical properties of the circuit between detectors, (3) it has uniform acoustic properties, allowing precision control over thermal conductance of the devices, and (4) the material is stress free, providing excellent mechanical properties for the device layer (Chuss et al., 2016; Rostem et al., 2016). The CLASS OMT is designed to couple to the TE_{11} mode of the circular waveguide and reject the unwanted modes, making the CLASS detectors single-moded.

The four OMT antenna probes (oriented like cross-dipole antennas) separate the two linear orthogonal polarizations into two pairs of microstrip lines. The CLASS OMT design uses a broadband vialess crossover (U-Yen et al., 2009) to route the orthogonal polarization signals from the opposite antenna probes to two separate magic-tees (U-Yen et al., 2008), as shown in Figure 3.1. A magic-tee involves no magic, of course. Sometimes called a hybrid-tee or 3 dB coupler, it is a four-port microwave component where the input signal on one port is equally split and emerges from the two adjacent ports, but not at all from the opposite port. The device is used as a power combiner or splitter. At the magic-tee in the CLASS OMTs, a sum port resistively terminates the symmetric modes, while a difference port capacitively couples the desired asymmetric signal onto a single microstrip line. The polarization signal on the microstrip then passes through a series of filters that define the passband and reject out-of-band radiation. Finally, the filtered signal is terminated on a PdAu resistor that is thermally coupled to the TES.

3.1.3 Photonic Chokes and Quarter-Wave Backshorts

The optical design for CLASS detectors includes several stray light control features to minimize systematic errors, which is crucial for detecting the low signal-to-noise CMB polarization. The low-frequency waveguide cutoff of the feedhorn and the thermal blocking filters on the microstrip lines prevent out-of-band radiation from entering the detector through the transmission lines. Above ~ 700 GHz (the niobium gap energy), the niobium transmission lines themselves act as lossy filters. In addition, direct stray light coupling to the TES and the OMT antenna region is minimized through metallized enclosures as shown in Figure 3.2. The stray light control enclosure is formed by bonding different wafers together in a process known as hybridization (Denis et al., 2016). During this process, a photonic choke wafer, a detector wafer, and a backshort assembly are bonded together through indium bumps to form the CLASS detector chip as shown in the cross-section in Figure 3.2.

The photonic choke wafer acts as an interface between the feedhorns and

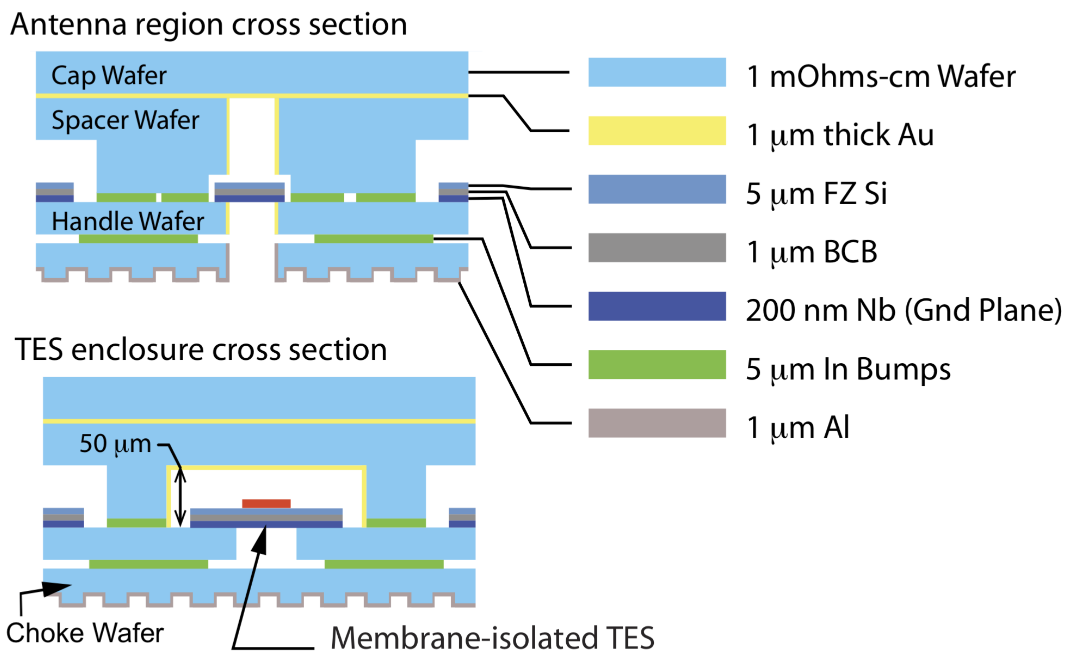
Antenna region cross section
Cap Wafer
Spacer Wafer
Handle Wafer
TES enclosure cross section
50 µm
Choke Wafer
Membrane-isolated TES
1 mOhms-cm Wafer
1 µm thick Au
5 µm FZ Si
1 µm BCB
200 nm Nb (Gnd Plane)
5 µm In Bumps
1 µm Al

Figure 3.2: Schematic of the cross-section of the CLASS detector chip showing the TES and the OMT antenna regions. The photonic choke wafer, the detector wafer, and the backshort assembly are bonded together using the indium bumps to form the CLASS detector chip. The photonic choke with array of square silicon pillars coated with aluminum acts as an interface between the feedhorns and the detector wafer. The detector wafer is patterned out of a 100 mm silicon-on-insulator wafer with the 5 µm float zone single-crystal silicon device layer, the Benzocyclobutene (BCB) polymer bonding layer, and the niobium ground plane. The backshort assembly consists of a spacer wafer that sets the quarter-wave distance and a cap wafer that provides the reflective surface for OMT termination and forms the metalized enclosure for stray light control. Figure from Rostem et al. (2016).

the detector wafer to improve the feedhorn coupling by preventing light leakage at this interface. The photonic choke joints (Wollack, U-yen, and Chuss, 2010) are realized by micro-machining an array of square Al-coated silicon pillars on the feedhorn side of the wafer[2]. The other side of the choke wafer is bonded using indium bumps to the detector wafer. The detector wafer is patterned out of a 100 mm silicon-on-insulator wafer with the 5 µm thick float-zone single-crystal silicon device layer that functions as the OMT membrane, TES thermal isolation membrane and microstrip dielectric. The third layer in the CLASS detector chip stack is the backshort assembly with spacer and cap wafers bonded together through Au-Au thermo-compression. The spacer wafer is approximately quarter-wave thick in-band, and the cap wafer has a reflective surface to form a short for the OMT termination. The Au-coated enclosure formed by the backshort assembly also suppresses the coupling of stray light to the OMT and the TES as shown in Figure 3.2. The TES optical coupling is therefore only possible through the band-filtered microstrip line discussed in section 3.1.2.

---

[2] For the Q-band detector array, these choke pillars are directly machined into the copper baseplate that the feedhorns sit on (Appel et al., 2014).

While the details of the TES microstrip termination specific to different CLASS detector arrays are discussed in Chapters 4 and 5, we now have a general understanding of how the incoming light through the telescope optics is coupled to the CLASS detectors. These detectors are background-limited TES bolometers that provide CLASS with the high sensitivity required to measure the CMB polarization. Before exploring the details of a TES, it is worth discussing why the TES bolometer is the detector of choice for CLASS.

3.2 CMB Detectors

For background-limited detectors, the detector sensitivity is limited by the fluctuations in the background radiation. For ground-based telescopes like CLASS, this background radiation is dominated by the thermal emission from the telescope and the atmosphere. (Space missions can avoid/improve on the ground-based background limit.) To motivate the detector choice for CLASS, let us look at the statistical properties of the thermal photon noise for CMB experiments following the formalism in Zmuidzinas (2003). CMB experiments operate at an interesting crossover regime between optical/near-IR and radio astronomy as the mean photon mode occupation number for the thermal background radiation $n \equiv [\exp(h\nu/kT) - 1]^{-1} \approx 1$. For shorter wavelengths with $h\nu \gg kT \Rightarrow n \ll 1$, and the background photon counts follow a Poisson distribution with fluctuations given by $\sqrt{N}$ for N photons received. For longer wavelengths with $h\nu \ll kT \Rightarrow n \gg 1$, photons do not arrive independently according to a Poisson process but instead are strongly bunched with the fluctuations of the order N instead of $\sqrt{N}$ (Zmuidzinas, 2003). Therefore, with $n \approx 1$ falling in the cross-over regime for the frequencies of interest for CMB experiments, CMB detectors have been built with a wide variety of techniques drawn from both optical and radio astronomy.

We can express detector sensitivity through noise-equivalent power (NEP), which is the incident power required to achieve a signal-to-noise of one after integrating for 0.5 s (corresponding to post-detection bandwidth of 1 Hz). For a background-limited detector that couples to a single spatial mode of the electromagnetic wave propagating through a waveguide (which is the case for CLASS detectors), the NEP (in W/$\sqrt{\text{Hz}}$ units) can be written as:

$$\mathrm{NEP} = h\nu \left[2\Delta\nu \frac{n_0(1 + \eta n_0)}{\eta} \right]^{1/2}, \tag{3.1}$$

where n_0 is the photon occupation number of the thermal radiation, η is the efficiency and $\Delta\nu$ is the optical bandwidth of the detector (Zmuidzinas, 2003). The first term in equation 3.1 gives the $\sqrt{N}$ Poisson fluctuations and is known as the shot noise, whereas the second term accounts for the photon correlations, and is known as the bunching noise. The shot noise is dominant for shorter wavelengths in the optical regime with $n \ll 1$, whereas the bunching noise is dominant for longer wavelengths in the Rayleigh-Jeans limit with $n \gg 1$.

In radio astronomy, coherent detectors that can read out both the phase and amplitude information of the incoming signal have been widely used as it is straightforward to achieve high spectral resolution and diffraction-limited performance (Goldsmith et al., 2009). Many CMB experiments (e.g. *WMAP*, *Planck*-LFI, QUIET, and DASI) have demonstrated coherent detection through high electron-mobility transistor (HEMT) amplifiers. HEMTs offer low noise, low power dissipation (in comparison to other technologies that can operate above 1 K), high reliability, wide bandwidths, insensitivity to electromagnetic and charged particle radiation, operation over a wide temperature range, and natural sensitivity to a single linear polarization (Cleary, 2010). Moreover, correlation techniques can be used with a reference load in coherent systems to reduce systematics arising from gain fluctuations (Jarosik et al., 2003). However, these benefits come at a cost of a quantum-noise floor which increases with frequency.

The NEP for detectors preceded by quantum-limited amplifiers with power gain $G \gg 1$ can be calculated as (Zmuidzinas, 2003):

$$NEP_{\text{coherent}} = (2\Delta\nu)^{1/2}\frac{h\nu}{\eta}[\eta n(\nu) + 1]. \tag{3.2}$$

By setting the noise contribution from the fluctuations in the background radiation to zero, i.e. $n(\nu) = 0$, we can extract the noise from the amplifier alone. Therefore, Equation 3.2 shows that the quantum-limit of the amplifier sets the minimum achievable NEP for coherent detectors. Equations 3.2 and 3.1 can be used to compare the sensitivities of coherent and direct detection. For $n \gg 1$, the two sensitivities are equal; therefore, the longer radio wavelengths do not suffer from the quantum-noise penalty for coherent detection. However, for CMB experiments, at $\nu \gtrsim 100$ GHz, HEMTs (for reasonable η) become less sensitive than background-limited bolometers.

Therefore, to achieve higher sensitivity, CMB experiments are increasingly using bolometers for direct detection. CMB experiments like *Planck*-HFI, MAXIMA, BOOMERanG, and BICEP demonstrated the use of semiconducting neutron transmutation doped Germanium (NTD-Ge) bolometers (Holmes et al., 2008). In these bolometers, a NTD-Ge thermistor is suspended on a spiderweb absorbing structure which maintains a weak thermal link with the heat-bath, reduces the absorber heat capacity, and minimizes the cross-section to cosmic rays. When radiation is absorbed, the absorber temperature T changes along with the resistance $R(T)$ of the thermistor. Since the device is biased at a constant current, the corresponding change in thermistor voltage can be measured through low-noise transistor preamplifiers to calculate the power deposited on the bolometer. The internal detector noise of these bolometers are dominated by the phonon noise in the thermal link to the heat-bath, and is usually much lower than the background photon noise given by equation 3.1.

For background-limited detectors, the only way to increase the overall sensitivity of the instrument is to use more detectors as the total array NEP for

N detectors scales as $1/\sqrt{N}$ with the NEP of individual detectors. Therefore, to make precise measurement of the CMB polarization, it is necessary to map the microwave sky with arrays of background-limited detectors. However, as the NTD-Ge bolometers with the spiderweb absorbers cannot be lithographed into close-packed monolithic arrays, it becomes increasingly challenging to package higher numbers of detectors on the focal plane. Individually biasing the array of detectors with separate lines also becomes cumbersome and increases thermal load on the colder stages of the receiver. In addition, the high impedance of NTD-Ge bolometers makes them unsuitable for a SQUID-based multiplexing scheme (described in section 3.4.2), which can read multiple voltage-biased detectors through one line. The high impedance bolometers also suffer from microphonics pickup, which is particularly challenging for CMB experiments using polarization modulators that have continuously moving mechanical parts (see section 2.4.2).

The CLASS detector choice was guided by the pros and cons of different detector technologies discussed in this section. CLASS uses antenna-coupled TES bolometers, which combine the high sensitivity of TES bolometers with the reduction in systematics through coherent-style antenna coupling. In addition, multiple TESs can be fabricated on a single monolithic array to achieve higher instrument sensitivity and can be multiplexed to read out multiple detectors through a single line. Although other detector technologies like microwave kinetic inductance detectors (MKIDs) are promising due to the ease at which they can be multiplexed into large arrays (Day et al., 2003), they have not yet been demonstrated extensively in the field compared to

TES arrays. TESs have therefore become the workhorse sensor for measuring CMB polarization. Now, after establishing the advantages of TESs for CMB detection, let us discuss how the TESs operate and provide the sensitivity and stability for CMB polarization measurement. The following section is primarily based on the description by Irwin and Hilton (2005).

3.3 Transition-Edge Sensors

A TES is a superconducting metal film that is voltage biased into its normal-superconducting phase transition. The CLASS TES is a molybdenum-gold (MoAu) bilayer with a transition temperature $T_\mathrm{c} \sim 150$ mK and a normal resistance $R_\mathrm{N} \sim 10$ mΩ. This normal-metal-on-superconductor bilayer uses the proximity effect (Nagel et al., 1994) to fine-tune the TES parameters like T_c and R_N that play an important role in determining device performance. Figure 3.3 illustrates a simple electrothermal model that describes the TES operation. The TES thermal circuit can be modeled as a bolometer pixel with heat capacity C, temperature T, and resistance R. The pixel contains the TES film (the yellow/gold bilayer in Figure 3.3) and an absorber [3], which is isolated from a thermal bath with temperature $T_\mathrm{bath} < T$ by a weak link of thermal conductance G. The bolometer is heated by the absorbed radiation power P_γ and the Joule power P_J from the voltage bias, while the power P_bath is conducted away from the bolometer to the bath through the weak link.

---

[3] For CLASS bolometer pixels, the incoming microwave signal is terminated on a palladium-gold (PdAu) absorber, and a significant volume of Pd is added around the TES to set the total heat capacity of the detector to ~ 4 pJK^{-1} (Rostem et al., 2014b).

The heat flow between the TES bolometer and the thermal bath is determined by the weak thermal link, and can be parameterized through a power law as follows:

$$P_{\text{bath}} = \int_{T_{\text{bath}}}^{T} G(T)dT = \kappa(T^n - T_{\text{bath}}^n), \tag{3.3}$$

where the proportionality constant κ and power-law index n depend on the geometry and material properties of the weak link, and are usually determined empirically. The thermal conductance G can now be expressed in terms of κ and n: $G = \mathrm{d}P_{\text{bath}}/\mathrm{d}T = n\kappa T^{n-1}$. Using Equation 3.3, we can also define one of the important properties of a TES – the saturation power P_{sat}. Above its T_{c}, a TES is not sensitive to the input radiation power. Therefore, for a given T_{bath}, P_{sat} is simply P_{bath} at T_{c} as this is the maximum power a TES bolometer can measure, i.e, $P_{\text{sat}} = \kappa(T_{\text{c}}^n - T_{\text{bath}}^n)$.

It is crucial that the bolometer properties like T_{c} and G are chosen carefully. If T_{c} and G are too low, the detectors will saturate during regular CMB observations, making the detector measurements useless. On the other hand, if T_{c} and G are too high, the detector thermal noise (discussed in section 3.3.3) will dominate the measured signal, decreasing the detector's sensitivity to the CMB. The CLASS detectors were designed to have the thermal conductance of the weak link dominated by ballistic phonon transport, where the link's length is smaller than or of the order of the phonon mean free path. Since the phonons carry heat with negligible internal scattering in this scenario, the conductance is effectively set by the beam area. Therefore, ballistic transport is desirable as G can be precisely controlled across the wafer during fabrication

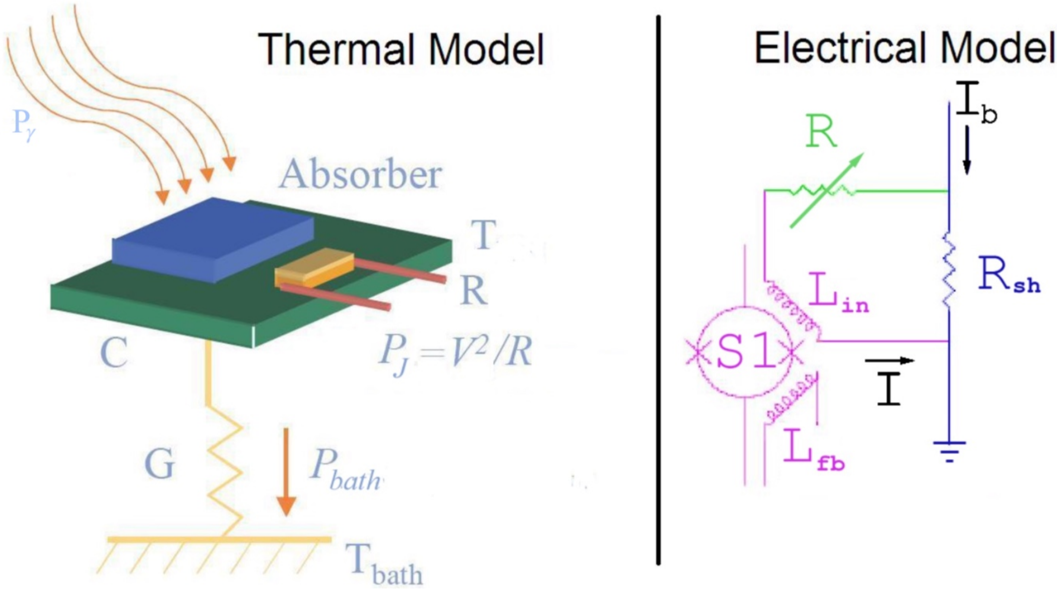

Figure 3.3: Illustration of the electrothermal circuit of a TES bolometer. (Left) The thermal circuit of a TES can be modeled as a bolometer with heat capacity C, temperature T, and resistance R that is connected to a thermal bath at temperature T_{bath} through a weak thermal link. The thermal conductance G of this link determines the power P_{bath} that flows from the bolometer to the bath. The TES is heated by the power from the absorbed radiation P_γ and the Joule power $P_J = V^2/R$, where V is the voltage bias across the TES. (Right) The electrical circuit of a TES can be modeled as a variable resistor R that is voltage biased by applying a DC current bias I_{b} to the circuit. The TES is connected in series with an input inductor L_{in} and in parallel with a shunt resistor $R_{\text{sh}} \ll R$ so that P_{J} decreases as R rises. A change in P_γ is transduced into a changing current I through the TES and the inductor, which changes the magnetic flux through the nearby DC SQUID S1 (described in Section 3.4.1). The feedback inductor L_{fb} cancels the changes in flux in S1 and thus maintains the SQUID in its linear regime. This flux feedback response is also our measured signal. Each color in the electrical model represents a different microfabricated chip in the CLASS detector assembly: the TES (green) is on the detector chip, while the shunt resistor (blue) and the SQUID (pink) are on separate chips thermally connected to the bath (see Figure 3.6). Figure from Niemack (2008).

leading to a higher detector uniformity across the array (Rostem et al., 2014a). This phonon transport sets the value of the power law index n to 4. With $n = 4$ and $T_{\text{bath}} \lesssim 90$ mK set by the dilution refrigerator (section 2.4.3), the T_c and κ (and hence G) values were optimized separately for different CLASS frequency bands depending on their expected background optical loading at the CLASS site (Appel et al., 2014). The optical loading and the detector parameters for all four CLASS frequency bands are discussed in detail in Chapter 6.

Now, let us discuss the electrical circuit of the TES as shown in Figure 3.3. In this circuit, the TES can be modeled as a variable resistor R biased in parallel with a shunt resistor $R_{\text{sh}} \ll R$ and in series with an input inductor L_{in}. The input inductor transduces the current I through the TES into a magnetic field, which then induces a voltage across a nearby superconducting quantum interference device (SQUID) amplifier described in section 3.4.1. The TES is voltage biased with a voltage V by applying a current bias I_b through the parallel circuit as shown in Figure 3.3. For $R_{\text{sh}} \ll R$, the TES becomes voltage biased as $V = I_b R_{\text{sh}}$ (which is constant). As P_γ increases, the TES temperature and therefore its resistance increases. The increase in R causes $P_J = V^2/R$ to decrease, driving the TES temperature lower. The exact opposite process occurs if P_γ decreases. This negative electrothermal feedback process keeps the total power dissipated in the device nearly constant for a constant applied voltage. For comparison, in a current-biased circuit with $P_J = I^2 R$ with fixed I, an increase in P_γ leads to an increase in P_J. This positive electrothermal feedback can cause a thermal runaway driving the TES normal (i.e. out of its transition range). The voltage-biased TES circuit is therefore crucial to stabilize the TES in its transition through negative electrothermal feedback.

3.3.1 Responsivity

The TES electrothermal circuit in Figure 3.3 can be represented by a coupled thermal and electrical differential equations (Irwin and Hilton, 2005):

$$\begin{aligned} C\frac{\mathrm{d}T}{\mathrm{d}t} &= -P_{\mathrm{bath}} + P_{\mathrm{J}} + P_{\gamma} \\ L\frac{\mathrm{d}I}{\mathrm{d}t} &= V - IR_{\mathrm{sh}} - IR(T, I), \end{aligned} \tag{3.4}$$

where L is the total inductance of the TES loop including L_{in}. Since the exact shape of the transition $R(T, I)$ must be determined experimentally and several terms including P_{bath} and P_{J} are non-linear, solving this coupled differential equation is not straightforward. However, it is worth exploring the solutions in the small signal limit as they tell us how the TES responds to a small change in the input power, which is how CLASS measures the CMB polarization anisotropy. Following Irwin and Hilton (2005), first, we linearize the variables in equation 3.4 around their steady-state values as follows:

$$\begin{aligned} P_{\mathrm{bath}} &\approx P_{\mathrm{bath}_0} + G\delta T = P_{\mathrm{J}_0} + P_{\gamma_0} + G\delta T \\ R(T, I) &\approx R_0 + \left.\frac{\partial R}{\partial T}\right|_{I_0}\delta T + \left.\frac{\partial R}{\partial I}\right|_{T_0}\delta I = R_0 + \alpha_I\frac{R_0}{T_0}\delta T + \beta_I\frac{R_0}{I_0}\delta I \\ P_{\mathrm{J}} &\approx P_{\mathrm{J}_0} + 2I_0R_0\delta I + \alpha_I\frac{P_{\mathrm{J}_0}}{T_0}\delta T + \beta_I\frac{P_{\mathrm{J}_0}}{I_0}\delta I, \end{aligned} \tag{3.5}$$

where the variables with subscript 0 denote the steady-state values of the respective variables, $P_{\mathrm{J}_0} = I_0^2R_0$, $\delta T \equiv T - T_0$, and $\delta I \equiv I - I_0$. To derive the final expression for $R(T, I)$ in equation 3.5, we substituted unitless logarithmic temperature and current sensitivities of the TES resistance defined as:

$$\begin{aligned} \alpha_I &\equiv \left.\frac{\partial \log R}{\partial \log T}\right|_{I_0} = \left.\frac{T_0}{R_0}\frac{\partial R}{\partial T}\right|_{I_0} \\ \beta_I &\equiv \left.\frac{\partial \log R}{\partial \log I}\right|_{T_0} = \left.\frac{I_0}{R_0}\frac{\partial R}{\partial I}\right|_{T_0}. \end{aligned} \tag{3.6}$$

To derive the expression for P_J in Equation 3.5, we used $P_\mathrm{J} = I^2 R$ and substituted the derived linear expansion of $R(T, I)$. To simplify the equations, let us define two more quantities – the negative electrothermal feedback loop gain $\mathscr{L}_I$ and the natural thermal time constant τ:

$$\mathscr{L}_I \equiv \frac{P_{\mathrm{J}_0}\alpha_I}{G T_0}; \qquad \tau \equiv \frac{C}{G}. \tag{3.7}$$

The τ in equation 3.7 is the time constant of the TES in absence of the electrothermal feedback. Using the definitions from equations 3.7 and 3.6, we can now substitute equation 3.5 into equation 3.4 to obtain the electrothermal differential equations in the small-signal limit:

$$\begin{aligned} \frac{\mathrm{d}\delta I}{\mathrm{d}t} &= -\frac{R_\mathrm{sh} + R_0(1+\beta_I)}{L}\delta I - \frac{\mathscr{L}_I G}{I_0 L}\delta T + \frac{\delta V}{L} \\ \frac{\mathrm{d}\delta T}{\mathrm{d}t} &= \frac{I_0 R_0 (2+\beta_I)}{C}\delta I - \frac{1-\mathscr{L}_I}{\tau}\delta T + \frac{\delta P_\gamma}{C}, \end{aligned} \tag{3.8}$$

where $\delta P_\gamma \equiv P_\gamma - P_{\gamma_0}$ and $\delta V \equiv V - V_0$ are small changes in the steady-state values of the sky loading P_{γ_0} and the TES voltage bias V_0, respectively.

Equation 3.8 can be expressed in a matrix form as follows:

$$\frac{\mathrm{d}}{\mathrm{d}t}\begin{pmatrix}\delta I\\ \delta T\end{pmatrix} = -\begin{pmatrix}\frac{1}{\tau_{\mathrm{el}}} & \frac{\mathscr{L}_I G}{I_0 L}\\ -\frac{I_0 R_0(2+\beta_I)}{C} & \frac{1}{\tau_I}\end{pmatrix}\begin{pmatrix}\delta I\\ \delta T\end{pmatrix} + \begin{pmatrix}\frac{\delta V}{L}\\ \frac{\delta P_\gamma}{C}\end{pmatrix}, \tag{3.9}$$

where τ_{el} and τ_I are electrical and current-biased thermal time constants:

$$\tau_{\mathrm{el}} = \frac{L}{R_{\mathrm{sh}} + R_0(1+\beta_I)}; \quad \tau_I = \frac{\tau}{1-\mathscr{L}_I}\,. \tag{3.10}$$

These time constants are the two limiting cases of equation 3.8. For a constant voltage bias $\delta V = 0$ and in the limit where $\mathscr{L}_I \to 0$ (for example, this is applicable for a normal resistor as it has a small α_I), $\frac{\mathrm{d}\delta I}{\mathrm{d}t}$ in equation 3.8 can be integrated to give an exponential decay of current to steady state with the electrical time constant τ_{el}. On the other hand, for a hard current bias $\delta I = 0$, $\frac{\mathrm{d}\delta T}{\mathrm{d}t}$ in equation 3.8 can be integrated to give an exponential decay of temperature to steady state with current-biased thermal time constant τ_I. For $\mathscr{L}_I > 1$, we get $\tau_I < 0$, which shows the instability due to thermal runaway in a current-biased circuit discussed earlier.

Equation 3.9 can now be solved using a change of variables by a matrix diagonalization approach to uncouple the two differential equations. I refer the readers to Lindeman (2000) and Irwin and Hilton (2005) for detailed discussion on this approach. Here I discuss the general idea, which is to first solve the homogeneous form of the matrix equation 3.9 (i.e., $\delta V = 0$ and $\delta P_\gamma = 0$), and then introduce a small perturbation (the inhomogeneous term) to the homogeneous solution. The full homogeneous solution can be written in the form:

$$\begin{pmatrix} \delta I \\ \delta T \end{pmatrix} = A_+ e^{-\lambda_+ t} \mathbf{v}_+ + A_- e^{-\lambda_- t} \mathbf{v}_- \, , \tag{3.11}$$

where $A_\pm$ are unitless constants, $\lambda_\pm$ are the two eigenvalues of the eigenvectors $\mathbf{v}_\pm$. For the 2×2 matrix in equation 3.9, the corresponding eigenvalues and eigenvectors are:

$$\begin{aligned} \frac{1}{\tau_\pm} \equiv \lambda_\pm &= \frac{1}{2\tau_{\mathrm{el}}} + \frac{1}{2\tau_I} \pm \frac{1}{2}\sqrt{\left(\frac{1}{\tau_{\mathrm{el}}} - \frac{1}{\tau_I}\right)^2 - 4\frac{R_0}{L}\frac{\mathscr{L}_I(2+\beta_I)}{\tau}} \\ \mathbf{v}_\pm &= \begin{pmatrix} \frac{1-\mathscr{L}_I-\lambda_\pm\tau}{2+\beta_I}\frac{G}{I_0 R_0} \\ \\ 1 \end{pmatrix} , \end{aligned} \tag{3.12}$$

where we have defined the time constants $\tau_\pm$ as the inverse of the eigenvalues $\lambda_\pm$. Finally, to explore the TES response to small changes in sky loading, we introduce a time varying perturbation to the steady-power absorbed by the bolometer $\delta P_\gamma = \mathrm{Re}(\delta P_{\gamma 0} e^{i\omega t})$ in equation 3.9. We keep $\delta V = 0$ as we are interested in the response of a voltage-biased TES circuit. A particular solution to equation 3.9 (i.e. values of $A_\pm$) can be found by substituting equation 3.11 into equation 3.9 including the inhomogeneous term δP_γ. The general solution to equation 3.9 therefore consists of this particular solution added to equation 3.11. However, the particular solution alone has enough information for us to calculate what we are looking for – the power-to-current responsivity of a TES at angular frequency ω (Irwin and Hilton, 2005):

$$
\begin{aligned}
s_I(\omega) \equiv \frac{\delta I}{\delta P_\gamma} &= -\frac{1}{I_0 R_0}\frac{1}{(2+\beta_I)}\frac{(1-\tau_+/\tau_I)}{(1+i\omega\tau_+)}\frac{(1-\tau_-/\tau_I)}{(1+i\omega\tau_-)} \\
&= -\frac{1}{I_0 R_0}\left[\frac{L}{\tau_{\mathrm{el}} R_0 \mathscr{L}_I} + \left(1-\frac{R_{\mathrm{sh}}}{R_0}\right)\right. \\
&\qquad \left. + i\omega \frac{L\tau}{R_0 \mathscr{L}_I}\left(\frac{1}{\tau_I}+\frac{1}{\tau_{\mathrm{el}}}\right) - \frac{\omega^2 \tau}{\mathscr{L}_I}\frac{L}{R_0}\right]^{-1}.
\end{aligned}
\tag{3.13}
$$

To derive the final expression for $s_I(\omega)$, we substitute $\tau_\pm$ from equation 3.12 to express the responsivity in terms of L. To summarize, starting from the coupled differential equations 3.4, we have derived $s_I(\omega)$ in a small-signal limit. This is one of the most important parameters of a TES bolometer as it allows us to calculate the change in input power from the measured change in current. For TES bolometers that have stiff voltage bias (i.e., $R_{\mathrm{sh}} \ll R_0$) and have strong electrothermal feedback such that $\mathscr{L}_I \gg [R_{\mathrm{sh}} + R_0(1+\beta_I)]/[R_0 - R_{\mathrm{sh}}]$, the low-frequency limit of equation 3.13 simplifies to:

$$
s_I(\omega \to 0) = -\frac{1}{I_0(R_0 - R_{\mathrm{sh}})}. \tag{3.14}
$$

In these conditions, the low-frequency responsivity of a TES bolometer depends only on the bias circuit parameters. Equation 3.14 is valid unless a TES is biased very low in its transition ($R_0 \approx R_{\mathrm{sh}}$) or if $\mathscr{L}_I$ is too low, for instance, when a TES is biased high in its transition ($R_0 \approx R_{\mathrm{N}}$). The responsivity values for the CLASS TES bolometers are around -8 µApW^{-1} for the 40 GHz detectors and around -2.5 µApW^{-1} for the rest of the frequency bands (see Chapter 6 for details).

3.3.2 Stability

In equation 3.12, we introduced two interacting time-constants $\tau_\pm$ that determine the temporal behavior of a TES (equation 3.13). To understand these time constants better, let us look at a low inductance limit with $\tau_+ \ll \tau_-$:

$$\begin{aligned}
\tau_+ &\rightarrow \tau_{\mathrm{el}} \\
\tau_- &\rightarrow \tau_{\mathrm{eff}} \equiv \tau \frac{1+\beta_I+R_{\mathrm{sh}}/R_0}{1+\beta_I+R_{\mathrm{sh}}/R_0+(1-R_{\mathrm{sh}}/R_0)\mathscr{L}_I} \qquad (3.15)\\
&\approx \frac{\tau}{\mathscr{L}_I} \quad \text{for } R_{\mathrm{sh}} \ll R_0 \text{ and } \mathscr{L}_I \gg 1+\beta_I.
\end{aligned}$$

While τ_+ describes the electrical time constant from equation 3.10, τ_- describes the detector thermal response sped up by the electrothermal feedback, referred to as the effective time constant (τ_{eff}). This highlights another important characteristic of the negative electrothermal feedback in the voltage-biased TES circuit. In addition to stabilizing the TES in its transition, the feedback speeds up the TES response to incident radiation by a factor of $\sim 1/\mathscr{L}_I$. For instance, while the CLASS 40 GHz TES bolometers have thermal time constant $\tau = C/G \sim 17$ ms, the measured effective optical time constant $\tau_{\mathrm{eff}} \sim 3.4$ ms (Appel et al., 2019).

However, as L increases, τ_+ becomes comparable to τ_-, which drives the TES into unstable electrothermal oscillations. In fact, from equation 3.12, we can see that there exist critically damped solutions for L such that the terms inside the square root get cancelled, i.e., $\tau_+ = \tau_-$. These critically damped solutions for L are as follows (Irwin and Hilton, 2005):

$$
\begin{aligned}
L_{\mathrm{crit}_\pm} = & \frac{R_0 \tau}{(\mathscr{L}_I - 1)^2} \left[\mathscr{L}_I \left(3 + \beta_I - \frac{R_{\mathrm{sh}}}{R_0} \right) + \left(1 + \beta_I + \frac{R_{\mathrm{sh}}}{R_0} \right) \right. \\
& \left. \pm 2 \sqrt{\mathscr{L}_I (2 + \beta_I) \left(\mathscr{L}_I - \frac{\mathscr{L}_I R_{\mathrm{sh}}}{R_0} + 1 + \beta_I + \frac{R_{\mathrm{sh}}}{R_0} \right)} \right] \qquad (3.16) \\
\approx & \frac{R_0 \tau}{\mathscr{L}_I} (3 + \beta_I \pm 2\sqrt{2 + \beta_I}) \quad \text{for } R_{\mathrm{sh}} \ll R_0 \text{ and } \mathscr{L}_I \gg 1 + \beta_I.
\end{aligned}
$$

The TES response is underdamped when $L_{\mathrm{crit}_-} < L < L_{\mathrm{crit}_+}$. Therefore, to prevent unstable oscillations, L needs to be in the over-damped region outside this range. Furthermore, large L can limit the TES responsivity due to high electrical time constant; therefore, $L < L_{\mathrm{crit}_-}$ is the necessary stability criterion for a voltage-biased TES.

The stability criterion alone would imply that the inductance of the TES loop could be designed as low as possible to ensure that $L < L_{\mathrm{crit}_-}$ is satisfied. However, the inductance of the TES loop needs to be high enough to minimize the aliasing of high-frequency detector noise into the signal band due to the limited sampling rate of the time-division multiplexing (described in section 3.4.2). Noise aliasing occurs when a signal is sampled with a Nyquist frequency (defined as half the sampling frequency) lower than its bandwidth. Therefore, L can be increased (while being safely below L_{crit_-}) to increase the effective time constant above the Nyquist sampling period, which then rolls off the high-frequency detector noise. The inductance for the CLASS bolometers were empirically optimized such that the bolometers can be sampled at 20 kHz without aliasing more than 2% of the detector noise in the signal band (Appel et al., 2014). While the intrinsic inductance from detector and readout traces of the CLASS W-band detectors was enough to keep the aliased noise below the 2% target, we added Nyquist inductors to the Q-band and G-band detectors to increase their inductance to ~ 500 nH.

3.3.3 Sensitivity

In section 3.2, we motivated the use of TES bolometers as they can achieve the high sensitivity required for measuring the CMB polarization. We used NEP as a figure of merit for comparing the sensitivities of different detector technologies. For the CLASS TES bolometers, since they are background-limited, the total NEP is dominated by the photon noise. In this section, we discuss the different noise sources that contribute to the total NEP, and the TES parameter optimization to achieve background-limited performance. For clarity, we categorize the NEP contribution from all intrinsic detector noise sources into $\mathrm{NEP_{det}}$ which is subdominant compared to the NEP from background photon noise NEP_γ. The detector noise can be further categorized into phonon noise, Johnson noise, SQUID noise, and any remaining "excess" noise. We now discuss these noise sources individually.

1. **Photon Noise:** The inherent fluctuations in the thermal background is the dominant noise source for CLASS detectors. The average variance in the number of incoming photons for thermal radiation $\langle(\Delta n)^2\rangle = n + n^2$, where n is the mean number of photons per mode. As discussed in Section 3.2, the first term in the variance represents the Poisson fluctuations, while the second term accounts for the photon correlations. The mean square energy fluctuations can therefore be written as $h^2\nu^2\langle(\Delta n)^2\rangle$, and

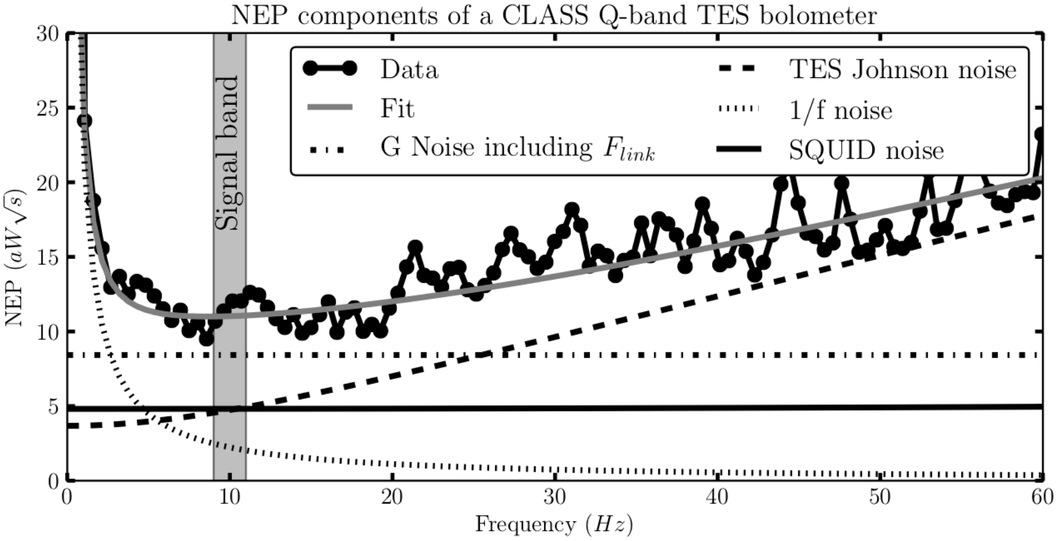

Figure 3.4: Different detector noise components of a CLASS Q-band TES bolometer. The measured NEP_{det} of 11 $\text{aW}\sqrt{\text{s}}$ at the 10 Hz CLASS signal band (set by the VPM modulation frequency) is dominated by the expected phonon noise (or G noise) of 8.5 $\text{aW}\sqrt{\text{s}}$. The difference can be accounted for by a combination of Johnson noise, SQUID noise, and $1/f$ noise. For comparison, the average photon noise for the CLASS Q-band detectors in the field is ~ 16 $\text{aW}\sqrt{\text{s}}$. As NEPs are added in quadrature, NEP_{det} makes a sub-dominant contribution to the total NEP, making CLASS detectors background-limited. Figure from Appel et al. (2014).

we can now calculate the photon NEP as (Richards, 1994):

$$\begin{aligned}
\text{NEP}_\gamma^2 &= \int h^2\nu^2 \langle(\Delta n)^2\rangle d\nu \\
&= \int P_\nu h\nu d\nu + \int P_\nu^2 d\nu \quad [\text{W}^2\text{s}] \\
&\approx h\nu_0 P_\gamma + \frac{P_\gamma^2}{\Delta\nu} \quad [\text{W}^2\text{s}],
\end{aligned} \tag{3.17}$$

where we have used the observed spectral power density $P_\nu = nh\nu$ in the second step. In the last step, we have expressed NEP_γ in terms of the power absorbed by the bolometer $P_\gamma = \int P_\nu d\nu \approx P_{\nu=\nu_0}\Delta\nu$, where $\Delta\nu$ and ν_0 are detector bandwidth and central frequency, respectively. Note that this final expression we derived for NEP_γ is same as equation 3.1 (with $P_\gamma = \eta h \nu n_0 \Delta\nu$)[4] with the first term representing the shot/Poisson noise and the second term representing the bunching/Dicke noise.

2. **Phonon Noise:** The noise from the thermal fluctuations associated with the transport of phonons on the thermal link between the TES and the bath is the primary contributor to the intrinsic detector noise. As these thermal fluctuations depend on the thermal conductance G of the weak link (Figure 3.3), this noise is also referred to as G noise (NEP_G), which can be calculated as (Irwin and Hilton, 2005):

$$\mathrm{NEP}_G^2 = 2k_\mathrm{B} T_\mathrm{c}^2 G F_\mathrm{link} \quad [\mathrm{W}^2\mathrm{s}], \tag{3.18}$$

where k_B is the Boltzmann constant, T_c is the critical temperature of the TES, and F_link is a dimensionless constant that depends on the physics of the thermal transport in the link. In the ballistic limit (applicable to the CLASS detectors), when the mean free path of the phonons is large compared to the length of the link, F_link can be calculated as (Boyle and Rodgers, 1959):

$$F_\mathrm{link} = \frac{1 + (T_\mathrm{bath}/T_\mathrm{c})^{n+1}}{2}, \tag{3.19}$$

---

[4] The factor of $\sqrt{2}$ in equation 3.1 is the conversion factor between the units of $\mathrm{W}\sqrt{\mathrm{s}}$ (equation 3.17) and $\mathrm{W}/\sqrt{\mathrm{Hz}}$ (equation 3.1). The NEP in equation 3.1 is defined in terms of incident power, thus the optical efficiency η is included in the NEP equation. However, for equation 3.17 (and for the rest of this dissertation), I follow the convention where NEP is defined in terms of the absorbed power. For the CLASS detector measurements, η includes the optical efficiency of the entire telescope system (not just the detectors) and is measured in the field using sources on the sky with previously-measured brightness temperatures. Therefore, it is preferable to express NEP in terms of the absorbed bolometer power and instead incorporate η in the power-to-temperature calibration to express the final telescope sensitivity in terms of noise-equivalent temperature (NET) as shown in equation 3.23.

where n is the power-law index from equation 3.3. For CLASS detectors, $T_\mathrm{c} \sim 150$ mK, $T_\mathrm{bath} \lesssim 90$ mK, and $n = 4$ (ballistic limit); therefore, $F_\mathrm{link} \approx 0.5$. In this case, equation 3.18 simplifies to $\mathrm{NEP}_G^2 = k_\mathrm{B} T_\mathrm{c}^2 G$. So, one can lower T_c and G for the detectors to decrease the detector noise. However, lowering T_c and G lowers the TES power saturation as well (equation 3.3). As discussed earlier in this section, T_c and G targets for the CLASS bolometers were therefore optimized to keep NEP_G sub-dominant to NEP_γ while maintaining P_sat safely above the expected optical loading at the site. For instance, the average P_sat for the Q-band detectors is 6.8 pW, which is safely above the median optical loading of 1.6 pW (with maximum $\lesssim 2$ pW) in the field (Appel et al., 2019). Figure 3.4 shows the measured detector noise of a typical CLASS Q-band bolometer. The total measured $\mathrm{NEP}_\mathrm{det}$ of 11 $\mathrm{aW}\sqrt{\mathrm{s}}$ for the detector is dominated by its NEP_G of 8.5 $\mathrm{aW}\sqrt{\mathrm{s}}$. Compared to the average total NEP of 19 $\mathrm{aW}\sqrt{\mathrm{s}}$ (i.e. $\mathrm{NEP}_\gamma \sim 15.5$ $\mathrm{aW}\sqrt{\mathrm{s}}$), NEP_G is sub-dominant. At higher frequencies, due to higher P_γ (primarily due to atmospheric emission), NEP_γ becomes more dominant as compared to NEP_G (see Chapter 6 for details).

3. **Johnson Noise:** The thermodynamic fluctuations associated with the agitated charged carriers like electrons in a resistor are referred to as Johnson noise (or Johnson-Nyquist noise). The Johnson noise NEP

component can be calculated as follows (Irwin and Hilton, 2005):

$$\begin{aligned}\mathrm{NEP}_{\mathrm{J}}^{2} = \frac{2k_{\mathrm{B}}I_0^2}{\mathscr{L}_I^2}\Big[&T_{\mathrm{c}}R_0(1+2\beta_I)(1+\omega^2\tau^2)\\ &+T_{\mathrm{sh}}R_{\mathrm{sh}}(\mathscr{L}_I-1)^2(1+\omega^2\tau_I^2)\Big] \quad [\mathrm{W^2 s}],\end{aligned} \tag{3.20}$$

where the first and the second terms represent the noise contributions from the TES and the shunt resistor, respectively. For CLASS detectors, β_I is small, and since $T_{\mathrm{sh}}R_{\mathrm{sh}} \ll T_{\mathrm{c}}R_0$, the Johnson noise contribution from the shunt resistor is subdominant. Therefore, we can approximate Equation 3.20 as $\mathrm{NEP}_{\mathrm{J}}^2 = 2k_{\mathrm{B}}I_0^2T_{\mathrm{c}}R_0(1+\omega^2\tau^2)/\mathscr{L}_I^2$. Notice that at lower frequencies, the detector Johnson noise is suppressed by electro-thermal feedback. Therefore, it does not make a significant noise contribution at the 10 Hz CLASS signal band as shown in Figure 3.4.

4. **SQUID Noise:** The CLASS TESs are read out by low-noise current amplifiers known as SQUIDs. The readout noise associated with these current amplifiers is called the SQUID noise. The time-division multiplexing increases the readout noise through aliasing as discussed in Section 3.3.2. For the multiplexing chips (discussed in Section 3.4.2) used to read out the CLASS detectors, we measure the current-referred amplifier noise $S_{I_{\mathrm{amp}}}(\omega)$ using the SQUIDs that are not connected to the TES bolometers (referred to as the "dark SQUIDs"). $S_{I_{\mathrm{amp}}}(\omega)$ of $\sim$ 20 pA$\sqrt{\mathrm{s}}$ was measured for the Q-band readout chips by taking the power spectral density (PSD) of the dark SQUID data at the $\sim$ 10 Hz CLASS signal band. We then use the responsivity $s_I(\omega)$ of the detectors

read out through the same chip to estimate the SQUID NEP as follows:

$$\mathrm{NEP}^2_{\mathrm{SQUID}} \equiv \frac{S_{I_{\mathrm{amp}}}(\omega)}{|s_I(\omega)|^2} \,. \tag{3.21}$$

As shown in Figure 3.4, the $\mathrm{NEP}_{\mathrm{SQUID}}$ of ~ 5 aW$\sqrt{\mathrm{s}}$ is small compared to other noise sources. Moreover, the lab measurement shown in Figure 3.4 was performed using a multiplexer chip with lower multiplexing rate as compared to the final detector configuration in the field. The higher multiplexing rate lowers the $\mathrm{NEP}_{\mathrm{SQUID}}$ down to ~ 3 aW$\sqrt{\mathrm{s}}$ (Appel et al., 2014), which only contributes a few percent to the total noise when added in quadrature with other noise components.

5. **Excess Noise:** We characterize any additional noise observed experimentally but not accounted for in the categories above as excess noise. Some sources of excess noise include RF pickup, fluctuations in the bath temperature, microphonics in the detector leads, contact resistance fluctuations, and internal thermal fluctuations between distributed heat capacities in the TES (Irwin and Hilton, 2005). The excess noise for the CLASS Q-band TES bolometer shown in Figure 3.4 can be characterized as a low-frequency noise with $1/f$ dependence, most likely caused by bath temperature fluctuations in the test setup. Such excess noise identified as being associated with imperfect experimental conditions can be mitigated to improve the TES performance. For instance, the measured detector noise in the signal band for the CLASS G-band detectors (see Chapter 5) can be primarily accounted for by the phonon noise, and does not have any measurable excess noise.

All the individual NEPs from these noise sources can be added in quadrature to obtain the total NEP for the TES bolometer as follows:

$$\begin{aligned}\mathrm{NEP}^2_{\mathrm{det}} &= \mathrm{NEP}^2_G + \mathrm{NEP}^2_{\mathrm{J}} + \frac{S_{I_{\mathrm{amp}}}(\omega)}{|s_I(\omega)|^2} + \mathrm{NEP}^2_{\mathrm{excess}} \\ \mathrm{NEP}^2_{\mathrm{total}} &= \mathrm{NEP}^2_{\mathrm{det}} + \mathrm{NEP}^2_{\gamma}.\end{aligned} \tag{3.22}$$

Since we are interested in measuring the CMB anisotropy, we can express the detector sensitivity to measure the CMB temperature fluctuations in terms of noise-equivalent temperature (NET) as:

$$\mathrm{NET} = \mathrm{NEP}_{\mathrm{total}} \times \frac{\mathrm{d}T_{\mathrm{cmb}}}{\mathrm{d}P_{\gamma}}, \tag{3.23}$$

where the power-to-CMB-temperature calibration factor ($\mathrm{d}T_{\mathrm{cmb}}/\mathrm{d}P_{\gamma}$) includes the total optical efficiency of the telescope. For CLASS detectors, we measure this factor by comparing the absorbed power in the bolometer to the known brightness of a source on the sky (including a conversion factor from antenna temperature to CMB thermodynamic temperature). Finally, the NET divided by the VPM modulation efficiency (which is ~ 0.7 for 40, 90, and 150 GHz detectors, and ~ 0.5 for 220 GHz detectors as the VPM throw in the 150/220 GHz dichroic instrument is optimized for 150 GHz) gives us the noise-equivalent Stokes-Q (NEQ), i.e, the detector sensitivity to measure the CMB linear polarization. The detailed sensitivity calculations for all the CLASS detectors in the field are presented in Chapter 6. To quote one of the results, the average NET for a CLASS Q-band bolometer is 225 $\mu\mathrm{K}_{\mathrm{cmb}}\sqrt{\mathrm{s}}$, which translates to a total array NET of 27 $\mu\mathrm{K}_{\mathrm{cmb}}\sqrt{\mathrm{s}}$. This implies $\mathrm{NEQ}_{\mathrm{array}}$ = NET/ 0.7 = 38.6 $\mu\mathrm{K}_{\mathrm{cmb}}\sqrt{\mathrm{s}}$. For comparison, the combined polarization sensitivity of the six 44 GHz radiometers in the *Planck* space mission was 174.2 $\mu\mathrm{K}_{\mathrm{cmb}}\sqrt{\mathrm{s}}$ (Planck Collaboration et al., 2016). This highlights the choice (and as expected performance) of the CLASS detector technology, which was mainly driven by the requirement for higher sensitivity to measure the CMB polarization.

3.4 Detector Readout

One of the key advantages of low-impedance voltage-biased bolometers like the TES is that they can be read out using SQUID amplifiers that are coupled to the TES via an inductor connected in series with the bolometer as shown in Figure 3.3. In addition to their use as low-noise current amplifiers, SQUIDs can be arranged in a time-division multiplexing (TDM) architecture[5] that enables the read out of large arrays of TESs. This multiplexing drastically reduces the number of wires between the cryogenic bolometers and the room temperature electronics. This is crucial for CLASS as increasing the detector count is the only way to increase the overall sensitivity of an instrument with background-limited detectors.

3.4.1 Superconducting Quantum Interference Devices

CLASS uses DC SQUIDs to read out and amplify the detector signal manifested in the form of changing magnetic flux through an inductor. A DC

---

[5] Other architectures like frequency-division multiplexing (FDM; Dobbs et al. 2012) and microwave multiplexing (μmux; Irwin and Lehnert 2004) can also be used, but TDM is a mature and well-characterized technology and has been demonstrated successfully by various CMB experiments in the field. While μmux is promising for next generation CMB experiments with significantly higher number of detector pixels, its performance has not yet been extensively studied through on-sky observations. In this thesis, I focus on the TDM architecture used to read out CLASS detectors and refer the readers to Abitbol et al. (2017) for the current status and prospects of different multiplexing schemes.

SQUID consists of two Josephson junctions (Josephson, 1962) connected in parallel on a superconducting loop as shown in Figure 3.5. A Josephson junction consists of two superconducting electrodes coupled through a weak link (like a thin insulator, a normal metal, or a narrow constriction) where a current can flow between the electrodes with no voltage difference. As shown in Figure 3.5, for a SQUID biased with current I, a current $I/2$ flows through each of the two junctions. If a small external magnetic flux is applied through the superconducting loop, a screening current J is induced to cancel the applied flux. Flux quantization requires that the total flux enclosed by the superconducting loop be $\phi = n\phi_0$, where n is an integer and $\phi_0 = h/2e \approx 2.07 \times 10^{15}$ Wb is the magnetic flux quanta (Doll and Näbauer, 1961). So, when the external flux is increased above $\phi_0/2$, it is energetically favorable for the SQUID to increase the enclosed flux to ϕ_0. Therefore, the screening current J changes direction every time the external flux increases by a half integer multiple of ϕ_0 (O'Sullivan and Murphy, 2012).

A Josephson junction has a limit on the maximum supercurrent, known as the critical current I_c, that can flow across the junction. If the current flow across the junction exceeds I_c, a voltage is induced across it. Therefore, when biased with current I, the SQUID acts as a flux-to-voltage transducer with a voltage V that is a periodic function of the applied magnetic flux as shown in Figure 3.5. The SQUID voltage response can be characterized through a resistively- and capacitively-shunted junction (RCSJ) model[6] as follows

---

[6] In absence of any added damping resistance, the $I - V$ characteristic of a Josephson junction is hysteretic. For a junction with critical current I_c and self-capacitance C, the hysteresis can be eliminated by adding a shunt resistance R such that $2\pi I_c R^2 C \leq \phi_0$ (Chesca, Kleiner, and Koelle, 2005). While high-T_c junctions are self-shunted, sufficient additional

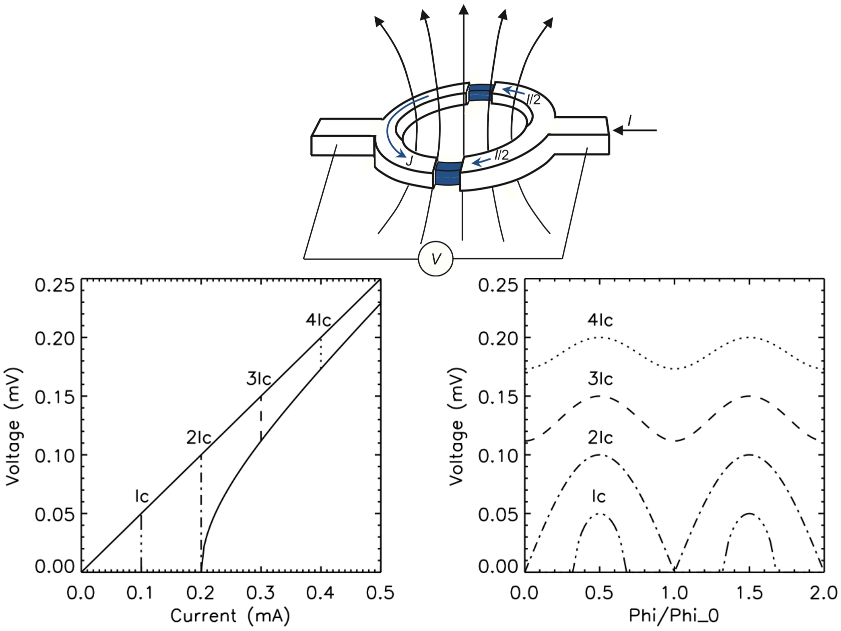

Figure 3.5: (Top) Schematic representation of a DC SQUID consisting of two Josephson junctions (blue) connected in parallel in a superconducting loop. The SQUID acts as a flux-to-voltage transducer that can be used to make sensitive measurements of changes in the TES bolometer current. Figure from O'Sullivan and Murphy (2012). (Bottom-Left) As described by equation 3.24, a change in the magnetic flux inside the SQUID loop results in periodic oscillations of the measured voltage within the two limits (solid lines) as shown by the dotted and dashed lines for different bias currents: I_c, $2I_c$, $3I_c$, and $4I_c$. (Bottom-Right) The SQUID voltage to applied flux (V–ϕ) curves corresponding to the different bias currents. The voltage oscillations are maximum when the bias current $I = 2I_c$. For $I > 2I_c$, the V–ϕ curves are more sinusoidal but have smaller peak-to-peak amplitudes. These plots were obtained for Josephson junctions with $R = 1\ \Omega$ and $I_c = 100\ \mu$A from Battistelli et al. (2008a).

(Tinkham, 2004):

$$V = \frac{R}{2}\sqrt{I^2 - \left[2I_c \cos\left(\frac{\pi\phi}{\phi_0}\right)\right]^2}, \tag{3.24}$$

where $R/2$ is the resistance of two resistively-shunted junctions in parallel. From equation 3.24, we can see that the maximum voltage oscillation is obtained at $I = 2I_c$ (assuming that both junctions have the same I_c) when

---

damping can be supplied for low-T_c junctions by fabricating the device with a metallic film strip as a shunt (Tinkham, 2004).

the voltage fluctuates between zero for integral numbers of ϕ_0, and $I_\mathrm{c}R$ for half-integral flux values as shown in Figure 3.5.

In this mode of operation, referred to as the open loop mode, the periodic SQUID voltage is a non-linear function of applied flux, and the flux change ($\delta\phi$) relates to the change in TES current (δI) as $\delta\phi = M_\mathrm{in}\,\delta I$, where M_in is the mutual inductance (a constant) of the TES input coil. Therefore, in order to keep the system response linear, CLASS operates the SQUIDs in a flux-locked loop (FLL). In this operation mode, SQUIDs are "locked" in the linear regime of the V–ϕ curve (i.e. $\mathrm{d}V/\mathrm{d}\phi$ is constant) through a feedback that cancels the input signal from the TES. Since this feedback exactly nulls the input flux, $M_\mathrm{in}\,\delta I = M_\mathrm{FB}\,\delta I_\mathrm{FB}$, where M_FB and I_FB relate to the feedback. The proportionality constant $M_\mathrm{in}/M_\mathrm{FB}$ is often referred to as M_ratio, and its value is 24.6 for the CLASS readout system. In the FLL configuration, the feedback current used to linearize the SQUID response is therefore also our signal of interest in order to obtain the input signal from the TES.

3.4.2 Time-Division Multiplexing

If each CLASS TES bolometer and SQUID readout pair were to be separately connected to the room temperature data acquisition and biasing electronics, the number of connections would be unmanageable. For instance, let us consider the CLASS G-band detector array with 1020 bolometers. With just the pairs of SQUID bias, SQUID feedback and TES bias lines, there would be $1020 \times 3 \times 2 = 6120$ individual wires from the cold detector array to the warm electronics. First of all, fitting all these wires along with their connections within the 16 cm × 16 cm area of the detector array would be very challenging. Secondly, the thermal load from these wires would be excessively high considering the limited cooling power at the coldest stages. This would prevent the TESs from being cooled below their critical temperature. Therefore, CLASS uses a TDM readout architecture to drastically reduce the number of wires from the cold detectors to the warm electronics.

For all CLASS detector arrays, multiplexing is achieved through two cold stages of SQUIDs connected to a room temperature multichannel electronics (MCE) developed by the University of British Columbia (Battistelli et al., 2008b). As shown in Figure 3.6, at the 100 mK stage, the TES signal is read out by the first stage SQUIDs (SQ1) coupled to a flux-activated switch (FAS) in a multiplexer (MUX) chip fabricated by NIST (Reintsema et al., 2003; Doriese et al., 2016). The SQ1 signal is then carried through twisted pairs of NbTi Tekdata[7] cables to the 4 K stage for futher amplification by the SQUID series array (SSA). The SSA is connected to the MCE that handles the data acquisition and biasing of the TES and the cold readout components.

A single MUX chip used by CLASS (the "MUX11d" provided by NIST, Boulder) can read out 11 TESs, and can be connected in series with other MUX11d chips (as shown in Figure 3.7) to read out more TESs. In a two-dimensional TDM scheme (shown in Figure 3.8), the MCE biases and reads out detectors per "column" with multiple "rows" that are turned on periodically such that only one row is active for a given column at any time. For instance, the CLASS G-band detector array uses a 24 column × 44 row TDM architecture

---

[7] Tekdata Interconnections Limited, Staffordshire, ST1 5SQ, UK

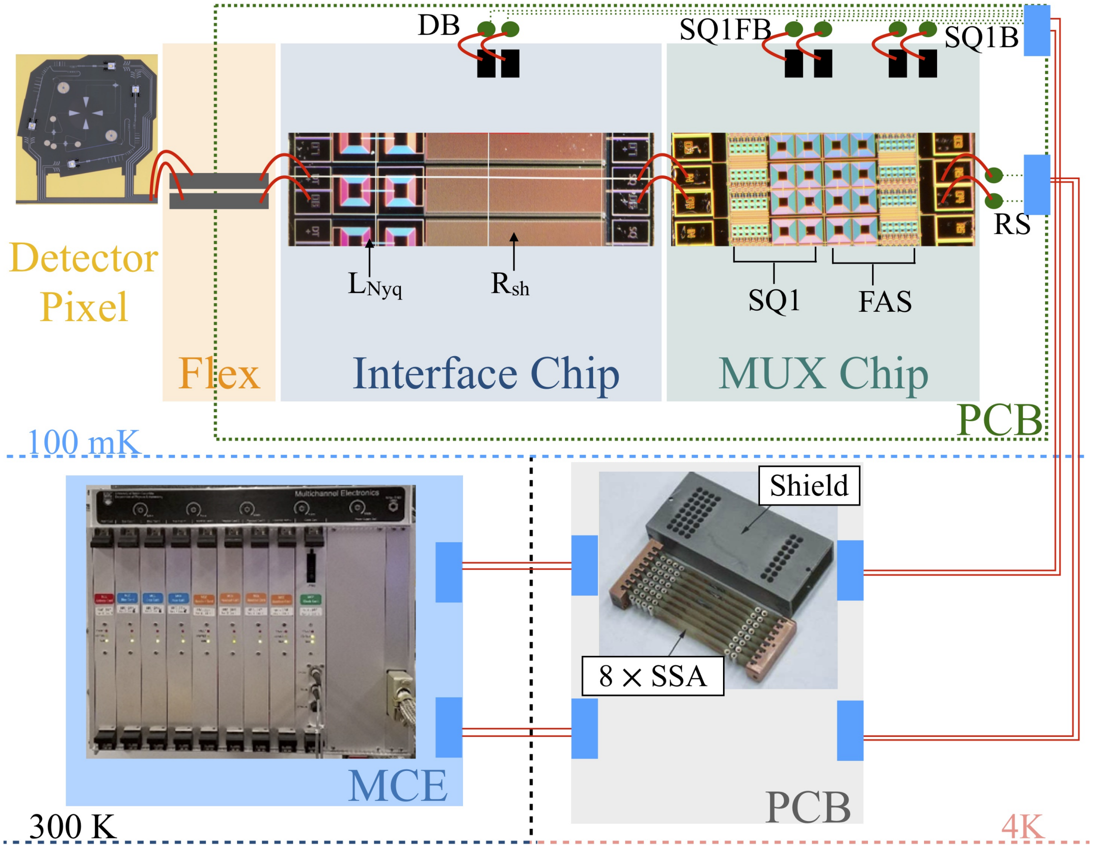

Figure 3.6: Schematic showing the readout for a single CLASS bolometer with zoomed-in images of the components at each stages. At 100 mK stage, the detector pixel is connected to the MUX chip through the Al flex circuit and the interface chip. The MUX chip contains the first-stage SQUID (SQ1) and the flux-activated switch (FAS). Refer to Figure 3.7 for the detailed circuit diagram of the MUX chip. The interface chip houses the Nyquist inductor and the shunt resistor. The MUX and interface chips are glued onto a printed circuit board (PCB) that connects the detector bias (DB), SQ1 bias (SQ1B), SQ1 feedback (SQ1FB), and row select (RS) lines to the twisted pairs of NbTi Tekdata cables (shown as straight red lines). The curved red lines are the Al wire-bonds used to electrically connect the components on the 100 mK stage. The connection between the MUX, interface, and detector is designed to be fully superconducting to avoid stray resistance affecting the bias loop circuit of the TES. The SQ1 signal is amplified by the SQUID series array (SSA) module within a magnetic shielding box mounted on the 4 K stage of the receiver. Finally, the 4 K PCB with the SSA modules is connected to the room temperature multichannel electronics (MCE) that handles the data acquisition and the biasing of the TES and the cold readout components. While the images shown here are for the CLASS G-band detectors, the overall schematics are same for all CLASS frequency bands.

that can read out 1056 bolometers[8]. The total number of wires connected to the 100 mK stage in this TDM scheme is (24 columns × 3 lines/col. + 44 RS lines) × 2 wires/line = 232. If connected individually, 1056 bolometers would require 6336 wires instead. This highlights the importance of multiplexing for reading out large arrays of detectors.

Figure 3.7 shows a schematic of a single column for the MUX11d system used to multiplex the CLASS detectors. The current signal from each TES is inductively coupled to its dedicated SQ1 via an inductor connected in series with the TES (Figure 3.3). Note that SQ1 is not a single SQUID but a series array of SQUIDs that amplify the TES signal. Each SQ1 is individually shunted with an FAS (Henderson et al., 2016), and this SQ1-FAS pair share a same bias line. The SQ1-FAS chain is voltage-biased through a 1 Ω resistor so that the change in impedance in each column can be measured by an SSA module located at the 4 K stage. During data acquisition, one of the switches is flux-biased into its normal state, while all the other switches in the given column remain superconducting. The higher resistance of the normal switch means that the entire bias voltage is dropped across this SQ1-FAS pair. All the other SQ1s in the column are bypassed as the bias current shorts through the switches left in their superconducting state. The summed SQ1 signal from the column is coupled through an inductor to the 4 K SSA for a second stage of amplification as shown in Figure 3.7. The amplified SSA signal is then transmitted to the warm electronics, i.e, the MCE.

---

[8] While the CLASS G-band detector array only requires 1020 channels to read out the 1020 bolometers in total, the additional 36 available channels are connected either to dark SQUIDs to monitor readout noise and magnetic pickup, or to bolometers with no optical coupling to monitor bath temperature fluctuations and detect any light leaks.

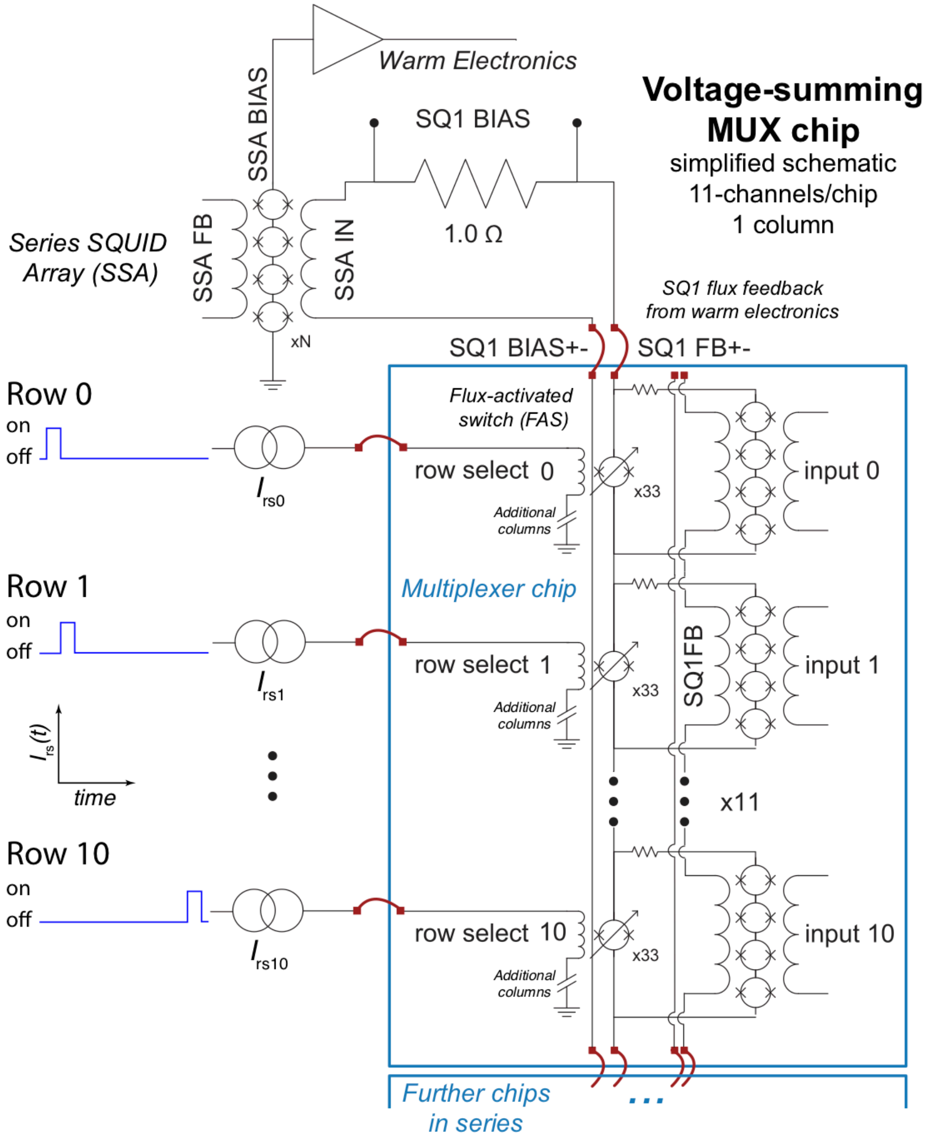
Warm Electronics
SSA BIAS
SQ1 BIAS
Voltage-summing MUX chip
simplified schematic
11-channels/chip
1 column
Series SQUID Array (SSA)
SSA FB
SSA IN
1.0 Ω
xN
SQ1 flux feedback from warm electronics
SQ1 BIAS+-
SQ1 FB+-
Row 0
on
off
I_{rs0}
Flux-activated switch (FAS)
row select 0
x33
input 0
Additional columns
Row 1
on
off
I_{rs1}
Multiplexer chip
row select 1
x33
SQ1FB
input 1
Additional columns
$I_{rs}(t)$
time
x11
Row 10
on
off
I_{rs10}
row select 10
x33
input 10
Additional columns
Further chips in series
...

Figure 3.7: Schematic of a single column for the MUX11d system used to read out the CLASS detectors. Each TES is inductively coupled to a distinctive SQ1 via the input coil. The summed signal from the SQ1s in a column is then amplified by the SSA before transmitting it to the warm electronics (the MCE). The MCE (illustrated in Figure 3.8) sequentially addresses each row by driving its FAS normal. At any given time, all but one row of SQ1s are bypassed through the switches. The SQUIDs operate in a flux-locked loop in order to linearize the readout through the SQ1 feedback. The red lines are the same Al wirebonds shown in Figure 3.6 that electrically connect the MUX chip to other 100 mK components. Figure from Henderson et al. (2016).

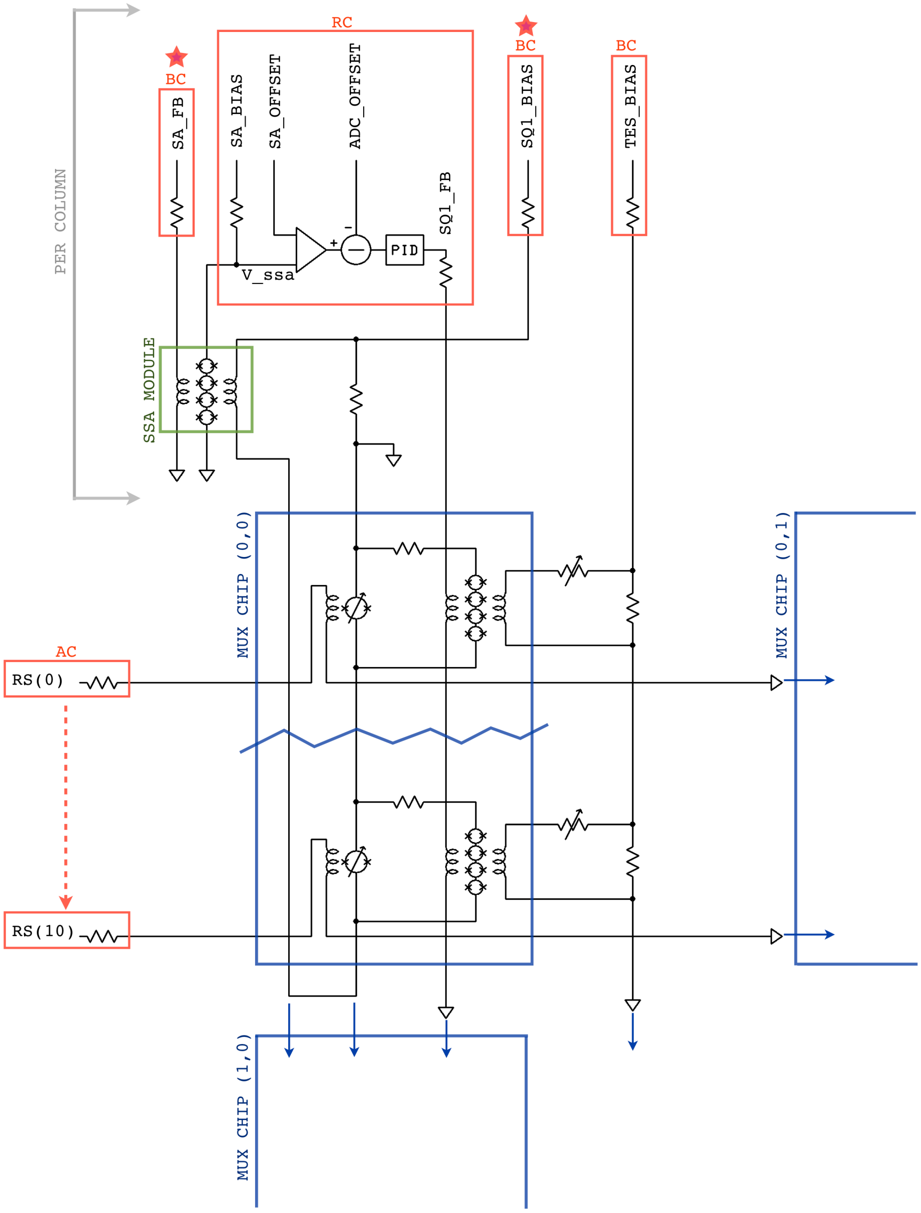
PER COLUMN
BC
SA_FB
RC
SA_BIAS
SA_OFFSET
ADC_OFFSET
SQ1_FB
+
-
PID
V_ssa
BC
SQ1_BIAS
BC
TES_BIAS
SSA MODULE
MUX CHIP (0,0)
MUX CHIP (0,1)
AC
RS(0)
RS(10)
MUX CHIP (1,0)

Figure 3.8: Extension of the schematic in Figure 3.7 illustrating the two-dimensional TDM architecture and showing the interaction of different MCE components with the cold readout. The blue outlines show the MUX chips, the green box highlights the SSA module, and the red outlines show the MCE-sourced signals. Except the row-select lines used to address different rows, the MCE signal lines run along each column and therefore must be shared with every detector in that column. The fast-switching lines (the red stars) can assign individual values to different rows within the column to fine-tune the SQUID biasing parameters. Figure from Grayson (2016).

3.4.3 Multi-channel Electronics

The MCE has multiple functions: (1) it biases the SQ1, the SSA, and the TES, (2) it handles the muliplexing by switching the row-select (RS) lines, (3) it provides the digital PID control for the flux locked loop operation with SQ1FB, and (4) it manages data acquisition by communicating with a computer via a pair of optical fibers. These functions are carried out by separate cards in the MCE as shown in the schematic in Figure 3.8. These swappable MCE cards can also be seen in the image in Figure 3.6. The MCE addressing card sequentially addresses each row through the RS lines with low-duty-cycle square waves that drive the FAS normal. Each row is sampled at a multiplexing frequency (f_{MUX}) set by the MCE clock as follows:

$$f_{\mathrm{MUX}} = \frac{f_{\mathrm{clock}}}{n_{\mathrm{row}} \times \mathrm{row\_len}} \quad , \tag{3.25}$$

where f_{clock} = 50 MHz is the MCE clock frequency, n_{row} is the number of multiplexed rows, and row_len is the dwell time per row in f_{clock} units, i.e. number of 50 MHz clock cycles before the next row switch. The row_len parameter needs to be optimized considering the SQ1 bandwidth for the lower limit and noise aliasing (section 3.3.2) for the upper limit. If row_len is set too low, SQ1s will not have enough time to turn ON/OFF, whereas if set too high the decreased f_{MUX} will increase high-frequency noise aliasing. The row_len parameters optimized through lab measurements and their corresponding f_{MUX} values for different CLASS detector arrays are listed in Table 3.1.

If each data sample were to be saved at the f_{MUX} rate for all the detectors, the data transfer and storage would be unmanageable. For instance, for the

Table 3.1: Multiplexing and readout parameters for CLASS detectors

Frequency band	n_{row}	row_len	data_rate	f_{MUX}	f_{readout}
Q	11	200	113	22.7 kHz	201.1 Hz
W	22	100	113	22.7 kHz	201.1 Hz
G	44	100	56	11.4 kHz	202.9 Hz

CLASS G-band array, the data transfer rate for the 1020 bolometers would be ~ 64 MBps (much higher than the maximum ~ 4 MBps MCE data transfer rate). Therefore, data timestreams are downsampled by a "data_rate" factor (in units of data frame period) shown in Table 3.1. This parameter (which must be an integer) is chosen such that the frequency of data readout $f_{\mathrm{readout}} \equiv f_{\mathrm{MUX}}/\mathrm{data\_rate} \sim 200$ Hz for all CLASS detector arrays. This downsampled detector data is synchronized through a "sync box" that provides timing signals to the MCE and the telescope housekeeping system, allowing the detector data to be precisely matched with the telescope pointing information.

Before the data is downsampled, the MCE applies a digital 4-pole Butterworth low pass filter to prevent high-frequency noise aliasing. Butterworth filters have a maximally flat passband response because, for a given order, they produce the sharpest roll-off possible without inducing in-band peaking or ripples (Ellis, 2012). The MCE firmware implements the low pass filter through four filter coefficients (b_{11}, b_{12}, b_{21}, and b_{22}) and two truncation factors (k_1 and k_2) that can be modified to generate filters with different gains and cutoff frequencies (f_{cutoff}). The filter and truncation parameters relate to the magnitude (gain) and phase of the frequency response through the filter transfer function ($H(z)$) as follows:

$$H(z) = \frac{1+2z^{-1}+z^{-2}}{1+b^*_{11}z^{-1}+b^*_{12}z^{-2}} \cdot 2^{-k_2} \cdot \frac{1+2z^{-1}+z^{-2}}{1+b^*_{21}z^{-1}+b^*_{22}z^{-2}} \cdot 2^{-k_1} \tag{3.26}$$

$$\text{Gain} = |H(z)|, \qquad \text{Phase} = \arg(H(z)),$$

where $z = i\omega$ is the complex frequency, and b^*_{xy} can be calculated from its quantized version of the MCE parameter b_{xy} as $b_{xy} = \left\lfloor \left| b^*_{xy} \right| \times 2^{14} \right\rfloor$, where $\lfloor \bullet \rfloor$ indicates the floor function. All CLASS MCEs use the same filter parameters $(b_{11}, b_{12}, b_{21}, b_{22}, k_1, k_2) = (32295, 15915, 32568, 16188, 5, 12)$ chosen to have the DC gain of 2048 and $f_{\mathrm{cutoff}}/f_{\mathrm{MUX}}$ = 75 Hz/30 kHz. The f_{cutoff} is defined as the -3 dB frequency (i.e. where the filtered signal is $1/\sqrt{2}$ of its maximum value), and its exact value depends on f_{MUX}. Figure 3.9 shows the frequency response (often refered to as a Bode plot) of the MCE filter used for the CLASS detector readout. While the G-band filter has $f_{\mathrm{cutoff}} = 28.4$ Hz, both the Q and the W band filters have $f_{\mathrm{cutoff}} = 56.8$ Hz corresponding to their respective f_{MUX} values from Table 3.1. Both of these cutoff frequencies are far enough from the 10 Hz CLASS signal band where the frequency response is flat as shown in Figure 3.9. These filters allow the detector readout sampling rate of ~ 200 Hz without adding any significant amount of aliased noise (Section 3.3.3) into the CLASS signal band.

3.4.4 SQUID Tuning

All the MCE signals shown in Figure 3.8 can be fine-tuned to achieve an optimal readout performance. As illustrated in Figure 3.5, the SQUID V–ϕ amplitude is maximized when $I = 2I_c$. Therefore, it is important to empirically

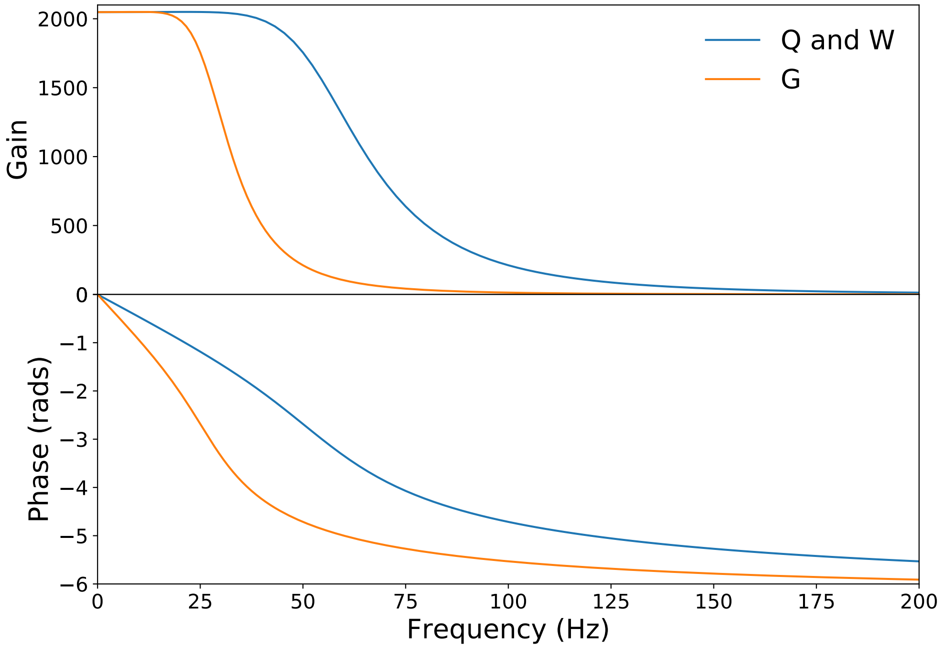

Figure 3.9: A Bode plot showing the magnitude (gain) and phase of the frequency response for the CLASS MCE Butterworth filter applied to the data timestream before downsampling the data. The gain and the phase are defined with respect to a 4-pole filter transfer function (equation 3.26). While the frequency response at the 10 Hz CLASS signal band is flat, the response at high frequencies is significantly reduced to prevent high-frequency noise aliasing. Although the MCE filter parameters for all the CLASS MCEs are the same, the f_{cutoff} for the G-band filter ($\sim$ 30 Hz) is half compared to the Q- and W-band filters as f_{cutoff} scales with f_{MUX} shown in Table 3.1.

determine I_c and bias the SQUIDs as close to $2I_c$ as possible. Moreover, since the SQUIDs are operated in a FLL mode during data acquisition, the baseline feedback current should be chosen to lock the SQUIDs in the zero-flux point (Figure 3.10) to achieve the highest possible linearity and $\mathrm{d}V/\mathrm{d}\phi$ gain. In addition, proper RS input fluxes need to be identified to accurately put individual FASes in normal vs superconducting states.

The SQUID tuning procedure for a CLASS-like readout is described in detail in Henderson et al. (2016) and Battistelli et al. (2008a). Here, I briefly discuss the major steps involved in the tuning of CLASS readout with an associated plot for each step in Figure 3.10.

1. Being the last stage of amplification and closet to the MCE, the SA is characterized first. In this step, the SA V–ϕ curves are obtained by ramping the current through the SA feedback coil while measuring the SA output voltage (Figure 3.4.4, top-left). These curves are obtained for different SA current biases and the bias current that gives the maximum peak-to-peak voltage (i.e. when $I = 2I_{\mathrm{c}}$) is chosen. At this optimum SA bias, the SA operating point is chosen where the $\mathrm{d}V/\mathrm{d}\phi$ is highest in order to maintain linearity for the following tuning stages.

2. In this step, the flux required to turn the RS switches ON (OFF), i.e. when the FAS is normal (superconducting), is determined. As the current through the FAS flux coil is ramped up, the SA feedback required to keep the SA locked is measured. During this step, the SA feedback current reflects the input flux to the SA from the RS resistance. Therefore, the maxima and minima of this curve correspond to the FAS being normal and superconducting, respectively (Figure 3.10, top-right). These two RS flux values are stored for every row and are used to turn the specific row ON/OFF during data acquisition.

3. Next, the SQ1 stage is tuned by ramping the current through the SQ1 feedback line while measuring the SA feedback required to keep the SA output voltage constant. This step is very similar to Step 2 where the FAS flux was ramped up instead of the SQ1 feedback. This step

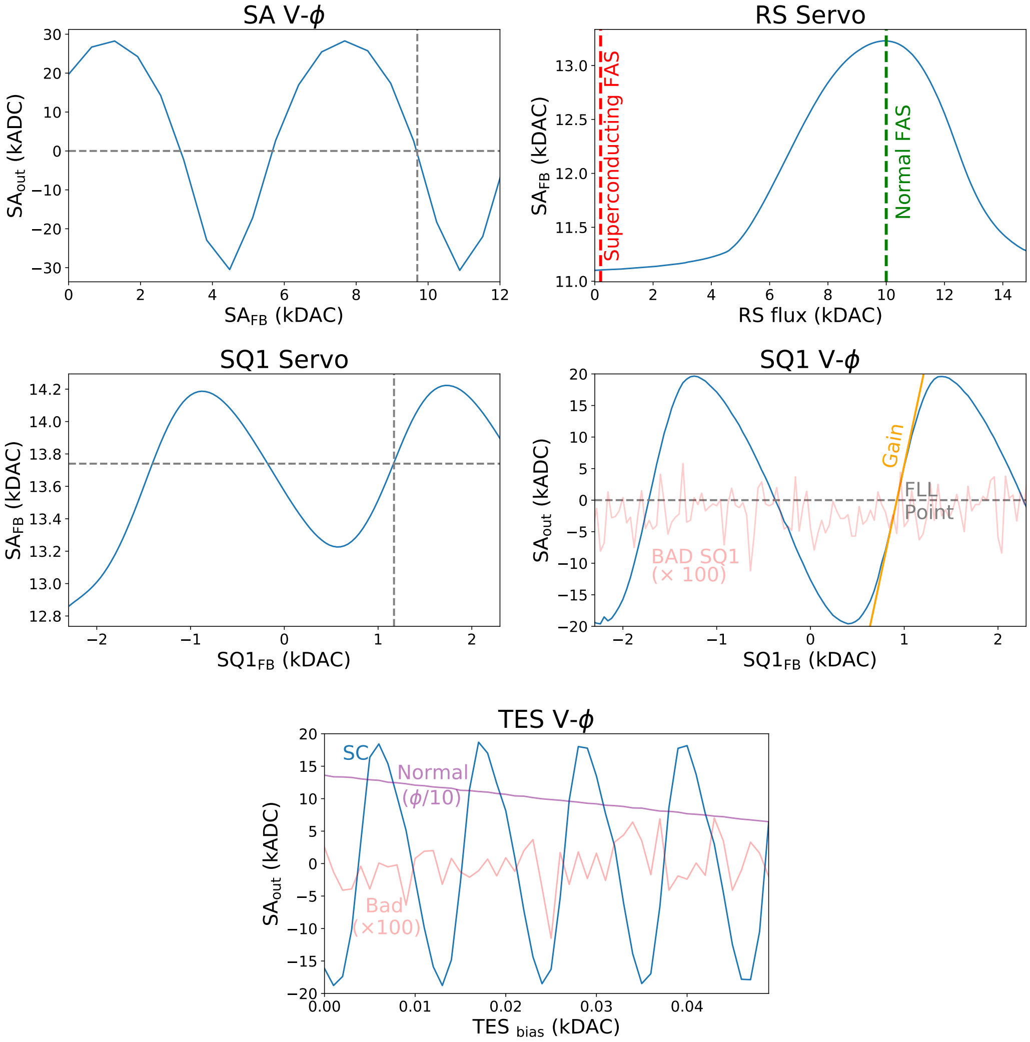

Figure 3.10: The SQUID tuning and screening procedure for a typical CLASS G-band readout channel. (Top-Left) The SQUID SA V–ϕ curves help select the SA bias that maximizes the peak-to-peak voltage response and the lock-point to linearize the SA (the dashed cross-hair) for further tuning steps. (Top-Right) The RS flux required to drive the FAS normal while keeping the SA locked is identified. (Middle-Left) The SQ1 feedback is ramped up, and the SA feedback required to keep the SA locked is measured for different SQ1 biases in order to optimize the SQ1 bias and the SA feedback for the FLL operation. (Middle-Right) Before initializing the FLL, these SQ1 V–ϕ curves are used to further optimize the SQUID parameters identified above, measure the gain of the entire SQUID chain, and identify the problematic SQUID channels. (Bottom) The diagnostic TES V–ϕ curves are used to screen the problematic detectors that are either broken or stay normal with very long V–ϕ period (visible here through the slopy V–ϕ response with reduced period for illustration).

is repeated for various SQ1 biases to choose the bias that gives the maximum peak-to-peak response, similar to Step 1. At this SQ1 bias, the highest $\mathrm{d}V/\mathrm{d}\phi$ point sets the SA feedback required to operate the SA during the regular data acquisition (Figure 3.10, middle-left). As the FASes are being switched, the SQ1 bias and the SA feedback values are optimized per-channel (since these signals are on the fast-switching lines) and are assigned accordingly while reading out the detector array.

4. All the SQUID tuning parameters have now been determined: SA bias in Step 1, RS bias in Step 2, and SQ1 bias and SA feedback in Step 3. Now, we measure the SA voltage output in an open loop configuration while sweeping the SQ1 feedback. This step can be used to (1) fine-tune the parameters obtained from the previous steps, (2) calculate the magnitude and sign of the gain of the whole SQUID chain for each detector channel (orange line in Figure 3.10, middle-right), and (3) screen the bad MUX channels. During lab testing, if we observe that a particular MUX channel does not show the expected V–ϕ signal and is connected to an optically-coupled TES, we connect the associated TES to a different MUX channel (that was initially connected to either a dark SQUID, a dark bolometer, or a bad TES) by shifting the Al wirebonds shown in Figure 3.6. We are now ready to initiate the FLL data-acquisition mode through the MCE firmware. In the FLL mode, the SQ1 feedback signal linearizes the SQUID response and tracks the incoming TES signal. Notice that the FLL can have multiple stable points as shown in the middle-right plot of Figure 3.10. For instance, at exactly one flux period

before the identified lock point, FLL has similar linear response with high $\mathrm{d}V/\mathrm{d}\phi$ gain (and with the same sign). Therefore, FLL could be operated at multiple points in the V–ϕ curve, highlighting that the SQUID current measurement is only a relative measurement of the device current.

5. This is a diagnostic step that can be used to screen the TESs. While the TES I–V curves (described in detail in Chapter 4) are used to select the TES bias and obtain the detector responsivity, the TES V–ϕ curves are useful in identifying problematic detectors. In this step, the MUX open loop response is measured while sweeping the TES bias voltage. At the operating bath temperature, the TES should be superconducting, resulting in the oscillating TES V–ϕ curve as shown in Figure 3.10 (bottom plot). However, if a TES is normal, the higher resistance would lead to a significantly longer V–ϕ period. On the other hand, if a trace connecting to the TES or a wirebond connecting the MUX to the TES is broken, no V–ϕ response is observed during this step.

After a detector array is assembled, Steps 1 through 5 are performed through an automated MCE algorithm (Battistelli et al., 2008a). These tuning results are then manually examined to further optimize the selected parameters if necessary, and flag any problematic channels. If possible any faulty channels are fixed (for example, by redoing a broken wirebond or by shifting a bolometer wirebond from a bad MUX channel to a spare one), otherwise the channel is disabled through the MCE firmware before fielding the detector array. During the nominal CMB observations in the field, the automated tuning procedure is performed before each observing cycle (i.e. $\sim$ once every

24 hours), and the FLL point with the steepest $\mathrm{d}V/\mathrm{d}\phi$ is selected to achieve the maximum stability and sensitivity to the TES current signal.

We now have a complete picture of how the incoming CMB polarization signal is coupled to the CLASS TES bolometer array, and how the bolometer signal is read out using DC SQUIDs arranged in two-dimensional TDM architecture. Throughout this chapter, we discussed the design features implemented in all the CLASS detector arrays to provide CLASS with high sensitivity, stability, and control of systematic errors required to measure the CMB polarization over large angular scales. Next, we will discuss the specific design and assembly features for different CLASS detector arrays that have been optimized according to their frequency bands. While I refer the readers to Appel et al. (2014) for details on the CLASS Q-band detector array, in Chapters 4 and 5, I discuss the details of the W-band and the G-band detector arrays, respectively.

References

Abitbol, Maximilian H., Zeeshan Ahmed, Darcy Barron, Ritoban Basu Thakur, Amy N. Bender, Bradford A. Benson, Colin A. Bischoff, Sean A. Bryan, John E. Carlstrom, Clarence L. Chang, David T. Chuss, Kevin T. Crowley, Ari Cukierman, Tijmen de Haan, Matt Dobbs, Tom Essinger-Hileman, Jeffrey P. Filippini, Ken Ganga, Jon E. Gudmundsson, Nils W. Halverson, Shaul Hanany, Shawn W. Henderson, Charles A. Hill, Shuay-Pwu P. Ho, Johannes Hubmayr, Kent Irwin, Oliver Jeong, Bradley R. Johnson, Sarah A. Kernasovskiy, John M. Kovac, Akito Kusaka, Adrian T. Lee, Salatino Maria, Philip Mauskopf, Jeff J. McMahon, Lorenzo Moncelsi, Andrew W. Nadolski, Johanna M. Nagy, Michael D. Niemack, Roger C. O'Brient, Stephen Padin, Stephen C. Parshley, Clement Pryke, Natalie A. Roe, Karwan Rostem, John Ruhl, Sara M. Simon, Suzanne T. Staggs, Aritoki Suzuki, Eric R. Switzer, Osamu Tajima, Keith L. Thompson, Peter Timbie, Gregory S. Tucker, Joaquin D. Vieira, Abigail G. Vieregg, Benjamin Westbrook, Edward J. Wollack, Ki Won Yoon, Karl S. Young, and Edward Y. Young (2017). "CMB-S4 Technology Book, First Edition". In: *arXiv e-prints*, arXiv:1706.02464, arXiv:1706.02464. arXiv: `1706.02464 [astro-ph.IM]`.

Ali, Aamir M., Thomas Essinger-Hileman, Tobias Marriage, John W. Appel, Charles L. Bennett, Matthew Berkeley, Berhanu Bulcha, Sumit Dahal, Kevin L. Denis, Karwan Rostem, Kongpop U-Yen, Edward J. Wollack, and Lingzhen Zeng (2018). "SiAl alloy feedhorn arrays: material properties, feedhorn design, and astrophysical applications". In: Proc. SPIE. Vol. 10708. Society of Photo-Optical Instrumentation Engineers (SPIE) Conference Series, 107082P. DOI: `10.1117/12.2312817`. arXiv: `1807.03398 [astro-ph.IM]`.

Andrews, D. H., W. F. Brucksch, W. T. Ziegler, and E. R. Blanchard (1942). "Attenuated Superconductors I. For Measuring Infrared Radiation". In: *Review of Scientific Instruments* 13.7, pp. 281–292. DOI: `10.1063/1.1770037`. eprint: `https://doi.org/10.1063/1.1770037`.

Appel, John W., Aamir Ali, Mandana Amiri, Derek Araujo, Charles L. Bennet, Fletcher Boone, Manwei Chan, Hsiao-Mei Cho, David T. Chuss, Felipe Colazo, Erik Crowe, Kevin Denis, Rolando Dünner, Joseph Eimer, Thomas Essinger-Hileman, Dominik Gothe, Mark Halpern, Kathleen Harrington, Gene Hilton, Gary F. Hinshaw, Caroline Huang, Kent Irwin, Glenn Jones, John Karakula, Alan J. Kogut, David Larson, Michele Limon, Lindsay Lowry, Tobias Marriage, Nicholas Mehrle, Amber D. Miller, Nathan Miller, Samuel H. Moseley, Giles Novak, Carl Reintsema, Karwan Rostem, Thomas Stevenson, Deborah Towner, Kongpop U-Yen, Emily Wagner, Duncan Watts, Edward Wollack, Zhilei Xu, and Lingzhen Zeng (2014). "The cosmology large angular scale surveyor (CLASS): 38-GHz detector array of bolometric polarimeters". In: Proc. SPIE. Vol. 9153. Society of Photo-Optical Instrumentation Engineers (SPIE) Conference Series, 91531J. DOI: 10.1117/12.2056530.

Appel, John W., Zhilei Xu, Ivan L. Padilla, Kathleen Harrington, Bastián Pradenas Marquez, Aamir Ali, Charles L. Bennett, Michael K. Brewer, Ricardo Bustos, Manwei Chan, David T. Chuss, Joseph Cleary, Jullianna Couto, Sumit Dahal, Kevin Denis, Rolando Dünner, Joseph R. Eimer, Thomas Essinger-Hileman, Pedro Fluxa, Dominik Gothe, Gene C. Hilton, Johannes Hubmayr, Jeffrey Iuliano, John Karakla, Tobias A. Marriage, Nathan J. Miller, Carolina Núñez, Lucas Parker, Matthew Petroff, Carl D. Reintsema, Karwan Rostem, Robert W. Stevens, Deniz Augusto Nunes Valle, Bingjie Wang, Duncan J. Watts, Edward J. Wollack, and Lingzhen Zeng (2019). "Onsky Performance of the CLASS Q-band Telescope". In: ApJ 876.2, 126, p. 126. DOI: 10.3847/1538-4357/ab1652. arXiv: 1811.08287 [astro-ph.IM].

Battistelli, E. S., M. Amiri, B. Burger, M. J. Devlin, S. R. Dicker, W. B. Doriese, R. Dünner, R. P. Fisher, J. W. Fowler, M. Halpern, M. Hasselfield, G. C. Hilton, A. D. Hincks, K. D. Irwin, M. Kaul, J. Klein, S. Knotek, J. M. Lau, M. Limon, T. A. Marriage, M. D. Niemack, L. Page, C. D. Reintsema, S. T. Staggs, D. S. Swetz, E. R. Switzer, R. J. Thornton, and Y. Zhao (2008a). "Automated SQUID tuning procedure for kilo-pixel arrays of TES bolometers on the Atacama Cosmology Telescope". In: Proc. SPIE. Vol. 7020. Society of Photo-Optical Instrumentation Engineers (SPIE) Conference Series, p. 702028. DOI: 10.1117/12.789738.

Battistelli, E. S., M. Amiri, B. Burger, M. Halpern, S. Knotek, M. Ellis, X. Gao, D. Kelly, M. Macintosh, K. Irwin, and C. Reintsema (2008b). "Functional Description of Read-out Electronics for Time-Domain Multiplexed Bolometers for Millimeter and Sub-millimeter Astronomy". In: *Journal of Low Temperature Physics* 151.3-4, pp. 908–914. DOI: 10.1007/s10909-008-9772-z.

Boyle, W. S. and Jr. Rodgers K. F. (1959). "Performance characteristics of a new low-temperature bolometer". In: *Journal of the Optical Society of America (1917-1983)* 49.1, p. 66.

Britton, Joe W., John P. Nibarger, Ki Won Yoon, James A. Beall, Dan Becker, Hsiao-Mei Cho, Gene C. Hilton, Johannes Hubmayr, Michael D. Niemack, and Kent D. Irwin (2010). "Corrugated silicon platelet feed horn array for CMB polarimetry at 150 GHz". In: Proc. SPIE. Vol. 7741. Society of Photo-Optical Instrumentation Engineers (SPIE) Conference Series, 77410T. DOI: 10.1117/12.857701.

Chesca, Boris, Reinhold Kleiner, and Dieter Koelle (2005). "SQUID Theory". In: *The SQUID Handbook*. John Wiley & Sons, Ltd. Chap. 2, pp. 29–92. DOI: 10.1002/3527603646.ch2.

Chuss, D. T., A. Ali, M. Amiri, J. Appel, C. L. Bennett, F. Colazo, K. L. Denis, R. Dünner, T. Essinger-Hileman, J. Eimer, P. Fluxa, D. Gothe, M. Halpern, K. Harrington, G. Hilton, G. Hinshaw, J. Hubmayr, J. Iuliano, T. A. Marriage, N. Miller, S. H. Moseley, G. Mumby, M. Petroff, C. Reintsema, K. Rostem, K. U-Yen, D. Watts, E. Wagner, E. J. Wollack, Z. Xu, and L. Zeng (2016). "Cosmology Large Angular Scale Surveyor (CLASS) Focal Plane Development". In: *Journal of Low Temperature Physics* 184.3-4, pp. 759–764. DOI: 10.1007/s10909-015-1368-9. arXiv: 1511.04414 [astro-ph.IM].

Cleary, Kieran A. (2010). "Coherent polarimeter modules for the QUIET experiment". In: Proc. SPIE. Vol. 7741. Society of Photo-Optical Instrumentation Engineers (SPIE) Conference Series, 77412H. DOI: 10.1117/12.857673.

Day, Peter K., Henry G. LeDuc, Benjamin A. Mazin, Anastasios Vayonakis, and Jonas Zmuidzinas (2003). "A broadband superconducting detector suitable for use in large arrays". In: Nature 425.6960, pp. 817–821. DOI: 10.1038/nature02037.

Denis, K. L., A. Ali, J. Appel, C. L. Bennett, M. P. Chang, D. T. Chuss, F. A. Colazo, N. Costen, T. Essinger-Hileman, R. Hu, T. Marriage, K. Rostem, K. U-Yen, and E. J. Wollack (2016). "Fabrication of Feedhorn-Coupled Transition Edge Sensor Arrays for Measurement of the Cosmic Microwave Background Polarization". In: *Journal of Low Temperature Physics* 184.3-4, pp. 668–673. DOI: 10.1007/s10909-015-1366-y. arXiv: 1511.05036 [astro-ph.IM].

Dobbs, M. A., M. Lueker, K. A. Aird, A. N. Bender, B. A. Benson, L. E. Bleem, J. E. Carlstrom, C. L. Chang, H. M. Cho, J. Clarke, T. M. Crawford, A. T.

Crites, D. I. Flanigan, T. de Haan, E. M. George, N. W. Halverson, W. L. Holzapfel, J. D. Hrubes, B. R. Johnson, J. Joseph, R. Keisler, J. Kennedy, Z. Kermish, T. M. Lanting, A. T. Lee, E. M. Leitch, D. Luong-Van, J. J. McMahon, J. Mehl, S. S. Meyer, T. E. Montroy, S. Padin, T. Plagge, C. Pryke, P. L. Richards, J. E. Ruhl, K. K. Schaffer, D. Schwan, E. Shirokoff, H. G. Spieler, Z. Staniszewski, A. A. Stark, K. Vanderlinde, J. D. Vieira, C. Vu, B. Westbrook, and R. Williamson (2012). "Frequency multiplexed superconducting quantum interference device readout of large bolometer arrays for cosmic microwave background measurements". In: *Review of Scientific Instruments* 83.7, 073113-073113-24, pp. 073113–073113–24. DOI: `10.1063/1.4737629`. arXiv: `1112.4215 [astro-ph.IM]`.

Doll, R. and M. Näbauer (1961). "Experimental Proof of Magnetic Flux Quantization in a Superconducting Ring". In: Phys. Rev. Lett. 7.2, pp. 51–52. DOI: `10.1103/PhysRevLett.7.51`.

Doriese, W. B., K. M. Morgan, D. A. Bennett, E. V. Denison, C. P. Fitzgerald, J. W. Fowler, J. D. Gard, J. P. Hays-Wehle, G. C. Hilton, K. D. Irwin, Y. I. Joe, J. A. B. Mates, G. C. O'Neil, C. D. Reintsema, N. O. Robbins, D. R. Schmidt, D. S. Swetz, H. Tatsuno, L. R. Vale, and J. N. Ullom (2016). "Developments in Time-Division Multiplexing of X-ray Transition-Edge Sensors". In: *Journal of Low Temperature Physics* 184.1-2, pp. 389–395. DOI: `10.1007/s10909-015-1373-z`.

Ellis, George (2012). "Chapter 9 - Filters in Control Systems". In: *Control System Design Guide (Fourth Edition)*. Ed. by George Ellis. Fourth Edition. Boston: Butterworth-Heinemann, pp. 165 –183. ISBN: 978-0-12-385920-4. DOI: `https://doi.org/10.1016/B978-0-12-385920-4.00009-6`.

Goldsmith, Paul F., John Carpenter, Neal Erickson, Rick Fisher, John Ford, Todd Gaier, Chris Groppi, Andy Harris, Mark Heyer, Craig Kulesa, Charles Lawrence, Matt Morgan, Lee Mundy, Gopal Narayanan, Karen O'Neil, Tony Readhead, Lorene Samoska, Peter Schloerb, Ron Snell, Christopher Walker, and Lucy Ziurys (2009). "Coherent Detector Arrays for Millimeter and Submillimeter Astronomy". In: *astro2010: The Astronomy and Astrophysics Decadal Survey*. Vol. 2010, p. 11.

Grayson, James A. (2016). "The BICEP3 Millimeter-wave Polarimeter: Measuring the Cosmic Microwave Background from the South Pole". PhD thesis. Stanford University.

Henderson, Shawn W., Jason R. Stevens, Mandana Amiri, Jason Austermann, James A. Beall, Saptarshi Chaudhuri, Hsiao-Mei Cho, Steve K. Choi, Nicholas F. Cothard, Kevin T. Crowley, Shannon M. Duff, Colin P.

Fitzgerald, Patricio A. Gallardo, Mark Halpern, Matthew Hasselfield, Gene Hilton, Shuay-Pwu Patty Ho, Johannes Hubmayr, Kent D. Irwin, Brian J. Koopman, Dale Li, Yaqiong Li, Jeff McMahon, Federico Nati, Michael Niemack, Carl D. Reintsema, Maria Salatino, Alessandro Schillaci, Benjamin L. Schmitt, Sara M. Simon, Suzanne T. Staggs, Eve M. Vavagiakis, and Jonathan T. Ward (2016). "Readout of two-kilopixel transition-edge sensor arrays for Advanced ACTPol". In: Proc. SPIE. Vol. 9914. Society of Photo-Optical Instrumentation Engineers (SPIE) Conference Series, 99141G. DOI: 10.1117/12.2233895.

Holmes, Warren A., James J. Bock, Brendan P. Crill, Timothy C. Koch, William C. Jones, Andrew E. Lange, and Christopher G. Paine (2008). "Initial test results on bolometers for the Planck high frequency instrument". In: *Appl. Opt.* 47.32, pp. 5996–6008. DOI: 10.1364/AO.47.005996.

Irwin, K. D. and G. C. Hilton (2005). "Transition-Edge Sensors". In: *Cryogenic Particle Detection*. Ed. by Christian Enss. Vol. 99, p. 63. DOI: 10.1007/10933596_3.

Irwin, K. D. and K. W. Lehnert (2004). "Microwave SQUID multiplexer". In: *Applied Physics Letters* 85.11, pp. 2107–2109. DOI: 10.1063/1.1791733.

Jarosik, N., C. Barnes, C. L. Bennett, M. Halpern, G. Hinshaw, A. Kogut, M. Limon, S. S. Meyer, L. Page, D. N. Spergel, G. S. Tucker, J. L. Weiland, E. Wollack, and E. L. Wright (2003). "First-Year Wilkinson Microwave Anisotropy Probe (WMAP) Observations: On-Orbit Radiometer Characterization". In: ApJS 148.1, pp. 29–37. DOI: 10.1086/377221. arXiv: astro-ph/0302224 [astro-ph].

Josephson, B. D. (1962). "Possible new effects in superconductive tunnelling". In: *Physics Letters* 1.7, pp. 251–253. DOI: 10.1016/0031-9163(62)91369-0.

Kuo, C. L., J. J. Bock, J. A. Bonetti, J. Brevik, G. Chattopadhyay, P. K. Day, S. Golwala, M. Kenyon, A. E. Lange, H. G. LeDuc, H. Nguyen, R. W. Ogburn, A. Orlando, A. Transgrud, A. Turner, G. Wang, and J. Zmuidzinas (2008). "Antenna-coupled TES bolometer arrays for CMB polarimetry". In: Proc. SPIE. Vol. 7020. Society of Photo-Optical Instrumentation Engineers (SPIE) Conference Series, p. 70201I. DOI: 10.1117/12.788588.

Lindeman, Mark Anton (2000). "Microcalorimetry and the transition-edge sensor". PhD thesis. University of California, Davis.

McMahon, J., J. W. Appel, J. E. Austermann, J. A. Beall, D. Becker, B. A. Benson, L. E. Bleem, J. Britton, C. L. Chang, J. E. Carlstrom, H. M. Cho, A. T. Crites, T. Essinger-Hileman, W. Everett, N. W. Halverson, J. W. Henning, G. C. Hilton, K. D. Irwin, J. Mehl, S. S. Meyer, S. Mossley, M. D. Niemack, L. P. Parker,

S. M. Simon, S. T. Staggs, C. Visnjic, E. Wollack, K. U. -Yen, K. W. Yoon, and Y. Zhao (2009). "Planar Orthomode Transducers for Feedhorn-coupled TES Polarimeters". In: *American Institute of Physics Conference Series*. Ed. by Betty Young, Blas Cabrera, and Aaron Miller. Vol. 1185. American Institute of Physics Conference Series, pp. 490–493. DOI: 10.1063/1.3292386.

Nagel, U., A. Nowak, H. J. Gebauer, P. Colling, S. Cooper, D. Dummer, P. Ferger, M. Frank, J. Igalson, and A. Nucciotti (1994). "Proximity effect in iridium-gold bilayers". In: *Journal of Applied Physics* 76.7, pp. 4262–4266. DOI: 10.1063/1.357310.

Nibarger, John P., James A. Beall, Dan Becker, Joe Britton, Hsiao-Mei Cho, Anna Fox, Gene C. Hilton, Johannes Hubmayr, Dale Li, Jeff McMahon, Michael D. Niemack, Kent D. Irwin, Jeff Lanen, and Ki Won Yoon (2012). "An 84 Pixel All-Silicon Corrugated Feedhorn for CMB Measurements". In: *Journal of Low Temperature Physics* 167.3-4, pp. 522–527. DOI: 10.1007/s10909-011-0428-z.

Niemack, Michael D. (2008). "Towards dark energy: Design, development, and preliminary data from ACT". PhD thesis. Princeton University.

O'Brient, Roger, Jennifer Edwards, Kam Arnold, Greg Engargiola, William Holzapfel, Adrian T. Lee, Michael Myers, Erin Quealy, Gabriel Rebeiz, Paul Richards, Helmuth Spieler, and Huan Tran (2008). "Sinuous antennas for cosmic microwave background polarimetry". In: Proc. SPIE. Vol. 7020. Society of Photo-Optical Instrumentation Engineers (SPIE) Conference Series, 70201H. DOI: 10.1117/12.788526.

O'Sullivan, C. and J. A. Murphy (2012). *Field guide to terahertz sources, detectors, and optics*. SPIE Field Guides. Bellingham: Society of Photo-Optical Instrumentation Engineers.

Planck Collaboration et al. (2016). "Planck 2015 results. II. Low Frequency Instrument data processings". In: A&A 594, A2, A2. DOI: 10.1051/0004-6361/201525818. arXiv: 1502.01583 [astro-ph.IM].

Reintsema, Carl D., JÃűrn Beyer, Sae Woo Nam, Steve Deiker, Gene C. Hilton, Kent Irwin, John Martinis, Joel Ullom, Leila R. Vale, and Mike MacIntosh (2003). "Prototype system for superconducting quantum interference device multiplexing of large-format transition-edge sensor arrays". In: *Review of Scientific Instruments* 74.10, pp. 4500–4508. DOI: 10.1063/1.1605259. eprint: https://doi.org/10.1063/1.1605259.

Richards, P. L. (1994). "Bolometers for infrared and millimeter waves". In: *Journal of Applied Physics* 76.1, pp. 1–24. DOI: 10.1063/1.357128.

Rostem, K., D. T. Chuss, F. A. Colazo, E. J. Crowe, K. L. Denis, N. P. Lourie, S. H. Moseley, T. R. Stevenson, and E. J. Wollack (2014a). "Precision control of thermal transport in cryogenic single-crystal silicon devices". In: *Journal of Applied Physics* 115.12, 124508, p. 124508. DOI: `10.1063/1.4869737`. arXiv: `1403.1326 [astro-ph.IM]`.

Rostem, Karwan, Aamir Ali, John W. Appel, Charles L. Bennett, David T. Chuss, Felipe A. Colazo, Erik Crowe, Kevin L. Denis, Tom Essinger-Hileman, Tobias A. Marriage, Samuel H. Moseley, Thomas R. Stevenson, Deborah W. Towner, Kongpop U-Yen, and Edward J. Wollack (2014b). "Scalable background-limited polarization-sensitive detectors for mm-wave applications". In: Proc. SPIE. Vol. 9153. Society of Photo-Optical Instrumentation Engineers (SPIE) Conference Series, 91530B. DOI: `10.1117/12.2057266`.

Rostem, Karwan, Aamir Ali, John W. Appel, Charles L. Bennett, Ari Brown, Meng-Ping Chang, David T. Chuss, Felipe A. Colazo, Nick Costen, Kevin L. Denis, Tom Essinger-Hileman, Ron Hu, Tobias A. Marriage, Samuel H. Moseley, Thomas R. Stevenson, Kongpop U-Yen, Edward J. Wollack, and Zhilei Xu (2016). "Silicon-based antenna-coupled polarization-sensitive millimeter-wave bolometer arrays for cosmic microwave background instruments". In: Proc. SPIE. Vol. 9914. Society of Photo-Optical Instrumentation Engineers (SPIE) Conference Series, p. 99140D. DOI: `10.1117/12.2234308`.

Tinkham, M. (2004). *Introduction to Superconductivity*. 2nd ed. Mineola, New York: Dover Publications.

U-Yen, K., E. J. Wollack, S Moseley, W. Stevenson T. R. amd Hsieh, and N. T. Cao (2009). "Via-less microwave crossover using microstrip-CPW transitions in slotline propagation mode". In: *2009 IEEE MTT-S International Microwave Symposium Digest*, pp. 1029–1032.

U-Yen, Kongpop, Edward J. Wollack, John Papapolymerou, and Joy Laskar (2008). "A Broadband Planar Magic-T Using Microstrip-Slotline Transitions". In: *IEEE Transactions on Microwave Theory Techniques* 56.1, pp. 172–177. DOI: `10.1109/TMTT.2007.912213`.

Wollack, E. J., K. U-yen, and D. T. Chuss (2010). "Photonic choke-joints for dual-polarization waveguides". In: *2010 IEEE MTT-S International Microwave Symposium*, pp. 1–1.

Zeng, Lingzhen (2012). "Polarimetry in astrophysics and cosmology". PhD thesis. The Johns Hopkins University.

Zeng, Lingzhen, Charles L. Bennett, David T. Chuss, and Edward J. Wollack (2010). "A Low Cross-Polarization Smooth-Walled Horn With Improved Bandwidth". In: *IEEE Transactions on Antennas and Propagation* 58.4, pp. 1383–1387. DOI: `10.1109/TAP.2010.2041318`.

Zmuidzinas, Jonas (2003). "Thermal noise and correlations in photon detection". In: Appl. Opt. 42.25, pp. 4989–5008. DOI: `10.1364/AO.42.004989`.

Chapter 4

90 GHz Detector Array

As discussed in Chapter 2, CLASS uses two 90 GHz (W-band) telescopes optimized for the CMB observation near the minimum of polarized Galactic emission. The first 90 GHz receiver was deployed to the CLASS site in May 2018, while the second is planned to be deployed in 2021. The detector arrays for both 90 GHz receivers share a similar design, which we discuss in Sections 4.1 and 4.2. Before deployment, we extensively tested and characterized the detectors in the first 90 GHz array. We measured the TES parameters, the optical passband, and the detector noise, which we discuss in Section 4.3. At the time of writing, the detectors for the second 90 GHz array are being fabricated and are designed to have similar detector properties as the first array. Based on the on-sky performance results of the first array, we have implemented a few modifications to the second 90 GHz detector fabrication, which will be discussed in Chapter 6. While most of the focal plane design and assembly features discussed in this chapter are the same for both arrays, the measured detector properties are for the first 90 GHz array. This chapter is a modified version of Dahal et al. (2018).

4.1 Focal Plane Design and Assembly

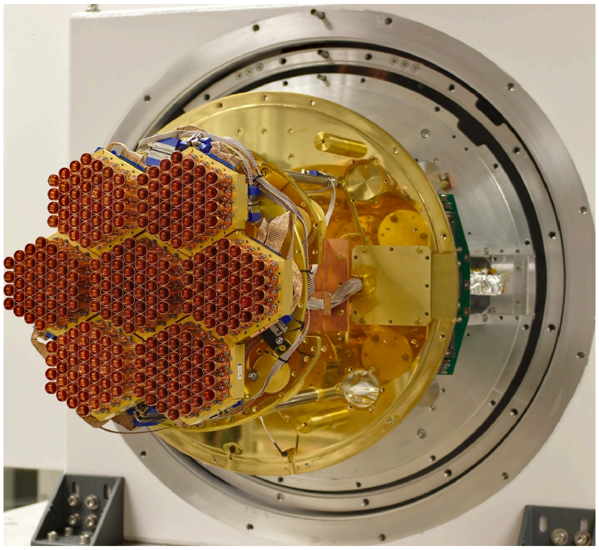

Figure 4.1: Fully assembled first CLASS W-band focal plane mounted in the cryostat. The focal plane consists of seven individual detector modules mounted on a Au-plated copper web interface, which is then mounted onto the mixing chamber plate of a pulse-tube cooled dilution refrigerator. Each module contains 37 smooth-walled copper feedhorns that guide light to the dual-polarization-sensitive detectors on the focal plane.

To achieve the required sensitivity for CLASS, the detectors need to be cooled to a stable bath temperature significantly below the T_c, which sets the detector noise level. We therefore mount the CLASS W-band focal plane onto the mixing chamber plate of a pulse-tube cooled dilution refrigerator (Section 2.4.3) using Au-plated copper posts for strong thermal contact. In the field, the focal plane is operated at a stable bath temperature of ~ 35 mK (Iuliano et al., 2018). Figure 4.1 shows the fully assembled first CLASS W-band focal plane mounted in the cryostat receiver. The focal plane has a hexagonal modular design consisting of seven individual modules. The modular design makes it straightforward to swap modules during testing and assembly.

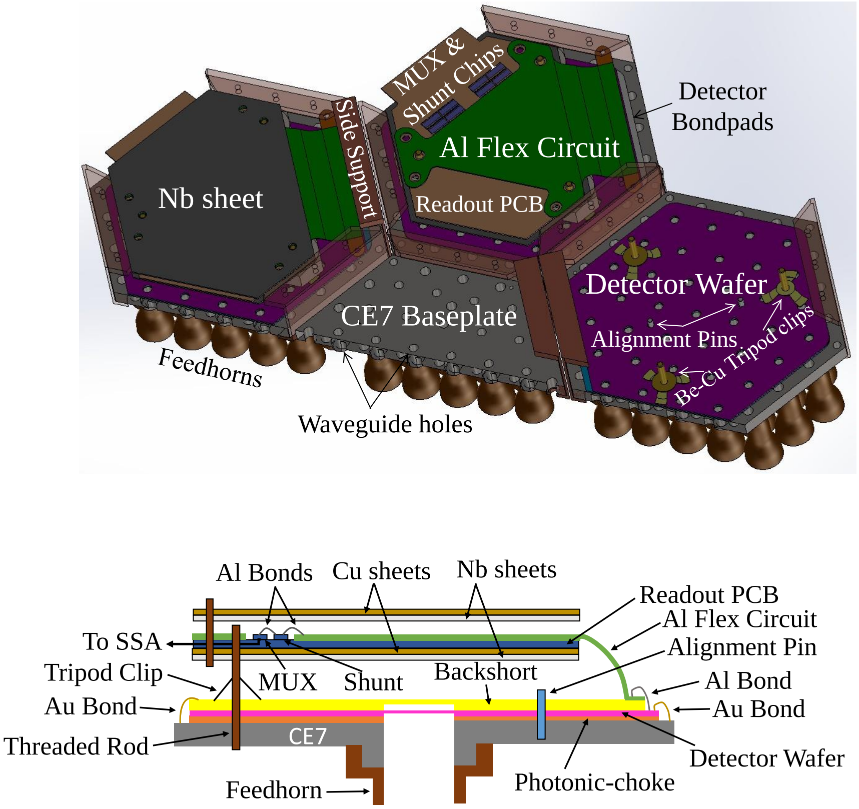
MUX &
Shunt Chips
Detector
Bondpads
Side Support
Al Flex Circuit
Nb sheet
Readout PCB
Detector Wafer
CE7 Baseplate
Alignment Pins
Be-Cu Tripod clips
Feedhorns
Waveguide holes
Al Bonds
Cu sheets
Nb sheets
Readout PCB
Al Flex Circuit
Alignment Pin
To SSA
Tripod Clip
MUX
Shunt
Backshort
Al Bond
Au Bond
Au Bond
Threaded Rod
CE7
Detector Wafer
Feedhorn
Photonic-choke

Figure 4.2: (Top) 3D model showing cut sections of the W-band focal plane. Starting from CE7 baseplate and moving counter-clockwise, we show the detector wafer and readout circuit stack. First, the hybridized detector wafer is mounted on a Au-plated CE7 baseplate using three BeCu tripod spring clips and a side spring (not shown). The readout circuit with MUX and shunt chips on a PCB is then stacked on top of the detector wafer. The entire readout circuit assembly is sandwiched between two niobium sheets for magnetic shielding. (Bottom) Cross-section view (not to scale) of the detector chip and readout circuit stack. The sketch highlights how the base of a feedhorn mates with a cylindrical extrusion on the CE7 baseplate. The photonic-choke (orange), the detector wafer (pink), and the backshort assembly (yellow) are all hybridized during fabrication and mounted onto the baseplate as a single assembly. The top of the backshort assembly and the heat-sink pads on the detector wafer are gold bonded to the baseplate for heat sinking. The sketch also shows sets of aluminum bonds used to connect the detector bond pads to the readout circuit. Two copper sheets in the readout stack are connected to the backplate of each module for heat sinking.

Each module has a regular hexagonal baseplate with 50.8 mm sides. The baseplate is made from Au-plated Controlled Expansion 7 (CE7)[1] alloy, which is 70% silicon and 30% aluminum. CE7 is machinable and has lower differential contraction to silicon detector wafers than copper or aluminum (Ali et al., 2018). The coefficient of thermal expansion (CTE) mismatch between the baseplate and the wafer is a bigger concern for W-band as compared to Q-band where smaller single-pixel detector chips were used (Rostem et al., 2014b; Appel et al., 2014). CE7 is a poor thermal conductor below its superconducting transition temperature. Therefore, we gold plate it so that the detector wafer can be thermalised with the baseplate via gold bonds. These baseplates have 37 circular waveguide holes machined into them as shown in Figure 4.2. The other side of the baseplate has matching cylindrical extrusions that mate with the slightly oversized cylindrical holes in the smooth-walled copper feedhorns. Due to the CTE mismatch between Cu and CE7, the feedhorn base tightens against the cylindrical extrusion as the focal plane is cooled.

CLASS W-band smooth-walled feedhorns (Based on Patent No.: 9166297; Filed: October 8, 2010; Date of Patent: October 20, 2015; Assignee: The Johns Hopkins University; Inventors: Charles L. Bennett, Lingzhen Zeng, Edward J. Wollack, David T. Chuss) are directly machined from oxygen-free high-conductivity (OFHC) copper. As discussed in Section 3.1.1, the monotonic and smooth-wall profile of these feedhorns makes their manufacturing less complex as compared to a corrugated profile. Figure 4.3 shows the 20-point approximation of the W-band feedhorn profile that has an 11.3 mm diameter aperture and a 2.97 mm throat that mates with the CE7 waveguide on the

---

[1] Sandvik Osprey, controlled-expansion CE7 alloy

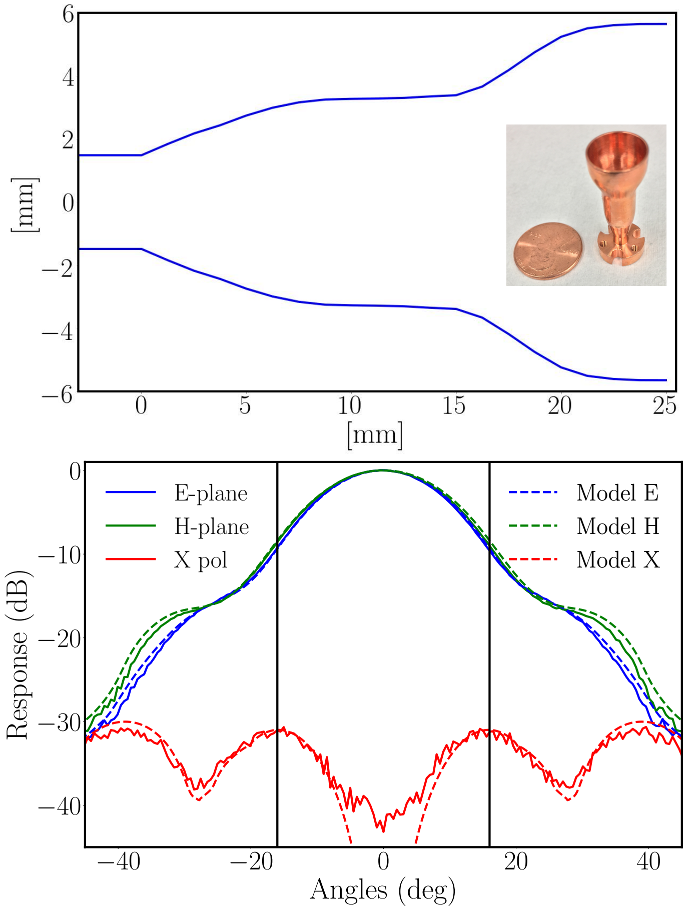

Figure 4.3: (Top) 20-point approximation of the W-band smooth-wall feedhorn profile. The inset shows a single feedhorn machined from oxygen-free high-conductivity copper. (Bottom) W-band feedhorn co-polar E-plane and H-plane, and cross-polar beam measurements averaged across the 77–108 GHz frequency band, along with their models. The measurements were done in the Goddard Electromagnetic Anechoic Chamber and show excellent agreement (within 2%) with the models. The cross polarization across the passband is less than -30 dB, and the beam has a FWHM of 18.7°. The two vertical lines at ±16° show where the beams truncate on the receiver cold stop. The edge taper at 16° is ≈ -9 dB.

focal plane. We measured the beam pattern of the feedhorn in the Goddard Electromagnetic Anechoic Chamber (GEMAC). Figure 4.3 shows the beam measurements averaged across the 77–108 GHz passband. The two vertical lines at $\pm 16^\circ$ show where the beams truncate on the receiver cold stop. The measurement shows that the cross polarization across the passband is less than -30 dB, and the beam has a FWHM of 18.7°. As shown in Figure 4.3, the measured beam pattern is in excellent agreement (within 2%) with the modeled beam (Zeng, 2012).

The feedhorns and the baseplate waveguides couple light to the detectors mounted on the other side of the baseplate as shown in the cross-section sketch in Figure 4.2. As discussed in Section 3.1.3, the CLASS W-band detector chip consists of three separate wafers (a silicon photonic choke wafer, a monocrystalline silicon detector wafer, and a silicon backshort assembly) hybridized together. This hybridized detector wafer package is mounted as a single assembly onto the CE7 baseplate using three Beryllium Copper (BeCu) tripod spring clips as shown in Figure 4.2. A custom designed step screw maintains ~ 0.5 mm deflection of each clip, which puts sufficient force on the wafer to keep it stationary and ensure proper operation of the photonic choke-joints. Two alignment pins and a side mounted BeCu spring clip on the baseplate ensure proper alignment of the baseplate waveguides to the OMTs on the wafer. We vertically stack the readout circuit assembly on top of the step screws to enable the compact format of the module for its close packing in the focal plane. The W-band module assembly procedure is described in detail in Ali (2017).

The W-band readout consists of a 28 column × 22 row TDM-architecture. This is implemented at the 100 mK stage as follows. The readout assembly consists of eight MUX and eight shunt chips per module glued onto a PCB using rubber cement, and a flex circuit with Al traces stacked on top. All the MUX and shunt chips are fabricated by NIST. Each MUX chip contains 11 rows of SQUIDs, which are flux activated to select one detector to read out at a time (refer to Section 3.4 for details). Each W-band module contains four pairs of MUX chips, with each pair strung together in order to multiplex over 22 rows. The shunt chips contain 250 $\mu\Omega$ shunt resistors.

The detector bond pads are electrically connected to the MUX chips through the Al traces and shunt chips by putting down Al bonds between each of these components. The MUX chips are also bonded to the bond pads on the PCB. As shown in Figure 4.2, the entire readout circuit assembly is sandwiched between a stack of 0.5 mm thick niobium (for magnetic shielding) and 0.1 mm thick copper sheets (for heat sinking) on both sides. The part of the PCB that protrudes out of the readout circuit assembly has twisted pairs of copper wires soldered onto it. These wires are soldered to the PCB vias on one end, and 3 MDM connectors on the other: one MDM for the bias and feedback signals and two for multiplexing signals. The SQUID channels are connected to the SSA on a PCB at the 4 K stage for signal amplification via NbTi superconducting cables. Using low-thermal-conductivity Manganin cables, the 4 K PCB is then connected to the room-temperature MCE (Section 3.4.3). All the wires are twisted pairs to reduce RF pick-up noise.

4.2 Detector Design

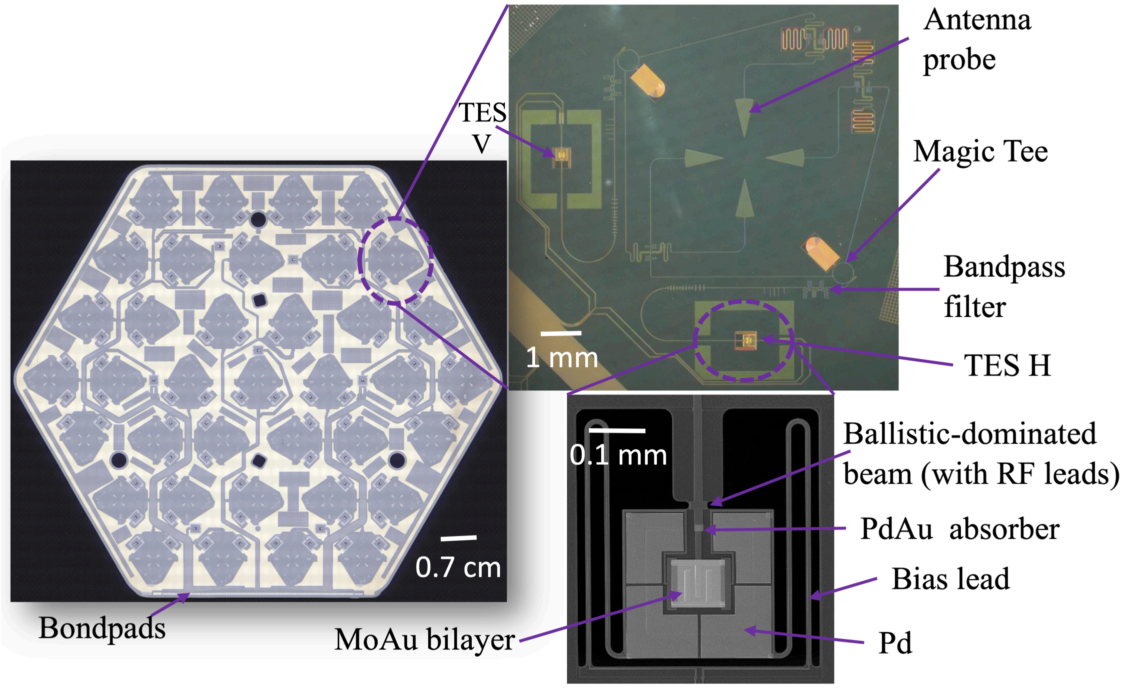
Antenna probe
TES V
Magic Tee
Bandpass filter
1 mm
TES H
0.1 mm
Ballistic-dominated beam (with RF leads)
PdAu absorber
Bias lead
0.7 cm
Bondpads
MoAu bilayer
Pd

Figure 4.4: (Left) CLASS W-band detector wafer showing the 37 dual-polarization-sensitive detectors. All the detectors are connected to the bond pads on the lower edge of the wafer. (Right) Zoomed-in images of the detector circuit (top) and the TES island (bottom). For a detailed description about the W-band detector architecture refer to Rostem et al. (2016).

Figure 4.4 shows the layout of the 37 dual-polarization-sensitive detector pixels fabricated on a single W-band detector wafer. For each pixel, the optical signal is feedhorn-coupled to a planar membrane OMT that separates orthogonal linear polarizations onto microstrip transmission lines terminated on the TES bolometers (see Section 3.1 for details on the optical coupling). The TES bolometers are made from Mo-Au bilayers that are superconducting below ~ 170 mK. These TESs have normal resistance (R_{N}) ~ 10 mΩ and are operated at $\sim 50\%$ R_{N}. They are stabilized through negative electrothermal feedback in a voltage-biased circuit using the 250 μΩ shunt resistor. The TES bilayer for CLASS detectors sits on an island that is thermally connected to the supporting structure through a set of silicon legs with weak thermal conductivity. The long and meandered legs, shown in the zoomed-in image of the TES island in Figure 4.4, support the TES bias leads. They have rough side walls leading to diffuse phonon propagation, and therefore by design contribute very little to the thermal conductance. The thermal conductance of the island is precisely controlled by a short stubby beam with ballistic-dominated phonon transport (Rostem et al., 2014a). For the W-band detectors, this stubby beam also carries the in-band microwave signal coming from the microstrips, which is terminated on a PdAu absorber thermally coupled to the TES as shown in Figure 4.4.

4.3 Detector Characterization

All fabricated detector wafers go through extensive testing to verify that the expected parameters are close to target. In this section, we report the in-lab measurements of the TES dark properties, optical passband, and detector noise for the first 90 GHz detector array.

4.3.1 Dark Properties

We characterize the dark properties of the detectors by acquiring I-V curves for each detector at multiple bath temperatures. First, we ramp up the voltage bias to drive all the detectors normal, then we sweep the bias downwards over a wide range and record the current response of the detectors. As the bias voltage is lowered, the detector transitions from its normal to superconducting state. The *I*-*V* curves help us select the appropriate voltage bias to put the detector in transition while operating it in the field. The inset in Figure 4.5 shows the *I*-*V* curves for a typical W-band detector obtained at multiple bath temperatures. The curves are in increasing order of bath temperature from red to blue starting at 70 mK with temperature steps of 5 mK till 165 mK.

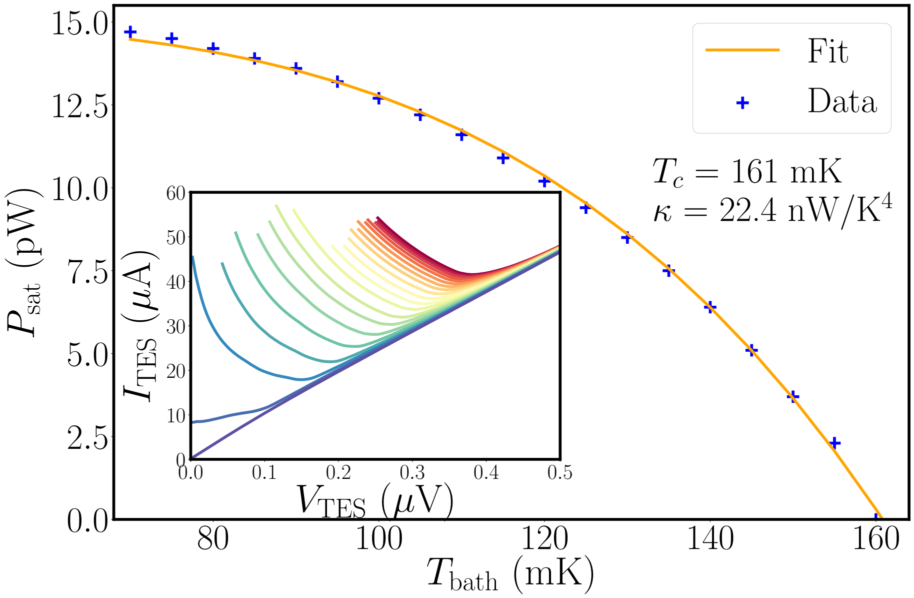

Figure 4.5: The main plot shows the $P_{\rm sat}$ values obtained for one of the W-band detectors at multiple bath temperatures. The orange line shows the model in Equation 4.1 fit to the data. The fit for this particular detector gives T_c and κ values of 161 mK and 22.4 nW/K^4, respectively. The inset shows the *I*-*V* curves used to calculate the $P_{\rm sat}$ values. The curves from red to blue correspond to bath temperatures from 70 mK to 165 mK with steps of 5 mK. Each curve terminates at the point where the TES becomes superconducting.

We acquire these *I*-*V* curves at multiple bath temperatures for all the detectors, and then calculate the TES saturation power ($P_{\rm sat}$) at each temperature through the product of the bias voltage ($V_{\rm TES}$) and response current ($I_{\rm TES}$) at the superconducting transition. We have discussed the $P_{\rm sat}$ parameter in detail in Section 3.3. To summarize, P_{sat} is the amount of power required to raise the TES island temperature to its critical temperature T_{c}, and for CLASS detectors it can be calculated as:

$$P_{\mathrm{sat}} = \kappa \left(T_{\mathrm{c}}^4 - T_{\mathrm{bath}}^4\right) , \tag{4.1}$$

where T_{bath} is the bath temperature and κ is the parameter determined by the thermal conductance of the ballistic-dominated beam shown in Figure 4.4.

We fit the model in Equation 4.1 to the P_{sat} vs T_{bath} data to obtain T_{c} and κ for each detector. Figure 4.5 shows this fit for a typical W-band detector obtained from the I-V curves at multiple T_{bath} shown in the inset. For this particular detector, the curve fit gives T_{c} = 161 mK and κ = 22.5 nW/K^4. We repeat this analysis for all the detectors in the focal plane. Figure 4.6 shows the T_{c} and P_{sat} (at T_{bath} = 50 mK) values for all the optically-sensitive detectors in the first W-band focal plane. The left and right sides of each circle show the H and V detectors, respectively, which are sensitive to separate orthogonal linear polarizations. The black spots in the plot indicate the detectors whose I-V curves could not be obtained. In addition to these optical bolometers, the W-band focal plane also contains several optically-isolated (dark) bolometers and SQUIDs. The dark bolometers are used for probing light leaks and monitoring T_{bath} stability, whereas the dark SQUIDs can monitor readout noise and magnetic pick-up.

For an experiment like CLASS aiming to make a high-sensitivity measurement of the CMB polarization, it is critical that the T_{c} and κ target values are chosen carefully. While lower T_{c} and κ values lead to lower detector noise,

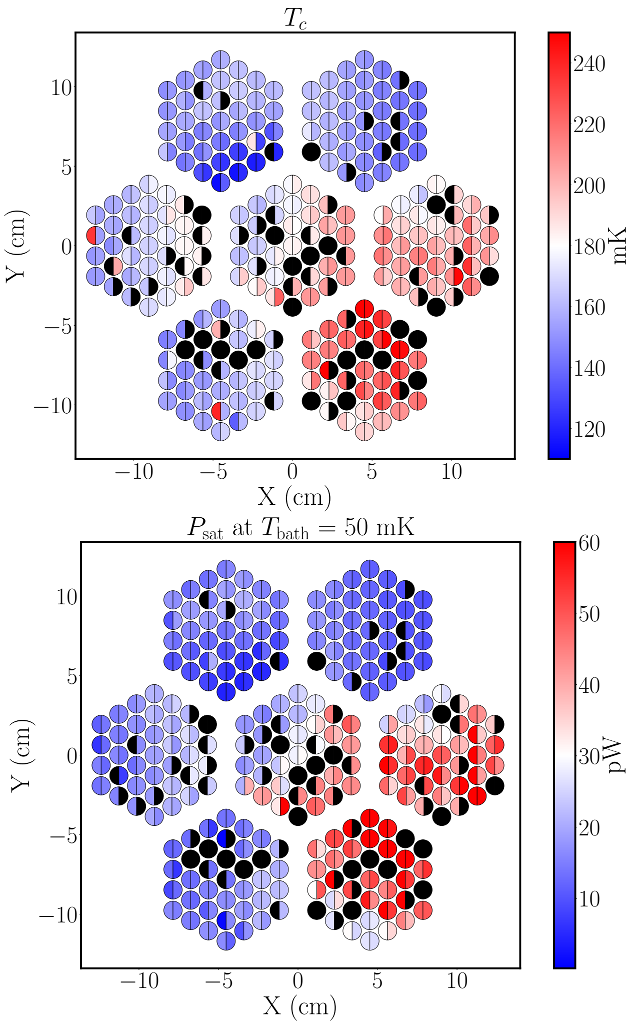

Figure 4.6: The distribution of T_c (top) and P_sat at T_bath = 50 mK (bottom) values for all the optically-sensitive detectors in the first W-band focal plane. The X and Y axes represent the focal plane position compared to the detector at the center. The left and right sides of each circle show the H and V detectors respectively which are sensitive to separate orthogonal linear polarizations. The black spots show the detectors that did not yield expected *I*-*V* response for analysis. These plots show the status of the first W-band detector array before deployment. The modular design of the focal plane makes it is possible to improve the TES uniformity across the focal plane by swapping modules to choose the best module combination possible among the assembled modules before deployment.

those values cannot be targeted too low; otherwise, the P_{sat} will be below the optical loading on the detectors (Section 3.3). The target parameter values optimized for the CLASS W-band detectors are listed in Table 4.1. The table also includes the measured average parameter values for all the optically-sensitive CLASS detectors in the first W-band focal plane. The thermal conductance (G) at the transition temperature, listed in the table, is related to T_{c} and κ through:

$$G = \left.\frac{\mathrm{d}P_{\mathrm{sat}}}{\mathrm{d}T}\right|_{T_{\mathrm{c}}} = 4\kappa T_{\mathrm{c}}^3 \tag{4.2}$$

where we replaced P_{sat} from Equation 4.1 to obtain the final expression for G.

Table 4.1: First W-band detector array average measured and target parameters

	Measured	**Target**
T_{bath}	35 mK	
T_{c}	175 mK	150 mK
κ	24.5 nW/K^4	25 nW/K^4
G @ T_{c}	548 pW/K	340 pW/K
P_{sat} @ 50 mK	25 pW	13 pW
$f_{3\mathrm{dB}}$	27 Hz	30 Hz
C	4 pJ/K	3 pJ/K
Yield	82%	

Table 4.1 shows the total array yield of 82%, which was calculated by counting the number of detectors that show good I-V response and fit Equation 4.1 well. The remaining 18% of the detectors are shown by the black spots in Figure 4.6. In addition to the parameters described so far, Table 4.1 also includes average $f_{3\mathrm{dB}}$ and C values calculated using the effective detector time

constant (τ_{eff}) measured from the response lag to a small square-wave excitation added to the detector bias voltage (Niemack, 2008). C is the TES heat capacity, and $f_{3\text{dB}}$ is the frequency range where the power drops by less than half: $f_{3\text{dB}} = 1/(2\pi\tau_{\text{eff}})$, and $\tau = C/G$. We calculate τ by multiplying τ_{eff} with the electro-thermal speed-up factor estimated from I-V curves. In the field, we use the VPM synchronous signal to get the actual optical time constant. This method is described in detail in Appel et al. (2019), and we calculate the optical time constants for all the CLASS frequency bands in Chapter 6. We estimated these values in lab to ensure that they are close to our target.

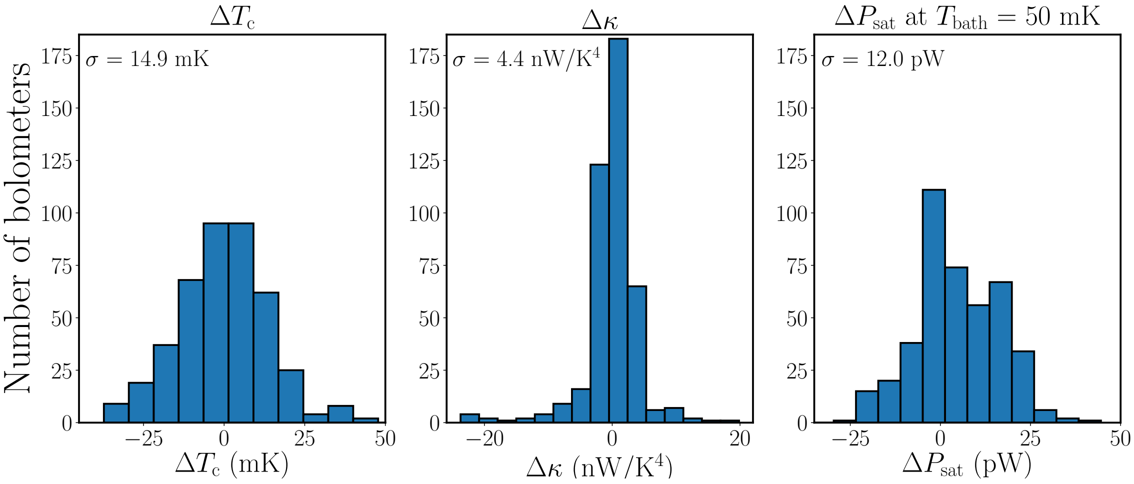

Figure 4.7: Histograms of ΔT_c, $\Delta\kappa$, and ΔP_{sat} for 426 optically-sensitive detectors on the first W-band focal plane. These values were calculated by taking the difference of the individual detector parameter values with the average within their modules. Since each module has a separate detector bias line and all the detectors within a module share the same bias line, uniformity across the Δ values reflects the optimal detector biasing condition. P_{sat} values were calculated at $T_{\text{bath}} = 50$ mK. The σ values on the upper left corner inside each box are the standard deviations for each distribution.

From Figure 4.6, we can see that there are noticeable T_c and P_{sat} gradients in the detectors across the focal plane. However, although uniformity of individual detector parameters across the entire focal plane is desirable, it is critical that the detector parameters across individual wafers are uniform. This is because each W-band module has one detector bias line and all the detectors within a module have to be biased using one bias voltage. Figure 4.7 shows the distribution of individual detector parameters as compared to the mean within their modules. The distribution includes values from 426 out of 518 optically-sensitive detectors in the focal plane (i.e. array yield of 82%) with good I-V curves as described before. As shown in Figure 4.7, the variance in the thermal conductance parameter κ across a wafer is very small ($\pm$ 18%) which is a result of the ballistic thermal transport in each detector. The spread in $P_{\rm sat}$ ($\pm$ 47%) is largely determined by the spread in $T_{\rm c}$ ($\pm$ 9%). All the parameter distributions reported in this section show the status of the first W-band detector array before deployment. In the future, we can improve TES uniformity across the focal plane by swapping modules in the current focal plane with the new ones with better uniformity. Moreover, we can also change the readout PCB to bias one column per bias line (like the G-band PCB described in Chapter 5) instead of four, so that we can fine-tune the TES biasing parameters per column.

4.3.2 Optical Passband

As described in Section 2.4.3.1, CLASS uses a combination of absorptive, reflective, and scattering filters inside the cryostat receiver to reject infrared radiation and reduce out-of-band thermal loading on the detectors. All these filters are tested and characterized in the lab for their out-of-band and in-band performance before being used in the field. However, the precise millimeter passband for CLASS detectors is defined through on-chip filtering (Chuss et al., 2016; Denis et al., 2009). As shown in Figure 4.4, after the OMT couples the optical signal to the microstrip circuits, a series of thermal-blocking and band-defining filters are used to both reject out-of-band radiation and precisely define the bandwidth. Therefore, it is crucial to test the passband of the detectors to check that the band edges are on target and there is no optical power coupled at higher frequencies.

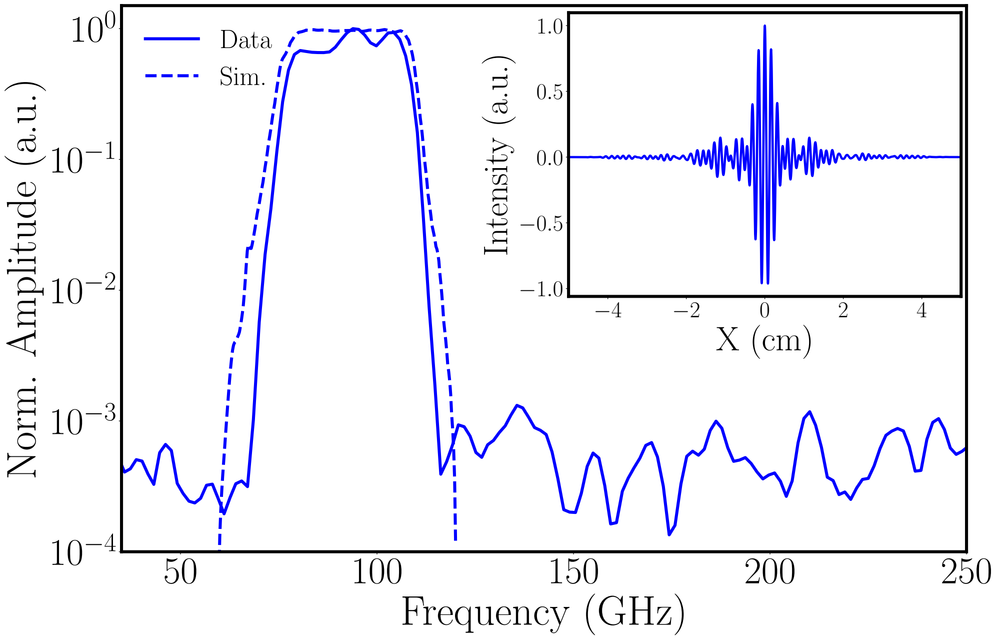

Figure 4.8: The main plot shows the simulated and the measured passbands of the W-band detectors measured using a Fourier Transform Spectrometer. The half-power points on the two band edges for this measurement are at 78 and 108 GHz, and the out-of-band response is less than -30 dB. This measured passband is in good agreement with the simulation, and we see no evidence of optical power coupled at higher frequencies. The inset shows the apodized interferogram used to obtain the passband through a fast Fourier transform. The interferogram is a result of co-adding noise-weighted FTS signals from 21 detectors in one of the modules in the focal plane. The x-axis of the interferogram represents the position (centered at the white-light point) of the FTS movable mirror on a linear stage. The y-axes for both plots have been normalized to arbitrary units (a.u.).

We use a Martin-Puplett (Martin and Puplett, 1970) Fourier Transform Spectrometer (FTS) in the lab (Wei, 2012) to measure the passband of CLASS W-band detectors. In order to not saturate the detectors with the FTS thermal source, the receiver was covered with a metal plate with a 5 cm diameter aperture in the center. In addition, anti-reflection coated Teflon and Nylon filters were placed at the 60 K and 4 K stages of the cryostat, respectively. As the FTS movable mirror scans back and forth from 0 to 150 mm at 0.5 mm/s on a linear stage, the detectors measure the output radiation intensity. We chopped the FTS wide-band thermal source at 20 Hz to modulate the FTS signal. The inset in Figure 4.8 shows an apodized interferogram obtained from detectors in one of the modules in the W-band focal plane. This interferogram is the result of co-adding noise-weighted FTS signals from 21 detectors in the module. The real component of the Fourier transform of the interferogram yields the passband shown in the main plot. The half-power points on the two band edges for this measurement are at 78 and 108 GHz, and the out-of-band response is less than -30 dB. This measured W-band detector passband is in good agreement with the simulation as seen in Figure 4.8, and we see no evidence of optical power coupled at higher frequencies.

4.3.3 Noise Performance

CLASS detectors are designed to be background limited (Section 3.2); therefore, the only way to achieve higher instrument sensitivity is by increasing the number of detectors. The detector dark noise (Section 3.3.3), which is measured with the cryostat closed so as to minimize noise from background

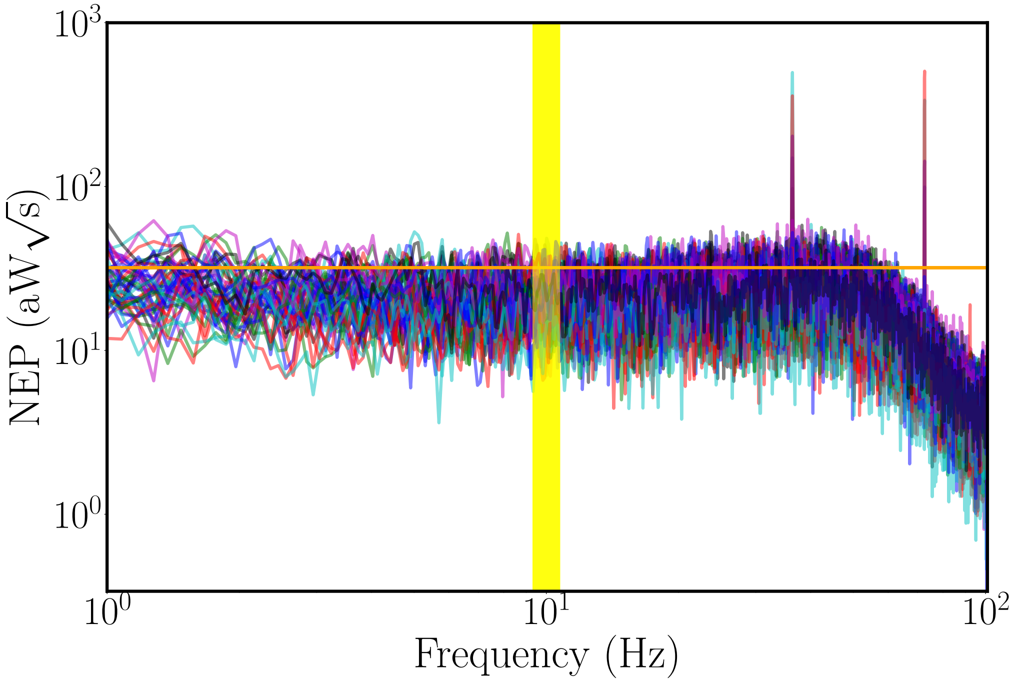

Figure 4.9: Noise spectra of 48 science-grade detectors in one of the modules in the W-band focal plane. The CLASS signal band is shown by the vertical yellow patch centered at the VPM modulation frequency of 10 Hz. The horizontal orange line indicates an estimated photon NEP in the field of 32 $\mathrm{aW}\sqrt{\mathrm{s}}$. The total NEP for CLASS detectors is dominated by photon noise.

radiation, is expected to be sub-dominant compared to the photon noise from the background in the field. To characterize the detector dark NEP, we took noise spectra of individual modules by capping off all the cold stages of the cryostat receiver with metal plates. Figure 4.9 shows the noise spectra of one of the modules in the W-band focal plane. The plot includes spectra from 48 science-grade detectors in the module. The vertical yellow band indicates the science band centered on the VPM modulation frequency of 10 Hz. This modulation was designed to put our signal band away from the $1/f$ noise at low frequency, which comes from a combination of instrumental and atmospheric drifts. The roll-off observed at ~ 60 Hz is due to the MCE digital Butterworth filter (Section 3.4.3) applied to the readout to suppress noise aliasing from higher frequencies. The horizontal orange line indicates an estimated photon NEP in the field of 32 $\mathrm{aW}\sqrt{\mathrm{s}}$ (Essinger-Hileman et al., 2014). The photon noise comes from a combination of the CMB and emission from the telescope and atmosphere. The total NEP, which is a sum of the detector dark NEP and the photon NEP added in quadrature, for CLASS detectors is dominated by the photon NEP as shown in Figure 4.9. At around 10 Hz, the mean detector dark NEP of all the 48 detectors shown in the spectra is 21 $\mathrm{aW}\sqrt{\mathrm{s}}$. Therefore, we expect the total NEP of the W-band detectors to be 38 $\mathrm{aW}\sqrt{\mathrm{s}}$. Through on-sky CMB data, we measured the average NEP to be 35 $\mathrm{aW}\sqrt{\mathrm{s}}$ (described in Chapter 6), very close to our expectations from lab measurements.

4.3.4 Sensitivity Projections

Based on the detector parameters obtained from lab measurements, we can estimate the sensitivity for the first W-band focal plane. For this calculation, we use the mean total NEP per detector of 38 $\mathrm{aW}\sqrt{\mathrm{s}}$. 426 detectors on the focal plane showed good I-V response. However, due to the spread in T_c and P_sat and having only one detector bias line per module, we will not be able to bias all the working detectors in the field simultaneously. We take a conservative estimate that we can only bias 90% of those detectors, i.e. 383 detectors (array efficiency of $\sim 74\%$). This puts the total array NEP for the first CLASS W-band focal plane at 2.1 $\mathrm{aW}\sqrt{\mathrm{s}}$.

For the 77–108 GHz CLASS measured passband, the conversion factor from sky power to CMB temperature ($\mathrm{d}P/\mathrm{d}T_\mathrm{CMB}$) is 0.34 pWK^{-1}. Using a preliminary detector efficiency estimate of 70% and the remaining telescope optics efficiency of $\sim$ 62% (Essinger-Hileman et al., 2014), the total array noise-equivalent CMB temperature ($\mathrm{NET_{CMB}}$) can be calculated as:

$$\mathrm{NET_{CMB}} == \frac{\mathrm{NEP_{array}}}{\epsilon_{\mathrm{total}}}\frac{\mathrm{d}T_{\mathrm{CMB}}}{\mathrm{d}P} = 14\ \mu\mathrm{K}\sqrt{\mathrm{s}}\,, \tag{4.3}$$

where $\epsilon_{\mathrm{total}}$ = detector efficiency × telescope optics efficiency. Assuming VPM modulation efficiency of 70% to measure the Stokes parameter Q, this array NET translates to noise-equivalent Q (NEQ) of 20 $\mu\mathrm{K}\sqrt{\mathrm{s}}$. The measured array average NET from the on-sky CMB data is 19 $\mu\mathrm{K}\sqrt{\mathrm{s}}$ (which leads to NEQ $\sim$ 27 $\mu\mathrm{K}\sqrt{\mathrm{s}}$). This discrepancy between the expected and the measured values is discussed in Chapter 6.

To summarize this chapter, the first CLASS 90 GHz detector array that is optimized for CMB observation near the minimum of polarized Galactic emission has been operational at the CLASS site since May 2018. The 90 GHz focal plane consists of seven individual modules with 37 feedhorns placed on a CE7 baseplate with cylindrical waveguide holes machined in them. Each module contains 37 dual-polarization-sensitive detectors fabricated on a single monocrystalline silicon wafer. Before being fielded, all the modules on the first W-band focal plane were extensively tested and characterized for their parameter uniformity and noise performance. The measured T_c, κ, and P_{sat} values are within margins targeted for the W-band instrument. The in-lab FTS measurement shows that the detector passband is in good agreement with the simulation, and we see no evidence of optical power coupling at higher frequencies. We measure the mean detector dark NEP for science-grade detectors in a module to be 21 aW$\sqrt{\mathrm{s}}$, and estimate the total array NEP of the focal plane to be 2.1 aW$\sqrt{\mathrm{s}}$. Using the detector parameters obtained from the lab measurements, we estimate the total array NET to be 14 μK$\sqrt{\mathrm{s}}$, which translates to total array NEQ of 20 μK$\sqrt{\mathrm{s}}$, assuming 70% VPM modulation efficiency. The on-sky performance of this detector array is presented in Chapter 6. The detectors for the second W-band array, which are similar to the ones presented here, are being fabricated at NASA Goddard Space Flight Center at the time of this writing.

References

Ali, Aamir M. (2017). “Detectors and Focal Planes for the Cosmology Large Angular Scale Surveyor”. PhD thesis. The Johns Hopkins University.

Ali, Aamir M., Thomas Essinger-Hileman, Tobias Marriage, John W. Appel, Charles L. Bennett, Matthew Berkeley, Berhanu Bulcha, Sumit Dahal, Kevin L. Denis, Karwan Rostem, Kongpop U-Yen, Edward J. Wollack, and Lingzhen Zeng (2018). “SiAl alloy feedhorn arrays: material properties, feedhorn design, and astrophysical applications”. In: Proc. SPIE. Vol. 10708. Society of Photo-Optical Instrumentation Engineers (SPIE) Conference Series, 107082P. DOI: `10.1117/12.2312817`. arXiv: `1807.03398 [astro-ph.IM]`.

Appel, John W., Aamir Ali, Mandana Amiri, Derek Araujo, Charles L. Bennet, Fletcher Boone, Manwei Chan, Hsiao-Mei Cho, David T. Chuss, Felipe Colazo, Erik Crowe, Kevin Denis, Rolando Dünner, Joseph Eimer, Thomas Essinger-Hileman, Dominik Gothe, Mark Halpern, Kathleen Harrington, Gene Hilton, Gary F. Hinshaw, Caroline Huang, Kent Irwin, Glenn Jones, John Karakula, Alan J. Kogut, David Larson, Michele Limon, Lindsay Lowry, Tobias Marriage, Nicholas Mehrle, Amber D. Miller, Nathan Miller, Samuel H. Moseley, Giles Novak, Carl Reintsema, Karwan Rostem, Thomas Stevenson, Deborah Towner, Kongpop U-Yen, Emily Wagner, Duncan Watts, Edward Wollack, Zhilei Xu, and Lingzhen Zeng (2014). “The cosmology large angular scale surveyor (CLASS): 38-GHz detector array of bolometric polarimeters”. In: *Proceedings of the SPIE, Volume 9153, id. 91531J 15 pp. (2014).* Vol. 9153. DOI: `10.1117/12.2056530`.

Appel, John W., Zhilei Xu, Ivan L. Padilla, Kathleen Harrington, Bastián Pradenas Marquez, Aamir Ali, Charles L. Bennett, Michael K. Brewer, Ricardo Bustos, Manwei Chan, David T. Chuss, Joseph Cleary, Jullianna Couto, Sumit Dahal, Kevin Denis, Rolando Dünner, Joseph R. Eimer, Thomas Essinger-Hileman, Pedro Fluxa, Dominik Gothe, Gene C. Hilton, Johannes Hubmayr, Jeffrey Iuliano, John Karakla, Tobias A. Marriage, Nathan J.

Miller, Carolina Núñez, Lucas Parker, Matthew Petroff, Carl D. Reintsema, Karwan Rostem, Robert W. Stevens, Deniz Augusto Nunes Valle, Bingjie Wang, Duncan J. Watts, Edward J. Wollack, and Lingzhen Zeng (2019). "On-sky Performance of the CLASS Q-band Telescope". In: ApJ 876.2, 126, p. 126. DOI: `10.3847/1538-4357/ab1652`. arXiv: `1811.08287 [astro-ph.IM]`.

Chuss, D. T., A. Ali, M. Amiri, J. Appel, C. L. Bennett, F. Colazo, K. L. Denis, R. Dünner, T. Essinger-Hileman, J. Eimer, P. Fluxa, D. Gothe, M. Halpern, K. Harrington, G. Hilton, G. Hinshaw, J. Hubmayr, J. Iuliano, T. A. Marriage, N. Miller, S. H. Moseley, G. Mumby, M. Petroff, C. Reintsema, K. Rostem, K. U-Yen, D. Watts, E. Wagner, E. J. Wollack, Z. Xu, and L. Zeng (2016). "Cosmology Large Angular Scale Surveyor (CLASS) Focal Plane Development". In: *Journal of Low Temperature Physics* 184, pp. 759–764. DOI: `10.1007/s10909-015-1368-9`. arXiv: `1511.04414 [astro-ph.IM]`.

Dahal, Sumit, Aamir Ali, John W. Appel, Thomas Essinger-Hileman, Charles Bennett, Michael Brewer, Ricardo Bustos, Manwei Chan, David T. Chuss, Joseph Cleary, Felipe Colazo, Jullianna Couto, Kevin Denis, Rolando Dünner, Joseph Eimer, Trevor Engelhoven, Pedro Fluxa, Mark Halpern, Kathleen Harrington, Kyle Helson, Gene Hilton, Gary Hinshaw, Johannes Hubmayr, Jeffery Iuliano, John Karakla, Tobias Marriage, Jeffrey McMahon, Nathan Miller, Carolina Nuñez, Ivan Padilla, Gonzalo Palma, Lucas Parker, Matthew Petroff, Bastian Pradenas, Rodrigo Reeves, Carl Reintsema, Karwan Rostem, Marco Sagliocca, Kongpop U-Yen, Deniz Valle, Bingjie Wang, Qinan Wang, Duncan Watts, Janet Weiland, Edward Wollack, Zhilei Xu, Ziang Yan, and Lingzhen Zeng (2018). "Design and characterization of the Cosmology Large Angular Scale Surveyor (CLASS) 93 GHz focal plane". In: Proc. SPIE. Vol. 10708. Society of Photo-Optical Instrumentation Engineers (SPIE) Conference Series, 107081Y. DOI: `10.1117/12.2311812`. arXiv: `1807.03927 [astro-ph.IM]`.

Denis, K. L., N. T. Cao, D. T. Chuss, J. Eimer, J. R. Hinderks, W.-T. Hsieh, S. H. Moseley, T. R. Stevenson, D. J. Talley, K. U.-yen, and E. J. Wollack (2009). "Fabrication of an Antenna-Coupled Bolometer for Cosmic Microwave Background Polarimetry". In: *American Institute of Physics Conference Series*. Ed. by B. Young, B. Cabrera, and A. Miller. Vol. 1185. American Institute of Physics Conference Series, pp. 371–374. DOI: `10.1063/1.3292355`.

Essinger-Hileman, Thomas, Aamir Ali, Mandana Amiri, John W. Appel, Derek Araujo, Charles L. Bennett, Fletcher Boone, Manwei Chan, Hsiao-Mei Cho, David T. Chuss, Felipe Colazo, Erik Crowe, Kevin Denis, Rolando Dünner, Joseph Eimer, Dominik Gothe, Mark Halpern, Kathleen Harrington, Gene

C. Hilton, Gary F. Hinshaw, Caroline Huang, Kent Irwin, Glenn Jones, John Karakla, Alan J. Kogut, David Larson, Michele Limon, Lindsay Lowry, Tobias Marriage, Nicholas Mehrle, Amber D. Miller, Nathan Miller, Samuel H. Moseley, Giles Novak, Carl Reintsema, Karwan Rostem, Thomas Stevenson, Deborah Towner, Kongpop U-Yen, Emily Wagner, Duncan Watts, Edward J. Wollack, Zhilei Xu, and Lingzhen Zeng (2014). "CLASS: the cosmology large angular scale surveyor". In: *Proceedings of the SPIE, Volume 9153, id. 91531I 23 pp. (2014).* Vol. 9153. DOI: 10.1117/12.2056701.

Iuliano, J., J. Eimer, L. Parker, A. Ali, J. W. Appel, C. Bennett, M. Brewer, R. Bustos, D. Chuss, J. Cleary, J. Couto, S. Dahal, K. Denis, R. Dünner, T. Essinger-Hileman, P. Fluxa, M. Halpern, K. Harrington, K. Helson, G. Hilton, G. Hinshaw, J. Hubmayr, J. Karakla, T. Marriage, N. Miller, J. J. McMahon, C. Nuñez, I. Padilla, G. Palma, M. Petroff, B. P. Márquez, R. Reeves, C. Reintsema, K. Rostem, D. A. N. Valle, T. Van Engelhoven, B. Wang, Q. Wang, D. Watts, J. Weiland, E. J. Wollack, Z. Xu, Z. Yan, and L. Zeng (2018). "The Cosmology Large Angular Scale Surveyor Receiver Design". In: *Millimeter, Submillimeter, and Far-Infrared Detectors and Instrumentation for Astronomy IX*. Vol. 10708. Proc. SPIE.

Martin, D. H. and E. Puplett (1970). "Polarised interferometric spectrometry for the millimeter and submillimeter spectrum." In: *Infrared Physics* 10, pp. 105–109. DOI: 10.1016/0020-0891(70)90006-0.

Niemack, Michael D. (2008). "Towards dark energy: Design, development, and preliminary data from ACT". PhD thesis. Princeton University.

Rostem, K., D. T. Chuss, F. A. Colazo, E. J. Crowe, K. L. Denis, N. P. Lourie, S. H. Moseley, T. R. Stevenson, and E. J. Wollack (2014a). "Precision control of thermal transport in cryogenic single-crystal silicon devices". In: *Journal of Applied Physics* 115.12, 124508, p. 124508. DOI: 10.1063/1.4869737. arXiv: 1403.1326 [astro-ph.IM].

Rostem, K., A. Ali, J. W. Appel, C. L. Bennett, D. T. Chuss, F. A. Colazo, E. Crowe, K. L. Denis, T. Essinger-Hileman, T. A. Marriage, S. H. Moseley, T. R. Stevenson, D. W. Towner, K. U-Yen, and E. J. Wollack (2014b). "Scalable background-limited polarization-sensitive detectors for mm-wave applications". In: *Millimeter, Submillimeter, and Far-Infrared Detectors and Instrumentation for Astronomy VII*. Vol. 9153. Proc. SPIE, 91530B. DOI: 10.1117/12.2057266. arXiv: 1408.4790 [astro-ph.IM].

Rostem, Karwan, Aamir Ali, John W. Appel, Charles L. Bennett, Ari Brown, Meng-Ping Chang, David T. Chuss, Felipe A. Colazo, Nick Costen, Kevin L. Denis, Tom Essinger-Hileman, Ron Hu, Tobias A. Marriage, Samuel H.

Moseley, Thomas R. Stevenson, Kongpop U-Yen, Edward J. Wollack, and Zhilei Xu (2016). “Silicon-based antenna-coupled polarization-sensitive millimeter-wave bolometer arrays for cosmic microwave background instruments”. In: *Proceedings of the SPIE, Volume 9914, id. 99140D 10 pp. (2016).* Vol. 9914. DOI: `10.1117/12.2234308`.

Wei, Tiffany (2012). “The Design, Construction, and Testing of a Wide-Band Fourier Transform Interferometer”. Undergraduate Thesis. The Johns Hopkins University.

Zeng, Lingzhen (2012). “Polarimetry in astrophysics and cosmology”. PhD thesis. The Johns Hopkins University.

Chapter 5

Dichroic 150/220 GHz Detector Array

The CLASS high-frequency (HF) dichroic detector array was delivered to the CLASS site in June 2019. In concert with existing 40 and 90 GHz telescopes, this 150/220 GHz instrument observes the CMB over large angular scales aimed at measuring the primordial B-mode signal, the optical depth to reionization, and other fundamental physics and cosmology as described in Chapter 2. Specifically, this HF array provides additional sensitivity to CLASS's CMB observations and helps to characterize the dust foreground. The 150/220 GHz focal plane detector array consists of three detector modules, seen in Figure 5.1, with 255 dichroic dual-polarization pixels in total. Each pixel has four TES bolometers to measure the two linear polarization states at 150 and 220 GHz frequency bands. In this chapter, we discuss the design, assembly, and in-lab characterization of the CLASS HF detector array. This chapter is an extended version of Dahal et al. (2020).

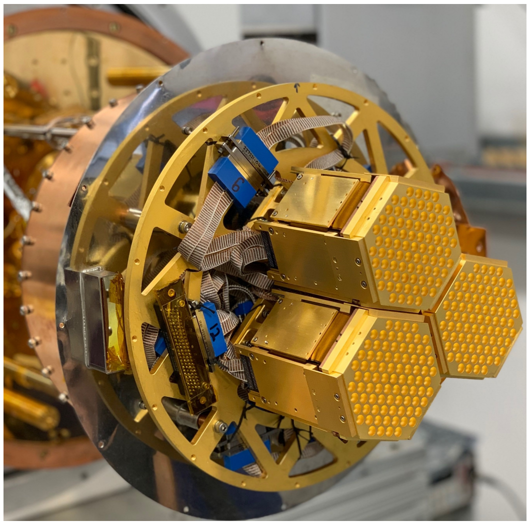

Figure 5.1: The HF detector array at the CLASS telescope site in Chile during the receiver assembly. The array consists of three identical hexagonal modules mounted onto the mixing chamber plate of a pulse-tube cooled dilution refrigerator using a Au-coated copper web interface seen here. There are 1020 polarization-sensitive TES bolometers on the focal plane split equally between 150 and 220 GHz frequency bands. The focal plane assembly procedure is described in detail in Appendix A.

5.1 Detector Design

The CLASS HF detectors are fabricated on 100 mm silicon wafers each consisting of 85 dichroic polarization-sensitive pixels as shown in Figure 5.2. The beam is defined by a smooth-walled CE7 feedhorn, which couples light onto an OMT. As described in Section 3.1.2, the OMT separates two orthogonal states of linear polarization and couples them to microstrip transmission lines. The signals from opposite OMT probes are combined onto a single microstrip line using the difference output of a magic-tee (U-Yen et al., 2008). Unlike the Q- and W-band detectors, the HF detectors contain a diplexer that splits each polarization signal into high and low frequency components, followed by on-chip filters that define the two separate frequency bands. The signal continues on the microstrip line to the TES membrane through a stubby beam and is terminated at a PdAu resistor. As for the case in the 90 GHz detectors, the stubby beam precisely controls the thermal conductance of the TES island with ballistic-dominated phonon transport (Rostem et al., 2014). Also similar to the 90 GHz detector design, the long and meandered legs that support the TES bias leads have rough side walls and contribute very little to the thermal conductance. The bias line filters seen in Figure 5.2 prevent the coupling of microwave radiation to the bias leads, improving the efficiency of the detectors. The Pd deposited on the TES island (see Figure 5.2) is used to define the detector time constant through the electronic heat capacity of Pd.

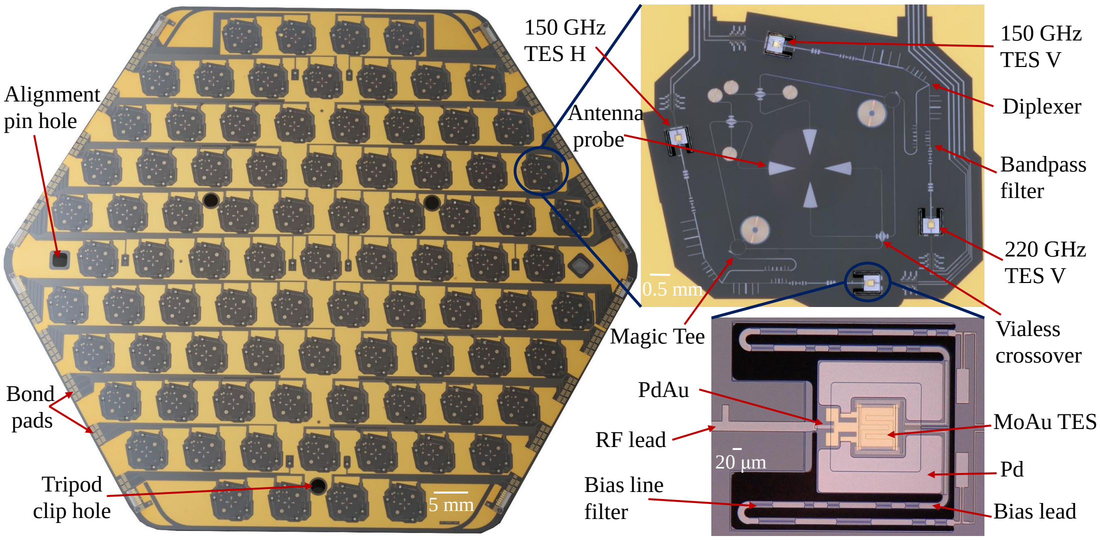
Alignment pin hole
Bond pads
Tripod clip hole
5 mm
150 GHz TES H
Antenna probe
0.5 mm
Magic Tee
PdAu
RF lead
20 µm
Bias line filter
150 GHz TES V
Diplexer
Bandpass filter
220 GHz TES V
Vialess crossover
MoAu TES
Pd
Bias lead

Figure 5.2: (Left) CLASS HF detector wafer with 85 dichroic dual-polarization pixels fabricated on a monocrystalline silicon layer. Detector readout signals are routed to the bond pads located near four edges of the wafer. (Right) Zoomed-in image of a single detector pixel (top) and a TES island (bottom). The optical signal on the microstrip transmission lines coming from the OMTs is separated into two bands by a diplexer plus on-chip filters and terminated on the TES bolometers. For a single frequency band, the detector architecture is similar to the CLASS 90 GHz design presented in Chapter 4.

Similar to the 40 and the 90 GHz detector architectures described in Section 3.1, the HF detector chip consists of three separate elements hybridized together: a photonic choke wafer, a detector wafer, and a backshort assembly. The photonic choke (Wollack, U-yen, and Chuss, 2010) acts as a waveguide interface between the CE7 feedhorn array and the detectors. The backshort assembly (Crowe et al., 2013), among its many functions (Rostem et al., 2016), forms a quarter-wavelength short for the OMT antenna probes. The middle detector wafer contains the detectors fabricated on single-crystal silicon that has excellent microwave and thermal properties as described in Section 3.1. The hybridized wafer package is mounted to the CE7 feedhorn array as a single assembly.

5.2 Module Design and Assembly

As shown in Figure 5.1, the HF focal plane consists of three identical modules mounted on a mixing chamber plate maintained at a stable bath temperature of $\sim$ 80 mK by a pulse-tube cooled dilution refrigerator (Section 2.4.3). Each module consists of 85 smooth-walled feedhorns made from a Au-plated CE7 alloy (Ali et al., 2018). Unlike the 90 GHz design (Section 4.1) where only the feedhorn baseplate is made from CE7, the entire HF feedhorn array is made from CE7, as shown in Figure 5.3, to ease the assembly process and reduce the manufacturing cost as compared to individual feedhorns. Figure 5.3 also shows the feedhorn profile and the co-polar E-plane, H-plane, and the cross-polar feedhorn response models. Across both the 150 and 220 GHz frequency bands, the cross-polar response is less than -20 dB.

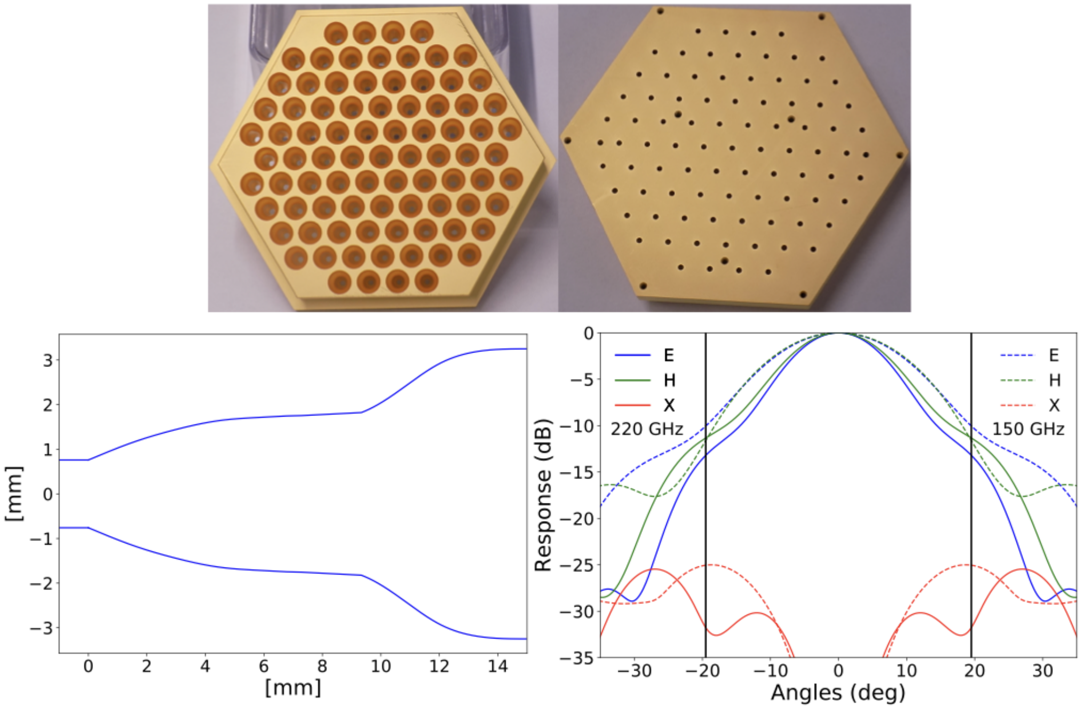

Figure 5.3: (Top) The front and back images of one of the HF feedhorn arrays made of Au-plated CE7. (Bottom-Left) The HF feedhorn profile that has approximately 15 mm length, 1.5 mm input waveguide diameter, and 6.5 mm horn diameter. The feedhorn has an input waveguide cutoff of 2.59 mm, i.e., 115.67 GHz. (Bottom-Right) The co-polar E-plane, H-plane, and cross-polar feedhorn response models. The responses shown for the 150 and the 220 GHz frequencies have been averaged across 132–162 GHz and 202–238 GHz passbands, respectively. The cross polarization response across both bands is less than -20 dB. The two vertical lines at ±19.5° show where the beams truncate at the receiver cold stop. The edge illumination at 19.5° is $\approx$ -11 dB for the 150 GHz frequency band and $\approx$ -12 dB for the 220 GHz band.

The detector wafer assembly is mounted and aligned onto the feedhorn array using the tripod clips, alignment pins, and the side spring as shown in Figure 5.4. During assembly, four layers of flexible aluminum circuits are stacked on top of each wafer package and wire bonded to the detector bond pads on four sides of the wafer. The other end of the circuits are mounted onto four separate readout packages as shown in Figure 5.4. The module assembly procedure is described in detail in Appendix A.

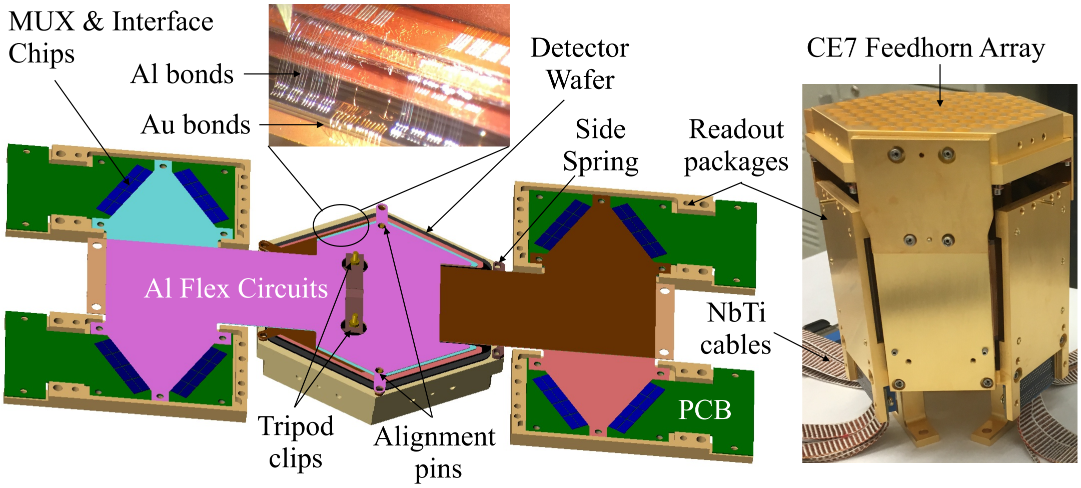
MUX & Interface Chips
Al bonds
Au bonds
Detector Wafer
CE7 Feedhorn Array
Side Spring
Readout packages
Al Flex Circuits
NbTi cables
PCB
Tripod clips
Alignment pins

Figure 5.4: (Left) Model of unfolded HF module during assembly. The detector wafer (black) is mounted on top of Au-plated CE7 feedhorn array using two BeCu tripod clips. Four layers of Al flex circuits with decreasing circumradius (starting from bottom: coral, brown, light blue, and pink) are stacked on top of the wafer and connected to separate readout packages. These packages contain MUX and interface chips (blue) mounted onto a PCB (green) sandwiched between two Nb sheets (not shown). The inset shows intricate layers of Al bonds from the wafer to different flex circuit layers (the topmost layer is not visible here). Au bonds heat sink the detector wafer to the feedhorn array. (Right) An assembled HF module. After assembly, all four readout packages are folded up and bolted to the CE7. Support structures are bolted to the bottom through a backplate. Refer to Appendix A for a detailed discussion on the assembly procedure.

Each readout package consists of eight MUX chips (Section 3.4.2) and eight interface chips mounted on a PCB, sandwiched between two Nb sheets for magnetic shielding. The interface chips have 200 μΩ shunt resistors and 310 nH Nyquist inductors. The inductance value was chosen to keep the readout noise aliased from higher frequencies below one percent of the noise level within the audio bandwidth of the TES. We also performed tests with and without this inductor to ensure that its addition does not affect the detector stability. Four MUX chips on each side of a readout package are combined into one readout column for multiplexing 44 rows i.e. a multiplexing factor, or number of detectors per readout channel, of 44:1. The 150 and 220 GHz detectors are mapped to separate readout packages, each with two columns, so that they can be biased separately, if needed.

Detector bias signals and MUX addressing, feedback, and output signals are routed via twisted pairs of NbTi superconducting cables (seen in Figure 5.4), soldered directly onto the PCB. In particular, this cabling connects the MUX output to a set of SQUID series array (SSA) amplifiers. The 4K SSA and the warm electronics are described in detail in Section 3.4. Figure 5.4 shows the layout of a module during and after assembly. After all the components are assembled and wire bonded, the readout packages are folded up and bolted to the feedhorn array on one side and attached to a backplate on the other. The backplate is finally bolted to the mixing chamber plate with the help of a web structure and posts as seen in Figure 5.1.

5.3 Detector Characterization

As with the 90 GHz detectors described in Chapter 4, the 150/220 GHz detectors were extensively tested and characterized for their TES electrothermal parameters, optical passband, and detector noise before deployment.

5.3.1 Electrothermal Parameters

As described in Section 4.3, we characterize the electrothermal properties of the detectors by capping off all the cold stages of the cryostat with metal plates so as to minimize optical loading. For the CLASS HF detectors, we measure the TES saturation power ($P_{\rm sat}$) at 80% TES normal resistance ($\rm R_N$) for multiple bath temperatures ($T_{\rm bath}$) from 70 to 250 mK through I-V curves. At each $T_{\rm bath}$, we ramp up the voltage bias to drive all the detectors normal, then sweep the bias down through the superconducting transition while recording the current response of the detectors. We fit the power law in Equation 4.1 to the $P_{\rm sat}$ vs $T_{\rm bath}$ data to obtain κ and $T_{\rm c}$ for each detector.

Figure 5.5 shows the distribution of $T_{\rm c}$, κ, and $P_{\rm sat}$ values for all the optically-sensitive bolometers in the HF detector array. The mean and the standard deviation values of these detector parameters calculated separately for the three HF modules are shown in Table 5.1. The $P_{\rm sat}$ values are calculated at $T_{\rm bath}$ = 50 mK. Table 5.1 also includes the yield values per module, which are the fractions (quoted in percentage) of detectors in each module that fit Equation 4.1 with median absolute deviation (MAD) $<$ 1 pW. Detectors with MAD $>$ 1 pW are not included in the mean and standard deviation calculations for Table 5.1 and are excluded from further analysis in this chapter.

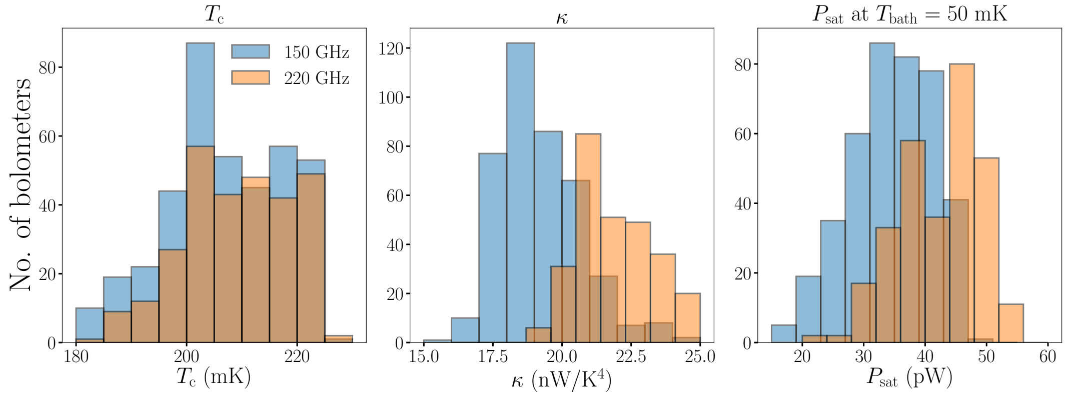

Figure 5.5: T_c, κ, and P_{sat} (at $T_{bath} = 50$ mK) distributions for the 408 (292) working 150 (220) GHz TES bolometers in the CLASS HF detector array. The mean and standard deviation of these parameters for individual HF modules are shown in Table 5.1.

The differences in P_{sat} values obtained with increasing vs decreasing bath temperatures were $\lesssim 0.2$ pW; therefore, measurement errors were ignored in the standard deviation values of Table 5.1. As seen in Table 5.1, the spreads of T_c (3 – 6%) and κ (4 – 10%) parameters across all three modules for both frequencies are small. This results from uniform and controlled fabrication processes, and ballistic thermal transport to the bath in all the TESs. The spread in P_{sat} (8 – 20%) is mostly explained by the spread in T_c. The uniformity of the detector parameters across the array and the observed in-lab detector stability over a wide range of bias voltages will allow the array to be optimally biased during sky observations. At the time of writing, the MCE (Section 3.4.3) firmware supports multiplexing over a maximum of 41 rows. Through a firmware upgrade, we could get all 44 rows working, which will increase the 150 GHz array yield to $\sim$ 86% and 220 GHz to $\sim$ 61%. Most of the remaining detectors are not operational due to complications in the bonding geometry. In particular, the lower yield in 220 GHz versus 150 GHz is due to wire bonding

Table 5.1: Mean and standard deviation of detector parameters, NEP_G (estimated from T_c and κ using Equation 3.18), and yield for the three CLASS HF modules

Module	ν **(GHz)**	T_c **(mK)**	κ **(nW/K^4)**	P_{sat} **(pW)**	NEP_G **(aW$\sqrt{\mathrm{s}}$)**	**Yield (%)**
1	150	214 ± 10	18 ± 1	39 ± 6	21 ± 2	81
	220	213 ± 10	22 ± 1	44 ± 6	23 ± 2	70
2	150	199 ± 7	20 ± 2	31 ± 4	18 ± 2	76
	220	200 ± 5	22 ± 2	36 ± 3	20 ± 1	41
3	150	204 ± 13	20 ± 1	34 ± 7	20 ± 3	82
	220	210 ± 10	23 ± 1	44 ± 6	23 ± 2	61
Total	150	206 ± 12	19 ± 2	35 ± 7	20 ± 3	80
	220	209 ± 10	22 ± 2	42 ± 7	22 ± 2	57

difficulty when trying to bond to the upper layers of the Al flex circuit stack shown in the inset of Figure 5.4.

5.3.2 Optical Passband

We use a polarizing FTS described in detail in Pan et al. (2019) to measure the passbands of the HF detectors in lab. While we use a different FTS (preferred for its compact size) to measure the HF passbands as compared to the 90 GHz measurements described in Section 4.3.2, the filter setup inside the cryostat is the same. Figure 5.6 shows the measured CLASS detector passbands compared to the simulation and the atmospheric transmission model at the CLASS site in the Atacama Desert with precipitable water vapor (PWV) of 1 mm. The raw measured passband values have been corrected for the feedhorn's frequency-dependent gain and the transmission through the cryostat filters used in the lab setup.

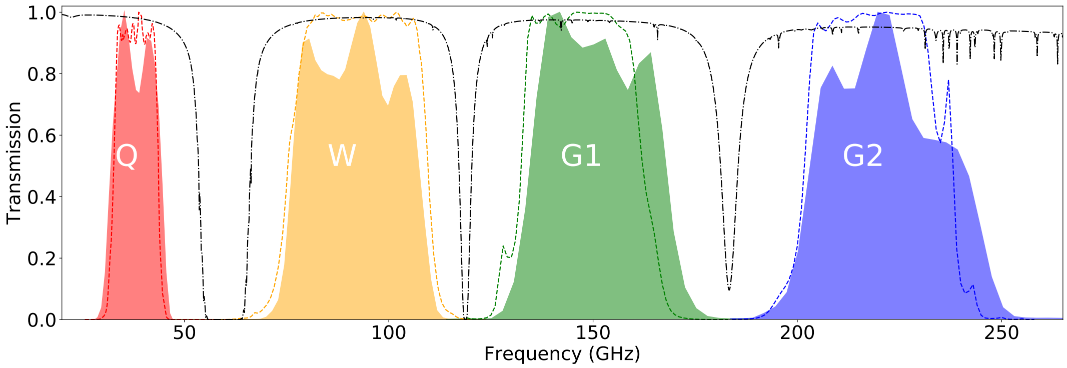

Figure 5.6: Measured passbands (filled) of CLASS detector arrays compared to simulation (dashed) and atmospheric transmission model (dash-dot) at the CLASS site with PWV of 1 mm. The atmospheric model is based on Pardo, Cernicharo, and Serabyn (2001). The passbands were measured in lab with a polarizing FTS and have been corrected for the feedhorn's frequency-dependent gain and the transmission through cryostat filters.

The measured CLASS passbands in Figure 5.6 have been averaged over all working detectors in the band. The CLASS Q and W passbands are added for completeness and are described further in Appel et al. (2019) and Chapter 4, respectively. The passbands safely avoid strong atmospheric emission lines, as designed. We also do not see any evidence of high frequency out-of-band leakage. The simulated passbands for the two HF bands are 132 – 162 GHz and 202 – 238 GHz as defined by their half-power points; whereas the respective measured bands are 134 – 168 GHz and 203 – 241 GHz. Compared to the simulation, the measured passbands for 150 and 220 GHz detectors are wider by 4 and 2 GHz, respectively, and both bands are shifted by a few GHz toward higher frequencies. After the HF detector array deployment, we investigated the source of these apparent frequency shifts in the bands, and found that the shifts are related to FTS systematics, which we discuss in Chapter 6.

5.3.3 Noise and Sensitivity

As with the 90 GHz detector array described in Section 4.3.3, we took noise spectra of the HF detectors "in the dark" (capping off all the cold stages of the cryostat with metal plates) and measured the detector dark noise-equivalent power ($\mathrm{NEP}_{\mathrm{dark}}$) shown in Figure 5.7. In the CLASS audio signal band centered at the VPM modulation frequency of 10 Hz, the mean and standard deviation of $\mathrm{NEP}_{\mathrm{dark}}$ is 22 ± 4 $\mathrm{aW}\sqrt{\mathrm{s}}$ and 25 ± 4 $\mathrm{aW}\sqrt{\mathrm{s}}$ for the 150 and the 220 GHz detectors, respectively.

As discussed in Section 3.3.3, TES phonon noise ($\mathrm{NEP}_{\mathrm{G}}$), Johnson noise, and SQUID readout noise contribute to the measured $\mathrm{NEP}_{\mathrm{dark}}$. The expected $\mathrm{NEP}_{\mathrm{G}}$ values calculated from the detector parameters are shown in Table 5.1. Using the parameters derived from the I-V curves, we estimate the detector Johnson noise to be ~ 1.5 $\mathrm{aW}\sqrt{\mathrm{s}}$ at the 10 Hz CLASS signal band. This noise component is highly suppressed through electro-thermal feedback at lower frequencies. Finally, we estimate the SQUID readout noise to be ~ 7 $\mathrm{aW}\sqrt{\mathrm{s}}$. We computed this by measuring the current noise of the dark SQUIDs, which is ~ 35 $\mathrm{pA}\sqrt{\mathrm{s}}$, and dividing this average SQUID current noise with an average detector responsivity of $\sim 5 \times 10^6$ V^{-1}. As highlighted in Figure 5.7, $\mathrm{NEP}_{\mathrm{G}}$ is the dominant noise source for $\mathrm{NEP}_{\mathrm{dark}}$ as the readout and the Johnson noise contribute only a few percent when added in quadrature.

As shown in Figure 5.7, the predicted photon NEP in the field for the 150 and the 220 GHz detectors are 44.4 and 62.3 $\mathrm{aW}\sqrt{\mathrm{s}}$, respectively (Essinger-Hileman et al., 2014). Given the measured $\mathrm{NEP}_{\mathrm{dark}}$ values, all the working detectors on the HF array are photon-noise limited. With the current array

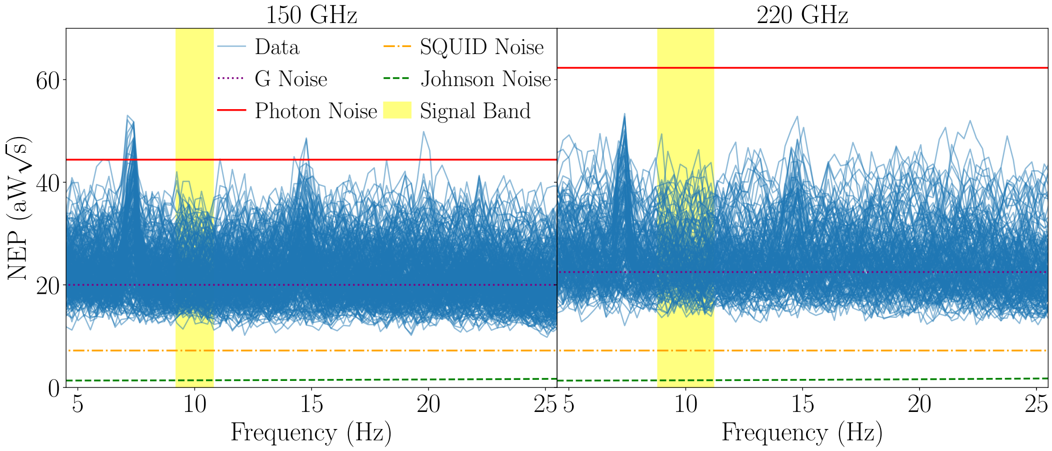

Figure 5.7: Noise spectra of CLASS HF detectors operated in the dark. The horizontal lines show the NEP_{dark} components and estimated photon noise. The vertical yellow patch shows the CLASS audio signal band centered at the VPM modulation frequency of 10 Hz. The measured average NEP of 22 aW$\sqrt{s}$ for 150 GHz and 25 aW$\sqrt{s}$ for 220 GHz match well with the expected G noise values (from Table 5.1) as the SQUID noise and the Johnson noise are negligible when added in quadrature. Given the noise spectra and estimated photon noise, all the working HF detectors are photon-noise limited.

yield, the total array NEP is 2.5 aW$\sqrt{s}$ for 150 GHz and 4 aW$\sqrt{s}$ for 220 GHz. Assuming nominal passband and 50% total optical efficiency, we estimate array NETs of 17 and 51 μK$\sqrt{s}$ for 150 and 220 GHz, respectively. Since the HF VPM is optimized for 150 GHz, we estimate the modulation efficiency to measure the Stokes parameter Q to be 70% for 150 GHz and 50% for 220 GHz. This leads to array noise-equivalent Q (NEQ) of 24 μK$\sqrt{s}$ for 150 GHz and 101 μK$\sqrt{s}$ for 220 GHz. In Chapter 6, we compare these estimates to the measured on-sky performance.

To summarize this chapter, the CLASS HF detector array was delivered to the CLASS site and installed inside the cryostat receiver in June 2019. This dichroic array sensitive to 150 and 220 GHz frequency bands will provide additional sensitivity to CLASS's CMB observations and help characterize the dust foreground. Before deployment, the HF detectors were extensively tested and characterized in the lab. The detectors within each HF module show uniform parameter distributions. FTS measurements performed in lab show that the detector passbands safely avoid strong atmospheric emission lines with no evidence for high frequency out-of-band leakage. The HF detectors are photon-noise limited with average $\mathrm{NEP_{dark}}$ of 22 $\mathrm{aW}\sqrt{\mathrm{s}}$ for 150 GHz and 25 $\mathrm{aW}\sqrt{\mathrm{s}}$ for 220 GHz. With current array yield and expectations for optical and VPM modulation efficiencies, we estimate the CLASS HF array NEQ of 24 $\mu\mathrm{K}\sqrt{\mathrm{s}}$ for 150 GHz and 101 $\mu\mathrm{K}\sqrt{\mathrm{s}}$ for 220 GHz. In Chapter 6, we will compare this in-lab estimate to the on-sky performance using the CMB observation data from the HF detector array.

References

Ali, Aamir M., Thomas Essinger-Hileman, Tobias Marriage, John W. Appel, Charles L. Bennett, Matthew Berkeley, Berhanu Bulcha, Sumit Dahal, Kevin L. Denis, Karwan Rostem, Kongpop U-Yen, Edward J. Wollack, and Lingzhen Zeng (2018). "SiAl alloy feedhorn arrays: material properties, feedhorn design, and astrophysical applications". In: Proc. SPIE. Vol. 10708. Society of Photo-Optical Instrumentation Engineers (SPIE) Conference Series, 107082P. DOI: `10.1117/12.2312817`. arXiv: `1807.03398 [astro-ph.IM]`.

Appel, John W., Zhilei Xu, Ivan L. Padilla, Kathleen Harrington, Bastián Pradenas Marquez, Aamir Ali, Charles L. Bennett, Michael K. Brewer, Ricardo Bustos, Manwei Chan, David T. Chuss, Joseph Cleary, Jullianna Couto, Sumit Dahal, Kevin Denis, Rolando Dünner, Joseph R. Eimer, Thomas Essinger-Hileman, Pedro Fluxa, Dominik Gothe, Gene C. Hilton, Johannes Hubmayr, Jeffrey Iuliano, John Karakla, Tobias A. Marriage, Nathan J. Miller, Carolina Núñez, Lucas Parker, Matthew Petroff, Carl D. Reintsema, Karwan Rostem, Robert W. Stevens, Deniz Augusto Nunes Valle, Bingjie Wang, Duncan J. Watts, Edward J. Wollack, and Lingzhen Zeng (2019). "Onsky Performance of the CLASS Q-band Telescope". In: ApJ 876.2, 126, p. 126. DOI: `10.3847/1538-4357/ab1652`. arXiv: `1811.08287 [astro-ph.IM]`.

Crowe, E. J., C. L. Bennett, D. T. Chuss, K. L. Denis, J. Eimer, N. Lourie, T. Marriage, S. H. Moseley, K. Rostem, T. R. Stevenson, D. Towner, K. U-yen, and E. J. Wollack (2013). "Fabrication of a Silicon Backshort Assembly for Waveguide-Coupled Superconducting Detectors". In: *IEEE Transactions on Applied Superconductivity* 23.3, pp. 2500505–2500505.

Dahal, S., M. Amiri, J. W. Appel, C. L. Bennett, L. Corbett, R. Datta, K. Denis, T. Essinger-Hileman, M. Halpern, K. Helson, G. Hilton, J. Hubmayr, B. Keller, T. Marriage, C. Nunez, M. Petroff, C. Reintsema, K. Rostem, K. U-Yen, and E. Wollack (2020). "The CLASS 150/220 GHz Polarimeter Array: Design, Assembly, and Characterization". In: *Journal of Low Temperature*

Physics 199.1-2, pp. 289–297. DOI: 10.1007/s10909-019-02317-0. arXiv: 1908.00480 [astro-ph.IM].

Essinger-Hileman, Thomas, Aamir Ali, Mandana Amiri, John W. Appel, Derek Araujo, Charles L. Bennett, Fletcher Boone, Manwei Chan, Hsiao-Mei Cho, David T. Chuss, Felipe Colazo, Erik Crowe, Kevin Denis, Rolando Dünner, Joseph Eimer, Dominik Gothe, Mark Halpern, Kathleen Harrington, Gene C. Hilton, Gary F. Hinshaw, Caroline Huang, Kent Irwin, Glenn Jones, John Karakla, Alan J. Kogut, David Larson, Michele Limon, Lindsay Lowry, Tobias Marriage, Nicholas Mehrle, Amber D. Miller, Nathan Miller, Samuel H. Moseley, Giles Novak, Carl Reintsema, Karwan Rostem, Thomas Stevenson, Deborah Towner, Kongpop U-Yen, Emily Wagner, Duncan Watts, Edward J. Wollack, Zhilei Xu, and Lingzhen Zeng (2014). "CLASS: the cosmology large angular scale surveyor". In: Proc. SPIE. Vol. 9153. Society of Photo-Optical Instrumentation Engineers (SPIE) Conference Series, p. 91531I. DOI: 10.1117/12.2056701.

Pan, Zhaodi, Mira Liu, Ritoban Basu Thakur, Bradford A. Benson, Dale J. Fixsen, Hazal Goksu, Eleanor Rath, and Stephan S. Meyer (2019). "Compact millimeter-wavelength Fourier-transform spectrometer". In: Appl. Opt. 58.23, p. 6257. DOI: 10.1364/AO.58.006257. arXiv: 1905.07399 [astro-ph.IM].

Pardo, J. R., J. Cernicharo, and E. Serabyn (2001). "Atmospheric transmission at microwaves (ATM): an improved model for millimeter/submillimeter applications". In: *IEEE Transactions on Antennas and Propagation* 49.12, pp. 1683–1694. DOI: 10.1109/8.982447.

Rostem, K., D. T. Chuss, F. A. Colazo, E. J. Crowe, K. L. Denis, N. P. Lourie, S. H. Moseley, T. R. Stevenson, and E. J. Wollack (2014). "Precision control of thermal transport in cryogenic single-crystal silicon devices". In: *Journal of Applied Physics* 115.12, 124508, p. 124508. DOI: 10.1063/1.4869737. arXiv: 1403.1326 [astro-ph.IM].

Rostem, Karwan, Aamir Ali, John W. Appel, Charles L. Bennett, Ari Brown, Meng-Ping Chang, David T. Chuss, Felipe A. Colazo, Nick Costen, Kevin L. Denis, Tom Essinger-Hileman, Ron Hu, Tobias A. Marriage, Samuel H. Moseley, Thomas R. Stevenson, Kongpop U-Yen, Edward J. Wollack, and Zhilei Xu (2016). "Silicon-based antenna-coupled polarization-sensitive millimeter-wave bolometer arrays for cosmic microwave background instruments". In: Proc. SPIE. Vol. 9914. Society of Photo-Optical Instrumentation Engineers (SPIE) Conference Series, p. 99140D. DOI: 10.1117/12.2234308.

U-Yen, Kongpop, Edward J. Wollack, John Papapolymerou, and Joy Laskar (2008). “A Broadband Planar Magic-T Using Microstrip-Slotline Transitions”. In: *IEEE Transactions on Microwave Theory Techniques* 56.1, pp. 172–177. DOI: `10.1109/TMTT.2007.912213`.

Wollack, E. J., K. U-yen, and D. T. Chuss (2010). “Photonic choke-joints for dual-polarization waveguides”. In: *2010 IEEE MTT-S International Microwave Symposium*, pp. 1–1.

Chapter 6

On-sky Performance of CLASS Detectors

In this chapter, I present the on-sky performance of the three CLASS detector arrays (spanning four different frequency bands) that are operational at the CLASS site. The results presented here were obtained from on-sky observations with the Q-band instrument after its upgrade in April 2018, and with the W-band and the G-band instruments since their respective deployments in May 2018 and September 2019 till March 2020. In Section 6.1, I describe the Q-band array upgrades and the after-deployment status of the W-band and G-band focal plane arrays. Section 6.2 shows the updated optical passband measurements and the on-sky optical loading extracted from the detector *I-V* measurements. In Section 6.3, I report the noise performance based on the power spectral density (PSD) of the time-ordered data (TOD), and compare it to our expectations from lab measurements presented in previous chapters. Finally, in Section 6.4, I report the temperature calibrations of the instruments obtained from dedicated planet observations and the CMB sensitivities of the detector arrays calculated from on-sky data.

6.1 Focal Plane Arrays

As discussed in Chapter 3, the focal planes for all CLASS telescopes consist of smooth-walled feedhorns that couple light to polarization-sensitive TES bolometers through planar OMTs. Table 6.1 summarizes the median bolometer properties for all four CLASS frequency bands. These parameters were derived using I-V measurements acquired throughout the observing campaign and represent the median values across the respective arrays. The optical time constant (τ_γ) was obtained by fitting the TODs for a detector time constant that minimizes the hysteresis of the VPM signal synchronous with the grid-mirror distance (Appel et al., 2019). We then multiply τ_γ by the electrothermal feedback speed-up factor (Equation 3.15) estimated from the I-V measurements to obtain the thermal time-constant (τ_ϕ). The heat capacity (C) is the product of τ_ϕ and G, and it matches the lab-measured value obtained from measuring the response lag to a small square-wave voltage excitation on the detector bias line (see Section 4.3.1). The optical loading (P_γ) calculation is described in Section 6.2.

6.1.1 Q-band

The on-sky performance of the Q-band array from its deployment (June 2016) until March 2018 is described in detail in Appel et al. (2019). In April 2018, the Q-band detector focal plane was returned to Johns Hopkins University from the CLASS site to recover eight readout channels on a multiplexing row that were lost during the Q-band deployment due to a readout electronics failure. The optically-sensitive TESs connected to the broken readout channels

Table 6.1: Summary of Median TES Bolometer Parameters

	40 GHz	**90 GHz**	**150 GHz**	**220 GHz**
Optical Loading P_γ [pW]	1.2	3.8	5.2	10.1
Optical Time Constant τ_γ [ms]	3.4	2.1	1.5	1.4
Thermal Time Constant τ_φ [ms]	17	7	8	6
Heat Capacity C [pJK^{-1}]	3	4	5	5
Responsivity S [μA pW^{-1}]	-8.2	-2.9	-2.3	-2.2
Thermal Conductivity G [pWK^{-1}]	177	548	672	808
Thermal Conductivity Constant κ [nWK^{-4}]	13.4	24.5	19.2	22.1
Critical Temperature T_c [mK]	149	175	206	209
Normal Resistance R_N [mΩ]	8.2	10.7	13.8	13.9
Shunt Resistance R_sh [μΩ]	250	250	200	200
TES Loop Inducatance L [nH]	500	300	600	600

were shifted to neighboring spare readout channels. After this fix we measure good I-V responses and can bias on transition all 72 optically-sensitive TESs in the array. We find two irregular bolometers in the array: one with good optical efficiency but high noise ($\sim 10\times$ higher), and another with low optical efficiency (1%) but typical noise. We remove these from the analysis presented in this chapter. These two detectors are not useful for mapping the sky but can be valuable in understanding and tracking systematics of the instrument.

During the Q-band instrument upgrade, we also removed eight photo-machined metal-mesh filters (Section 2.4.3.1) from the cryogenic receiver filter stack, located inside the vacuum can at 4 K, 60 K and 300 K stages. Lab measurements of the photo-machined filters yielded high in-band reflection, and significant gap differences were observed in the x and y axes of the filter pattern. The on-sky optical efficiency after the upgrade was measured at 0.53, i.e., 10% higher than 0.48 measured during the first era of observations (Appel et al., 2019). The in-band optical loading stayed at 1.2 pW even though the optical efficiency increased. This means more of the in-band power is mapped on the cold sky as opposed to being reflected on the warm sections of the receiver or spilled on to the 300 K cage. Hence the detector sensitivity improved by 10% to 225 $\mu K\sqrt{s}$ as shown in Table 6.3.

The VPM control system was updated and the baffle and cage enclosures were replaced to accommodate the Q-band and W-band receivers on the same mount. The new electro-magnetic environment resulted in increased susceptibility of the Q-band receiver to RF noise, in particular to RF signals synchronous to the VPM controller. To improve data quality and stability we installed a thin grille (TG) filter at the front of the vacuum window. The TG filter is a 0.51 mm thick brass plate with 5.25 mm diameter circular holes in a 5.75 mm pitch hexagonal packing. The TG filter greatly reduced RF pickup by the array improving data quality at the cost of reducing optical efficiency to 0.43, while keeping the detector optical loading at 1.2 pW, and hence decreasing per detector sensitivity to 261 $\mu K\sqrt{s}$. We are actively exploring TG designs with improved transmission that would return the receiver sensitivity to the benchmarks achieved with no TG filter installed. While the data with no TG filter installed was acquired between May 2018 and January 2019, the remaining data since February 2019 till March 2020 was obtained with the TG filter installed.

6.1.2 W-band

The W-band instrument started observation at the CLASS site in May 2018. As described in Chapter 4, the W-band focal plane contains a total of 518 bolometers read out using 28 TDM-columns, each multiplexing 22 rows of SQUIDs for a total of 616 readout channels. The remaining SQUID channels that are not connected to one of the 518 “optical” bolometers are either used to characterize readout noise and magnetic field pickup or are connected to a TES bolometer without optical coupling to monitor bath-temperature stability. These non-optical bolometers are not considered for analysis in this chapter; therefore, “bolometers” refer to the optically-sensitive bolometers hereon.

Through in-lab characterization, we had reported in Chapter 4 that 426 out of 518 bolometers were functional (i.e. array yield of 82%). During the deployment, we lost 19 bolometers on a single multiplexing row due to a failure in the readout. Out of the remaining 407 bolometers, we only consider 343 of them that detect Venus for further analysis in this chapter. (The detection criteria for planets are explained in detail in Section 6.4.) The lower yield of operable W-band detectors in the field can be mostly attributed to three coupled effects: (1) variations in detector properties within a wafer resulted in variations in their optimal bias points; (2) a TES electronically isolated from the bulk palladium metalization resulted in a narrow stable bias range, which prevented accommodating variations in bias point (Effect 1) with a single bias line; and (3) all the detectors within a module shared a single bias line, which prevented providing more than one bias. We suspect that the stability of the detectors is limited because there is no direct electronic coupling between the TES and the significant volume of palladium added for heat capacity around the TES. This was not an issue for the 40 GHz detectors, which had significantly lower TES thermal conductivity G (see Table 6.1). It is also not an issue for the 150/220 GHz detectors, for which we incorporated direct electrical contact between the TES and the palladium (see Figure 5.2). We do not see stability issues in the G-band detectors as described in Section 6.1.3. To address this issue in the second W-band instrument, we have modified the TES design to make electronic contact with the palladium. The modified TES design will be discussed further in an upcoming publication R. Datta et al. 2020 (in prep.). These new W-band detectors are being fabricated at NASA Goddard at the time of writing.

6.1.3 G-band

The CLASS G-band instrument, which started observation in September 2019, has a total of 255 dichroic dual-polarization pixels spread among three identical modules (see Chapter 5). Each pixel contains four bolometers to measure the two linear polarization states at 150 and 220 GHz frequency bands defined through on-chip filtering. These detectors are read out with 24 columns multiplexing 44 rows of SQUIDs. Before the deployment of the G-band instrument, we had reported array yields of 80% and 57% for the 150 and the 220 GHz frequency bands, respectively (see Chapter 5). For 150 GHz, 98% of the bolometers considered in the array yield before deployment detect Jupiter (i.e. 400 out of 408 working ones in the lab) and they do not suffer from the stability issues discussed in Section 6.1.2. In addition, the G-band detectors are biased per column (as opposed to per module for W-band), which helps to better optimize the detector biasing. For 220 GHz, 189 bolometers (out of 290 working ones in the lab) detect Jupiter. This is mostly due to failure of two readout columns during deployment, which could be fixed during our next deployment campaign in 2021. For this chapter, only those G-band detectors that detect Jupiter are considered for further analysis.

6.2 Optical Loading

As discussed in Section 2.4.3.1, a combination of absorptive, reflective, and scattering filters inside the receiver cryostat suppresses the infrared power reaching the focal plane. On the detector chip, frequencies above the niobium gap energy ($\sim$ 700 GHz) are suppressed, and below this, additional low-pass transmission-line filtering is applied. Finally, a separate set of on-chip filters defines the precise band edges for all CLASS detectors. The following subsections describe the measurements and show results for the passbands measured in the lab, and the in-band optical power measured in the field.

6.2.1 Frequency Bands

We measured the CLASS detector passbands using Martin-Puplett Fourier transform spectrometers (FTSs; Martin and Puplett 1970) in the lab. For the 40 and the 90 GHz detectors, a tabletop FTS made at the Johns Hopkins University with $\sim$ 1 GHz resolution (Wei, 2012) was used to obtain the spectrum shown in Figure 6.2. The passband measurements and FTS testing setup for the 40 and the 90 GHz detectors are described in Appel et al. (2019) and Chapter 4, respectively. For the 150 and 220 GHz detectors, the lab cryostat and FTS testing setup did not allow the use of a tabletop FTS; therefore, a smaller and compact FTS shown in Figure 6.1 with $\sim$ 2 GHz resolution (Pan

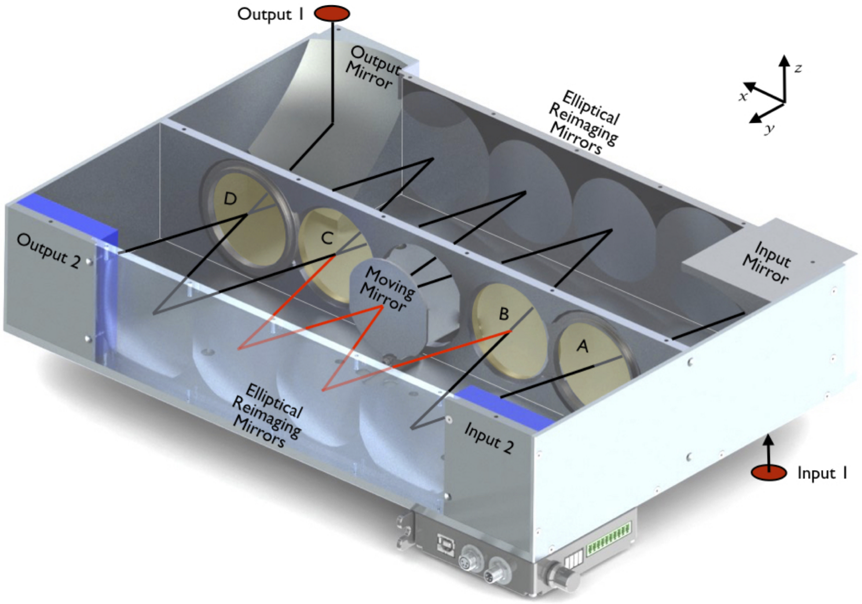
Output 1
Output Mirror
Elliptical Reimaging Mirrors
z
x
y
D
C
Output 2
Moving Mirror
B
A
Input Mirror
Elliptical Reimaging Mirrors
Input 2
Input 1

Figure 6.1: Model of the compact (355 × 260 × 64 mm) FTS used to measure the passbands of the CLASS 150 and 220 GHz detectors. (Refer to Wei 2012 for details on the FTS used for the passband measurements of the 40 and 90 GHz detectors.) The four polarizers in the FTS are labeled A through D. The black lines trace one of the two paths of the central ray through the FTS for one polarization, whereas the red lines show the other path between the two beam splitters labelled B and C for the same polarization. The optical delay between the two paths created by the moving mirror results in an interference pattern at the output, which is used to measure the passband of the detector placed in front of the output. Figure from Pan et al. (2019).

et al., 2019) was used instead. The measured and simulated passbands for the CLASS detectors are shown in Figure 6.2. All four passbands safely avoid strong atmospheric emission lines, as designed. The measured passbands have been corrected for the transmission through cryostat filters and the frequency-dependent gain for the detector feedhorns that were placed a meter behind a 10-cm diameter cold stop. We co-added measured passbands from a sub-set of detectors with high signal-to-noise (S/N) in each array to obtain the plot shown in Figure 6.2.

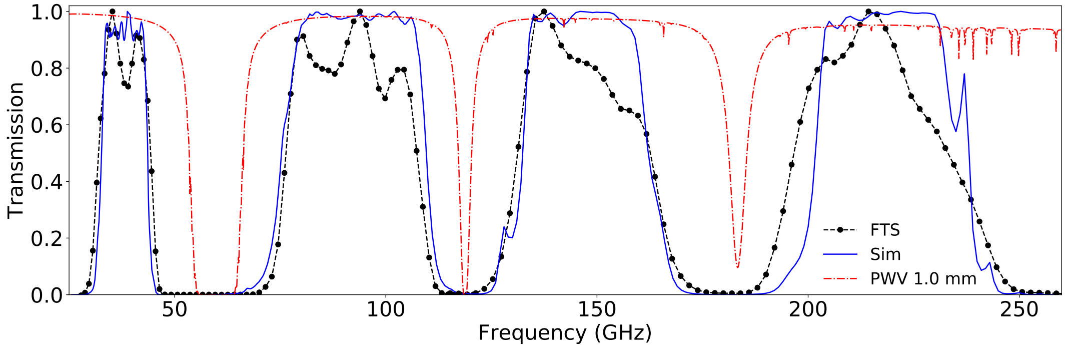

Figure 6.2: Average measured (dotted-black) and simulated (solid-blue) spectral response for different CLASS frequency bands overplotted with the atmospheric transmission model at the CLASS site with PWV = 1 mm (red dash-dot). The atmospheric transmission model was obtained from the ALMA atmospheric transmission calculator based on the ATM code described in Pardo, Cernicharo, and Serabyn (2001). The bandwidths and center frequencies for these passbands for different diffuse sources are shown in Table 6.2. (Refer to the text for the comparison of this plot to the one presented in Chapter 5.)

For the measured and simulated passbands in Figure 6.2, we calculate detector bandwidths in two different ways – full width at half power (FWHP) and Dicke bandwidth (Dicke, 1946), which is defined as:

$$\Delta\nu_{\text{Dicke}} \equiv \frac{\left[\int f(\nu)d\nu\right]^2}{\int f(\nu)^2 d\nu}, \tag{6.1}$$

where ν is the frequency and $f(\nu)$ is the spectral response. Following Page et al. (2003b), we also calculate the effective central frequencies for the measured passbands as:

$$\nu_{\text{e}} \equiv \frac{\int \nu f(\nu)\sigma(\nu)d\nu}{\int f(\nu)\sigma(\nu)d\nu}, \tag{6.2}$$

where $\sigma(\nu)$ describes the frequency dependence for different sources. For a beam-filling Rayleigh-Jeans (RJ) source, the detector has a flat spectral response as the source spectrum is exactly cancelled by the single-moded

Table 6.2: Measured (and Simulated) Bandwidths $\Delta\nu$ and Effective Center Frequencies ν_{e} for Diffuse Sources (in GHz)

	Q-band	**W-band**	**G-band (Lower)**	**G-band (Upper)**
$\boldsymbol{\Delta\nu}$				
FWHP	12.3 (10.9) ± 0.9	31.0 (34.3) ± 1.5	31.4 (29.7) ± 1.0	36.5 (36.4) ± 0.7
Dicke	14.0 (12.1) ± 0.9	34.4 (37.5) ± 1.5	37.6 (35.1) ± 0.3	47.0 (40.1) ± 0.8
$\boldsymbol{\nu_{\mathrm{e}}}$				
Sync.	37.0 (37.3) ± 0.3	89.1 (89.3) ± 0.2	144.5 (145.5) ± 2.2	213.9 (217.6) ± 3.0
RJ	38.1 (38.1) ± 0.03	91.7 (92.5) ± 0.2	146.4 (147.2) ± 2.2	216.0 (219.1) ± 2.9
Dust	38.7 (38.6) ± 0.1	93.4 (94.4) ± 0.2	147.7 (148.2) ± 2.2	217.3 (220.1) ± 2.9
CMB	38.0 (38.1) ± 0.04	91.3 (92.0) ± 0.2	145.7 (146.6) ± 2.2	214.5 (218.0) ± 2.9

throughput; therefore, we set $\sigma(\nu) = 1$. For the diffuse synchrotron and dust sources, we use $\sigma(\nu) \propto \nu^{-2.7}$ and $\sigma(\nu) \propto \nu^{1.7}$, respectively. For the CMB, since the source measured is the anisotropy, we set $\sigma(\nu) \propto \frac{1}{\nu^2}\frac{\partial B(\nu,T)}{\partial T}\Big|_{T=T_{\mathrm{cmb}}} \propto \nu^2 \exp(h\nu/k_{\mathrm{B}}T_{\mathrm{cmb}})/(\exp(h\nu/k_{\mathrm{B}}T_{\mathrm{cmb}}) - 1)^2$, where h and k_{B} are the Planck and the Boltzmann constants, respectively, $B(\nu, T)$ is the Planck blackbody, and $T_{\mathrm{cmb}} = 2.725$ K. The calculated bandwidths and effective central frequencies for all these diffuse sources for both the measured and the simulated passbands are tabulated in Table 6.2.

The measurement uncertainties presented in Table 6.2 reflect our current best estimates associated with different FTS setups used to obtain the passbands. For Q- and W-band, the bandwidth errors are the measurement resolutions of their respective FTS data. The W-band center-frequency error bars are the standard errors on the mean of the measured values for different W-band detectors, while the Q-band center-frequency error bars are the differences between the measured and the simulated values (since the Q-band measurement was performed on a single detector as described in Appel et al. 2019).

For the G-band detectors, the uncertainties in both the bandwidths and the center frequencies are dominated by the systematics in the compact FTS used to make the measurement.

The passbands for the 150 and the 220 GHz detectors presented in Chapter 5 (Figure 5.6) were based on the measurements performed with the longer side of the compact FTS (the x-direction in Figure 6.1) placed parallel to the vertical axis of the CLASS cryostat. As the FTS was rotated by 90° aligning the longer side of the FTS to the horizontal axis of the cryostat, the measured passbands shifted lower by a few GHz to produce the result shown in Figure 6.2. After the deployment of the G-band instrument, we investigated the FTS systematics in the lab in order to verify the accuracy of the measured passbands. We performed FTS measurements on spare 90 GHz CLASS detectors (identical to the ones in the field) using a single-frequency HMC-C030[1] voltage-controlled oscillator (VCO) source. We tuned the VCO source to 7.5 GHz and used a ×12 frequency multiplier to produce 90 GHz input to the FTS optically coupled to the 90 GHz CLASS detectors inside the cryostat. While the vertical FTS configuration did not produce enough S/N output for the analysis, the horizontal configuration performed as expected showing a peak at 89.8 ± 1.0 GHz in response to the 90 GHz input. Therefore, we use FTS measurements from the horizontal configuration (Figure 6.2) for further G-band analysis in this chapter. The G-band uncertainties in Table 6.2 are equal to half the difference between the values obtained from the two orientations, used as an estimate for the FTS systematics. We plan to further investigate the FTS systematics using a vector network analyzer (VNA).

---

[1] www.analog.com/products/hmc-c030

6.2.2 Optical Power

The CLASS observation strategy is to scan azimuthally across 720° at a constant elevation of 45°. The telescope boresight angle is changed every day by 15° once per 24-hour observing cycle, nominally covering seven boresight angles from -45° to $+45^\circ$ each week. At the beginning of the observing cycle for the day, we acquire *I*-*V* curves in order to select the optimal voltage bias for detectors. For W-band, we apply one voltage bias per module (i.e. four columns), whereas for Q- and G-band, we choose one bias per column. To acquire an *I*-*V* curve, we first ramp up the detector voltage bias (V) to drive the detectors normal, then we sweep the bias downwards over a wide range and record the current response (I) of the detectors. Using this *I*-*V* data, we measure the detector bias power (P_{bias}) defined as $P_{\text{bias}} = I \times V$ at 80% TES normal resistance (R_{N}). The detector optical loading P_γ can then be calculated by subtracting this P_{bias} from the detector saturation power P_{sat} calculated in the lab by capping off all the cold stages of the cryostat with metal plates, i.e., $P_\gamma = P_{\text{sat}} - P_{\text{bias}}$. We show the spread of array-averaged P_γ during the observing campaign in Figure 6.3. The plot highlights the stability of atmospheric loading at lower frequencies as compared to the higher frequencies at the CLASS site. The average P_γ during the observing campaign for the 40, 90, 150 and 220 GHz detector arrays were 1.2, 3.8, 5.2, and 10.1 pW, respectively.

6.3 Noise Performance

Since CLASS detectors are background-limited, the optical loading drives the total detector noise measured. The NEP for TES bolometers is related to P_γ as

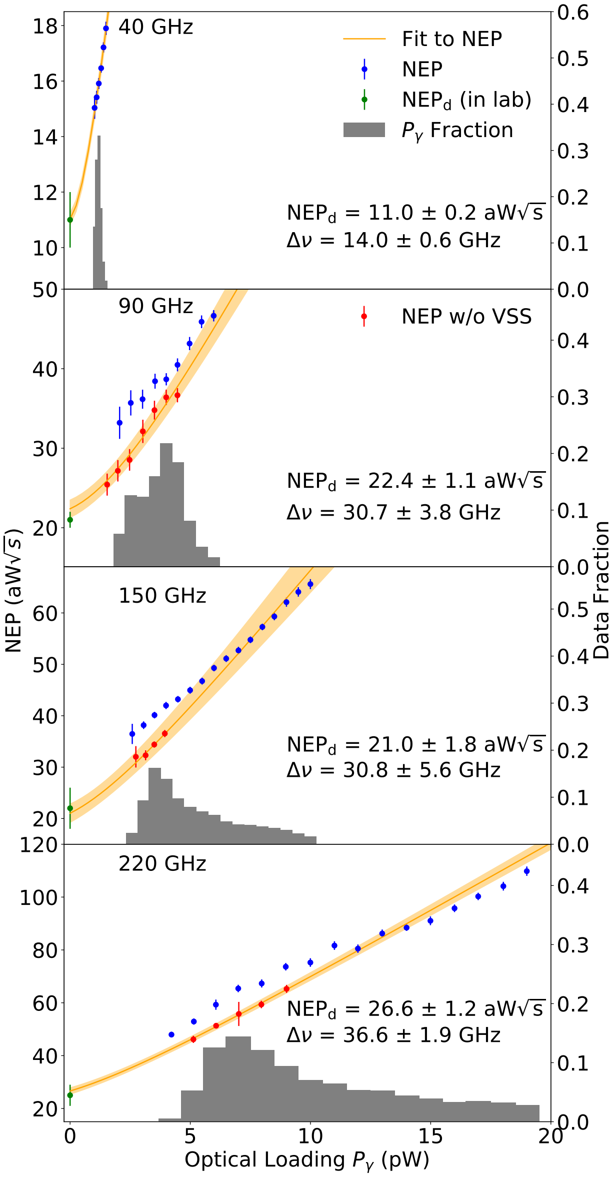

Figure 6.3: Array-averaged NEP vs P_γ for different CLASS frequency bands. The blue data points were acquired with the VPM ON, characterized by the presence of the VPM synchronous signal (VSS), whereas the red data points were acquired either with the VPM OFF or with the cryostat window covered. The orange curves are the fits for Equation 6.3 with NEP$_d$ and $\Delta\nu$ as free parameters, and the shaded regions are the 1σ uncertainties. The best-fit values are shown for each frequency band. While the Q-band NEP model was fitted to the blue points, the fit for the three higher frequencies were obtained from the red points (see text for details). The green points are the lab-measured NEP$_d$ values. The histograms show the spread of P_γ during the observing campaign.

follows:

$$\mathrm{NEP}^2 = \mathrm{NEP}_\mathrm{d}^2 + h\nu_0 P_\gamma + \frac{P_\gamma^2}{\Delta\nu}, \tag{6.3}$$

where NEP_d is the dark detector noise (Section 3.3.3), h is Planck constant, and ν_0 and $\Delta\nu$ are center frequency and bandwidth, respectively. To study the underlying NEP vs P_γ relation for CLASS detectors, we first pair-difference the TODs to reduce the correlated noise. For pair-differencing, we subtract the TODs of detector pairs within a pixel and then compute the PSD of the difference. Finally, we take the average of the PSD in the side bands of the 10 Hz modulation frequency, and divide the average by two to recover the per-detector NEP. While the side bands need to be near but not at the modulation frequency, the precise frequency range of the side-bands for averaging the PSDs were optimized separately for different CLASS arrays in order to avoid any prominent noise peaks in the raw detector timestreams. For both the 40 and 90 GHz detectors, the NEP values shown in Figure 6.3 are the averages obtained from 8.0 – 9.8 Hz and 10.2 – 12.0 Hz, whereas for the 150 and 220 GHz detectors, we took an average from 8.0 – 9.0 Hz and 11.0 – 12.0 Hz.

Figure 6.3 shows the binned pair-differenced NEP averaged across the array vs the average P_γ for all four CLASS frequency bands. Since the P_γ values are based on the I-V measurements and we only acquire I-V data once per day during nominal CMB scans, we only bin the NEP values from the TODs acquired within four hours after an I-V is acquired. This is especially important for the G-band detectors as they can have larger variations in the atmospheric loading throughout the day. We fit the binned NEP vs P_γ to Equation 6.3 with NEP_d and $\Delta\nu$ as free parameters and set ν_0 to the RJ center frequency (simulated) from Table 6.2. As shown in the top plot of Figure 6.3, the Q-band on-sky data (with TG filter installed) fits the NEP model with $\mathrm{NEP_d} = 11.0 \pm 0.2\ \mathrm{aW}\sqrt{s}$ and $\Delta\nu = 14.0 \pm 0.6$ GHz. The $\mathrm{NEP_d}$ fit value is same as the $\mathrm{NEP_d}$ value measured in lab and the $\Delta\nu$ fit is consistent with the measured Dicke bandwidth shown in Table 6.2.

For the W-band and G-band detector arrays, the NEP values are offset higher (especially at lower P_γ values) compared to the expectation from the lab-measured $\mathrm{NEP_d}$ and $\Delta\nu$ values. However, we notice that this overall NEP offset is not present when there is no VPM synchronous signal (VSS) in the TODs. While the blue data points in Figure 6.3 were obtained from regular CMB observations with the VPM operational (i.e. with the VSS present in the TOD), the red data points were acquired either when the cryostat window was covered or the VPM was turned OFF (i.e. no VSS was present in the TOD). The $\mathrm{NEP_d}$ and $\Delta\nu$ fit values obtained from the dataset with no VSS are consistent with the lab-measured $\mathrm{NEP_d}$ values (see Chapters 4 and 5) and the bandwidths shown in Table 6.2, respectively. We are actively investigating why the VSS effects our measured NEP and if this feature is present in the demodulated data as well. This will be discussed further in an upcoming publication S. Dahal et al. 2020 (in prep.).

It is worth noting that although single detectors without an operational pair were not included in the NEP vs P_γ plot in Figure 6.3, they could still be mapped for the CMB analysis. This is particularly important for the W-band detectors as a separate analysis shows that pair-differencing does not have a significant impact on its noise performance. To calculate the total sensitivity of the CLASS detector arrays, for each 10-min TOD throughout the observing season, we measure the NEP for all the operational detectors individually. We then calculate the median NEP per detector for all the TODs throughout the observing campaign, and show the noise-weighted array average in Table 6.3. These values reflect the total array sensitivity including the single detectors that were not included in the NEP vs P_γ analysis in Figure 6.3 due to pair-differencing.

6.4 Planet Observations

Venus and Jupiter are the two brightest "point sources" on the sky in the CLASS survey. Unlike for the CLASS Q-band instrument, the Moon is not a point source for W-band and G-band instruments, and more importantly, it saturates most of these detectors. Therefore, while we use the Moon for Q-band, we use Venus and Jupiter to obtain detector calibrations and characterize the main beam response of the W-band and G-band instruments. The calibration for the Q-band instrument before the April 2018 upgrade is presented in Appel et al. (2019), and we repeat the same steps to obtain the calibration after the upgrade. For W-band, we performed 70 dedicated Venus scans and 15 Jupiter scans. For these dedicated observations, we scan across the source over small ranges of azimuth angle at a fixed elevation. At W-band, since Venus is brighter and thus has higher signal-to-noise than Jupiter, we use Venus to obtain the detector calibrations shown in Table 6.3. For G-band, since Venus was not available for observation since its deployment in September 2019, the calibrations were obtained from 15 dedicated Jupiter scans.

Both Venus and Jupiter are effectively point sources whose brightness temperature (T_p) relates to the peak response measured by CLASS detectors (T_m) as:

$$T_\mathrm{p}\Omega_\mathrm{p} = T_\mathrm{m}\Omega_\mathrm{B}, \tag{6.4}$$

where Ω_B is the beam solid angle and Ω_p is the solid angle subtended by the planet (Page et al., 2003a). Since Ω_p changes between scans, we stack the individual maps per detector relative to a fiducial solid angle $\Omega_\mathrm{p}^\mathrm{ref}$. The method used to stack individual planet maps is similar to the stacking of the individual Moon maps for CLASS Q-band detectors as described in detail in Xu et al. (2019). In this chapter, we only consider those detectors that detect a planet more than 5 times with SNR > 3 during the observing campaign. We conservatively reject the individual maps that fail to converge for a Gaussian fit with beam-widths between 0.39° and 1.45° (0.19° and 1.0°) for W-band (G-band) or produce a solution with elliptical beam-width ratio > 2. Only those detectors that survive these data cuts are used for instrument characterization presented here.

Furthermore, Jupiter is an oblate planet with equatorial radius (R_eq) of 71492 km and polar radius (R_pol) of 66854 km (Seidelmann et al., 2007). This leads to changes in Ω_p with time due to changes in viewing angle for the oblate planet. Therefore, we correct $\Omega_\mathrm{p}^\mathrm{ref}$ with a "disk oblateness correction" factor (f_A). Following Weiland et al. (2011), f_A can be calculated as:

$$f_A = A_\mathrm{disk}^\mathrm{proj} / A_\mathrm{ref}, \tag{6.5}$$

where A_ref is a fixed fiducial disk area and $A_\mathrm{disk}^\mathrm{proj}$ is the projected area of

Jupiter's planetary disk. $A_{\mathrm{disk}}^{\mathrm{proj}}$ can be computed as:

$$A_{\mathrm{disk}}^{\mathrm{proj}} = \pi R_{\mathrm{pol}}^{\mathrm{proj}} R_{\mathrm{eq}}, \tag{6.6}$$

where $R_{\mathrm{pol}}^{\mathrm{proj}}$ is the projected polar radius given by:

$$R_{\mathrm{pol}}^{\mathrm{proj}} = R_{\mathrm{pol}}[1 - \sin^2(D_W)(1 - (R_{\mathrm{eq}}/R_{\mathrm{pol}})^2]^{1/2}, \tag{6.7}$$

where D_W is Jupiter's sub-Earth latitude. During this entire observing campaign, D_W varied by less than 1% as compared to its average value of 3.55°. Therefore, we set $D_W = 3.55°$ for all the dedicated Jupiter scans. Finally, A_{ref} is simply $A_{\mathrm{disk}}^{\mathrm{proj}}$ evaluated at $D_W = 0$. This gives the Jupiter disk oblateness correction factor $f_A = 0.93$.

The brightness temperature (T_{p}) is another unknown in Equation 6.4. For CLASS 150 and 220 GHz frequency bands, we use the Jupiter brightness temperatures of 174.1 ± 0.9 K and 175.8 ± 1.1 K obtained from *Planck* HFI 143 and 217 GHz frequency bands, respectively (Planck Collaboration et al., 2017). For W-band, in order to obtain the detector calibrations through higher SNR Venus observations, we need the W-band Venus brightness temperature. To our knowledge, the tightest experimental constraint so far on the disk-averaged Venus brightness temperature at W-band is $T_{\mathrm{p}}^{\mathrm{Ven}} = 357.5 \pm 13.1$ K from Ulich et al. (1980) measured at 86.1 GHz. However, we obtained better constraints on $T_{\mathrm{p}}^{\mathrm{Ven}}$ by comparing our W-band Venus and Jupiter observations. First, we obtained the Venus-to-Jupiter brightness temperature ratio of 2.11 ± 0.01 by calculating the ratio of their peak amplitudes for a specific fiducial reference solid angle. We then muliplied this ratio by *WMAP*'s nine-year mean W-band Jupiter temperature $T_{\mathrm{p}}^{\mathrm{Jup}}$ = 172.8 ± 0.5 K (Bennett et al., 2013) to obtain $T_{\mathrm{p}}^{\mathrm{Ven}}$ = 365 ± 2.6 K. We use this Venus brightness temperature value (which depends on both Venus and Jupiter observations through the CLASS W-band telescope) to obtain our W-band detector calibration presented in Section 6.4.1. Refer to Appendix B for further details on the Venus W-band brightness temperature calculation.

6.4.1 Calibration to Antenna Temperature

We use the dedicated planet (and the Moon for Q-band) observations to obtain the calibration factor from power deposited on the CLASS bolometers dP_γ to antenna (RJ) temperature on the sky dT_{RJ} as:

$$\frac{dT_{\mathrm{RJ}}}{dP_\gamma} = \frac{T_{\mathrm{m}}}{P_0} = \frac{T_{\mathrm{p}}}{P_0}\frac{\Omega_{\mathrm{p}}^{\mathrm{ref}}}{\Omega_B}, \tag{6.8}$$

where P_0 is the peak power amplitude observed by the CLASS bolometer. The antenna temperature dT_{RJ} can be converted to the CMB thermodynamic temperature dT_{cmb} as:

$$\frac{dT_{\mathrm{cmb}}}{dT_{\mathrm{RJ}}} \approx \frac{(e^{x_0}-1)^2}{x_0^2 e^{x_0}} \tag{6.9}$$

where $x_0 = \frac{h\nu_0}{kT_{\mathrm{cmb}}}$ (h: Planck constant, ν_0: bandpass center frequency, k: Boltzmann constant, $T_{\mathrm{cmb}} = 2.725$ K). Finally, we can write the calibration factor from dP_γ to dT_{cmb} as follows:

$$
\begin{aligned}
\frac{dT_{\mathrm{cmb}}}{dP_\gamma} = \frac{dT_{\mathrm{cmb}}}{dT_{\mathrm{RJ}}}\frac{dT_{\mathrm{RJ}}}{dP_\gamma} &= 11.2 \pm 1.2\ \mathrm{KpW}^{-1}\ (40\ \mathrm{GHz}) \\
&= 7.2 \pm 5.0\ \mathrm{KpW}^{-1}\ (90\ \mathrm{GHz}) \\
&= 8.9 \pm 1.6\ \mathrm{KpW}^{-1}\ (150\ \mathrm{GHz}) \\
&= 13.2 \pm 2.8\ \mathrm{KpW}^{-1}\ (220\ \mathrm{GHz}),
\end{aligned} \tag{6.10}
$$

where we calculate $dT_{\mathrm{cmb}}/dT_{\mathrm{RJ}}$ and $dT_{\mathrm{RJ}}/dT_{\mathrm{cmb}}$ from Equations 6.9 and 6.8, respectively. These values were calculated using the CLASS Moon observations for 40 GHz, Venus observations for 90 GHz, and Jupiter observations for 150 and 220 GHz detectors. Multiplying these calibration factors with the NEP values calculated in Section 6.3 gives the detector NET values, which are summarized in Table 6.3. We can also use the $dT_{\mathrm{RJ}}/dP_\gamma$ calibration factor to obtain the telescope optical efficiency (η) as follows:

$$
\begin{aligned}
\eta = \left(k\Delta\nu\frac{dT_{\mathrm{RJ}}}{dP_\gamma}\right)^{-1} &= 0.53 \pm 0.06\ (40\ \mathrm{GHz};\ 0.43 \pm 0.05\ \text{with TG filter}) \\
&= 0.37 \pm 0.16\ (90\ \mathrm{GHz}) \\
&= 0.46 \pm 0.08\ (150\ \mathrm{GHz}) \\
&= 0.47 \pm 0.09\ (220\ \mathrm{GHz}),
\end{aligned} \tag{6.11}
$$

where $\Delta\nu$ is the detector bandwidth from Table 6.2. The values in Equations 6.10 and 6.11 are array medians and the error bars are the standard deviations for the array. Figure 6.4 shows the distribution of η for all four

CLASS frequency bands. The total efficiency for the 40, 150, and 220 GHz instruments match our pre-deployment expectation of ~ 50 % (see Chapters 4 and 5). However, as shown in Figure 6.4, while some 90 GHz detectors have the expected efficiency similar to other frequency bands, the spread in the efficiency values is large and skewed towards low efficiency. We are actively investigating the cause of this larger efficiency spread by simulating various detector components in HFSS and analyzing their tolerance to variations in fabrication. Refer to R. Datta et al. 2020 (in prep.) for further details.

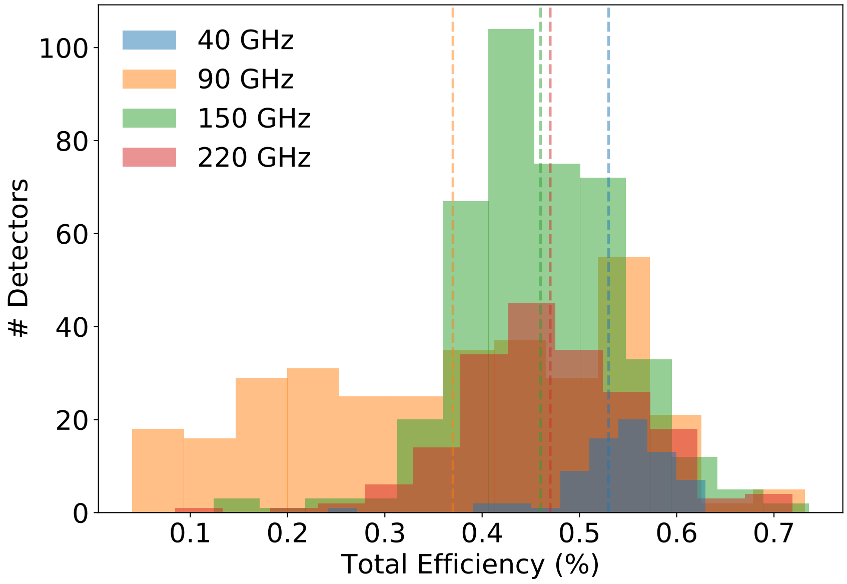

Figure 6.4: The distribution of total optical efficiency for CLASS detectors. The efficiency numbers for the 40, the 90, and the 150 and 220 GHz detectors were obtained from the dedicated Moon, Venus, and Jupiter observations, respectively. The dashed lines represent the respective array median values shown in Equation 6.11. The 40 GHz efficiency values shown here were obtained after the April 2018 upgrade and without the TG filter installed; the TG filter lowers the array median shown here by $\sim 19\%$ to 0.43.

Table 6.3: On-sky Optical Performance Summary of CLASS telescopes

	40 GHz [a]	**90 GHz**	**150 GHz**	**220 GHz**
RJ Point-source Center [GHz]	38.7	94.7	148.4	220.2
Beam FWHM [$'$]	91	37	23	17
Beam Solid Angle [μsr]	796	136	51	28
Telescope Efficiency	0.53 (0.43)	0.37	0.46	0.47
$dT_{\mathrm{RJ}}/dP_{\gamma}$ [KpW^{-1}]	10.8 (13.7)	5.8	5.2	4.3
$dT_{\mathrm{cmb}}/dT_{\mathrm{RJ}}$	1.04	1.24	1.70	3.07
Detector NEP$_{\mathrm{d}}$ [aW$\sqrt{\mathrm{s}}$]	11	21	22	25
Detector NEP [aW$\sqrt{\mathrm{s}}$]	18 (17)	35	57	60
Detector NET [μK$_{\mathrm{cmb}}\sqrt{\mathrm{s}}$]	225 (261)	360	506	786
No. of detectors	72	343	400	189
Array NET [μK$_{\mathrm{cmb}}\sqrt{\mathrm{s}}$]	27 (31)	19	25	57

[a] 40 GHz optical performance after April 2018 upgrade. The values in parenthesis correspond to the telescope's performance with the TG filter installed.

In Table 6.3, we show the instantaneous array sensitivity (array NET) for all four CLASS frequency bands by taking a noise-weighted average of per-detector NETs in the array. During the observing campaign reported in this chapter, the CLASS 40, 90, 150, and 220 GHz detector arrays achieved array sensitivities of 27, 19, 25, and 57 μK$_{\mathrm{cmb}}\sqrt{\mathrm{s}}$, respectively. For comparison at similar frequency bands, the *Planck* 44 GHz LFI had a total sensitivity of 174 μK$_{\mathrm{cmb}}\sqrt{\mathrm{s}}$ (Planck Collaboration et al., 2016a) , and the *Planck* 100, 143, and 217 GHz HFI instruments had total sensitivities of 40, 17, and 24 μK$_{\mathrm{cmb}}\sqrt{\mathrm{s}}$, respectively (Planck Collaboration et al., 2016b). Therefore, while CLASS is more sensitive at lower frequencies, *Planck* had better sensitivity at higher frequencies, primarily due to higher photon noise from atmospheric loading for CLASS. As designed, the CLASS 90 GHz detector array has the highest CMB sensitivity among the four CLASS arrays (and compared to *Planck*), and the addition of a second 90 GHz instrument will drive this sensitivity even higher. Combined with the *Planck* high-frequency data for dust foreground removal, CLASS can produce the most precise CMB polarization map at large angular scales. This will be crucial for detecting and characterizing the primordial gravitational waves, and measuring the optical depth to reionization.

References

Appel, John W., Zhilei Xu, Ivan L. Padilla, Kathleen Harrington, Bastián Pradenas Marquez, Aamir Ali, Charles L. Bennett, Michael K. Brewer, Ricardo Bustos, Manwei Chan, David T. Chuss, Joseph Cleary, Jullianna Couto, Sumit Dahal, Kevin Denis, Rolando Dünner, Joseph R. Eimer, Thomas Essinger-Hileman, Pedro Fluxa, Dominik Gothe, Gene C. Hilton, Johannes Hubmayr, Jeffrey Iuliano, John Karakla, Tobias A. Marriage, Nathan J. Miller, Carolina Núñez, Lucas Parker, Matthew Petroff, Carl D. Reintsema, Karwan Rostem, Robert W. Stevens, Deniz Augusto Nunes Valle, Bingjie Wang, Duncan J. Watts, Edward J. Wollack, and Lingzhen Zeng (2019). "On-sky Performance of the CLASS Q-band Telescope". In: ApJ 876.2, 126, p. 126. DOI: `10.3847/1538-4357/ab1652`. arXiv: `1811.08287 [astro-ph.IM]`.

Bennett, C. L., D. Larson, J. L. Weiland, N. Jarosik, G. Hinshaw, N. Odegard, K. M. Smith, R. S. Hill, B. Gold, M. Halpern, E. Komatsu, M. R. Nolta, L. Page, D. N. Spergel, E. Wollack, J. Dunkley, A. Kogut, M. Limon, S. S. Meyer, G. S. Tucker, and E. L. Wright (2013). "Nine-year Wilkinson Microwave Anisotropy Probe (WMAP) Observations: Final Maps and Results". In: ApJS 208.2, 20, p. 20. DOI: `10.1088/0067-0049/208/2/20`. arXiv: `1212.5225 [astro-ph.CO]`.

Dicke, R. H. (1946). "The Measurement of Thermal Radiation at Microwave Frequencies". In: *Review of Scientific Instruments* 17.7, pp. 268–275. DOI: `10.1063/1.1770483`. eprint: `https://doi.org/10.1063/1.1770483`.

Martin, D. H. and E. Puplett (1970). "Polarised interferometric spectrometry for the millimeter and submillimeter spectrum." In: *Infrared Physics* 10, pp. 105–109. DOI: `10.1016/0020-0891(70)90006-0`.

Page, L., C. Barnes, G. Hinshaw, D. N. Spergel, J. L. Weiland, E. Wollack, C. L. Bennett, M. Halpern, N. Jarosik, A. Kogut, M. Limon, S. S. Meyer, G. S. Tucker, and E. L. Wright (2003a). "First-Year Wilkinson Microwave Anisotropy Probe (WMAP) Observations: Beam Profiles and Window

Functions". In: ApJS 148.1, pp. 39–50. DOI: 10.1086/377223. arXiv: astro-ph/0302214 [astro-ph].

Page, L., C. Jackson, C. Barnes, C. Bennett, M. Halpern, G. Hinshaw, N. Jarosik, A. Kogut, M. Limon, S. S. Meyer, D. N. Spergel, G. S. Tucker, D. T. Wilkinson, E. Wollack, and E. L. Wright (2003b). "The Optical Design and Characterization of the Microwave Anisotropy Probe". In: ApJ 585.1, pp. 566–586. DOI: 10.1086/346078. arXiv: astro-ph/0301160 [astro-ph].

Pan, Zhaodi, Mira Liu, Ritoban Basu Thakur, Bradford A. Benson, Dale J. Fixsen, Hazal Goksu, Eleanor Rath, and Stephan S. Meyer (2019). "Compact millimeter-wavelength Fourier-transform spectrometer". In: Appl. Opt. 58.23, p. 6257. DOI: 10.1364/AO.58.006257. arXiv: 1905.07399 [astro-ph.IM].

Pardo, J. R., J. Cernicharo, and E. Serabyn (2001). "Atmospheric transmission at microwaves (ATM): an improved model for millimeter/submillimeter applications". In: *IEEE Transactions on Antennas and Propagation* 49.12, pp. 1683–1694. DOI: 10.1109/8.982447.

Planck Collaboration et al. (2016a). "Planck 2015 results. II. Low Frequency Instrument data processings". In: A&A 594, A2, A2. DOI: 10.1051/0004-6361/201525818. arXiv: 1502.01583 [astro-ph.IM].

Planck Collaboration et al. (2016b). "Planck 2015 results. VII. High Frequency Instrument data processing: Time-ordered information and beams". In: A&A 594, A7, A7. DOI: 10.1051/0004-6361/201525844. arXiv: 1502.01586 [astro-ph.IM].

Planck Collaboration et al. (2017). "Planck intermediate results - LII. Planet flux densities". In: *A&A* 607, A122. DOI: 10.1051/0004-6361/201630311.

Seidelmann, P. Kenneth, B. A. Archinal, M. F. A'Hearn, A. Conrad, G. J. Consolmagno, D. Hestroffer, J. L. Hilton, G. A. Krasinsky, G. Neumann, J. Oberst, P. Stooke, E. F. Tedesco, D. J. Tholen, P. C. Thomas, and I. P. Williams (2007). "Report of the IAU/IAG Working Group on cartographic coordinates and rotational elements: 2006". In: *Celestial Mechanics and Dynamical Astronomy* 98.3, pp. 155–180. DOI: 10.1007/s10569-007-9072-y.

Ulich, B., J. Davis, P. Rhodes, and J. Hollis (1980). "Absolute brightness temperature measurements at 3.5-mm wavelength". In: *IEEE Transactions on Antennas and Propagation* 28.3, pp. 367–377. DOI: 10.1109/TAP.1980.1142330.

Wei, Tiffany (2012). "The Design, Construction, and Testing of a Wide-Band Fourier Transform Interferometer". Undergraduate Thesis. The Johns Hopkins University.

Weiland, J. L., N. Odegard, R. S. Hill, E. Wollack, G. Hinshaw, M. R. Greason, N. Jarosik, L. Page, C. L. Bennett, J. Dunkley, B. Gold, M. Halpern, A.

Kogut, E. Komatsu, D. Larson, M. Limon, S. S. Meyer, M. R. Nolta, K. M. Smith, D. N. Spergel, G. S. Tucker, and E. L. Wright (2011). “Seven-year Wilkinson Microwave Anisotropy Probe (WMAP) Observations: Planets and Celestial Calibration Sources”. In: ApJS 192.2, 19, p. 19. DOI: `10.1088/0067-0049/192/2/19`. arXiv: `1001.4731 [astro-ph.CO]`.

Xu, Zhilei, Michael K. Brewer, Pedro Fluxa, Yunyang Li, Keisuke Osumi, Bastian Pradenas, Aamir Ali, John W. Appel, Charles L. Bennett, Ricardo Bustos, Manwei Chan, David T. Chuss, Joseph Cleary, Jullianna Couto, Sumit Dahal, Rahul Datta, Kevin Denis, Rolando Dunner, Joseph Eimer, Thomas Essinger-Hileman, Kathleen Harrington, Jeffrey Iuliano, Tobias A. Marriage, Nathan Miller, Carolina Núñez, Ivan L. Padilla, Lucas Parker, Matthew A. Petroff, Rodrigo Reeves, Karwan Rostem, Duncan J. Watts, Janet Weiland, and Edward J. Wollack (2019). “Two-year Cosmology Large Angular Scale Surveyor (CLASS) Observations: 40 GHz Telescope Pointing, Beam Profile, Window Function, and Polarization Performance”. In: *arXiv e-prints*, arXiv:1911.04499, arXiv:1911.04499. arXiv: `1911.04499 [astro-ph.IM]`.

Appendix A

150/220 GHz Detector Array Assembly Procedure

This appendix is an extension to Chapter 5. Here I describe the assembly procedure for the CLASS 150/220 GHz focal plane detector array in detail. The following series of images with their associated captions are arranged sequentially to describe the steps followed in assembling the CLASS high-frequency (HF) detector array.

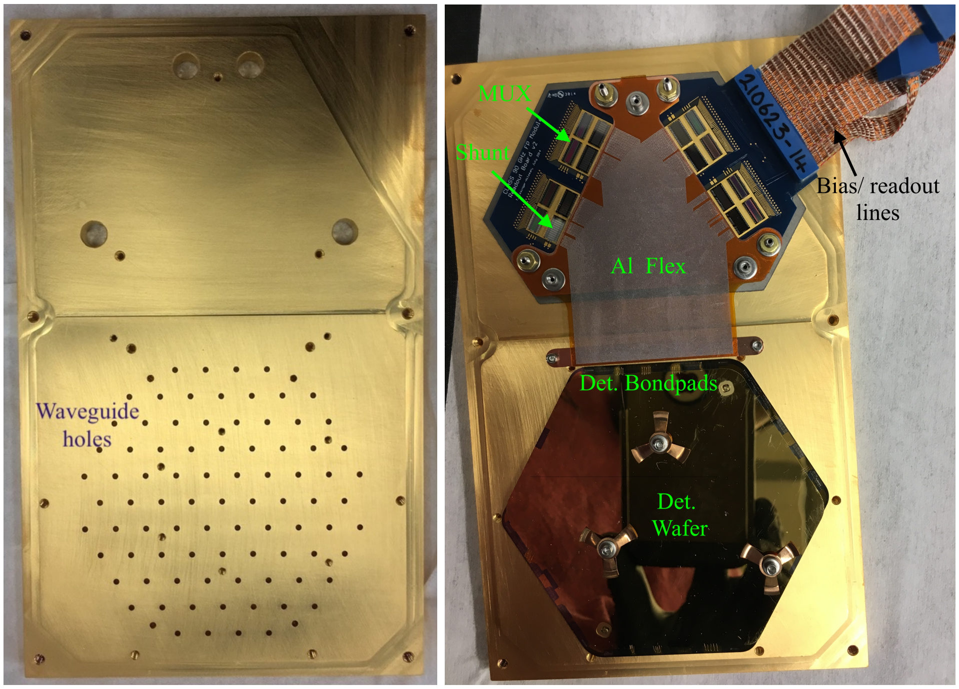

Figure A.1: Test Setup: Before the detector wafers are assembled in a final module configuration, we assemble and test them in a simpler test setup shown here. The setup is designed for a quick turnaround to verify that the detectors in a particular wafer are optically sensitive and the TES parameters are close to target. Assembling this setup takes a few days as compared to a few weeks for the final module assembly. The feedback from this detector testing helps improve the fabrication of the subsequent batch of wafers, if necessary. In this test setup, we mount the detector wafer on a Au-plated copper baseplate with cylindrical waveguide holes (left). For the ease of testing, we wirebond only quarter of the total number of detectors with bond pads located on one of the sides of the hexagon. In the image shown (right), we have bonded this particular wafer to the Al flex circuit, the shunt and MUX chips, and the PCB designed for the CLASS 90 GHz readout (see Chapter 4). After an initial testing, we replaced one of the shunt chips with an interface chip containing both the shunt resistor and a Nyquist inductor to analyze the readout noise and detector stability. The data from this test setup helped us choose a 310 nH Nyquist inductor for the final module assembly to keep the high-frequency detector noise aliasing below 1% of the noise level in the TES audio bandwidth.

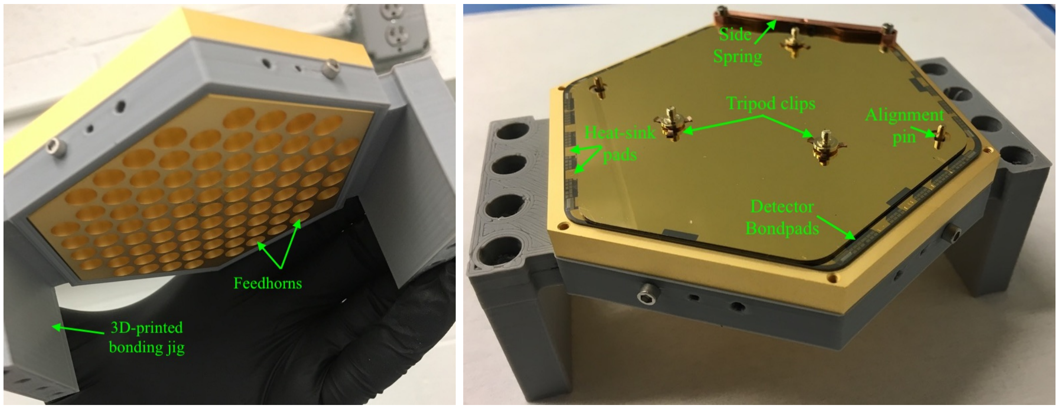

Figure A.2: Feedhorn and Detector Wafer Assembly: The CLASS HF module assembly begins by assembling the Au-plated CE7 feedhorn array and the hybridized detector wafer assembly. (Left) First, we mount the feedhorn array on a 3D-printed jig that mechanically supports the feedhorn array and can be mounted on a wirebonder. (Right) The wafer assembly is then mounted on the feedhorn array using three BeCu tripod clips. Each clip is deflected by ~ 0.5 mm using a custom-made screw, which puts sufficient force on the wafer to keep it stationary and ensures proper operation of the photonic choke-joints. Since the screws have #1-64 threads, a one and a quarter turn of the screw head after it comes in contact with the tripod clip provides the desired 0.5 mm deflection. The two alignment pins and a BeCu side spring maintain proper alignment of the feedhorn waveguides to the OMTs on the detector wafer. The two square alignment holes on the wafer assembly are designed such that the alignment is achieved when one of the pins is pushed against a corner of the square (locking the wafer from sliding across that point) and the other pin is pushed against a side of the square (locking the wafer from rotating about that point). This entire assembly is then mounted on a wirebonder. Next, a series of Au wirebonds are put down to thermally connect the heat-sink pads on the detector wafer and the top of the backshort to the CE7.

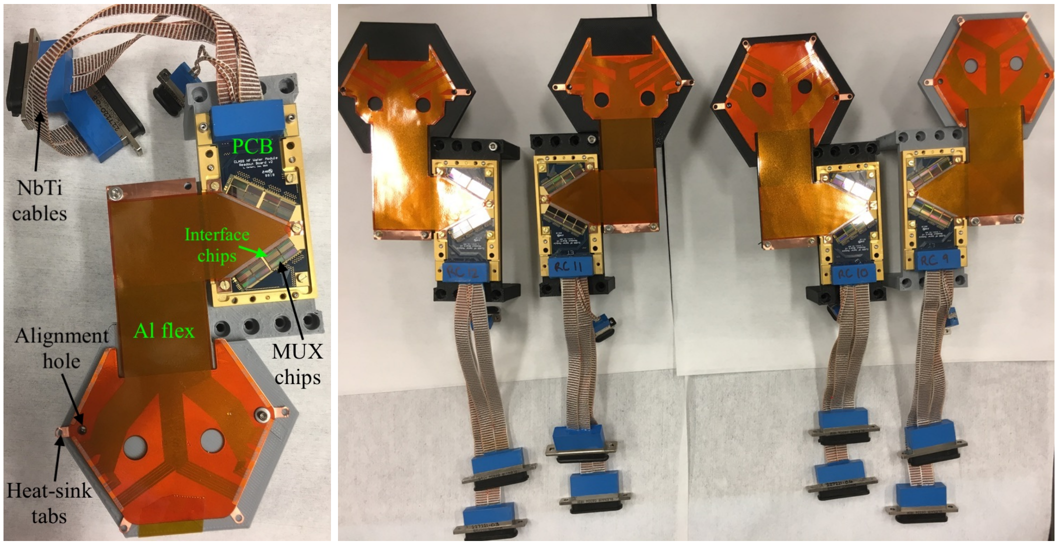

Figure A.3: Readout Circuit Assembly: While the feedhorn and detector wafer are being assembled as shown in Figure A.2, the readout circuits can be assembled simultaenously in a separate setup. As shown in the image on the left, first, a Au-plated copper structure that supports the readout package in the HF module is mounted on a 3D-printed jig. A PCB with twisted pairs of NbTi signal cables soldered onto it is bolted to the copper support. A Nb sheet (not shown here) is sandwiched between the PCB and the copper support for magnetic shielding. Then, the MUX and the interface (containing shunt resistors and Nyquist inductors) chips are glued onto the PCB with rubber cement. One end of the Al flex circuit is also bolted to the copper package as shown here. The jig is then moved to the wirebonder. A set of Al wirebonds are put down to electrically connect the Al traces to the signal cables through the interface and the MUX chips, and the vias on the PCB. The four MUX chips on each side of the readout package are also strung together through Al wirebonds to form a multiplexing column with 44 channels each. For a schematic of the wirebonds used to connect the different readout components, refer to Figure 3.6. The above readout package assembly is repeated for three more circuits as shown in the image on the right. While the Al flex circuit for the four readout packages are different, the assembly procedure is the same.

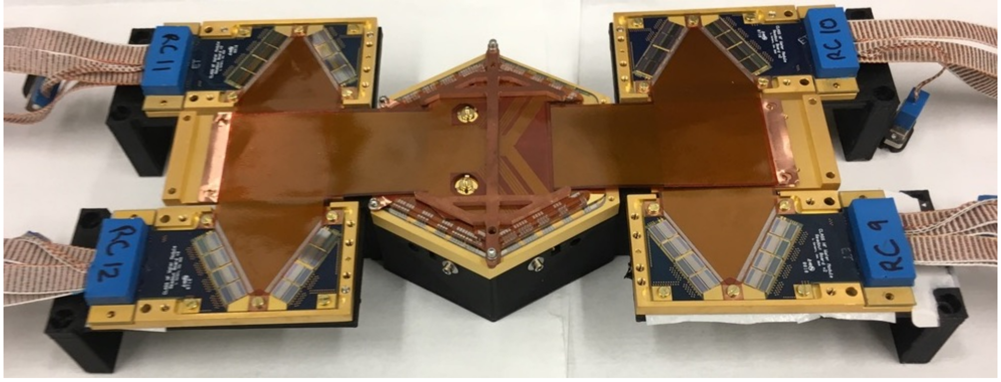

Figure A.4: Stacking the Readout Circuits: The detector-feedhorn assembly (Figure A.2) and the four readout circuits (Figure A.3) are carefully moved to a new jig to form a single assembly shown here. The readout circuits (RCs) labelled RC 9, RC 10, RC 11, and RC 12 here are stacked on top of the detector wafer in that particular order so that the top layers do not cover the exposed Al traces of the bottom layers. This ensures that we can wirebond from the detector bond pads to all the four layers of the flex circuits. A stiff copper structure is mounted on the top to keep the flex circuits stationary while wirebonding. Notice that the third tripod clip is removed during this process, which could be re-introduced after the flex circuits are folded up. However, since this third clip is not entirely necessary to keep the detector wafer stationary, we instead tighten the remaining two screws to achieve a 0.75 mm deflection on each (as compared to 0.5 mm for three screws shown in Figure A.2).

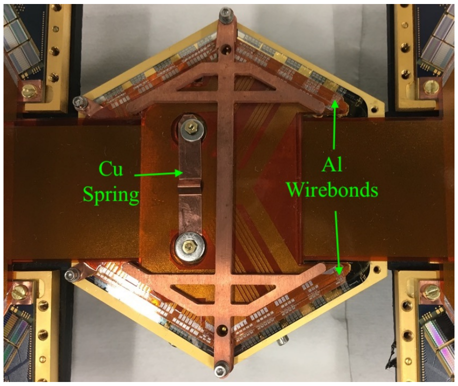

Figure A.5: Final Wirebonding: Next, we move the jig in Figure A.4 to a wirebonder to put down the final set of Al wirebonds from the detector bond pads to the Al traces on four sides of the wafer as shown here. While the bottom two flex circuit layers (RCs 9 and 10) are bonded to the detector bond pads located on the right half of the wafer, the top two layers (RCs 11 and 12) are bonded to the left half of the wafer. The RCs are designed such that the 150 and the 220 GHz detectors are mapped separately to two RCs per frequency band. Finally, a Cu spring is connected across the two tripod clip screws to prevent the screw from turning during cryogenic cycling.

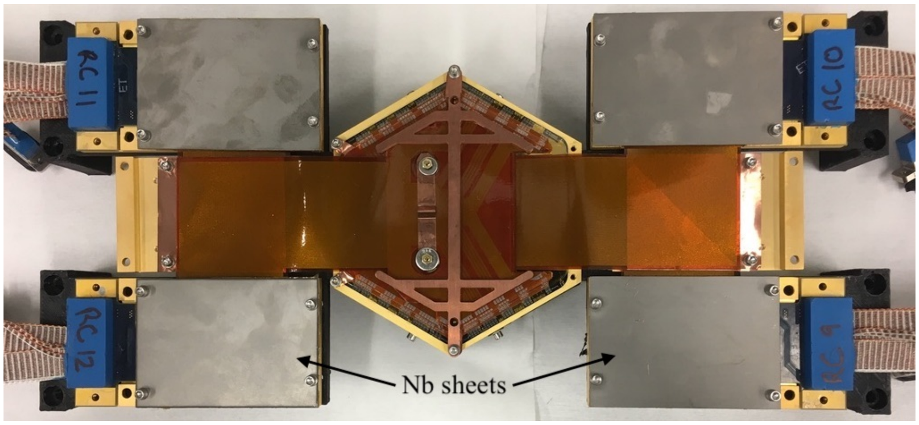
RC 11
RC 10
RC 12
RC 9
Nb sheets

Figure A.6: Magnetic Shielding: A Nb sheet is placed on top of each PCB using four Cu spacers (not shown). The spacers thermally connect the Nb to the module and keep the sheets safely above the Al wirebonds. The inner side of these sheets facing the wirebonds are also lined with polyimide Kapton insulation. Together with the Nb underneath the PCBs, these sheets form a magnetic insulation for the MUX chips.

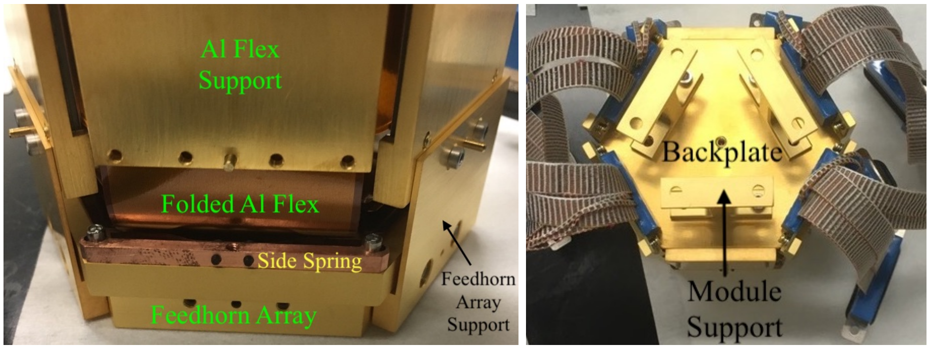
Al Flex Support
Folded Al Flex
Side Spring
Feedhorn Array
Feedhorn Array Support
Backplate
Module Support

Figure A.7: Folding: This is the final step of the module assembly where we remove the 3D-printed jig and fold up the Al flex circuits. The left and the right images show the side view (near the feedhorn array) and the back view of the folded module, respectively. On the feedhorn side, three Au-plated copper supports (only two of them are visible here) are used to mechanically support the feedhorn array to the rest of the module. (In the final module configuration, as shown in Figure A.9, the screws and the alignment pins on the feedhorn array supports are replaced so that their heads are flush with the support's surface.) A hexagonal backplate is used on the opposite side to support the readout packages and the flex circuits. Finally, three I-shaped supports are bolted to the backplate, which will be used to mount the module to the cryostat.

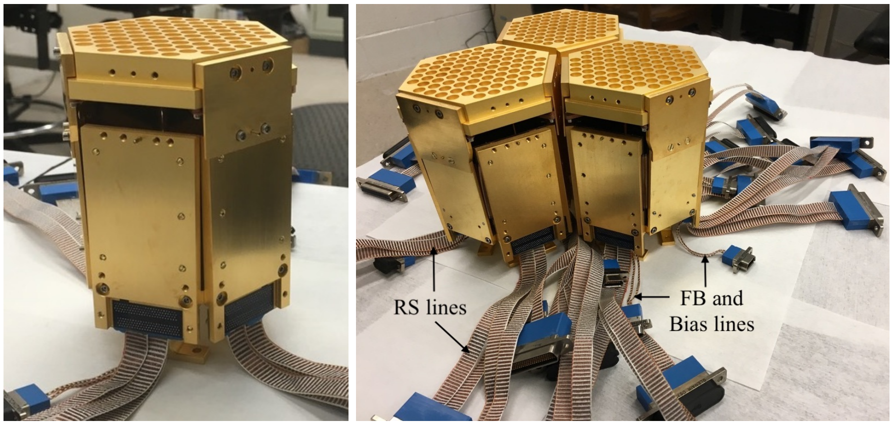

Figure A.8: Assembled Modules: (Left) A fully assembled HF module. The module contains 340 polarization-sensitive bolometers split equally between the 150 GHz and the 220 GHz frequency bands. (Right) The entire assembly procedure described from Figure A.1 to Figure A.7 is repeated two more times to assemble a total of three modules for the CLASS HF detector array. The wider NbTi cables seen here with the 100-pin connectors carry the row select (RS) lines, while the smaller cables with the 15-pin connectors carry the SQUID feedback (FB) and the SQUID and TES bias lines.

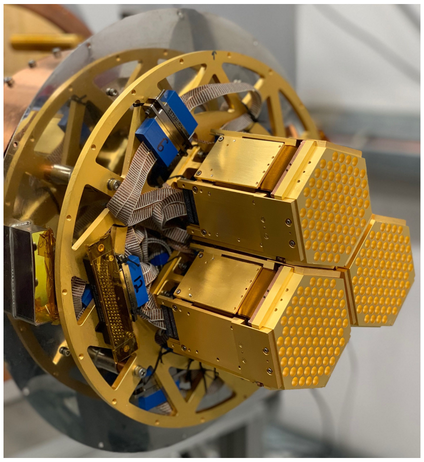

Figure A.9: CLASS HF Focal Plane: A Au-plated copper web interface is used to mount the three CLASS HF modules to the cryostat. While the feedback and bias lines seen in Figure A.8 are directly connected to the 4K SQUID Series Array board (not shown), the RS lines are daisy-chained together (one of the chain links is visible here with a Connector-9). The end of this chain (shown here with Connector-12) is shorted using a custom-made connector to complete the electrical circuit. Refer to Section 3.4 for further details on the CLASS detector readout. The reflective surface visible behind the modules is the backplate of a magnetic shielding can.

Appendix B

Venus Observations

While CLASS is designed primarily to observe the CMB polarization, its high sensitivity allows it to observe other microwave sources within its field of view. Aside from its regular CMB observations, CLASS sporadically observes on-sky calibration sources (primarily the Moon, Venus, and Jupiter) to obtain the telescope pointing information, characterize the beam response, and calibrate the detector power response to the antenna temperature of the source. As discussed in Chapter 6, since the Moon saturates most of the W-band detectors, we use the next brightest on-sky source, Venus, to calibrate the W-band instrument. However, the Venus W-band brightness temperature has not been studied extensively, primarily because telescopes are usually designed to point away from the Sun. However, due to its unique design and scan strategy, CLASS is well suited to observe Venus. Between 25 August 2018 and 11 October 2018, the CLASS Q-band and W-band telescopes performed 70 dedicated Venus observations. Since these instruments also observed the Moon and Jupiter, we can use the Moon (for Q-band) and Jupiter (for W-band) as calibrators to constrain the brightness temperature of Venus.

The microwave observations of Venus can be used to probe the hot and dense atmosphere of Venus that mostly (~ 96 %) consists of CO_2. The greenhouse effect from the thick Venusian atmosphere, that reaches ~ 90 bars at the surface, maintains the surface temperature at ~ 750 K (Muhleman, Orton, and Berge, 1979). While radio wavelengths $\gtrsim 4$ cm probe the surface, shorter wavelengths successively probe higher levels in the atmosphere with steep decrease in temperature due to the adiabatic temperature structure of the atmosphere (de Pater, 1990; Butler et al., 2001). The measurement of the brightness temperature and its phase dependence at different microwave frequencies can therefore reveal important information about the composition and properties of various layers of the Venusian atmosphere. Here we present the microwave observations of Venus at 40 and 90 GHz that roughly correspond to the effective altitude of emission around 35 km and 50 km from the surface, respectively.

B.1 Observations and Results

During the dedicated observations of the Moon or the planets, we scan the telescope across the source over small ranges of azimuth angle at a fixed elevation. As the telescope scans across the source, we obtain time-ordered data (TOD) for each detector at ~ 200 Hz. The raw TOD is converted to measured optical power and combined with the telescope pointing information during analysis. While we observed all three sources (the Moon, Venus, and Jupiter) with both telescopes, the Moon provides the highest signal-to-noise. However, it saturates the W-band detectors, hence it cannot be used as an absolute calibrator for the W-band instrument. Therefore, while we use the Moon to calibrate the Q-band Venus brightness temperature, we use Jupiter to calibrate the W-band temperature.

For a given CLASS frequency band, both Venus and its calibration source can be approximated as point sources given the CLASS beam sizes ($\sim 1.5^\circ$ FWHM for Q-band and $\sim 0.6^\circ$ for W-band). For a point source, its brightness temperature T_s relates to the peak response measured by CLASS detectors (T_m) as $T_\mathrm{s}\Omega_\mathrm{s} = T_\mathrm{m}\Omega_\mathrm{B}$ (Equation 6.4), where Ω_B is the CLASS beam solid angle and Ω_s is the solid angle subtended by the source (Page et al., 2003). To increase the signal-to-noise of the measurement, we stack the per-detector maps from individual observations. Since Ω_s changes between observations, the stacking is done relative to a fiducial solid angle Ω_ref. The data reduction and stacking of dedicated Moon observations for the CLASS Q-band instrument is described in detail in Xu et al. (2019). We followed a similar method to stack Venus and Jupiter maps as well. The data cuts applied for stacking the Venus and Jupiter observations are described in Section 6.4.

B.1.1 Brightness Temperature

As shown by Equation 6.4, if we scale the per-detector stacked maps for both the Venus and its calibration source to the same $\Omega_\mathrm{s} = \Omega_\mathrm{ref}$, the ratio of the peak response measured by CLASS detectors is equal to the ratio of their brightness temperatures. Figure B.1 shows the Venus peak amplitudes scaled to $\Omega_\mathrm{ref} = 5.5 \times 10^{-8}$ sr (i.e. $54.55''$ diameter) and the brightness temperature ratio of Venus to its calibrating source as measured by different CLASS detectors. For

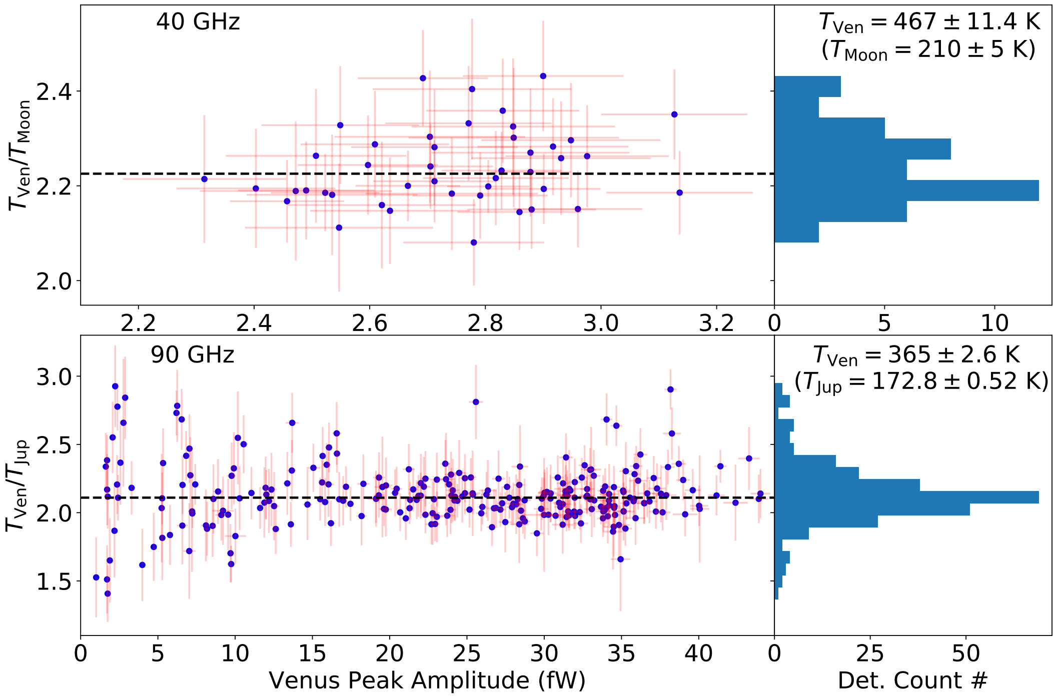

Figure B.1: (Left) The Venus to Moon (top) and Venus to Jupiter (bottom) brightness temperature ratios as compared to the Venus peak amplitude measured by the CLASS 40 and 90 GHz detectors, respectively. Each data point corresponds to the result obtained from the stacked maps for a particular detector. For a given detector, the brightness temperature ratio was calculated by scaling the measured peak amplitudes to a fiducial reference solid angle $\Omega_{\rm ref} = 5.5 \times 10^{-8}$ sr . The inverse-variance weighted mean ratios (dashed-line) for the 40 and 90 GHz detectors are 2.23 ± 0.01 and 2.11 ± 0.01, respectively. (Right) Histograms of the brightness temperature ratios. Multiplying the CLASS-measured ratios with the known brightness temperatures of the Moon and Jupiter gives the final Venus brightness temperatures at 40 and 90 GHz, respectively.

the 40 and the 90 GHz detector arrays, the inverse-variance weighted mean ratios are $T_{\mathrm{Ven}}/T_{\mathrm{Moon}} = 2.23 \pm 0.01$ and $T_{\mathrm{Ven}}/T_{\mathrm{Jup}} = 2.11 \pm 0.01$, respectively, where the uncertainties are the standard errors.

As the measured Moon peak response (T_{m} in Equation 6.4) depends both on its angular size and phase, the Moon's antenna temperature model presented in Appel et al. (2019) was used to stack the individual Moon maps. To obtain the absolute calibration for Q-band, we use the Moon's brightness temperature averaged across its Earth-facing hemisphere and across the lunar cycle $T_{\mathrm{Moon}} = 210 \pm 5$ K (Appel et al., 2019; Krotikov and Pelyushenko, 1987). Multiplying T_{Moon} with the CLASS-measured $T_{\mathrm{Ven}}/T_{\mathrm{Moon}}$ gives the Q-band Venus brightness temperature $T_{\mathrm{Ven}} = 467 \pm 11.4$ K.

For W-band, we use the CLASS-measured $T_{\mathrm{Ven}}/T_{\mathrm{Jup}}$ along with the *WMAP*-measured $T_{\mathrm{Jup}} = 172.8 \pm 0.5$ K (Bennett et al., 2013) to obtain $T_{\mathrm{Ven}} = 365 \pm 2.6$ K. Unlike the Moon, stacking of the individual Jupiter maps requires no phase correction. However, we corrected for the oblateness of Jupiter when scaling the measured peak response to the reference solid angle. Refer to Section 6.4 for details on the calculation of the Jupiter disk oblateness factor. To our knowledge, the tightest experimental constraint so far on the disk-averaged Venus brightness temperature at W-band is $T_{\mathrm{Ven}} = 357.5 \pm 13.1$ K from Ulich et al. (1980), measured at the band center of 86.1 GHz. Our measurement is within the error bars measured by Ulich et al. (1980) and is the most precise W-band Venus brightness temperature measured to date.

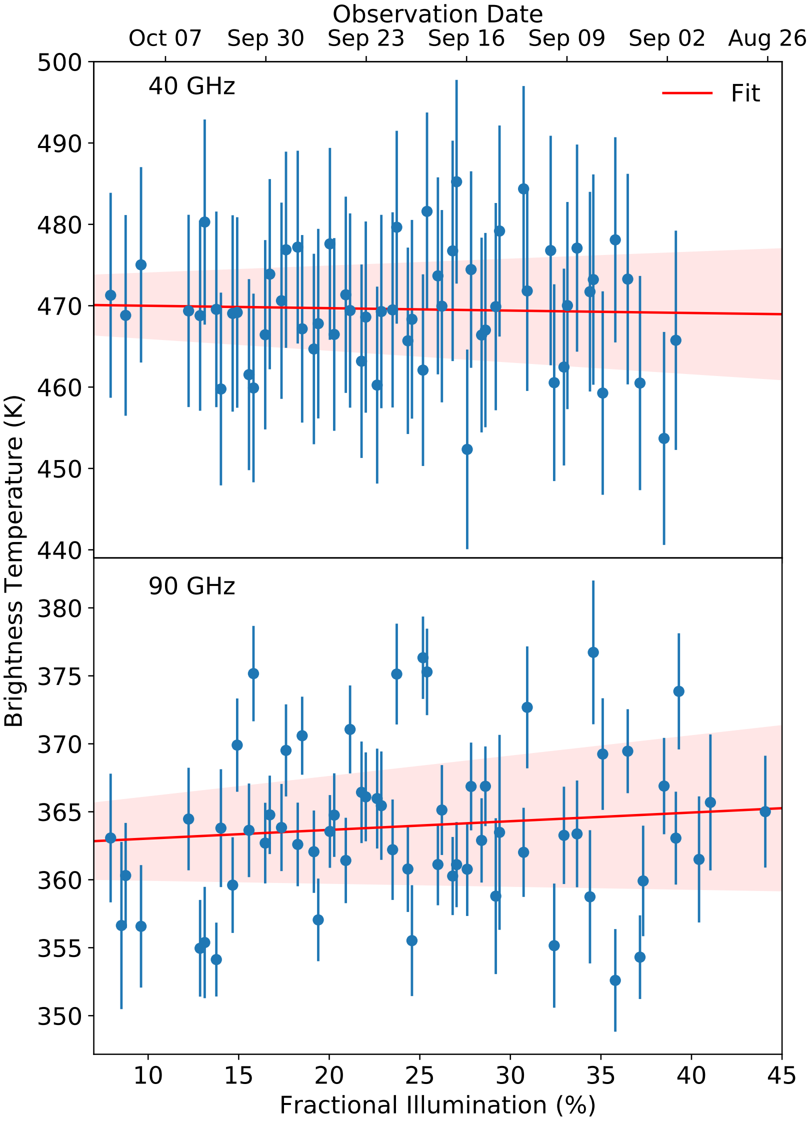

Figure B.2: Fractional solar illumination of Venus vs measured brightness temperature during the Venus observing campaign. Each data point corresponds to an array-averaged brightness temperature value obtained from that particular date. While the fractional illumination decreases from 44% to 8% during these observations, we do not observe any statistically significant phase-dependence of the measured temperatures. The best fit lines (red) correspond to a gradient of -0.03 ± 0.11 and 0.06 ± 0.09 for the 40 and the 90 GHz observations, respectively. The shaded regions show the 1σ uncertainties for the fits.

B.1.2 Phase

During the CLASS Venus observing campaign, the fractional solar illumination of Venus changed from 44% to 8% (with full illumination happening at the superior conjunction). To examine the phase dependence of the Venus brightness temperature, we calculate the array-averaged brightness temperature values for individual observations (i.e. before stacking the maps) using the calibration discussed in Section B.1.1. Figure B.2 shows the array-averaged Venus brightness temperatures plotted against the fractional solar illumination and its corresponding observation date. During this observing period, we observe no phase dependence of the Venus brightness temperature, i.e., the gradient of the array-averaged temperature values for different solar illuminations is statistically consistent to a flat line at both frequency bands. As highlighted in Figure B.2, the best fit lines have gradients of -0.03 ± 0.11 and 0.06 ± 0.09 for the 40 and the 90 GHz frequency bands, respectively.

B.2 Discussion

The microwave thermal emission from Venus is strongly affected by its atmospheric opacity. The Venusian atmospheric model used in Pater, Schloerb, and Rudolph (1991) shows that the opacity provided by CO_2 alone gives a W-band brightness temperature of 367 K. Therefore, our W-band measurement of 365 ± 2.6 K is consistent with a CO_2-dominant atmospheric layer. The modeled value being within the precision of our measurement also suggests that the Venus W-band emission coming from ~ 50 km altitude can be explained with a CO_2-alone atmosphere, without any significant presence of additional absorbers like SO_2 and H_2SO_4. Such absorbers in that layer would have added additional opacity for the thermal emission coming from the Venusian surface, hence decreasing the expected W-band brightness temperature from the CO_2-only model.

At Q-band, based on their observations near the superior conjunction, Basharinov et al. (1965) had reported $T_{\mathrm{Ven}} = 427 \pm 41\cos(\Phi - 21^\circ)$ K, where $0^\circ < \Phi < 360^\circ$ is the Venus phase angle. To explain this observation, Pollack and Sagan (1965) used an atmospheric model with dust distributed through the lower atmosphere with preferential abundance in the illuminated hemisphere which could lead to the $\sim \pm 10\%$ variation in brightness temperature amplitude relative to the Venus phase. However, our Q-band results are inconsistent with the Basharinov et al. (1965) results: our measured brightness temperature is much higher, and we observe no phase dependence. Instead, our Q-band results are consistent with the more recent measurement (at 33 GHz) from Hafez et al. (2008) where they report a Q-band brightness temperature of 462 ± 3.2 K[1] with no phase dependence throughout the 1.5 Synodic cycles of their Venus observations. Our results combined with Hafez et al. (2008) suggest that Basharinov et al. (1965) results might have some unaccounted for systematic error. Our observations suggesting no phase-dependence is also consistent with the atmospheric CO_2 being the dominant source of the millimeter opacity, making the dust-distributed model from Pollack and Sagan (1965) obsolete. While we could not find the W-band phase variation reported in published literature, we expect the variation amplitude (if any) to be even lower as compared to Q-band as the W-band emission comes from a higher and colder atmospheric layer.

---

[1] Hafez et al. (2008) report $T_{\mathrm{Ven}} = 460.3 \pm 3.2$ K relative to $T_{\mathrm{Jup}} = 146.6$ K. We scale the reported T_{Ven} slightly higher corresponding to $T_{\mathrm{Jup}} = 147.1$ K from Bennett et al. (2013).

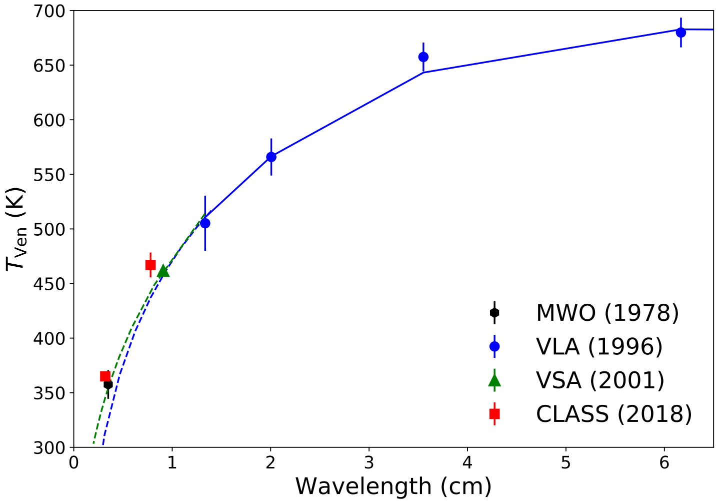

Figure B.3: Microwave spectrum of Venus. We compare the CLASS measurements with previous measurements from Millimeter Wave Observatory (MWO; Ulich et al. 1980), Very Large Array (VLA; Butler et al. 2001), and Very Small Array (VSA; Hafez et al. 2008). The solid blue line is an atmospheric model with no SO_2 and H_2SO_4 from Butler et al. (2001). The blue dashed line is a linear extrapolation (in log space) of the model towards shorter wavelengths. The green dashed line is the expected temperature from the best-fit spectral index at 33 GHz from Hafez et al. (2008).

Figure B.3 compares the CLASS results with other microwave Venus observations. We also extrapolate the brightness temperature model from Butler et al. (2001) and the best-fit temperature spectra from Hafez et al. (2008) to compare their predictions to our observations. The extrapolation of the Venusian atmospheric model with no SO_2 and H_2SO_4 presented in Butler et al. (2001) slightly underpredicts the brightness temperatures at CLASS frequency bands. However, the expected 90 GHz brightness temperature from the best-fit temperature spectral index of -0.278 ± 0.026 at 33 GHz presented in Hafez et al. (2008) matches the CLASS measurement well.

References

Appel, John W., Zhilei Xu, Ivan L. Padilla, Kathleen Harrington, Bastián Pradenas Marquez, Aamir Ali, Charles L. Bennett, Michael K. Brewer, Ricardo Bustos, Manwei Chan, David T. Chuss, Joseph Cleary, Jullianna Couto, Sumit Dahal, Kevin Denis, Rolando Dünner, Joseph R. Eimer, Thomas Essinger-Hileman, Pedro Fluxa, Dominik Gothe, Gene C. Hilton, Johannes Hubmayr, Jeffrey Iuliano, John Karakla, Tobias A. Marriage, Nathan J. Miller, Carolina Núñez, Lucas Parker, Matthew Petroff, Carl D. Reintsema, Karwan Rostem, Robert W. Stevens, Deniz Augusto Nunes Valle, Bingjie Wang, Duncan J. Watts, Edward J. Wollack, and Lingzhen Zeng (2019). "On-sky Performance of the CLASS Q-band Telescope". In: ApJ 876.2, 126, p. 126. DOI: `10.3847/1538-4357/ab1652`. arXiv: `1811.08287 [astro-ph.IM]`.

Basharinov, A. E., Yu. N. Vetukhnovskaya, A. D. Kuz'min, B. G. Kutuza, and A. E. Salomonovich (1965). "Measurements of the Brightness Temperature of Venus at 8 mm." In: Soviet Ast. 8, p. 563.

Bennett, C. L., D. Larson, J. L. Weiland, N. Jarosik, G. Hinshaw, N. Odegard, K. M. Smith, R. S. Hill, B. Gold, M. Halpern, E. Komatsu, M. R. Nolta, L. Page, D. N. Spergel, E. Wollack, J. Dunkley, A. Kogut, M. Limon, S. S. Meyer, G. S. Tucker, and E. L. Wright (2013). "Nine-year Wilkinson Microwave Anisotropy Probe (WMAP) Observations: Final Maps and Results". In: ApJS 208.2, 20, p. 20. DOI: `10.1088/0067-0049/208/2/20`. arXiv: `1212.5225 [astro-ph.CO]`.

Butler, Bryan J., Paul G. Steffes, Shady H. Suleiman, Marc A. Kolodner, and Jon M. Jenkins (2001). "Accurate and Consistent Microwave Observations of Venus and Their Implications". In: Icarus 154.2, pp. 226–238. DOI: `10.1006/icar.2001.6710`.

de Pater, Imke (1990). "Radio images of the planets." In: ARA&A 28, pp. 347–399. DOI: `10.1146/annurev.aa.28.090190.002023`.

Hafez, Yaser A., Rod D. Davies, Richard J. Davis, Clive Dickinson, Elia S. Battistelli, Francisco Blanco, Kieran Cleary, Thomas Franzen, Ricardo

Genova-Santos, Keith Grainge, Michael P. Hobson, Michael E. Jones, Katy Lancaster, Anthony N. Lasenby, Carmen P. Padilla-Torres, José Alberto Rubiño-Martin, Rafael Rebolo, Richard D. E. Saunders, Paul F. Scott, Angela C. Taylor, David Titterington, Marco Tucci, and Robert A. Watson (2008). "Radio source calibration for the Very Small Array and other cosmic microwave background instruments at around 30 GHz". In: MNRAS 388.4, pp. 1775–1786. DOI: `10.1111/j.1365-2966.2008.13515.x`. arXiv: `0804.2853 [astro-ph]`.

Krotikov, V. D. and S. A. Pelyushenko (1987). "On Using the Moon as a Source with a Standard Intensity in the 0.1-30 CM Wavelength Range". In: Soviet Ast. 31, pp. 216–219.

Muhleman, D. O., G. S. Orton, and G. L. Berge (1979). "A model of the Venus atmosphere from radio, radar, and occultation observations." In: ApJ 234, pp. 733–745. DOI: `10.1086/157550`.

Page, L., C. Barnes, G. Hinshaw, D. N. Spergel, J. L. Weiland, E. Wollack, C. L. Bennett, M. Halpern, N. Jarosik, A. Kogut, M. Limon, S. S. Meyer, G. S. Tucker, and E. L. Wright (2003). "First-Year Wilkinson Microwave Anisotropy Probe (WMAP) Observations: Beam Profiles and Window Functions". In: ApJS 148.1, pp. 39–50. DOI: `10.1086/377223`. arXiv: `astro-ph/0302214 [astro-ph]`.

Pater, Imke de, F.Peter Schloerb, and Alexander Rudolph (1991). "Venus imaged with the Hat Creek interferometer in the J = 1 - 0 CO line". In: *Icarus* 90.2, pp. 282 –298. DOI: `https://doi.org/10.1016/0019-1035(91)90107-5`.

Pollack, James B. and Carl Sagan (1965). "The microwave phase effect of Venus". In: *Icarus* 4.1, pp. 62 –103. DOI: `https://doi.org/10.1016/0019-1035(65)90018-7`.

Ulich, B., J. Davis, P. Rhodes, and J. Hollis (1980). "Absolute brightness temperature measurements at 3.5-mm wavelength". In: *IEEE Transactions on Antennas and Propagation* 28.3, pp. 367–377. DOI: `10.1109/TAP.1980.1142330`.

Xu, Zhilei, Michael K. Brewer, Pedro Fluxa, Yunyang Li, Keisuke Osumi, Bastian Pradenas, Aamir Ali, John W. Appel, Charles L. Bennett, Ricardo Bustos, Manwei Chan, David T. Chuss, Joseph Cleary, Jullianna Couto, Sumit Dahal, Rahul Datta, Kevin Denis, Rolando Dunner, Joseph Eimer, Thomas Essinger-Hileman, Kathleen Harrington, Jeffrey Iuliano, Tobias A. Marriage, Nathan Miller, Carolina Núñez, Ivan L. Padilla, Lucas Parker, Matthew A. Petroff, Rodrigo Reeves, Karwan Rostem, Duncan J. Watts, Janet Weiland, and Edward J. Wollack (2019). "Two-year Cosmology Large

Angular Scale Surveyor (CLASS) Observations: 40 GHz Telescope Pointing, Beam Profile, Window Function, and Polarization Performance”. In: *arXiv e-prints*, arXiv:1911.04499, arXiv:1911.04499. arXiv: `1911.04499 [astro-ph.IM]`.

Sumit Dahal

Department of Physics and Astronomy
Johns Hopkins University
sumit.dahal@jhu.edu

201 Bloomberg Center
3701 San Martin Dr.
Baltimore, MD 21218, USA

RESEARCH:

Cosmology, Cosmic Microwave Background, Inflation,
Microwave Instrumentation, Low Temperature Detectors,
Cryogenics, TES Bolometers, SQUIDs

EDUCATION:

2015 – 2020 Johns Hopkins University
Ph.D. Physics and Astronomy
Advisor: Charles L. Bennett
Thesis: Detectors for the Cosmology Large Angular Scale Surveyor (CLASS)

2011 – 2015 New York University Abu Dhabi
B.S. Physics and Mathematics, cum laude, Minor in Astronomy, ΦΒΚ
Advisor: Francesco Arneodo
Thesis: Characterization of Muon Events in XENON100 Dark Matter Detector

COLLABORATIONS:

2015 – Cosmology Large Angular Scale Surveyor (CLASS)
2013 – 2015 XENON Dark Matter Experiment
2012 – 2013 NYU Center for Cosmology and Particle Physics

OUTREACH:

2015 – 2019 Planetarium Manager, JHU Physics and Astronomy Outreach

CONFERENCE PRESENTATIONS:

1. Low Temperature Detectors (LTD), *The CLASS 150/220 GHz Polarimeter Array: Design, Assembly, and Characterization*, Milan, July 2019
2. SPIE Astronomical Telescopes + Instrumentation, *Design and characterization of the Cosmology Large Angular Scale Surveyor (CLASS) 93 GHz focal plane*, Austin, June 2018
3. Joint Meeting of American Physical Society and Astronomical Society of New York, *Is supernova remnant G12.8-0.0 really associated with the star forming region W33?*, New York, April 2014

INVITED TALKS:

1. Research and Innovation Conference, United Arab Emirates University, *Cosmology with the Cosmology Large Angular Scale Surveyor (CLASS)*, Al Ain, February 2019
2. New York University Abu Dhabi, *Cosmology and Technology with the Cosmic Microwave Background*, Abu Dhabi, February 2019

SELECTED PUBLICATIONS:

1. **S. Dahal**, J.W. Appel, C. Bennett, L. Corbett, R. Datta, K. Denis, T. Essinger-Hileman, K. Helson, G. Hilton, J. Hubmayr, B. Keller, T. Marriage, C. Nunez, M. Petroff, C. Reintsema, K. Rostem, K. U-Yen, E. Wollack. "The CLASS 150/220 GHz Polarimeter Array: Design, Assembly, and Characterization," J. Low Temp. Phys., 289-297, 2020

2. **Sumit Dahal**; Aamir Ali; John W. Appel; Thomas Essinger-Hileman; Charles Bennett; Michael Brewer; Ricardo Bustos; Manwei Chan; David T. Chuss; Joseph Cleary; Felipe Colazo; Jullianna Couto; Kevin Denis; Rolando Dünner; Joseph Eimer; Trevor Engelhoven; Pedro Fluxa; Mark Halpern; Kathleen Harrington; Kyle Helson; Gene Hilton; Gary Hinshaw; Johannes Hubmayr; Jeffery Iuliano; John Karakla; Tobias Marriage; Jeffrey McMahon; Nathan Miller; Carolina Nuñez; Ivan Padilla; Gonzalo Palma; Lucas Parker; Matthew Petroff; Bastian Pradenas; Rodrigo Reeves; Carl Reintsema; Karwan Rostem; Marco Sagliocca; Kongpop U-Yen; Deniz Valle; Bingjie Wang; Qinan Wang; Duncan Watts; Janet Weiland; Edward Wollack; Zhilei Xu; Ziang Yan; Lingzhen Zeng. "Design and characterization of the Cosmology Large Angular Scale Surveyor (CLASS) 93 GHz focal plane," Proc. SPIE, 107081Y, 2018

3. Aamir M. Ali, Thomas Essinger-Hileman, Tobias Marriage, John W. Appel, Charles L. Bennett, Matthew Berkeley, Berhanu Bulcha, **Sumit Dahal**, Kevin L. Denis, Karwan Rostem, Kongpop U-Yen, Edward J. Wollack, Lingzhen Zeng. "SiAl Alloy Feedhorn Arrays: Material Properties, Feedhorn Design, and Astrophysical Applications," Proc. SPIE, 107082P, 2018

4. Eric C. Bellm, David L. Kaplan, Rene P. Breton, E. Sterl Phinney, Varun B. Bhalerao, Fernando Camilo, **Sumit Dahal**, S. G. Djorgovski, Andrew J. Drake, J. W. T. Hessels, Russ R. Laher, David B. Levitan, Fraser Lewis, Ashish A. Mahabal, Eran O. Ofek, Thomas A. Prince, Scott M. Ransom, Mallory S. E. Roberts, David M. Russell, Branimir Sesar, Jason A. Surace, Sumin Tang. "Properties and Evolution of the Redback Millisecond Pulsar Binary PSR J2129-0429," ApJ, 816:74, 2016

5. F. Arneodo, M.L. Benabderrahmane, **S. Dahal**, A. Di Giovanni, M. D'Incecco, G. Franchi, L. Pazos Clemens. "An amplifier for VUV photomultiplier operating in cryogenic environment," Nuclear Instruments and Methods in Physics Research A, 275-276, 2016

6. F. Arneodo, M.L. Benabderrahmane, **S. Dahal**, A. Di Giovanni, L. Pazos Clemens, A. Candela, M. D'Incecco, D. Sablone, G. Franchi. “Muon tracking system with Silicon Photomultipliers,” Nuclear Instruments and Methods in Physics Research A, 166-171, 2015

ALL PUBLICATIONS:

7. John W. Appel, Zhilei Xu, Ivan L. Padilla, Kathleen Harrington, Bastián Pradenas Marquez, Aamir Ali, Charles L. Bennett, Michael K. Brewer, Ricardo Bustos, Manwei Chan, David T. Chuss, Joseph Cleary, Jullianna Couto, **Sumit Dahal**, Kevin Denis, Rolando Dünner, Joseph R. Eimer, Thomas Essinger-Hileman, Pedro Fluxa, Dominik Gothe, Gene C. Hilton, Johannes Hubmayr, Jeffrey Iuliano, John Karakla, Tobias A. Marriage, Nathan J. Miller, Carolina Núñez, Lucas Parker, Matthew Petroff, Carl D. Reintsema, Karwan Rostem, Robert W. Stevens, Deniz Augusto Nunes Valle, Bingjie Wang, Duncan J. Watts, Edward J. Wollack, Lingzhen Zeng. “On-Sky Performance of the CLASS Q-band Telescope,” ApJ, 876:126, 2019

8. Duncan J. Watts, Bingjie Wang, Aamir Ali, John W. Appel, Charles L. Bennett, David T. Chuss, **Sumit Dahal**, Joseph R. Eimer, Thomas Essinger-Hileman, Kathleen Harrington, Gary Hinshaw, Jeffrey Iuliano, Tobias A. Marriage, Nathan J. Miller, Ivan L. Padilla, Lucas Parker, Matthew Petroff, Karwan Rostem, Edward J. Wollack, Zhilei Xu. “A Projected Estimate of the Reionization Optical Depth Using the CLASS Experiment's Sample-Variance Limited E-Mode Measurement,” ApJ, 863:121, 2018

9. Jeffrey Iuliano; Joseph Eimer ; Lucas Parker; Gary Rhoades; Aamir Ali; John W. Appel; Charles Bennett ; Michael Brewer ; Ricardo Bustos ; David Chuss ; Joseph Cleary ; Jullianna Couto; **Sumit Dahal**; Kevin Denis; Rolando Dünner ; Thomas Essinger-Hileman; Pedro Fluxa ; Mark Halpern ; Kathleen Harrington ; Kyle Helson; Gene Hilton ; Gary Hinshaw ; Johannes Hubmayr ; John Karakla ; Tobias Marriage ; Nathan Miller ; Jeffrey John McMahon; Carolina Nuñez; Ivan Padilla ; Gonzalo Palma ; Matthew Petroff ; Bastian Pradenas Márquez; Rodrigo Reeves ; Carl Reintsema ; Karwan Rostem ; Deniz Augusto Nunes Valle; Trevor Van Engelhoven; Bingjie Wang ; Qinan Wang ; Duncan Watts ; Janet Weiland ; Edward J. Wollack ; Zhilei Xu; Ziang Yan ; Lingzhen Zeng. “The Cosmology Large Angular Scale Surveyor receiver design,” Proc. SPIE, 1070828, 2018

10. Kathleen Harrington; Joseph Eimer; David T. Chuss; Matthew Petroff; Joseph Cleary; Martin DeGeorge; Theodore W. Grunberg; Aamir Ali; John W. Appel; Charles L. Bennett; Michael Brewer; Ricardo Bustos; Manwei Chan; Jullianna Couto; **Sumit Dahal**; Kevin Denis; Rolando Dünner; Thomas Essinger-Hileman; Pedro Fluxa; Mark Halpern; Gene Hilton; Gary F. Hinshaw; Johannes Hubmayr; Jeffrey Iuliano; John Karakla; Tobias Marriage; Jeffrey McMahon; Nathan J. Miller; Carolina Nuñez; Ivan L. Padilla; Gonzalo Palma; Lucas Parker; Bastian Pradenas Marquez; Rodrigo Reeves; Carl Reintsema; Karwan Rostem; Deniz Augusto Nunes Valle; Trevor Van Engelhoven;

Bingjie Wang; Qinan Wang; Duncan Watts; Janet Weiland; Edward Wollack; Zhilei Xu; Ziang Yan; Lingzhen Zeng. “Variable-delay polarization modulators for the CLASS telescopes,” Proc. SPIE, 107082M, 2018

11. Kathleen Harrington; Tobias Marriage; Aamir Ali; John W. Appel; Charles L. Bennett; Fletcher Boone; Michael Brewer; Manwei Chan; David T. Chuss; Felipe Colazo; **Sumit Dahal**; Kevin Denis; Rolando Dünner; Joseph Eimer; Thomas Essinger-Hileman; Pedro Fluxa; Mark Halpern; Gene Hilton; Gary F. Hinshaw; Johannes Hubmayr; Jeffrey Iuliano; John Karakla; Jeff McMahon; Nathan T. Miller; Samuel H. Moseley; Gonzalo Palma; Lucas Parker; Matthew Petroff; Bastián Pradenas; Karwan Rostem; Marco Sagliocca; Deniz Valle; Duncan Watts; Edward Wollack; Zhilei Xu; Lingzhen Zeng, “The Cosmology Large Angular Scale Surveyor,” SPIE Proc., 99141K, 2016

SUCCESSFUL TELESCOPE PROPOSALS:

1. Joseph Gelfand, Liam Coatman, **Sumit Dahal**, Adam Dolan, “Radio Emission from SWIFT J0003.3-5254: Relic of Particle Acceleration in a Merging Galaxy Cluster?” Australia Telescope Compact Array (ATNF) Proposal, 2013